

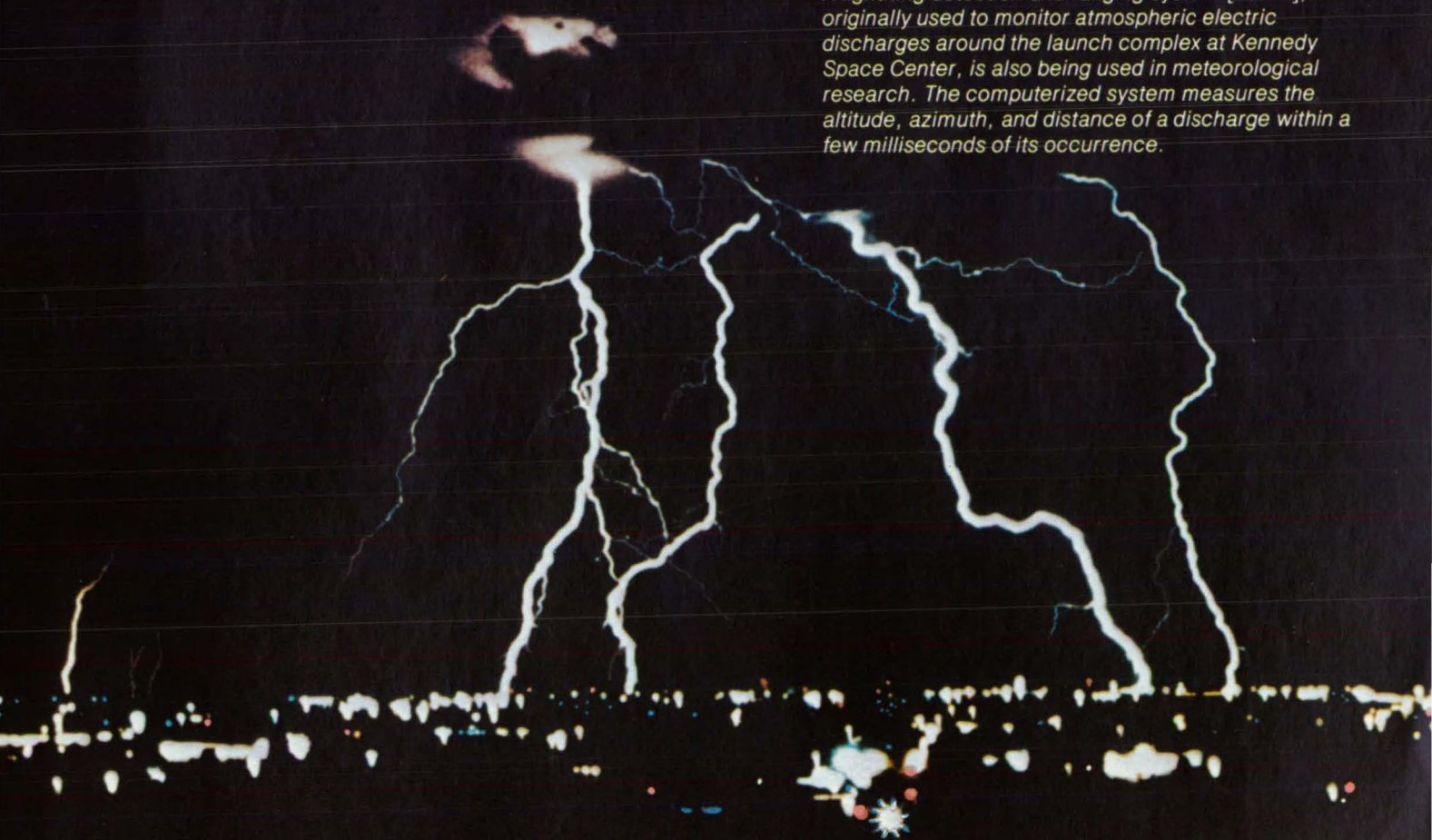
NASA Tech Briefs

National
Aeronautics and
Space
Administration

For information on
the NASA Tech Briefs
Cumulative Index . . . See Page A2.



A lightning detection and ranging system [LDAR], originally used to monitor atmospheric electric discharges around the launch complex at Kennedy Space Center, is also being used in meteorological research. The computerized system measures the altitude, azimuth, and distance of a discharge within a few milliseconds of its occurrence.



About the NASA Technology Utilization Program

The National Aeronautics and Space Act of 1958, which established NASA and the United States civilian space program, requires that "The Administration shall provide for the widest practicable and appropriate dissemination of information concerning its activities and the results thereof."

To help carry out this objective, NASA's Technology Utilization (TU) Program was established in 1962. Now, as an element of NASA's Technology Transfer Division, this program offers a variety of valuable services to help transfer aerospace technology to nonaerospace applications, thus assuring American taxpayers maximum return on their investment in space research; thousands of spinoffs of NASA research have already occurred in virtually every area of our economy.

The TU program has worked for engineers, scientists, technicians, and businessmen; and it can work for you.

NASA Tech Briefs

Tech Briefs is published quarterly and is free to engineers in U.S. industry and to other domestic technology transfer agents. It is both a current-awareness medium and a problem-solving tool. Potential products . . . industrial processes . . . basic and applied research . . . shop and lab techniques . . . computer software . . . new sources of technical data . . . concepts . . . can be found here. The short section on New Product Ideas highlights a few of the potential new products contained in this issue. The remainder of the volume is organized by technical category to help you quickly review new developments in your areas of interest. Finally, a subject index makes each issue a convenient reference file.

Further Information on Innovations

Although some new technology announcements are complete in themselves, most are backed up by Technical Support Packages (TSP's). TSP's are available without charge and may be ordered by simply completing a TSP Request Card found at the back of this volume. Further information on some innovations is available for a nominal fee from other sources, as indicated. In addition, Technology Utilization Officers at NASA Field Centers will often be able to lend necessary guidance and assistance.

Patent Licenses

Patents have been issued to NASA on some of the inventions described, and patent applications have been submitted on others. Each announcement indicates patent status, if applicable.

Other Technology Utilization Services

To assist engineers, industrial researchers, business executives, city officials, and other potential users in applying space technology to their problems, NASA sponsors Industrial Applications Centers. Their services are described on page A6. In addition, an extensive library of computer programs is available through COSMIC, the Technology Utilization Program's outlet for NASA-developed software.

Applications Program

NASA conducts applications engineering projects to help solve public-sector problems in such areas as safety, health, transportation, and environmental protection. Applications teams, staffed by professionals from a variety of disciplines, assist in this effort by working with Federal agencies and health organizations to identify critical problems amenable to solution by the application of existing NASA technology.

Reader Feedback

We hope you find the information in *NASA Tech Briefs* useful. A reader-feedback card has been included because we want your comments and suggestions on how we can further help you apply NASA innovations and technology to your needs. Please use it; or if you need more space, write to the Director, Technology Transfer Division, P. O. Box 8256, Baltimore/Washington International Airport, Maryland 21240.

NASA TU Services

A3

Technology Utilization services that can assist you in learning about and applying NASA technology.



New Product Ideas

A9

A summary of selected innovations of value to manufacturers for the development of new products.



Tech Briefs

1

Electronic Components and Circuits



15

Electronic Systems



37

Physical Sciences



65

Materials



79

Life Sciences



87

Mechanics



115

Machinery



133

Fabrication Technology



147

Mathematics and Information Sciences



Subject Index

153

Items in this issue are indexed by subject; a cumulative index will be published yearly.



COVERS: The photographs on the front and back covers illustrate developments by NASA and its contractors that have resulted in commercial and nonaerospace spinoffs. For information about the lightning detection and ranging system [KSC-11006], circle 105 on the TSP Request Card; for more facts about the high-temperature bearings [LEW-11930], circle 106.

About This NASA Publication

NASA Tech Briefs, a quarterly publication, is distributed free to qualified U.S. citizens to encourage commercial application of U.S. space technology. For information on publications and services available through the NASA Technology Utilization Program, write to the Director, Technology Transfer Division, P. O. Box 8757, Baltimore/Washington International Airport, Maryland 21240.

"The Administrator of National Aeronautics and Space Administration has determined that the publication of this periodical is necessary in the transaction of the public business required by law of this Agency. Use of funds for printing this periodical has been approved by the Director of the Office of Management and Budget."

This document was prepared under the sponsorship of the National Aeronautics and Space Administration. Neither the United States Government nor any person acting on behalf of the United States Government assumes any liability resulting from the use of the information contained in this document, or warrants that such use will be free from privately owned rights.

Change of Address

If you wish to have NASA Tech Briefs forwarded to your new address, use one of the Subscriptions cards enclosed in the back of this volume of NASA Tech Briefs. Be sure to check the appropriate box indicating change of address.

Communications Concerning Editorial Matter

For editorial comments or general communications about NASA Tech Briefs, you may use the Feedback card in the back of NASA Tech Briefs, or write to: The Publications Manager, Technology Transfer Division (ETU-6), NASA Headquarters, Washington, DC 20546. Technical questions concerning specific articles should be directed to the Technology Utilization Officer of the sponsoring NASA Center (addresses listed on page A4).

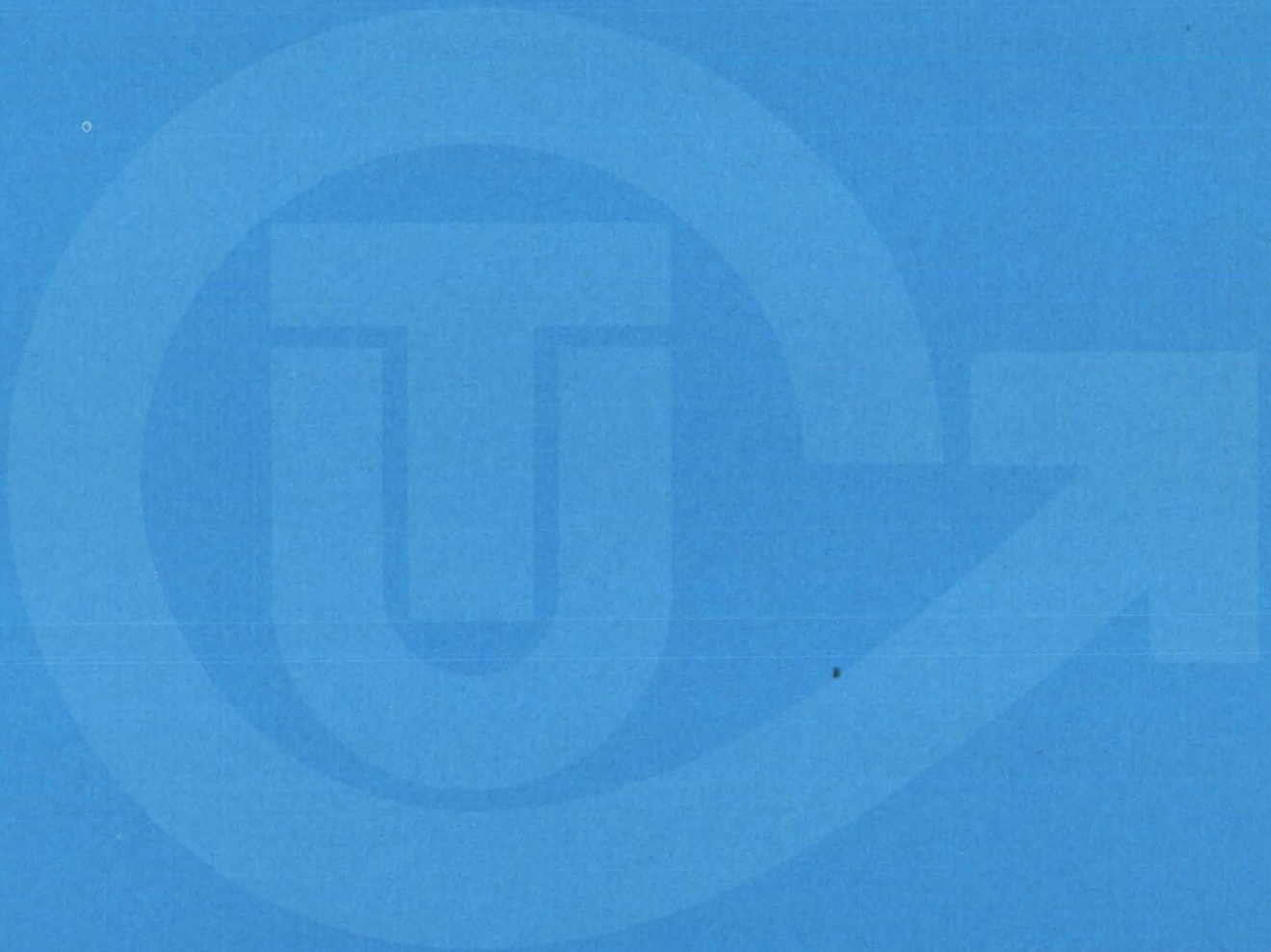
Cumulative Index [1970 Through 1975]

A limited supply of the NASA Tech Briefs Cumulative Index for the years 1970 through 1975 is available at a cost of \$7.50 each from the National Technical Information Service, Springfield, Virginia 22161. Order by NTIS Accession Number N-79-90067.

Acknowledgements

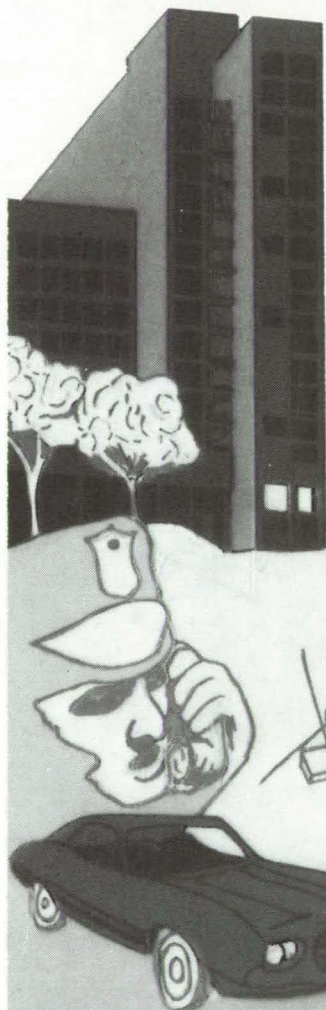
NASA Tech Briefs is published quarterly by the National Aeronautics and Space Administration, Technology Utilization Branch, Washington, DC: Administrator: **Robert A. Frosch**; Director, Technology Transfer Division: **Floyd I. Roberson**; Publications Manager: **D. W. Orrick**. Prepared for the National Aeronautics and Space Administration by **Logical Technical Services Corp.**: Editor-in-Chief: **Graham L. Gross**; Art Director: **Ernest Gillespie**; Managing Editor: **Jay Kirschenbaum**; Senior Editor: **Donald Blattner**; Chief Copy Editor: **Oden Browne**; Staff Editors: **Ted Selinsky**, **George Watson**; Graphics: **Bruce Appel**, **Concetto Auditore**, **Judy Tenenbaum**; Editorial & Production: **Richard Johnson**, **Rose Giglietti**, **Vincent Susinno**, **John Tucker**, **Madeline Tucker**, **Ernestine Walker**.

NASA TU SERVICES



THE NASA TECHNOLOGY UTILIZATION OFFICERS

They will help you apply the innovations described in Tech Briefs.



The Technology Utilization Officer (TUU)

Each NASA Center has a Technology Utilization Officer — An applications engineer whose job is to help you make use of new technology developed at his center. He brings you the NASA Tech Briefs and other special publications, sponsors conferences, and arranges for expert assistance in solving technical problems.

Technical Assistance

Working together with NASA Scientists and Engineers and the Industrial Applications Centers, the center TUO's can answer specific questions about innovations and related NASA technology.

Technical Support Package (TSP's)

For many of the innovations described in Tech Briefs, the center TUO has prepared additional material that will help you in detailed evaluation and actual use or construction of the new technology. You may get TSP's free of cost by using the TSP Request Card or writing the center TUO.

Who to Contact.

Of course, many technical questions about Tech Briefs are answered in the TSP's, but when no TSP is available, or you have further questions, write the Technology Utilization Officer at the center that sponsored the research at the address listed below.

Charles C. Kubokawa
Ames Research Center
Code AU: 240-2
Moffett Field, CA 94035
(415) 965-5554

Donald S. Friedman
Goddard Space Flight Center
Code 702.1
Greenbelt, MD 20771
(301) 344-6242

John T. Wheeler
Johnson Space Center
Code AT3
Houston, TX 77058
(713) 483-3809

Raymond J. Cerrato
John F. Kennedy Space Center
Code SA-RTP
Kennedy Space Center, FL 32899
(305) 867-2780

John Samos
Langley Research Center
Mail Stop 139A
Hampton, VA 23665
(804) 827-3281

Paul Foster
Lewis Research Center
21000 Brookpark Rd.
Cleveland, OH 44135
(216) 433-4000, Ext. 6832

Aubrey D. Smith
George C. Marshall Space Flight Center
Code AT01
Marshall Space Flight Center, AL 35812
(205) 453-2224

John C. Drane
NASA Resident Legal Office-JPL
4800 Oak Grove Drive
Pasadena, CA 91103
(213) 354-6420

Gilmore H. Trafford
Wallops Flight Center
Wallops Island, VA 23337
(804) 824-3411, Ext 201

D. W. Orrick
NASA Headquarters
Code ETU-6
Washington, DC 20546
(202) 755-2244

COSMIC

(Computer Software Management & Information Center)

AN ECONOMICAL SOURCE OF COMPUTER PROGRAMS DEVELOPED BY THE GOVERNMENT.

COSMIC is sponsored by NASA to give you access to over 1400 computer programs developed by NASA and the Department of Defense, and selected programs from other government agencies. It is one of the Nation's largest software libraries.

COSMIC charges very reasonable fees for programs to help cover part of their expenses—and NASA pays for the remainder. Programs generally cost from \$500 to \$1000, but a few are more expensive and many are less. Documentation is available separately and very inexpensively.

COSMIC collects and stores software packages, insures that they are complete, prepares special announcements (such as Tech Briefs), publishes an indexed software catalog, and reproduces programs for distribution. COSMIC helps customers to identify their software needs, follows up to determine the successes and problems, and provides updates and error corrections. In some cases, NASA engineers can offer guidance to users in installing or running a program.

COSMIC programs range from management (pert scheduling) to information science (retrieval systems) and computer operations (hardware and software). Hundreds of engineering programs perform such tasks as structural analysis, electronic circuit design, chemical analysis, and design of fluid systems. Others determine building energy requirements, optimize mineral exploration, and draw maps of water-covered areas using NASA satellite data. In fact, the chances are, if you use a computer, you can use COSMIC.

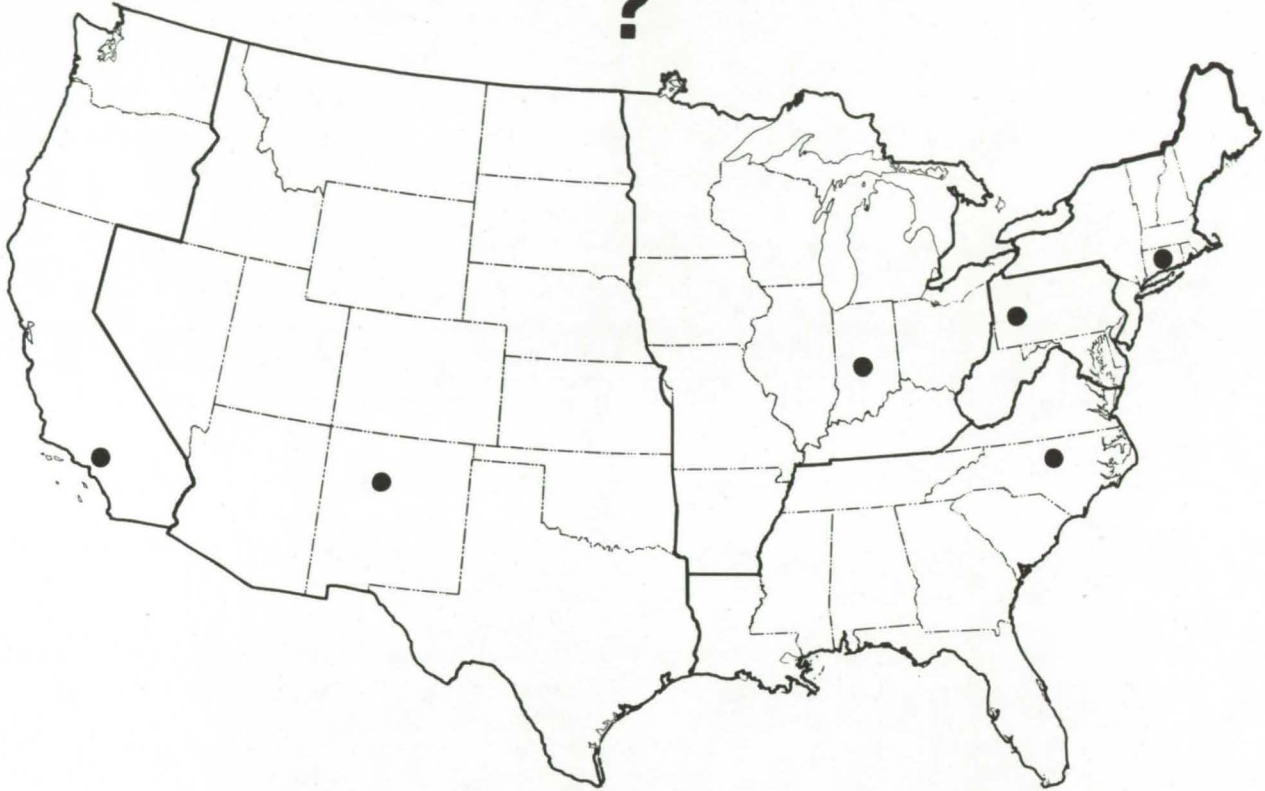
***COSMIC** is eager to help you get the programs you need. For more information about services or software available from COSMIC, fill out and mail the COSMIC Request Card in this issue.*

COSMIC: Computer Software Management and Information Center

Suite 112, Barrow Hall, University of Georgia, Athens, Georgia 30602 Phone: (404) 542-3265

WHERE IS THE WORLD'S LARGEST BANK OF TECHNICAL DATA

?



It's in Indianapolis and Pittsburgh, it's in Storrs, Connecticut and Research Triangle Park, North Carolina; and it's in Albuquerque and Los Angeles.

NASA IAC's — INDUSTRIAL

You can get more information and more data on more technical subjects through NASA's network of IAC's than anywhere else in the world. About 8,000,000 documents and growing at the rate of 50,000 more each month!

Major sources include:

- 750,000 NASA Technical Reports
- Selected Water Resources Abstracts
- NASA Scientific and Technical Aerospace Reports
- Air Pollution Technical Information Center
- NASA International Aerospace Abstracts
- Chem Abstracts Condensates
- Engineering Index
- Energy Research Abstracts
- NASA Tech Briefs
- Government Reports Announcements

and many other specialized files on food technology, textile technology, metallurgy, medicine, business, economics, social sciences, and physical science.

The IAC's are one of the most economical ways of staying competitive in today's world of exploding technology. The help available from the network ranges from literature searches through expert technical assistance.

Literature Searches

Help in designing your search, typically from 30 to 300 abstracts in as narrow or broad an area as you need, and complete reports when you need them. The most complete "search before research" available!

Current Awareness

Consult with our applications engineers to design your personal program — selected monthly or quarterly abstracts on new developments in your speciality. It's like having your own journal!

Technical Assistance

Our applications engineers will help you evaluate and apply your literature-search results. They can help find answers to your technical problems and put you in touch with scientists and engineers at NASA Field Centers.

To obtain more information about how NASA's IAC's can help you — Check the IAC box on the TSP Request Card in this issue, Or write or call the IAC nearest you.

APPLICATIONS CENTERS

How to get reports and other documents discussed in this issue of Tech Briefs

Many of the innovations in Tech Briefs are described in detail in reports available at a reasonable cost through one or more of the IAC's. To order a report, call or write the IAC referenced at the end of the Tech Brief article at the address below. Be sure to list the titles and accession numbers (N76-..., N75-..., etc.) of those you wish to purchase.

Aerospace Research Application Center (ARAC)
Indiana University-Purdue University at Indianapolis
1201 E. 38th St.
Indianapolis, IN 46205
E. Guy Buck, Director
(317) 264-4644

Knowledge Availability Systems Center (KASC)
University of Pittsburgh
Pittsburgh, PA 15260
Dr. Edmond Howie, Director
(412) 624-5211

New England Research Application Center (NERAC)
Mansfield Professional Park
Storrs, CT 06268
Dr. Daniel U. Wilde, Director
(203) 486-4533

North Carolina Science & Technology
Research Center (NC/STRC)
P. O. Box 12235
Research Triangle Park, NC 27709
Peter J. Chenery, Director
(919) 549-0671

Technology Application Center (TAC)
University of New Mexico
Albuquerque, NM 87131
Stanley A. Morain, Director
(505) 277-4000

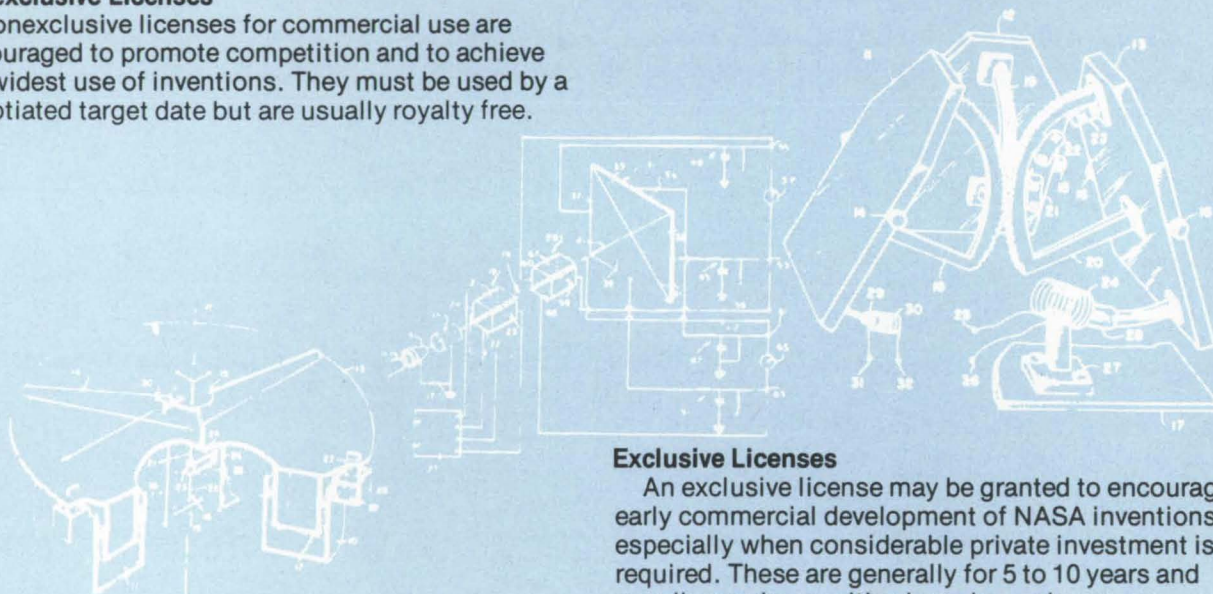
NASA Industrial Application Center
Denney Research Building - 3rd Fl.
University of Southern California
University Park
Los Angeles, CA 90007
Dr. Robert Y. Mixer, Director
(213) 741-6132

NASA INVENTIONS AVAILABLE FOR LICENSING

Over 3,500 NASA inventions are available for licensing in the United States - both exclusive and nonexclusive.

Nonexclusive Licenses

Nonexclusive licenses for commercial use are encouraged to promote competition and to achieve the widest use of inventions. They must be used by a negotiated target date but are usually royalty free.



Exclusive Licenses

An exclusive license may be granted to encourage early commercial development of NASA inventions, especially when considerable private investment is required. These are generally for 5 to 10 years and usually require royalties based on sales or use.

The NASA patent licensing program also provides for licensing of NASA-owned foreign patents. In addition to inventions described in Tech Briefs, "NASA Patent Abstract Bibliography," containing abstracts of all NASA inventions, can be purchased from: National Technical Information Service, Springfield, Va., 22161. This document is updated semi-annually.

Patent Licenses and the NASA Tech Brief

Many of the inventions reported in Tech Briefs are patented or are under consideration for a patent at the time they are published. When this is the case, the current patent status is described at the end of the article; otherwise, there is no statement about patents. **If you want to know more about the patent program or are interested in license for a particular invention, write the Patent Counsel at the NASA Field Center that sponsored the research. Be sure to refer to the NASA reference number in parenthesis at the end of the Tech Brief.**

Gayle Parker
NASA Headquarters, Code GP-4
400 Maryland Ave., S.W.
Washington, DC 20546
(202) 755-3954

Darrell G. Brekke
Ames Research Center
Mail Code: 200-11A
Moffett Field, CA 94035
(415) 965-5104

John O. Tresansky
Goddard Space Flight Center
Mail Code: 204
Greenbelt, MD 20771
(301) 344-7351

Marvin F. Matthews
Lyndon B. Johnson Space Center
Mail Code: AM
Houston, TX 77058
(713) 483-4871

James O. Harrell
John F. Kennedy Space Center
Mail Code: SA-PAT
Kennedy Space Center, FL 32899
(305) 867-2544

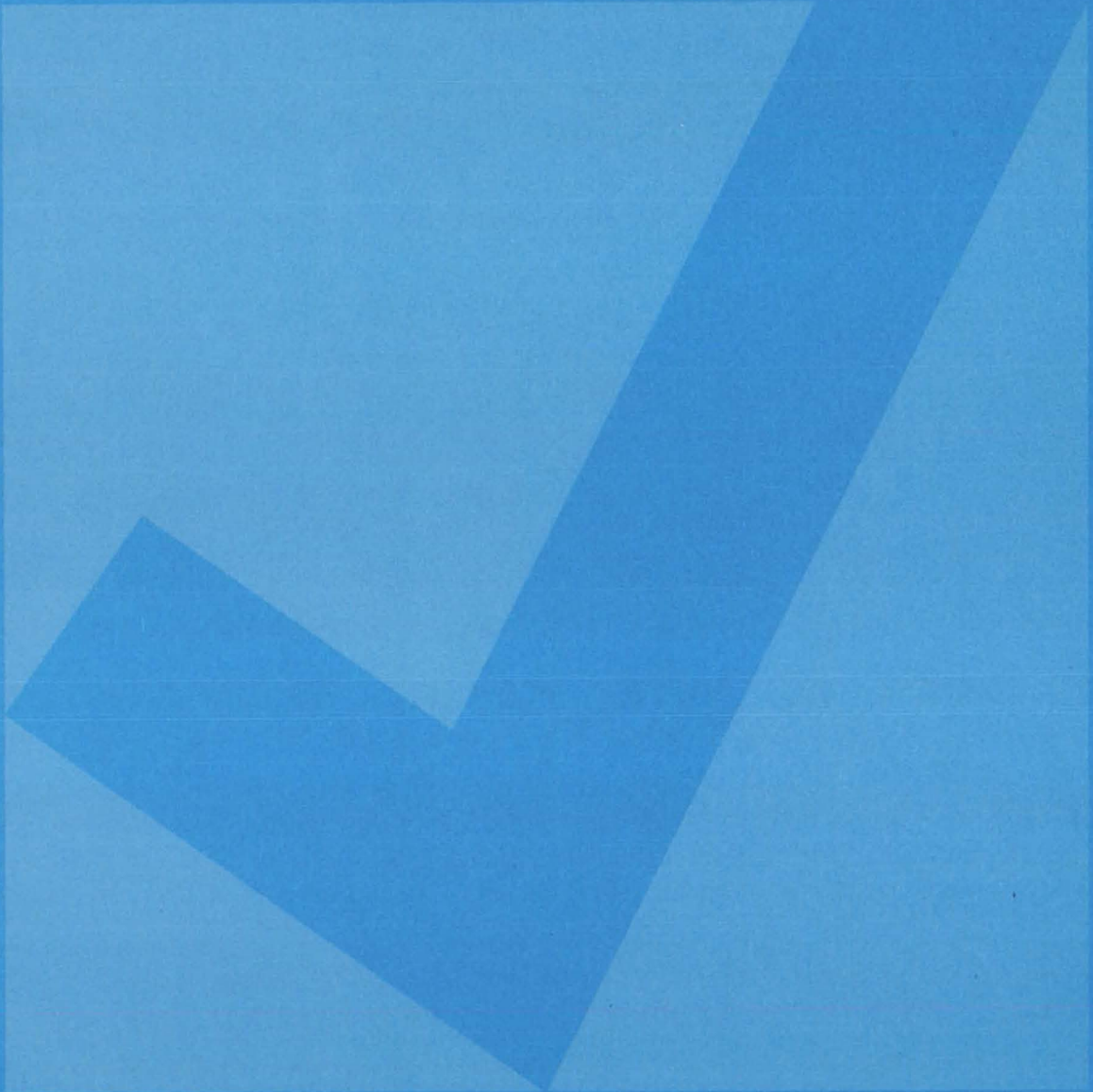
Howard J. Osborn
Langley Research Center
Mail Code: 279
Hampton, VA 23665
(804) 827-3725

Norman T. Musial
Lewis Research Center
Mail Code: 500-311
21000 Brookpark Road
Cleveland, OH 44135
(216) 433-4000 ext. 346

Leon D. Wofford, Jr.
George C. Marshall Space Flight Center
Mail Code: CC01
Marshall Space Flight Center, AL 35812
(205) 453-0020

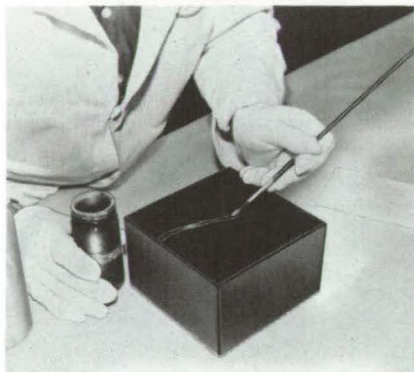
Monte F. Mott
NASA Resident Legal Office
Mail Code: 180-601
4800 Oak Grove Drive
Pasadena, CA 91103
(213) 354-2700

NEW PRODUCT IDEAS



NEW PRODUCT IDEAS are just a few of the many innovations described in this issue of NASA Tech Briefs and having promising commercial applications. Each is discussed further on the referenced page in the appropriate section in this issue. If you are interested in developing a product from these or other NASA innovations, you can receive further technical information by requesting the TSP referenced at the end of the full-length article or by writing the Technology Utilization Office of the sponsoring NASA center (see page A4). NASA's patent-licensing program to encourage commercial development is described on page A8.

Repairing Cracked Glass

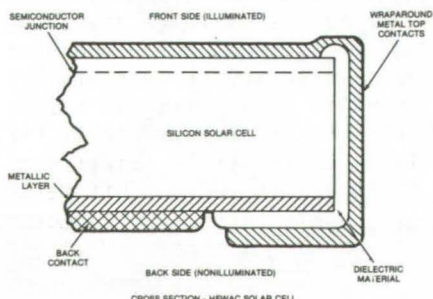


Punctures and cracks in cryogenic Dewars, X-ray tubes, and other glass objects are quickly repaired by a procedure originally used on insulating tiles for the Space Shuttle. A slurry of glass frits is applied with a brush or spray gun, and the coating is cured under a heat lamp. Careful inspection shows the resulting seal to be homogeneous and durable. In contrast to other methods, which require that the object be removed for the repair, the new technique is done *in situ*, saving time and effort. Thus far, the procedure has been applied to glass layers 0.01 to 0.02 inch in thickness, although it should also work for thicker glass.

(See page 135.)

Wraparound-Contact Solar Cells

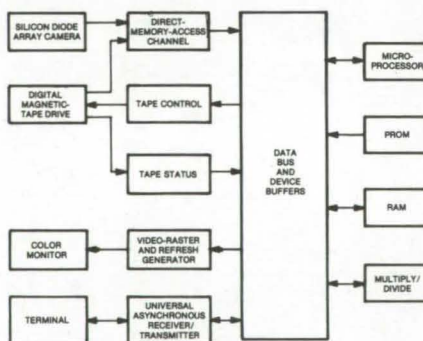
The positive and negative electrical contacts are on the back (nonilluminated) surface of a new wraparound-contact solar cell. With both terminals



on the nonilluminated side, cells can be connected back-to-back, and the interconnection of many cells can be automated by using printed-circuit techniques. The new cells are made by screen-printing a layer of dielectric around the edge of the cell and extending the top contact over the dielectric to the back surface. The wraparound also facilitates the application of transparent covers and encapsulants. Efficiencies of the new cells are in excess of 17 percent (air mass zero).

(See page 3.)

Microcomputer-Based Burn Analyzer

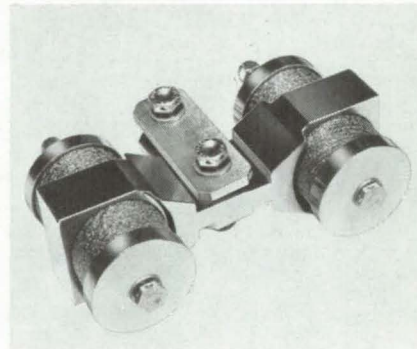


Burn victims are diagnosed more quickly and more effectively by a new microcomputer-controlled burn analyzer. Reflectances of the burn area are measured in three spectral bands and, using algorithms developed during previous and continuing experiments, are correlated with burn depth by the computer. A color-coded image of the burn area is then displayed on a video monitor: Yellow or white areas represent deep full-thickness burns, shallow full-thickness burns are red, and partial-thickness burns are blue. By helping the physician decide exactly how much tissue to remove early in treatment, the system can reduce infection, scarring, and the loss of function in burn victims.

(See page 82.)

Metallic Vibration Isolators

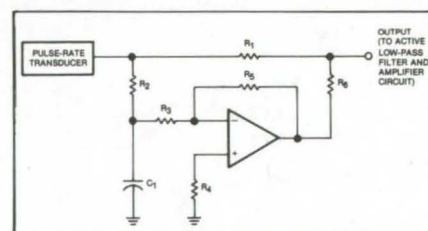
Woven-steel vibration isolators that behave like cantilever springs under an applied load could find uses where the strength and durability of conventional rubber shock absorbers are inadequate. Originally developed to operate in the harsh environment of outer space, the isolators withstand temperatures to 250° C, pressures to 150 psig, and shocks of up to 70 psi.



High-strength corrosion-resistant steel forms the isolator outer casing, and "biscuits" made of woven steel are the load-bearing material. The isolators can be tailored to absorb loads in one, two, or three mutually orthogonal directions.

(See page 127.)

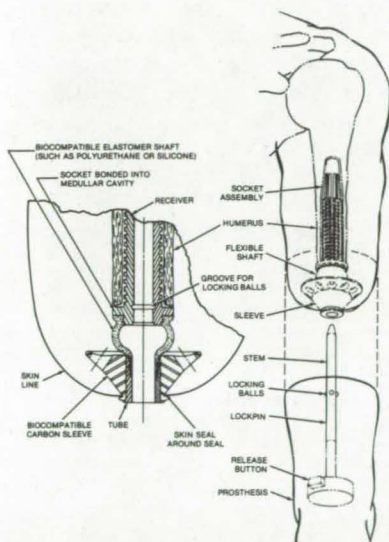
Miniature Low-Frequency Attenuator



A low-frequency attenuator uses only a single operational amplifier and a few passive components to remove background noise from a miniature "wristwatch" pulse detector. It could be applied in other systems where background noise is slowly varying,

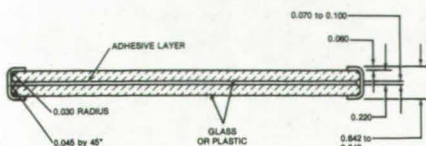
such as ultrasonics, strain-gage sensors, and accelerometers. The circuit filters the large dc background that is due to light reflected off the outer skin surface and the roughly sinusoidal signal that develops as the person walks; left unfiltered is the photosensor signal generated in response to light reflected off blood vessels just under the skin. The circuit monitors the average dc level of the photosensor output, generates the algebraic negative, and adds it to the raw output. Slowly varying components are thus subtracted before further processing. (See page 11.)

Artificial Limb Connector



An improved connector for an arm or a leg prosthesis promotes healing and relieves skin stresses around the artificial limb. It consists of a flexible shaft attached to a socket at one end and to a carbon sleeve at the other end. The assembly is surgically implanted in the bone, and a skin seal forms around the sleeve. A stem on the prosthesis is inserted and locked in the socket. Since the shaft is flexible, it allows the sleeve to "float" without breaking the skin seal. (See page 83.)

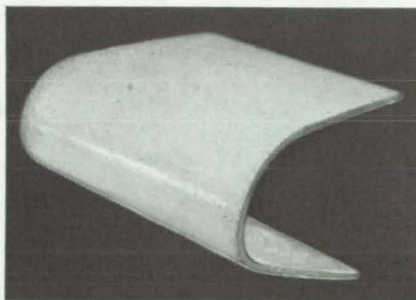
Window With Integral Seal



A proposed "self-sealing" laminated window would be considerably easier to install than conventional laminated or double-pane windows. By extending the pliable inner layer of laminating adhesive around the window edge, a built-in gasket is formed that replaces conventional O-rings, gaskets, and sealants. Estimates of the costs for special tooling to cast the overlapping adhesive layer indicate that they would be offset by savings in costs for installation hardware and for assembly. Potentially useful where space is limited, the new window could be installed in aircraft and in marine and land vehicles. (See page 140)

Low-Absorptance Porcelain-on-Aluminum Coating

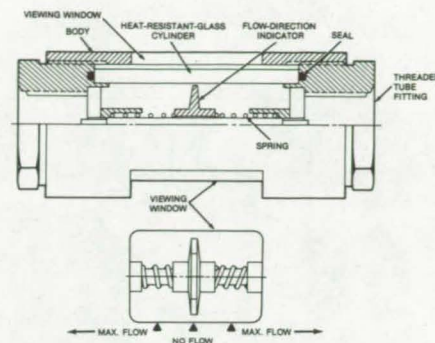
A porcelain coating for aluminum, originally developed to protect satellites from overheating under the intense rays of the Sun, could have terrestrial applications protecting sensitive components. The coating has a solar absorptance of only 0.22,



as compared to 0.31 for commercial porcelain-enameled aluminum. It is made by combining two ground-glass frits. After firing, one frit becomes a "host" having a low index of refraction, and the other frit precipitates as a high-index-of-refraction pigment. The porcelain resists humidity, high temperatures, cleaning agents, quenching, and other postporcelainization treatments. (See page 75.)

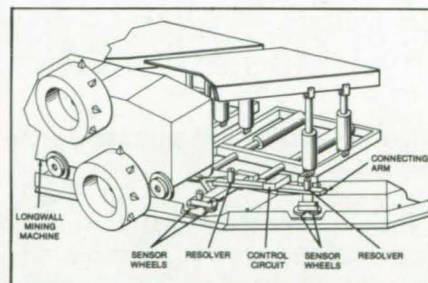
Bidirectional Fluid-Flow Monitor

A proposed bidirectional fluid-flow monitor would detect flow rates as low as 0.1 gal/min at temperatures up to 350° F and pressures up to 500 psig.



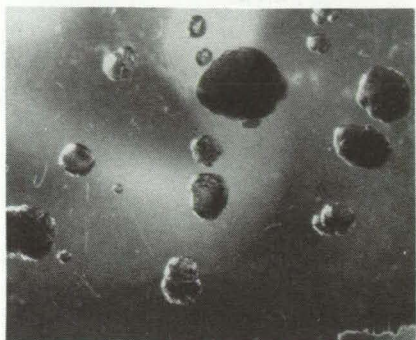
The monitor shows "no flow" and "maximum flow" conditions and approximately indicates intermediate flow rates. Relatively simple in design, the monitor consists of a disk riding on a shaft and balancing springs that push against the sides of the disk. The pressure of the flowing fluid displaces the disk by an amount that is a measure of the flow rate. The balancing springs are calibrated so that the disk aligns with NO FLOW or MAX. FLOW decals on viewing windows when either of these flow conditions prevails. (See page 92.)

Ensuring Flat Cuts in Longwall Mining



A microcomputer-controlled towed vehicle automatically determines the flatness of a wall of coal as it is being won by a mining machine. The vehicle thus allows the machine operator to correct the cut if it deviates from the planned path. Already built and successfully tested as a prototype, the towed vehicle measures the angle between adjacent track sections and computes the mine face contour from these data. Repeated checks reduce errors due to uncertainties in the starting angle and the curvature of individual track sections. The measurements and calculations are printed out, and a plot of the path is displayed on a cathode-ray tube. (See page 117.)

"Self-Packaging" Desiccant



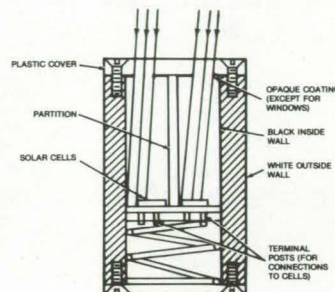
A new desiccant, consisting of a water-soluble filler in an elastomeric matrix, absorbs large quantities of water without becoming sticky or releasing corrosive agents. Possible applications include the protection of electronic components, optical instruments, pharmaceuticals, and chemicals. The composition can be cast as a thin film for lining the walls of a

container, as an insert for a screw-on cap, or in many other shapes. As moisture diffuses through the elastomer into the filler, it is collected in spaces that gradually grow into spherical pockets. When the filler has absorbed its full capacity, it can be regenerated by heating to drive off the moisture.
(See page 67.)

Sun Tracker for Clear or Cloudy Weather

Solar concentrators can follow the Sun to within 0.25° of arc by using an improved tracking device. Superior to many conventional trackers, the new device is not "fooled" by bright clouds, by a hole in the cloud cover, or by other atmospheric conditions. When the Sun is hidden, an internal clock duplicates the Sun motion to within $\pm 5^\circ$ over an entire day. Two

solar cells separated by a partition sense the direction of incoming Sunlight. Exactly one-half of each cell



is illuminated when the Sun is overhead. As the Sun moves, the output of one cell drops, and the output of the other cell increases, creating a difference signal. The tracker electronics process the difference signal to correct the concentrator orientation.
(See page 42.)

ANNOUNCING . . .

A NEW NASA TECHNOLOGY UTILIZATION SERVICE in Cooperation With STATE GOVERNMENTS

NASA recently inaugurated a State Technology Applications Center (STAC) program with the opening of facilities in Florida and Kentucky.

The purpose of the experimental STAC program is to provide technical information services to state and local government agencies as well as to industry within each state.

The STAC's differ from the NASA Industrial Applications Centers (see page A7) primarily in that the STAC's are integrated into existing state technical assistance programs and serve only the host state, whereas the Industrial Applications Centers serve multistate regions.

The STAC's have access to several commercial data bases, as well as the NASA data base, and they normally charge a fee for their services.

Persons wishing **further information** should write to:

In Florida

NASA/Florida State Technology Applications Center (STAC)
311 Weil Hall
University of Florida
Gainesville, Florida 32611

or phone, Gainesville: (904) 392-6760
Orlando: (305) 275-2706
Tampa: (813) 974-2499

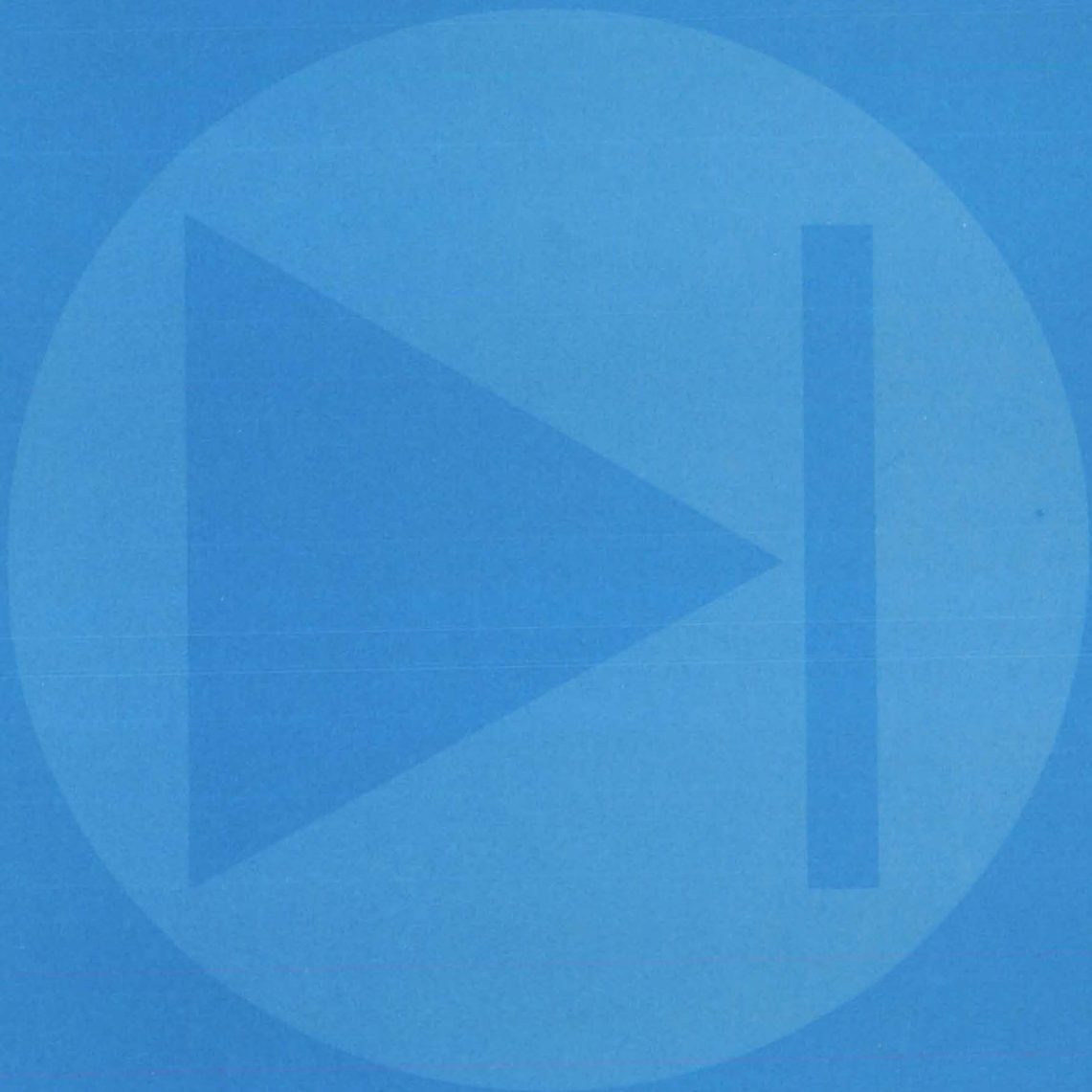
or contact the local State Department of Commerce
Business Development Representative

In Kentucky

NASA/University of Kentucky State Technology Applications Program (STAP)
109 Kinkead Hall
University of Kentucky
Lexington, Kentucky 40506

phone: (606) 258-4632

Electronic Components and Circuits



Hardware, Techniques, and Processes

- 3 Wraparound-Contact Solar Cells
- 4 Efficient Dichroic Plate for Microwaves
- 5 Low-Backlobe Microwave Transmitting Horn
- 6 Fast-Response Power Saver for Induction Motors
- 7 VHF Frequency Multiplier
- 8 Fiber-Optic Crossbar Switch
- 9 Improved InSb Photodiode Preamplifier Circuit
- 10 Decision-Directed Automatic Gain Control
- 10 Self-Calibrating Threshold Detector for Noisy Signals
- 11 Low-Frequency Attenuator Circuit
- 12 Low-Noise Current Regulator
- 13 Improved Isolation in Double-Balanced Mixers

Books and Reports

- 14 Reliability of Imaging CCD's
- 14 Group-Delay Standards

Wraparound-Contact Solar Cells

Wraparound contacts make automated production easier and increase efficiency.

Lewis Research Center, Cleveland, Ohio

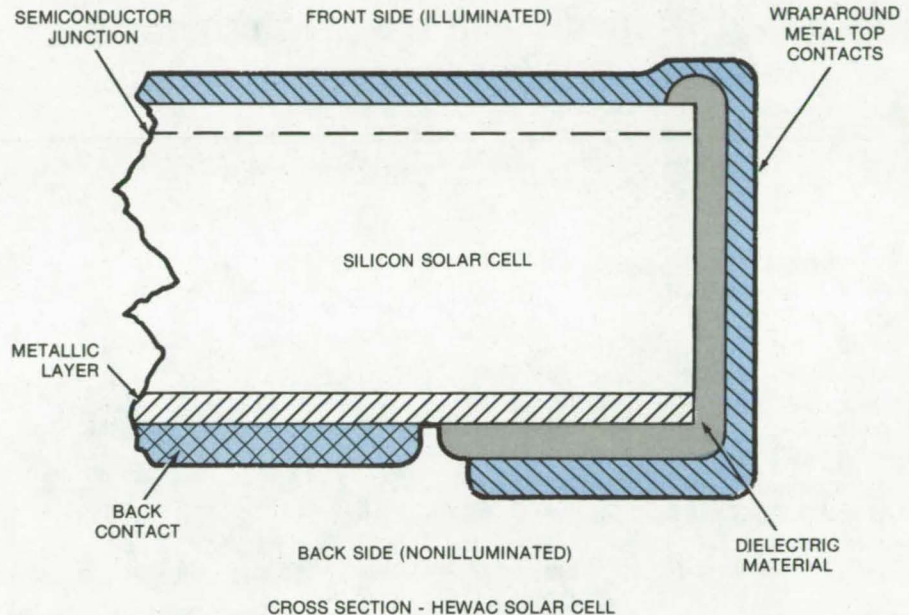
The High Efficiency Wraparound Contact (HEWAC) Solar Cell is the first high-performance silicon solar cell in a form that permits low-cost, high-volume production using efficient automated printed-circuit technology. Both positive and negative electrical contacts are on the back (nonilluminated) side of the cell. Efficiencies in excess of 15 percent air mass zero or 17 percent air mass one combined with the production cost advantages of wraparound contact construction make it exceedingly attractive for both space and ground applications.

The HEWAC solar cell, like all photovoltaic energy-conversion devices, converts solar (light) energy directly into electrical energy according to well-known semiconductor principles.

The HEWAC solar cell consists of a semiconductor base material, a screen-printed wraparound insulating layer, wraparound metal top-surface contacts with minimum area, a screen-printed aluminum back-surface field, a texturized front (illuminated) surface with a vacuum-evaporated antireflection coating, and a shallow diffused junction.

The wraparound contact design greatly simplifies interconnection of cells in an array (i.e., a group of cells connected together to produce power) and makes possible the use of low-cost, automated, printed-circuit interconnection methods. For conventional cells, interconnects must be made from the front of one cell to the back of the next, and typically a stress relief loop is used to minimize thermally-induced stress failure in the connecting wire.

With wraparound contact cells, interconnects are coplanar and nearly stress-free, resulting in a significant increase in reliability along with increased producibility. In addition, by eliminating stress relief loops and top contact pads, application of protective transparent covers or encapsulants is facilitated and front grid coverage



Wraparound Contact permits efficient solar cells to be manufactured in large quantities, using automated printed-circuit methods. The wraparound contacts allow cells in an array to be connected back-to-back, a distinct advantage over conventional front-to-back connections requiring strain reliefs. This design also facilitates the application of transparent covers or encapsulants and increases efficiency by reducing front grid coverage.

reduced, thus increasing the illuminated area and the efficiency. The HEWAC solar cell offers substantial performance improvement over previous wraparound insulator designs. Its unique construction combining conventional solar-cell technology with low-cost screen-printing fabrication processes gives both high efficiency and automated-production suitability.

During fabrication, the illuminated surface is texturized and coated with antireflection material such as Ta_2O_5 , and the semiconductor junction is formed by conventional methods. A metallic layer such as aluminum is screen-printed onto the entire back surface, dried, and fired, forming a back-surface field to enhance cell performance. A dielectric material such as SiO_2 or Al_2O_3 is screen-printed around the edge of the cell.

Careful control of screen and squeegee interaction causes the paste to flow around the edge of the cell, barely overlapping onto the illuminated surface. This dielectric insulator also partially overlaps the back-surface field and electrically isolates the wraparound metal top contacts from the back contact material, the silicon substrate, and the p and n regions of the junction on the edge of the cell. Multiple layers of dielectric are printed, dried, and fired, to produce the wraparound insulator.

This work was done by Cosmo R. Baraona and Thomas M. Klucher of Lewis Research Center and Jay W. Thornhill and John Scott-Monck of Spectrolab, Inc. Further information may be found in:

NASA CP-2020 [N78-13527], page 91/94, "Advanced High Efficiency" (continued on next page)

Wraparound Contact Solar Cell" [N78-13536], April 1977; and NASA CR-135202 [N77-32590], "Automated Fabrication and Back Surface Field Silicon Solar Cells

with Screen Printed Wraparound Contacts." Copies of these reports may be obtained at cost from the New England Research Application Center [see page A7].

Inquiries concerning rights for the commercial use of this invention should be addressed to the Patent Counsel, Lewis Research Center [see page A8]. Refer to LEW-13089.

Efficient Dichroic Plate for Microwaves

Signal separator for dual-frequency antennas has interlaced crossed slots, or dipole elements.

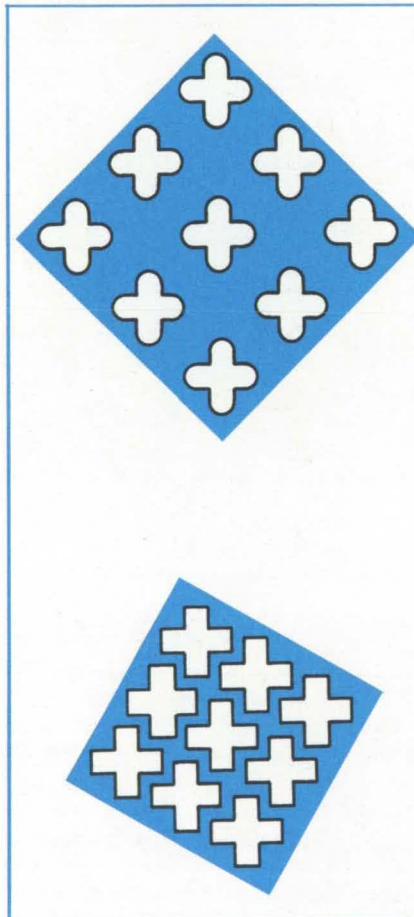
Goddard Space Flight Center, Greenbelt, Maryland

A dichroic plate for separating microwave frequencies uses interlaced crossed slots, or dipoles, to transmit microwave signals in one band and to reflect signals in a second band. The plate reflects or transmits more efficiently than conventionally-designed microwave dichroic plates in which the elements are not interlaced. The interlaced plate also increases the bandwidth of the dual-frequency antenna in which it is used.

"Interlaced" means that the crossed arms of adjacent slots or dipole elements nest together without touching. The arms of conventional dichroic-plate elements are arrayed in a tip-to-tip fashion (see figure). With interlacing, the element center-to-center distance can be reduced to close to the theoretical minimum of $0.37 \lambda_0$, compared to $0.47 \lambda_0$ for tip-to-tip elements, where λ_0 is equal to twice the element arm length.

The closer spacing of interlaced elements further reduces grating-lobe losses of waves that impinge the dichroic plate and also reduces the adverse effects of higher order modes that occur at unique angles-of-incidence and frequency. For example, it has been shown that the reduced spacing can reduce higher-order-mode null depths and increase the usable bandwidth by shifting the nulls lower, or out of, the band pass compared to more-widely-spaced tip-to-tip crossed slots.

The interlaced-slot concept was used in the design and fabrication of a 1.22-meter (48-inch) subreflector for dual-frequency operation in a 9-meter (30-foot) Cassegrain antenna. This subreflector reflects S-band radiation



In a Dichroic Plate for separating microwave signals, interlaced arms on the crossed dipoles (bottom) allow closer center-to-center spacing than the conventional tip-to-tip arrangement (top). The crossed dipoles may be metal protuberances above a dielectric plate or slots in a metal plate. A dichroic plate contains hundreds of such elements.

from 2.0 to 2.3 GHz and passes Ku-band radiation between 13.75 and 15.25 GHz. The measured midband loss was 0.4 dB. The 1-dB normalized bandwidth was 17 percent, a value for superior to other tested arrays, including circular and square apertures and crossed slots arranged tip-to-tip.

In practice, the crossed-slot apertures are adaptable to a variety of fabrication techniques. For large surfaces, the apertures can be punched in metal plates and formed to the desired shape. The minimum separation between adjacent arms is limited to approximately the thickness of the metal plate — usually aluminum. For smaller surfaces, for either crossed slots or crossed-dipole elements, printed-circuit techniques can be utilized by using a metalized dielectric substrate and a conformal mask.

The interlacing concept, moreover, allows much more flexibility in optimizing the dichroic-plate design. The element center-to-center spacing, the length and width of the arms, and the gap between adjacent arms can be traded off in a variety of ways to meet such performance requirements as power handling, bandwidth, and fabrication constraints.

This work was done by Thomas E. Wise of The Bendix Corp. for **Goddard Space Flight Center**. For further information, Circle 1 on the TSP Request Card.

This invention is owned by NASA, and a patent application has been filed. Inquiries concerning nonexclusive or exclusive license for its commercial development should be addressed to the Patent Counsel, Goddard Space Flight Center [see page A8]. Refer to GSC-12171

Low-Backlobe Microwave Transmitting Horn

By superimposing two hybrid modes the backlobes of an S-band gain calibration horn are down by 70 to 80 dB.

NASA's Jet Propulsion Laboratory, Pasadena, California

The backlobe radiation of a microwave transmitting horn can be suppressed by designing the horn so that it supports two hybrid modes.

In an application at NASA's Jet Propulsion Laboratory, the need for a low-backlobe S-band horn arose when calibrating a proposed fragile, unfurlable reflecting antenna that was 100 feet (30.4 meters) in diameter. To insure good mechanical stability, the horn had to be mounted near the prime focus of the reflector, rather than near its rim, as can be done with conventional solid reflectors. However, at the central location, the calibration horn backlobes are partially collimated by the reflector dish and interfere with the forward-directed horn pattern.

In the final design (see Figure 1) backlobe radiation was down by about 80 dB. The unfurlable parabola had a focal length/diameter ratio of 0.35, which means that the included angle from the focal point to the edge of the reflector is $\pm 71.1^\circ$. Thus, the back radiation of the reference between $\pm 108.9^\circ$ and 180.0° had to be kept to a minimum.

The gain requirement for the S-band calibration antenna was 15 dB. By combining the HE_{11} and the HE_{12} hybrid modes in the horn aperture, in an amplitude ratio of 1.0 to 1.2 (with proper phasing), the back radiation is canceled at $\pm 108.9^\circ$. (See Figure 2.)

The horn requires a 13.0-in. (33-cm) aperture for 15 dB gain. The axial length of the flared section is 12.0 in. (30.5 cm), and the diameter of the phasing section is 9.5 in. (24.1 cm) with a length of 10.0 in. (25.4 cm). The groove depth is $\lambda/4$, and at 2.3 GHz it equals 1.285 in. (32.64 mm).

This work was done by Dan A. Bathker, Samuel A. Brunstein, Paul W. Cramer, and William N. Moule of Caltech for NASA's Jet Propulsion Laboratory. For further information, Circle 2 on the TSP Request Card. NPO-14077

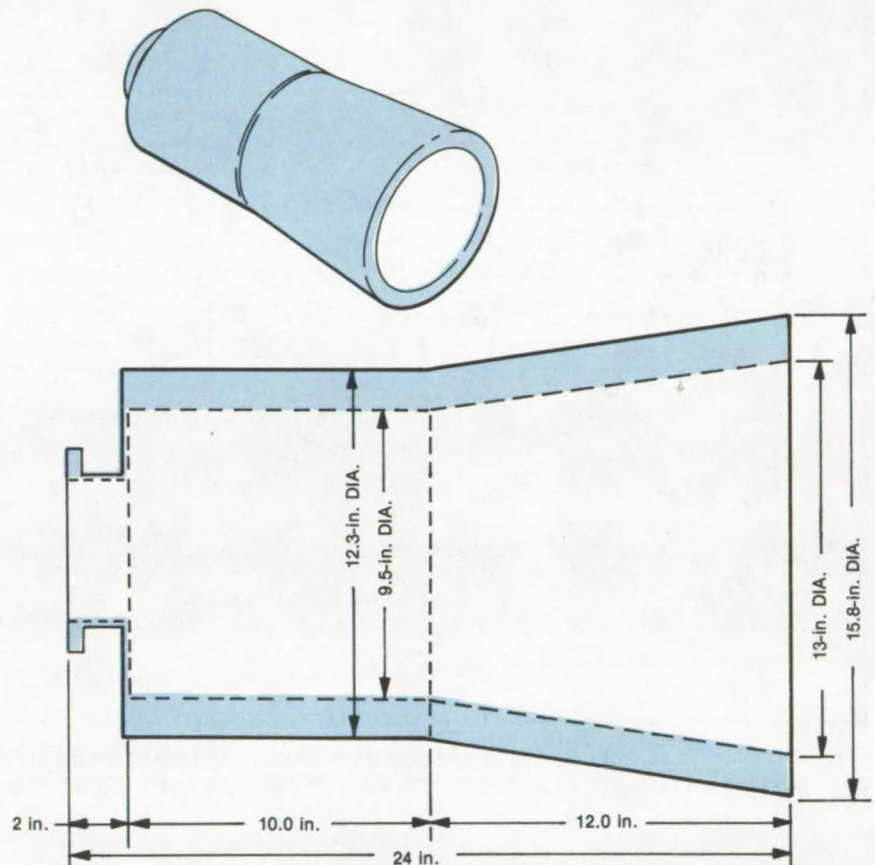


Figure 1. This S-Band Calibration Horn combines HE_{11} and HE_{12} hybrid modes to cancel backlobe radiation. The step change in waveguide size at the input to the phasing section generates the higher-order hybrid mode.

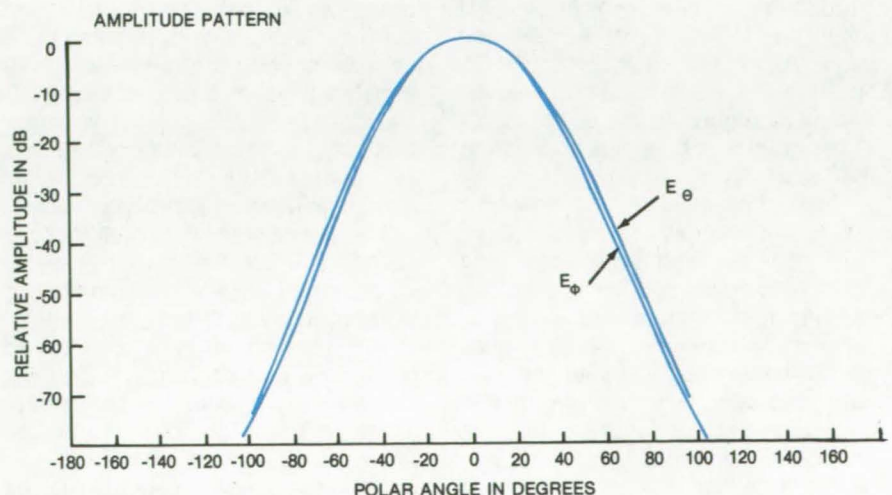
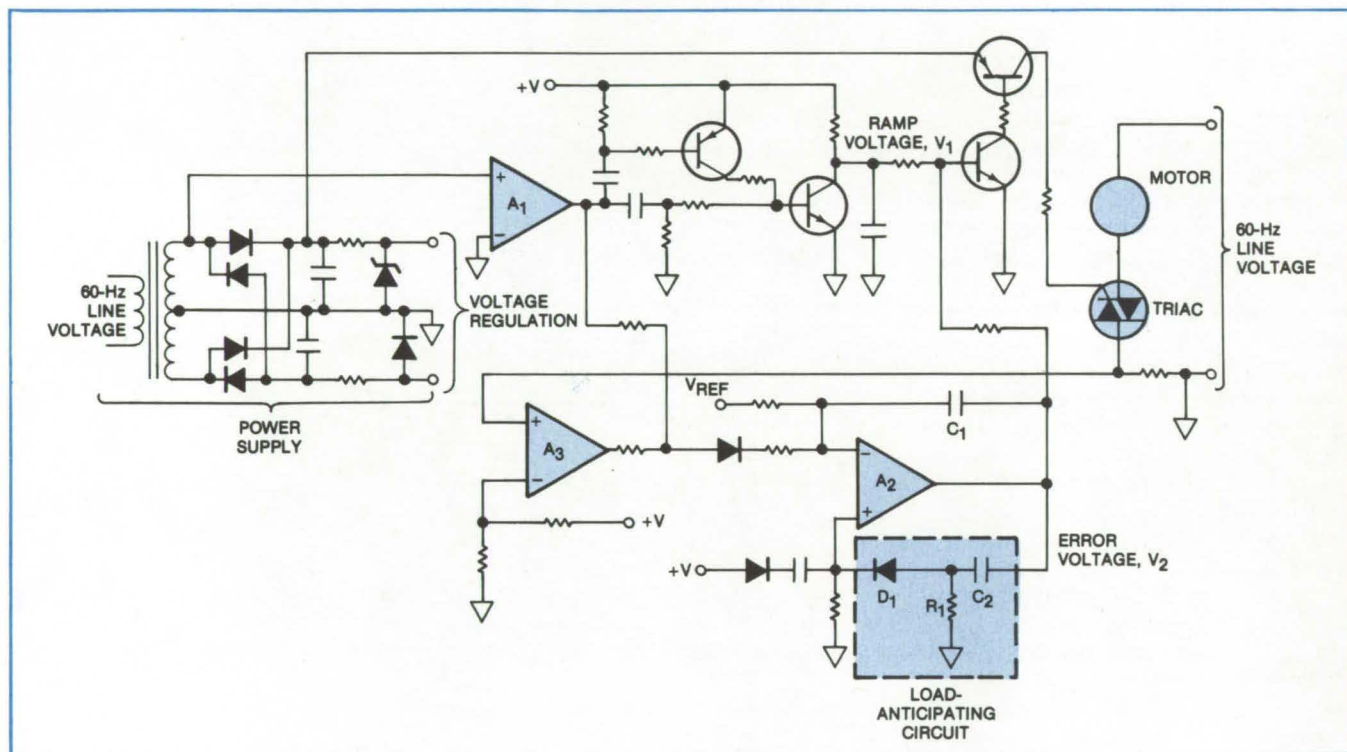


Figure 2. Radiation Pattern is shown for an 18-inch 15 dB hybrid horn.

Fast-Response Power Saver for Induction Motors

With an improved control circuit, induction motors run more efficiently at light loads and respond to sudden load changes.

Marshall Space Flight Center, Alabama



Diode D_1 in the **Load-Anticipating Circuit** applies a feedback voltage to amplifier A_2 when the error voltage rises sharply (such as when a load is abruptly placed on the motor). A_2 then turns the Triac fully on so that the motor has enough power to handle the new load.

A new motor-control circuit reduces the energy wasted by induction motors, yet it allows the motor to respond to abrupt changes in the load. Like a previously-developed control circuit (see "Save Power in AC Induction Motors," MFS-23280 on page 179 of *NASA Tech Briefs*, Vol. 2, No. 2), the new circuit conserves energy by regulating the power factor of the current and voltage supplied to the motor.

Unlike its predecessor, however, the new circuit also senses sudden load changes and anticipates the power needs so that the motor can respond instantly (to a load applied by a clutch, for example). The improved circuit is also much simpler than the earlier version; two transformers and six operational amplifiers have been eliminated; a critical-value resistor used in the earlier version has also been eliminated (see figure).

In an induction motor, the current remains high even when the motor is running at no load or low load. The power input is equal to the product of the voltage, current, and the cosine of phase angle between voltage and current. Since no work is being done by an unloaded motor and the current remains high, the phase angle between voltage and current is large. Typically, a loaded motor will have a 30° phase angle and an unloaded motor will have an 80° phase angle.

The motor-control circuit reduces no-load and low-load power by sensing the phase angle and, by controlling the applied voltage, forcing the motor to run at a constant, predetermined phase angle. It does this by varying the voltage applied to the motor through a Triac. The Triac is turned on for a variable portion of each half-cycle of the 60-Hz supply voltage. Its turn-on point is varied by biasing a

ramp voltage (V_1 in the figure) with an error voltage (V_2 from amplifier A_2).

The response of the motor-control circuit is delayed by the action of the filter capacitor C_1 . This lag is overcome by a load anticipator circuit consisting of capacitor C_2 , diode D_1 , and resistor R_1 . For slowly-changing loads, the variation of the error voltage V_2 is small, and the voltage across R_1 is not enough to overcome the threshold voltage of D_1 ; therefore, no signal is fed back to the positive input of A_2 .

However, when a sudden load is applied, V_2 changes rapidly, and the voltage across R_1 (which is determined by the time constant of R_1 and C_2) exceeds the threshold of D_1 . D_1 then applies a positive feedback voltage to A_2 .

A_2 turns the Triac fully on, allowing the motor to respond to the full load. This process takes a few milliseconds;

during this brief interval, the inertia of the motor prevents it from losing speed significantly. When A₂ drops out of saturation, the voltage across R₁ is blocked by D₁, and the circuit

returns to normal operation.

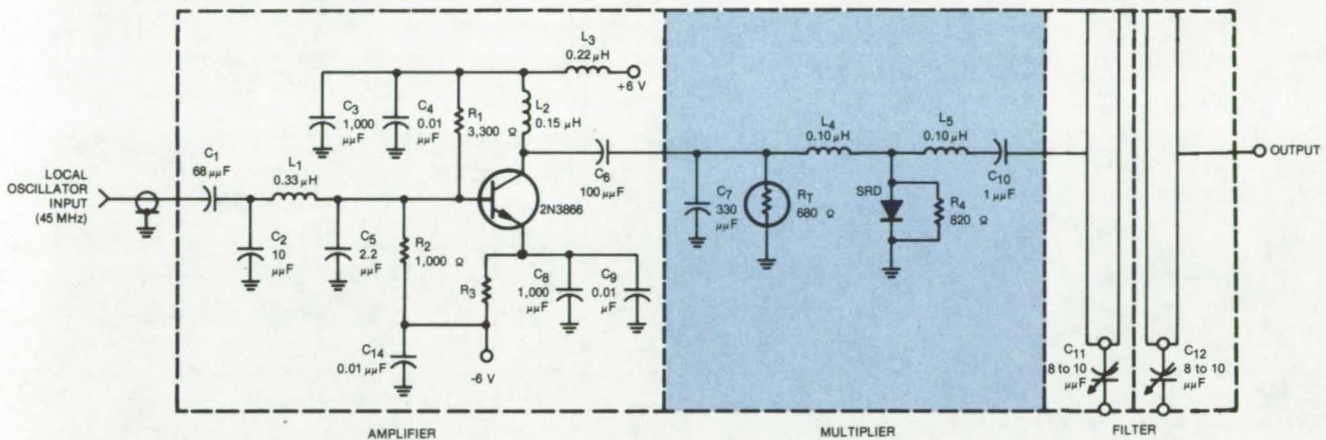
This work was done by Frank J. Nola of **Marshall Space Flight Center**. For further information, Circle 3 on the TSP Request Card.

Inquiries concerning rights for the commercial use of this invention should be addressed to the Patent Counsel, Marshall Space Flight Center [see page A8]. Refer to MFS-23988.

VHF Frequency Multiplier

A low-power step-recovery-diode frequency multiplier generates a 361-MHz signal.

NASA's Jet Propulsion Laboratory, Pasadena, California



In this **Frequency Multiplier Circuit** (in color), a step recovery diode generates a voltage spike during each cycle of the 45-MHz input signal. The spike causes the L₅/C₁₀ resonant circuit to ring at 361 MHz. The input signal is amplified before being multiplied, and the output is filtered.

A low-power, high-reliability radio receiver includes a step-recovery-diode (SRD) frequency multiplier. The diode circuit, driven by an RF amplifier, multiplies an input 45-MHz signal to generate a 361-MHz output.

The frequency multiplier is shown in the figure as part of the local-oscillator-signal conditioner circuit for the RF receiver. The output, which feeds a quadrature balanced mixer, is +8±2 dBm. A 361-MHz, two-pole filter, 4 MHz wide, reduces the level of undesirable side products of the SRD.

As shown in the schematic, a local oscillator signal is amplified by a transistor to a level sufficient to drive the SRD. Inductor L₂ and the capaci-

tor combination C₆ and C₇ resonate in the transistor collector circuit. Capacitor C₇ lowers the driving impedance for the SRD pulse circuit consisting of L₄ and the diode junction. Also, C₇ sets up a low impedance path for all harmonics generated by the SRD.

In operation, the diode conducts when the ac waveform is positive at its upper terminal. In this instance, energy is stored in inductor L₄, and charge is stored in the diode junction. When the voltage is negative, the diode continues to conduct the stored charge in its junction. As soon as the charge runs out, current in L₄ is cut off, generating a large, brief voltage spike. This occurs once every cycle of the 45-MHz drive signal. The

voltage spike causes a 361-MHz series resonant circuit (L₅ and C₁₀) to ring, producing a damped oscillation at 361 MHz.

A temperature-compensating resistor R_T serves as a dc return for the diode current. This sets the bias voltage to assure that the spike pulse occurs at the proper part of the cycle. The local oscillator filter smooths the waveform from the L₅/C₁₀ resonant circuit by cutting off sidebands. The filters are tuned so that the flat part of the response is centered at 361 MHz.

This work was done by Joseph A. Cusack of Motorola, Inc., for **NASA's Jet Propulsion Laboratory**. For further information, Circle 4 on the TSP Request Card. NPO-13700

Fiber-Optic Crossbar Switch

Switch automatically crosspatches optical signals with little loss.

John F. Kennedy Space Center, Florida

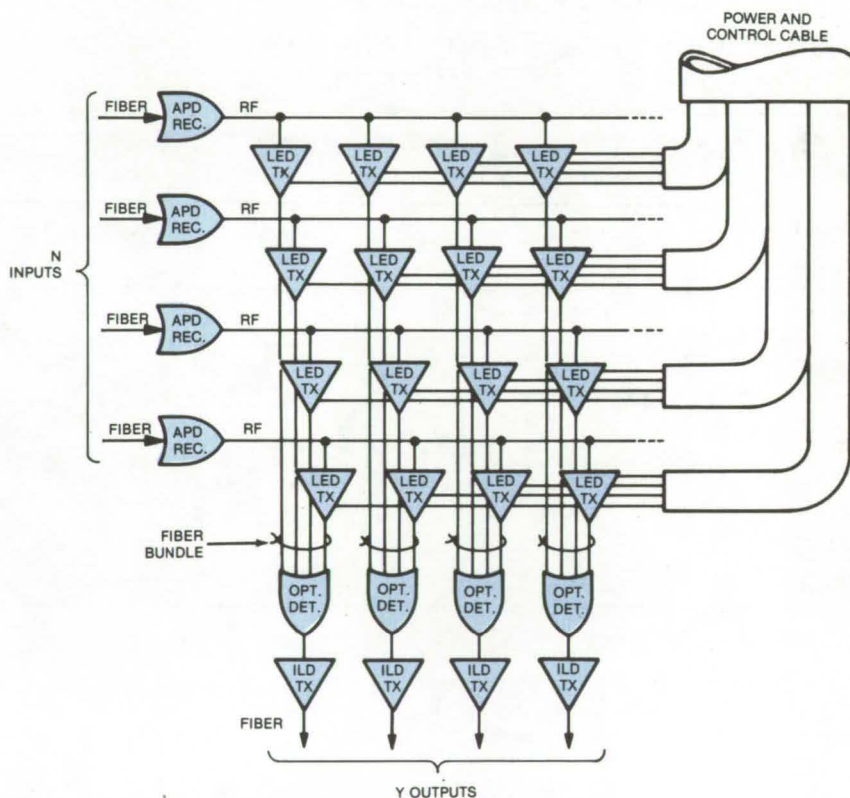
In conventional patching and switching of fiberoptic signal conductors, the fibers are manually disconnected and reconnected, using mechanical connectors and/or patch plugs. These connections tend to be very lossy and do not lend themselves to automation. In addition they are susceptible to contamination, are difficult to align, and have poor throughput loss repeatability.

A new fiberoptic crossbar switch resolves these problems. The switch (see figure) automatically switches or patches N fiber inputs to Y fiber outputs. The number N may be equal to Y , or they may vary independently over a reasonable range. Any switching combination between N inputs and Y outputs is available with one exception: Connection of multiple inputs simultaneously to a single output is prohibited by the switching logic.

Each of the N input fibers is connected to an optical detector, usually an avalanche-photodetector (APD) module that functions as an optical receiver and converts a light signal into a radio-frequency (RF) signal. This RF signal is distributed to various driver circuits that reconvert the RF signal to light by modulating a light-emitting diode (LED) or an injection-laser diode (ILD).

There are one driver and one LED or ILD optical source for each output fiber, all tied electrically to a common-input fiber-optic receiver. Thus each incoming fiberoptic signal is converted into an RF signal and distributed to Y optical sources or transmitters (TX's), which can be switched on and off to supply optical outputs as required.

There are Y optical detectors that use APD's or PIN (p-intrinsic-n) detector diodes, as required. These serve as terminations for the N fibers tied optically to N of the optical sources described above. By activating one of the optical sources (LED TX's) that are optically tied to the Y optical receivers, one particular N input is patched to a Y output. The optical detector then directly drives an



A Fiber-Optic Crossbar Switch is used for switching or patching N fiber inputs to Y fiber outputs. The avalanche-photodetector (APD) modules act as optical receivers, converting light into RF signals that are distributed to various driver circuits and converted back to light by LED's or ILD's.

ILD TX that converts the output of the APD receiver back to a high-level light output. The ILD is coupled directly to the output fiber.

The switch is housed in a gold-anodized machined aluminum case that reduces crosstalk between driver circuits. All the optical transmitters common to an input are contained within a machined aluminum cavity. Data exit these cavities only by optical fibers. Supply-voltage and switching-logic lines all pass through RF isolators prior to entering the optical cavities. Crosstalk among the data lines passing through the switch is below -120 dBm.

A four-input/four-output switch measures 5 by 5 by 2 inches (12.7 by 12.7 by 5.1 cm) and weighs between 2

and 3 lb (0.9 and 1.4 kg), depending on the cavity wall thickness. The switch cavities need no external cooling.

The device is furnished with local control and remote control. The local control can be manual from a control panel or by a computer data bus. In remote control the switch is slaved to a remote manual panel or a computer data bus.

This work was done by Charles H. Bell of Kennedy Space Center. For further information, Circle 5 on the TSP Request Card.

Inquiries concerning rights for the commercial use of this invention should be addressed to the Patent Counsel, Kennedy Space Center [see page A8]. Refer to KSC-11104.

Improved InSb Photodiode Preamplifier Circuit

An integrator compensates for background noise in Fourier spectrometer.

NASA's Jet Propulsion Laboratory, Pasadena, California

Johnson noise produced by a background-noise-compensation feedback resistor reduces the performance of a Fourier spectrometer. The resistor is part of a cryogenic InSb detector system (Figure 1) used in the spectrometer. Due to its high resistance, high offset voltages are created that endanger the costly detector chip. The problem is coped with by continuous monitoring and hand setting the voltages — a tedious and time-consuming task.

An effective alternative is to replace background resistor with an integrator in the InSb preamplifier feedback loop. The integrator improves the system operation and performs the compensation automatically.

In Figure 2, the modified circuit, the preamplifier output signal is fed through an integrator (AD171K, or equivalent), and the background level is taken from the integrator output and applied to the feedback resistor R_f . Resistor R_B is effectively eliminated.

The integrator passes the 240-Hz ac components unattenuated to the feedback resistor, while the loop dc gain is zero. The compensation is automatic.

This work was done by Richard L. Ulrich of Caltech for NASA's Jet Propulsion Laboratory. No further documentation is available.
NPO-14418

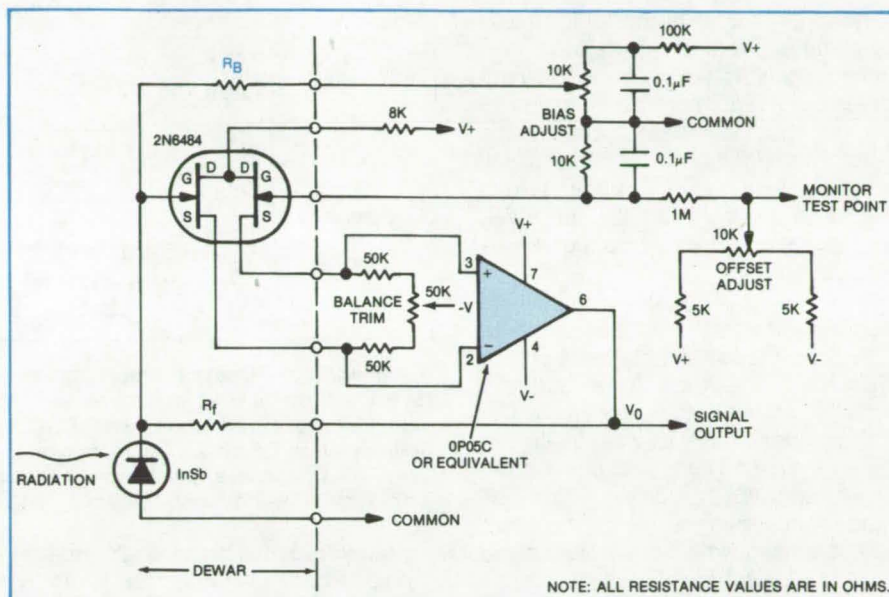


Figure 1. The **InSb Preamplifier Circuit** used a high value for resistor R_B for background radiation compensation. This setup required constant monitoring to prevent damage to the costly detector chip from high-voltage offsets.

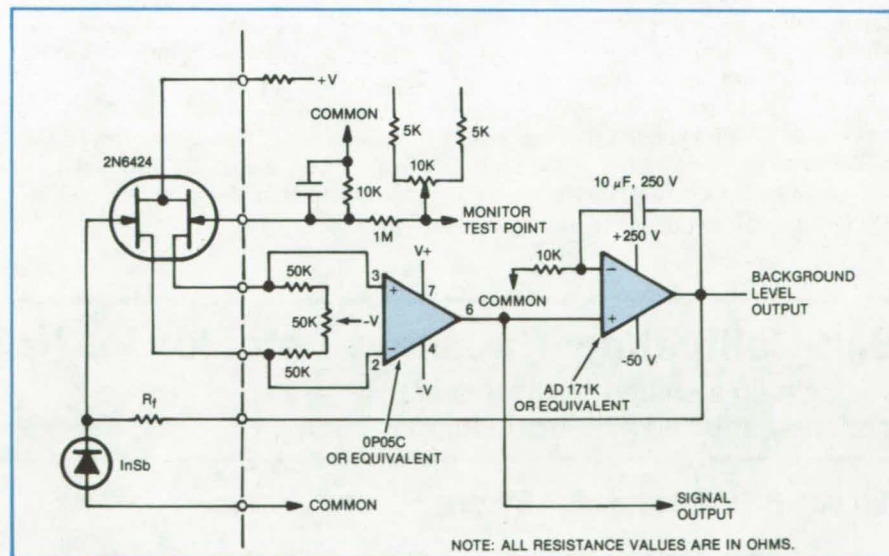


Figure 2. The **Modified Preamplifier Circuit** eliminates R_B and uses an integrator chip in the feedback loop.

Decision-Directed Automatic Gain Control

Logic circuitry determines whether gain fluctuations are a result of signal-strength changes or of atypical strings of like data symbols.

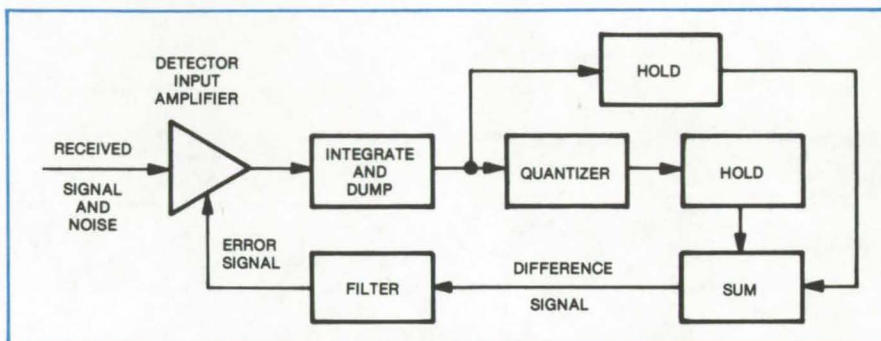
NASA's Jet Propulsion Laboratory, Pasadena, California

An automatic gain-control for multi-amplitude digital-transmission systems, regulates amplitude in the data detectors even when a long string of similar data levels appears at the input. In ordinary AGC circuits, which are based on average signal levels, such a string would shift the gain level, and detection errors would thereby be introduced.

The new AGC system employs a decision-directed feedback scheme based on the difference between the estimated amplitude level and the amplitude level actually received. The decision-directed AGC was developed for multiple-amplitude and phase-shift-keying (MAPSK) receivers. MAPSK data transmission systems conserve valuable bandwidth, but demand close control of amplitude levels.

In the system (see figure) the gain of a voltage-controlled amplifier at the input to the demodulator is regulated by an error signal, derived by the following sequence of operations on the received signal:

- The demodulator-input amplifier signal is applied to an integrate-and-dump circuit so that it is integrated over a predetermined time period.
- The absolute value of this integration is passed on to a holding circuit.
- Meanwhile, the output of the inte-



Automatic Gain Control circuit changes the amplitude level of a coherent MASK (M-ary amplitude shift keying) receiver so that the output signal reacts only to true signal-strength variations. The AGC amplifier can be put before or after the demodulation process. Thus, in one case it is an RF amplifier; when it follows demodulation it is a baseband amplifier. The figure above applies to a baseband amplifier following demodulation.

grate-and-dump circuit is applied to a logic circuit, which decides the likely level of the received signal. Data-bit detection is based on these detected amplitude levels.

- The absolute value of this level is stored in another holding circuit.
- The difference in the values in the two holding circuits is determined by a summing circuit.
- The difference signal from the summer is applied, through a filter, as the AGC error signal to the voltage-controlled amplifier at the demodulator input.

The AGC system provides tight control that is independent of the short-term, average, received signal energy and has negligible degrading effect on the probability of error for a symbol. The principle is applicable to quadrature-amplitude shift-keying (QASK) transmission which is a specific form of MAPSK.

This work was done by William J. Weber III of Caltech for NASA's Jet Propulsion Laboratory. For further information, Circle 6 on the TSP Request Card.
NPO-13639

Self-Calibrating Threshold Detector for Noisy Signals

A single time-shared channel is not seriously affected by temperature and aging.

Lyndon B. Johnson Space Center, Houston, Texas

A digital threshold-detection circuit can determine the presence of a signal in a high-noise environment, yet, unlike conventional parallel-channel threshold detectors, is not seriously affected by temperature variations or changes in component values with age. Although designed for receivers on spacecraft, the circuit should also be useful in industrial and

consumer equipment. For example, it might be incorporated in telemetry for security systems. Because the circuit employs a single time-shared channel instead of the usual two parallel channels, fewer components are needed, and the circuit therefore costs less and consumes less power.

An incoming signal is fed into the time-shared channel (see figure). For

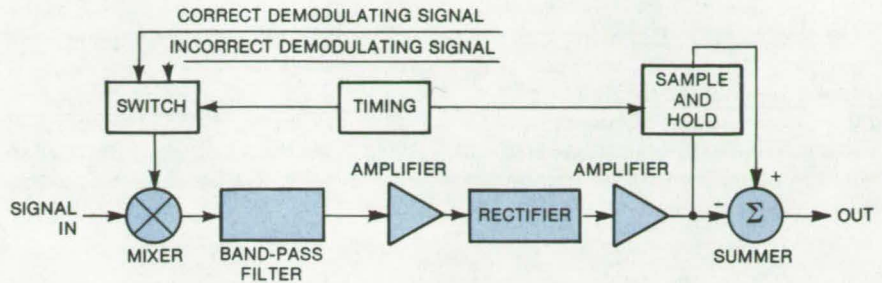
a short interval, a demodulator applies another signal that will surely demodulate the incoming signal incorrectly. The output of the channel is sampled and stored.

Next, the correct demodulation is applied to the signal, and the stored sample is subtracted from the correctly demodulated sample. As in the parallel-channel detector, a zero

remainder means that no signal is present, and a remainder greater than zero means that a signal is present. A dc offset voltage can be inserted at this point so that, for example, a negative output indicates the absence of a signal and a positive output indicates the presence of a signal.

The new detector requires fewer initial adjustments for balance and much less compensation for temperature variations. Moreover, unpredictable changes in gain, bandwidth, and dc offset with age do not affect performance as seriously as in a parallel-channel detector because components are shared rather than duplicated.

This work was done by James R. Barnes and Marshall Y. Huang of



This **Threshold Detector Circuit** employs one time-shared channel through which incorrect and correct demodulating signals are alternately switched. More conventional circuits use two parallel channels, but are more complex and susceptible to drift and aging.

TRW, Inc., for **Johnson Space Center**. No further documentation is available.

Inquiries concerning rights for the

commercial use of this invention should be addressed to the Patent Counsel, Johnson Space Center [see page A8]. Refer to MSC-16370.

Low-Frequency Attenuator Circuit

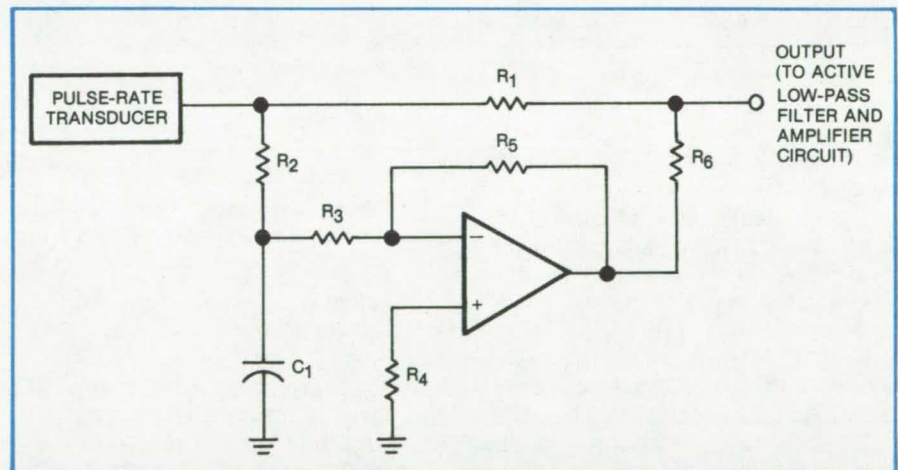
A compact attenuator reduces large-amplitude background signals in a wristwatch-sized pulse-rate detector.

Dryden Flight Research Center, Edwards, California

One type of existing, noninvasive, miniaturized pulse-rate detector includes a light-emitting diode (LED) source that illuminates the blood vessels just under the outer skin layers. Solid-state photosensors pick up the reflected light, which is modulated by the pulse pressure wave.

In this application, two forms of low-frequency background noise are superimposed on the pulse signal; (1) a large constant dc level caused by light reflected off the outer skin surface and (2) a roughly sinusoidal signal that develops in response to movements of the sensor (as the person walks or jogs).

Since the dc and slowly varying components are roughly 100 to 200 times greater than the pulse signal, it is necessary to separate the pulse-rate signal (typically 10 to 20 mV) from this background before filtering and amplifying. For the low frequencies involved (0.5 to 4 Hz), ac coupling the pulse-rate transducer directly to filter/amplifier circuits would require bulky capacitors that are too large for the otherwise wristwatch-sized detector package.



This **Miniature Attenuator Circuit** eliminates large-amplitude low-frequency (0.4- to 5-Hz) noise in a pulse-rate detector. Typical component values are $R_2 = R_3 = R_5 = 100 \text{ k}\Omega$, $R_4 = 68 \text{ k}\Omega$, $R_6 = 50 \text{ k}\Omega$, and $C_1 = 1 \text{ }\mu\text{F}$.

A new attenuator circuit, shown in the figure, uses only a single operational amplifier and a few passive components to remove low-frequency background, and it is small enough to fit in the miniaturized package. In the attenuator, resistor R_2 and capacitor C_1 cause the input terminal of the inverting amplifier to follow the average value of the pulse transducer

output. This signal is inverted by the amplifier and summed with the transducer output. The amplifier closed-loop gain is determined by resistors R_3 and R_5 . Resistor R_4 is included for drift compensation, and R_6 is a summing resistor.

The circuit monitors the average dc level of the sensor output and generates the algebraic negative of
(continued on next page)

this level; then it adds this signal to the raw output. In this way, dc and slowly varying components are subtracted from the sensor output before any further processing occurs:

The attenuator is also applicable to other systems where background noise is slowly varying, such as

ultrasound measuring systems, strain-gage measuring systems, and accelerometers.

This work was done by Wilbur H. Cash, Jr., and John T. Polhemus of Martin Marietta Corp. for **Dryden Flight Research Center**. For further information, Circle 7 on the TSP Request Card.

This invention is owned by NASA, and a patent application has been filed. Inquiries concerning nonexclusive or exclusive license for its commercial development should be addressed to the Patent Counsel, Dryden Flight Research Center [see page A8]. Refer to FRC-11012.

Low-Noise Current Regulator

Modification of a conventional regulator minimizes current drift.

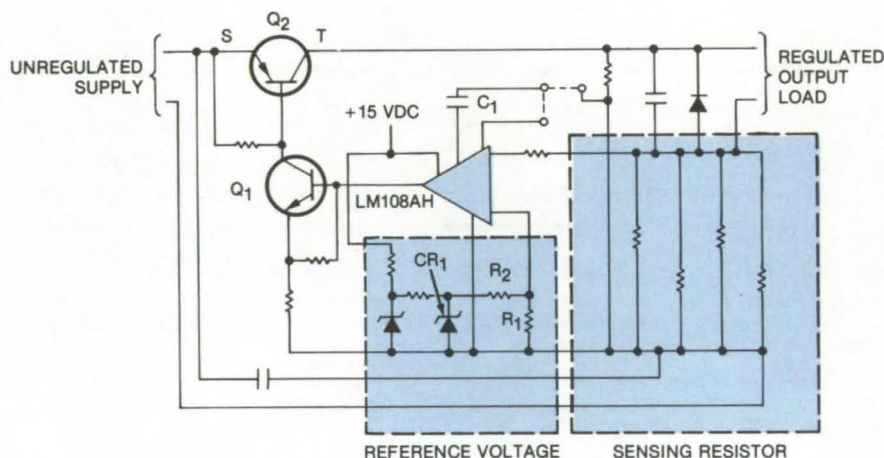
NASA's Jet Propulsion Laboratory, Pasadena, California

In the design of current-regulator circuits, the emphasis is on minimizing the drift. The major areas of drift in such a circuit are shown shaded in the figure. The current to be regulated flows through a sensing resistor in series with the load, producing a voltage that is fed into an operational amplifier. The other input into the amplifier is a reference voltage from a Zener diode network. Any difference between these two signals causes the amplifier to drive transistor Q_1 , which provides the bias for power transistor Q_2 . Changing the bias voltage of Q_2 effectively changes the resistance between points S and T and thereby regulates the current.

The greatest source of current drift is the operational amplifier; the higher its offset voltage, the greater the drift. The resistors in the circuit are subject to time and temperature fluctuations that vary inversely with their resistances. The Zener diode tolerances and transistor operating characteristics are additional sources of drift noise.

The circuit shown attempts to minimize load-current drift in several ways:

- The operational amplifier was chosen for low offset current and voltage. Negative-power-supply noise was eliminated by operating the operational amplifier single ended from the +15-Vdc supply. The positive-power-supply noise



This **Current-Regulator Circuit** minimizes the drift of load current by using high-quality resistors and using a single bias voltage on the operational amplifier.

rejection was improved by connecting compensation capacitor C to ground.

- The sense voltage level was increased to minimize the amplifier offset drift error and to make reference attenuator resistors R_1 and R_2 equal valued. The improved tracking derived from the equal-valued resistors serves to minimize thermal drift of the reference.
- The increase of sense voltage level also increased the value of the current-sensing resistors, making possible the selection of more stable resistors to improve long-term circuit stability.

- Further reduction in drift error was achieved by selecting reference diode CR_1 for 1 percent tolerance and by operating the reference circuit from the regulated +15-Vdc supply.

With these modifications the maximum drift noise of the regulator is only 0.44 percent.

This work was done by James Bunn of Xerox Corp. for **NASA's Jet Propulsion Laboratory**. For further information, Circle 8 on the TSP Request Card.
NPO-14070

Improved Isolation in Double-Balanced Mixers

Bypass circuit eliminates unwanted leakage in output RF signal.

NASA's Jet Propulsion Laboratory, Pasadena, California

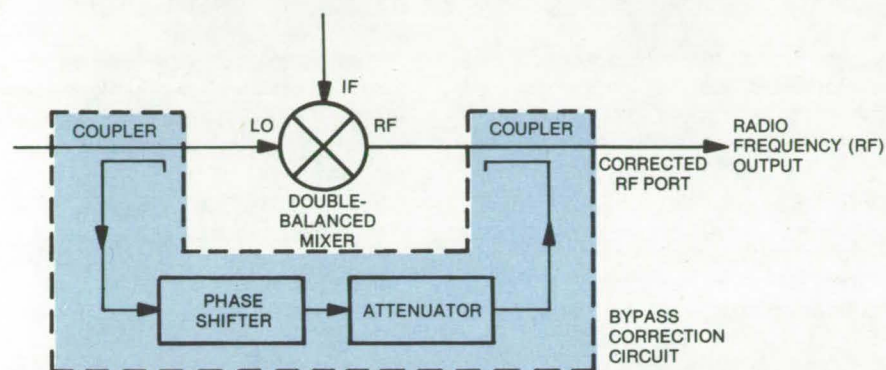


Figure 1. **Bypass Circuit** extracts a small amount of LO energy, then adjusts its phase and amplitude so that it just cancels out the leakage.

A bypass circuit eliminates the leakage of unwanted local-oscillator (LO) energy into the output of double-balanced mixers. These mixers, used in advanced radio transmitters, modulate a carrier frequency supplied by a local oscillator with an information-containing baseband signal. Since the mixers do not provide high-level isolation between the LO port and the radio-frequency (RF) output port, a small amount of unmodulated LO signal appears in the output.

The unwanted LO energy distorts the linearity, amplitude balance, and phase accuracy of the output. The new bypass circuit corrects this condition and thereby extends the double-balanced range of linear operation of the mixer to lower RF signal levels, providing a greater linear dynamic range.

The bypass circuit (Figure 1) couples a small amount of the LO energy into a line that circumvents the mixer from the LO port to the RF port. The circuit adjusts the phase and amplitude of this energy so that, when it is recombined with the mixer output, it cancels the LO leakage as shown in Figure 2.

The new correction circuit was developed for phase-shift-keyed transmitters. The principle can be adapted to correct leakage in other types of RF circuitry as well.

This work was done by Philip H. Stanton of Caltech for NASA's Jet Propulsion Laboratory. For further information, Circle 9 on the TSP Request Card.
NPO-14415

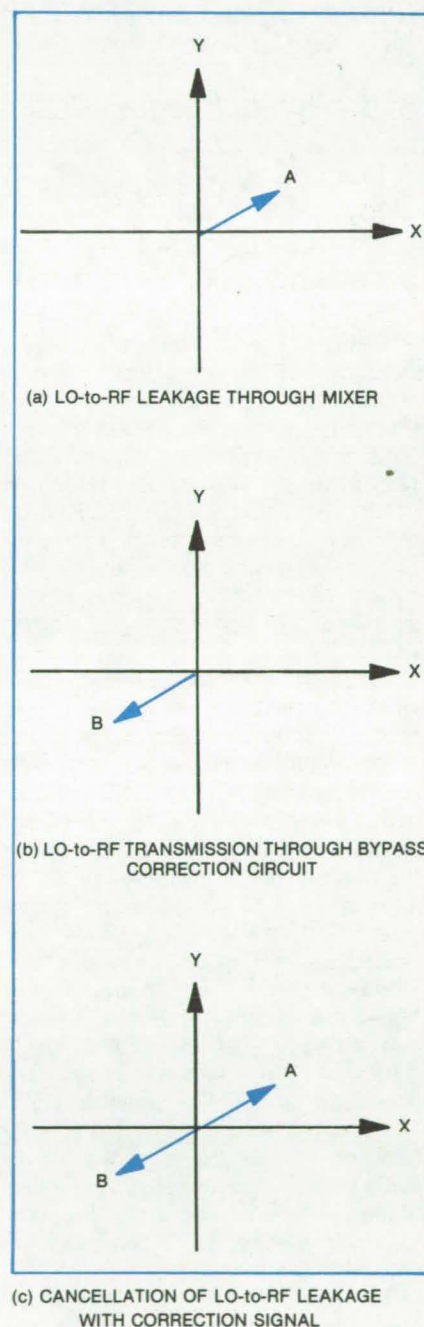


Figure 2. **Phasor Diagram** shows the leakage and correction scheme.

Books and Reports

These reports, studies, and handbooks are available from NASA as Technical Support Packages (TSP's) when a Request Card number is cited; otherwise they are available from one of NASA's Industrial Application Centers or the National Technical Information Service.

Reliability of Imaging CCD's

A comprehensive study of electrical and optical performance, packaging constraints, and failure modes

Designers and users of imaging systems will be interested in a new study report on the reliability of imaging charge-coupled devices (CCD's). Intended to augment the rather-meager existing information on CCD reliability, the study focuses on electrical and optical performance tests, packaging constraints, and failure modes of one commercially available device (the Fairchild CCD121H).

Although one must exercise care when generalizing the results of the study to other devices, many of the fundamental properties encountered are representative of all CCD's. Moreover, since it includes detailed discussions of CCD principles and of the theoretical basis for the reliability analyses, the 107-page report will be useful to those who may have only limited experience in this field. Complementing the text material are numerous graphs, photographs, circuit diagrams, tables, and a list of references. Several failure modes are described, and device construction is analyzed. In addition, the relationship between reliability and packaging is investigated. The concluding section of the report proposes a test program for a more-general reliability evaluation of CCD's.

The study is divided into three phases: (1) construction analysis, (2) electrical tests, and (3) mechanical tests. In phase 1, etching and precision sectioning were used to remove chip layers successively and, in

cooperation with scanning electron microscopy, to obtain an accurate diagram of the circuit. Physical properties, such as the degree of gate overlays, oxide thicknesses, and diffusion depths, were observed for correlation with electrical performance.

In phase 2, nine electro-optical and electrical properties were measured on test specimens. Included were tests for responsivity (in volts per joule/m² of light-energy density), transfer efficiency, noise, dark signal, response uniformity, linearity, dynamic range, spectral response, and crosstalk. Also described are the optical and electrical test setups and the automatic data-collection and reduction methods used.

Tests were implemented to measure dark signal versus strain in phase 3. In these tests, intended to simulate the effects encountered when large chips are bonded to dissimilar metals, a CCD was bonded to a zirconium pull-test specimen. As a calibration test, a strain gage was first mounted on a similar sample bonded to the CCD surface to measure the strain transmitted to the CCD up to the point of bond failure.

This work was done by J. R. Beall, M. D. Borenstein, R. A. Homan, D. L. Johnson, D. D. Wilson, and V. F. Young of Martin Marietta Corp. for Marshall Space Flight Center. Further information may be found in NASA MCR-78752 [N78-29352], "Preliminary Study of the Reliability of Imaging Charge-Coupled Devices," a copy of which may be obtained at cost from the New England Research Application Center [see page A7]. MFS-25039

Group-Delay Standards

A compilation of data obtained in evaluating a set of group-delay standards

A set of data has been generated to be used in conjunction with newly-developed delay-line standards. The delay lines comprising a 15-, 30-, and 60-ns envelope delay of a 500-kHz

square wave modulating S- and X-band carriers have been tested over carrier-frequency values of 2,113, 2,295, and 8,415 MHz. This is a first effort in establishing envelope or group-delay standards that would be operable over a broad carrier-frequency range of from 500 kHz to 12 GHz.

Each of the three cable-delay standards has type N male and female connectors. The cables are coiled and potted, and the connectors are arranged for convenient insertion into the measurement system. Each cable has an inner diameter of outer conductor of 8.255 mm (0.325 in.), a characteristic impedance of 50 ohms, a solid aluminum outer conductor, and a foam polyethylene dielectric having a nominal permittivity of 1.50. The outer diameter of the inner conductor is 2.972 mm (0.117 in.). The phase temperature for this type of cable is typically smaller than ± 15 parts per million per $^{\circ}\text{F}$ ($\pm 27\text{ppm}/^{\circ}\text{C}$) over the temperature range of 60° to 90°F (15.6° to 32.2°C).

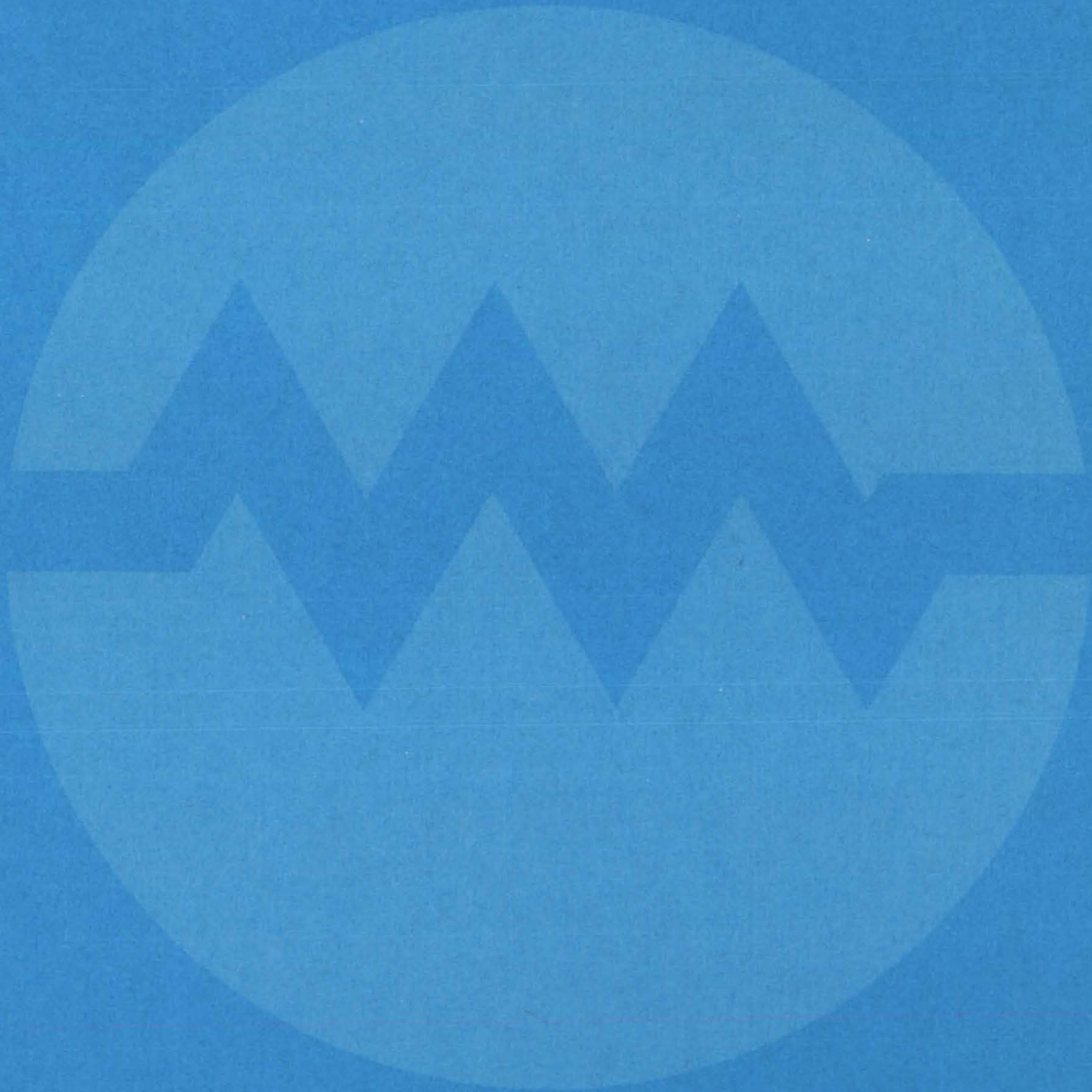
The cables have been tested by three independent laboratories using six different methods. The results are published in a report showing the delay values obtained from 15-, 30-, and 60-ns cables by different laboratories.

Analysis of the test results shows that the cables are suitable for calibrating range-measuring equipment as envelope delay standards for 500-kHz square-wave modulation over the specified carrier-frequency range of 500 kHz to 12 GHz. They can be combined or used individually to test 15-, 30-, 60-, 45-, 75-, 90-, and 105-ns delays. Their accuracies are estimated to be better than ± 0.3 ns.

A study of potential error sources indicates that reflection errors due to the discontinuities at the ends of the cables are usually small (less than ± 0.1 ns). The noncyclical dispersion due to skin effect is negligible at the tested microwave frequencies.

This work was done by Robert W. Beatty, Lloyd J. Derr, and Tom Y. Otoshi of Caltech for NASA's Jet Propulsion Laboratory. To obtain a copy of the report, Circle 10 on the TSP Request Card. NPO-13938

Electronic Systems



Hardware, Techniques, and Processes

- 17 Electronic Pictures From Charged-Coupled Devices
- 18 Improving Low-Illumination Video
- 19 TV Audio and Video on the Same Channel
- 20 Real-Time Video-Image Analysis
- 21 Eliminating Clutter in Synthetic-Aperture Radar
- 22 Azimuth Correlator for Synthetic Aperture Radar
- 23 Signal Separator for Dual-Frequency Antenna
- 24 Components for an S-Band Communication Subsystem
- 26 LED Display for Solo Aircraft Instrument Navigation
- 27 Cable-Fault Locator
- 28 Cloud-to-Ground Lightning Detector
- 29 Reliable Inverter Systems
- 30 Monitoring Disaster Areas Via Satellites
- 30 Simpler Cabling and Power Link for Remote Readouts
- 32 A Closed-Loop Control-Loading System
- 33 A Telephone Multiline Signaling System
- 34 Fader and Ramp Shaper Replace Linear Filters
- 35 Optical Memories in Digital Computing

Electronic Pictures From Charged-Coupled Devices

Transparent phase electrodes make integrated silicon array sensitive.

Goddard Space Flight Center, Greenbelt, Maryland

An imaging system uses charge-coupled devices (CCD's) to generate TV-like pictures with high resolution, sensitivity, and signal-to-noise ratio. The CCD system was developed for Landsat satellites, in which a mirror scans an array of light detectors as the satellite moves in its orbit, thereby generating electrical signals representing a continuous moving image of the Earth below.

Previously, Landsat satellites employed an array of point detectors as the imaging devices. Twenty of these detectors were required for each of five spectral bands from visible to near-infrared wavelengths. Since each detector needed its own pre-amplifier and video channel, this system was mechanically complex, had a large number of parts, and consumed considerable power. At the data rates and resolution demanded for satellite pictures, this system had little signal-to-noise margin, and still more electronic circuitry was necessary for multiplexing to combine many point-detector outputs into a single data stream.

The new CCD system combines detectors for five spectral bands as well as processing and control circuitry all on a single silicon chip (Figure 1). The satellite moves the chip in the y direction while the scanning mirror sweeps the scene (and the chip) in the x direction. The chip contains 20 columns of CCD sensor elements, and each column contains 9 sensor stages. As movement progresses in the y direction, each increment of the image falling on any column is electrically delayed in the y direction while the scene is scanned in the x direction. If the outputs from all nine stages in a column are added, the output signal is nine times as large as that from a single imaging element. (This is the "time-delay-and-integration" mode of operation.) The net result is that the output signal strength is increased by a factor of 9 while the geometrical resolution is essentially unchanged.

(continued on next page)

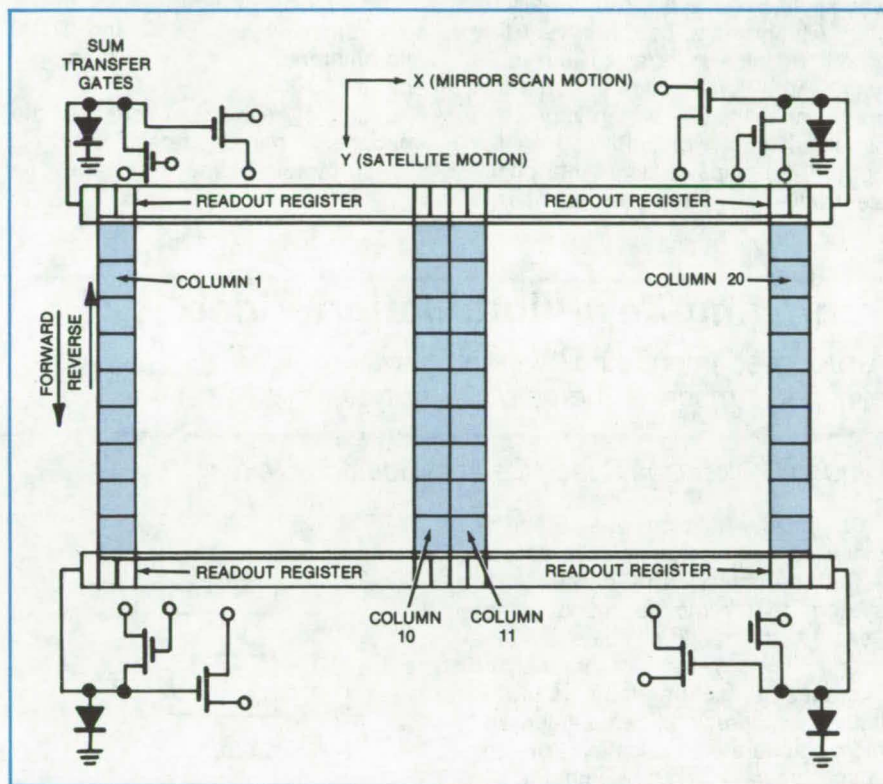


Figure 1. **CCD Chip** for imaging contains 20 columns (channels) of 9 time-delay-and-integration stages each. A readout register terminates each channel.

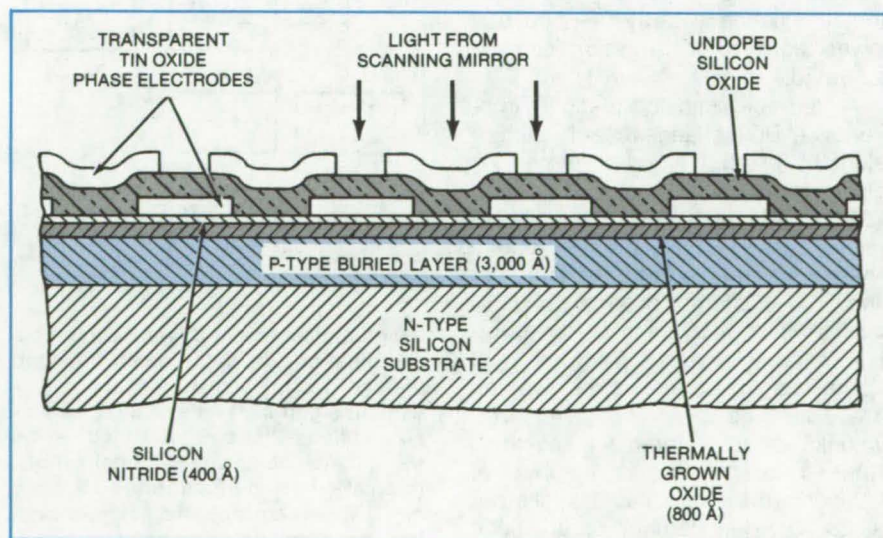


Figure 2. **Imaging Array**, shown here in cross section, is based on a p-type buried layer (ion-implanted boron in silicon). The tin oxide phase electrodes transmit at least 80 percent of the light in the spectrum passed by an aluminum light shield (not shown).

The output of each column is fed by a built-in shift register to an amplifier that also is integrated into the silicon chip. The register multiplexes the column outputs into a continuous bit stream.

In the past, to ensure high quantum efficiency in CCD imaging arrays, light was applied to the back of the silicon chip, which had to be made very thin (about 15 micrometers) so that it did not absorb too much light. Such a thin chip was difficult to fabricate and handle. If light were directed on the front of the chip, however, the phase electrodes — which move charge

from stage to stage — would prevent a large part of the light from reaching the sensor.

In the new CCD imager, light enters at the front of the chip, and the phase electrodes are made of tin oxide instead of polycrystalline silicon (Figure 2). Tin oxide transmits at least 80 percent of the light energy in the spectrum between 0.400 and 1.100 micrometers, where the CCD imager operates.

Each picture element (pixel) of the imager is 76 micrometers square. It is formed by four of the transparent tin

oxide electrodes, each 19 micrometers square.

This work was done by David H. McCann, Alfred P. Turly, and Marvin White of Westinghouse Electric Corp. for Goddard Space Flight Center. For further information, Circle 11 on the TSP Request Card.

This invention is owned by NASA, and a patent application has been filed. Inquiries concerning nonexclusive or exclusive license for its commercial development should be addressed to the Patent Counsel, Goddard Space Flight Center [see page A8]. Refer to GSC-12324.

Improving Low-Illumination Video

A proposed integrating/averaging system eliminates much of the noise — in real time.

Lyndon B. Johnson Space Center, Houston, Texas

Nonmoving TV pictures — such as those used in radiographic diagnosis — can be improved by an electronic system that removes much of the "snow," or random noise, in the image. The system integrates and averages the picture elements in real time and thereby allows easier and more accurate evaluation of the image, visually and by computer.

The system makes it possible to use lower illumination levels on the subject — particularly beneficial when the illumination is X-rays — because lower signal-to-noise ratios can be tolerated.

A high-speed analog-to-digital converter (ADC) changes each picture element (pixel) in a video frame to a digital format and stores each pixel value in a ferrite core memory (see figure). Since there are 479 useful lines in a frame and 512 elements per line, the system converts 245,760 pixels within 1/30 second (the duration of a single frame). Then the next frame is digitized, and its pixel values are added to the respective pixel values already stored in memory. After a predetermined number of additions, the accumulated values are divided by the number of additions and transferred to a computer for processing. Simultaneously, the averaged values are converted to analog form and transferred to a TV monitor display. This averaging process improves the image quality.

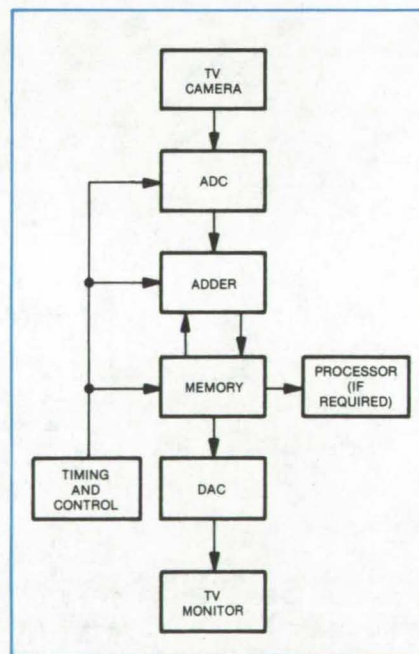


Image Enhancement System employs a combination of data-processing and storage techniques to reduce noise without significant time delay. Inexpensive options that can be added to the system include "picture normalization" (correction for nonuniformity of X-ray or TV field flatness) and "picture subtraction" (removal of one of two superimposed images so that the difference can be observed — useful in repositioning patients for radiation therapy, for example).

The ADC is a 32-channel parallel output device that generates digital values at a rate of 7.5 megahertz. Values are stored sequentially in the first word of each of a group of core memories, then the second word of each is filled, and so on until the entire frame is stored. The memory words are 12 bit or more in length. The memories are multiplexed to minimize the speed that is required of them.

As subsequent frames are digitized, the stored value of a given pixel is retrieved and placed in an adder, where the stored value is added to the latest value. The sum is then replaced in the memory. After a predetermined number of values 2^n (where n is an integer) have been added and stored, the sums are divided by 2^n .

Commercially-available TV cameras, monitors, and core memories can be used with the system. The integrator/averager hardware, however, is specially constructed.

Core memory proved to be the least expensive approach, at the time of the study, with cycle time less than 1 microsecond and access time of about 300 nanoseconds.

This work was done by Robert L. Sapirstein of Lockheed Missiles & Space Co., Inc., for Johnson Space Center. For further information, Circle 12 on the TSP Request Card. MSC-14841

TV Audio and Video on the Same Channel

Transmitting technique adds audio to video signal during vertical blanking interval.

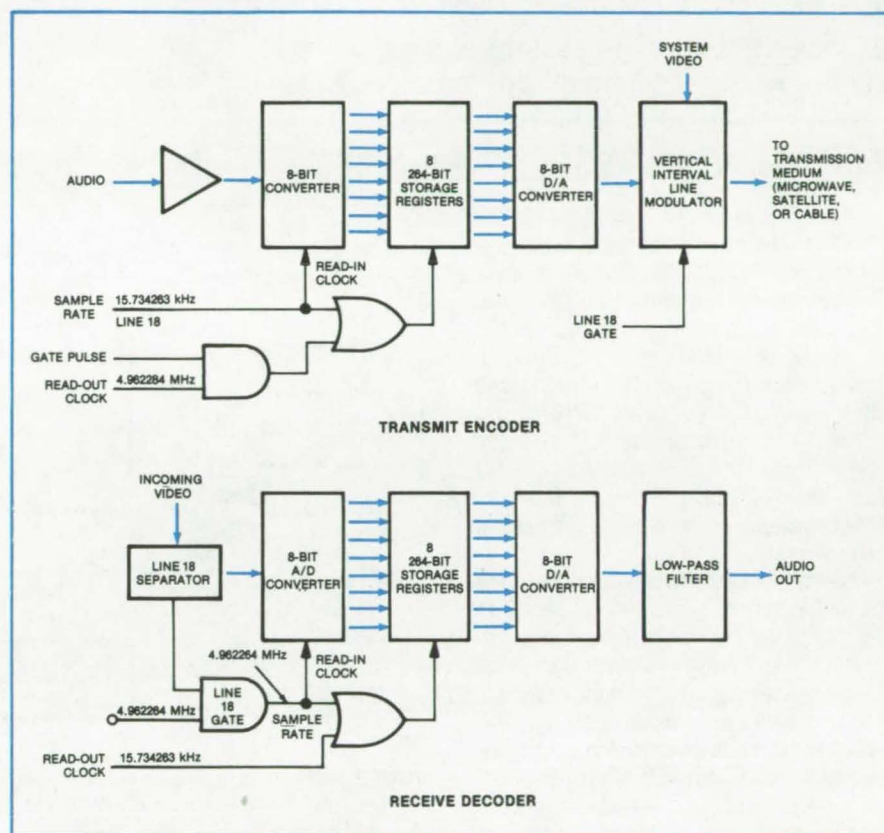
Lyndon B. Johnson Space Center, Houston, Texas

A technique for transmitting television signals incorporates the audio portion of a program with the picture information, making a separate sound channel unnecessary. The audio is compressed into the time of a single picture field and is placed on an inactive line of the video raster during the vertical blanking interval.

Today, television audio travels over long-distance telephone facilities that are distinct from those carrying the video, a practice that has several disadvantages. The audio transmission routes, although separate, must be about the same length as those for the video to keep the two signals synchronized. Also, the audio switching must be correlated with that for the video, even though different types of switching equipment must be used for each type. Moreover, the audio often picks up crosstalk from other audio and data signals transmitted simultaneously.

The new technique, called SIVI for sound in the vertical interval, avoids these problems since it integrates audio with a standard video signal. In addition, it allows higher-fidelity stereo sound for television, since it can accommodate a higher frequency range. SIVI does not preempt any video lines, it is compatible with color-reference bursts, and it does not conflict with horizontal-line and vertical-field synchronization pulses. The composite TV signal can be sent over the existing microwave and coaxial cable facilities normally used for television.

SIVI can be used by TV networks and stations to transmit cuing and automatic-switching tone signals to augment automatic and manual operations. It can also be used to transmit one-way instructional information, such as bulletin alerts, program changes, and commercial-cutaway aural cues from the networks to affiliates. Additionally, it can be used as an extra sound channel for second-language transmission to bilingual stations.



SIVI System transmit encoder compresses the audio signal and inserts it in the video signal. At the receiving end, the decoder reverses the process and re-creates the original audio signal.

In the SIVI technique, digital samples of the audio for a picture-field period are accumulated and stored. Then the stored samples are transmitted within the time period of a single predetermined line in the vertical interval. At the receiving terminal, the time-compressed sample pulses are expanded to restore the original audio. (This restoration is done at the local TV station — not in the home receiver. Audio is transmitted from the station to home viewers in the usual way.) Samples are taken at the horizontal-line rate. This sample rate provides an audio spectrum of 7.86 kilohertz (based on two samples per horizontal line).

The audio sample pulses are approximately 4 microseconds in width

and occur at 63.5-microsecond intervals. The samples are converted to 8-bit words by an analog-to-digital converter and are stored in eight random-access memories or shift registers (see figure). The 263 words in a picture field are clocked out of the digital storage at a 5-megabit rate to a digital-to-analog converter. This process positions the sample pulses directly adjacent to each other and eliminates the original time interval, yielding a time-compression ratio of 314.78 to 1. The output of the digital-to-analog converter is gated into the preselected line of the raster by a line counter.

(continued on next page)

At the receiving end, the 263 time-compressed sound samples are converted to 8-bit words and are successively stored in digital storage devices. Each 8-bit word is periodically clocked

at the horizontal-line rate into a digital-to-analog converter, which produces an amplitude-modulated signal representing the original audio.

This work was done by Jack B.

Hopkins of Westinghouse Electric Corp. for Johnson Space Center. For further information, Circle 13 on the TSP Request Card. MSC-16241

Real-Time Video-Image Analysis

Digitizer and storage system allow rapid random access to video data by a computer.

NASA's Jet Propulsion Laboratory, Pasadena, California

The digital system shown in the block diagram analyzes video data in real time. Called RAPID for random-access picture digitizer, the system could be used for pattern recognition in artificial-intelligence systems, in remote sensing, and in medical diagnosis instrumentation. RAPID digitizes the video information and stores it in a random-access memory (RAM). Data elements are retrieved from the RAM for analysis by a minicomputer in real time.

RAPID uses two commercially-available, charge-injection, solid-state TV cameras as sensors (see figure). These are high-resolution cameras with 50-millimeter automatic-iris lenses. Two cameras are included for stereographic analysis and triangulation. A third camera with a 12.5-millimeter lens can be added for crude wide-area observations. (RAPID handles black-and-white pictures at present.) The system can be switched among seven camera channels so that many scenes can be monitored.

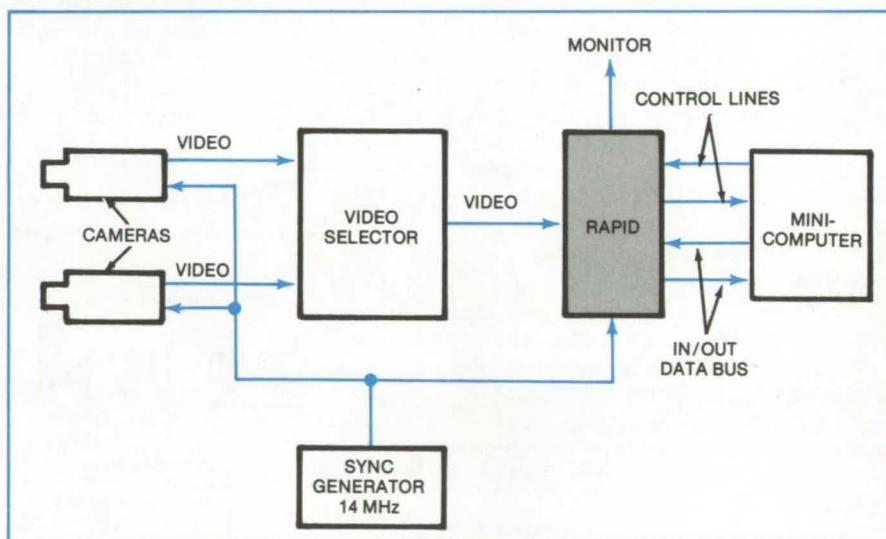
RAPID can continuously update its memory with each frame of the video signal, or it can hold a given frame in memory. In either mode, it generates a composite video output signal representing the digitized image in memory.

Each camera has an array of 188 by 244 photosensitive elements, which are scanned to generate the composite video. RAPID digitizes each picture element into a byte, and 192 by 240 bytes constitute a full frame scan. The

system memory is a 256 by 256-byte array. Since this is more than enough capacity for a complete scan, 64 bytes on the right-hand side of each row and the bottom 16 rows can be used as auxiliary memory.

The memory is assembled from 128 4K-by-1-bit dynamic metal-oxide-semiconductor (MOS) integrated circuits. The 128 chips are on four identical circuit cards. Each card is divided into two blocks, and each block is divided into two parts. The computer can retrieve a byte for analysis by sending a 16-bit address word to RAPID.

RAPID Accepts and Digitizes video picture elements, storing them so that they can be selected by a minicomputer for analysis.



Using a double buffering scheme, eight picture elements of the digitized video signal are written into the memory during 700 nanoseconds, every 2.24 microseconds. This leaves 1.54 microseconds during which the memory can be randomly accessed by the computer.

This work was done by Raymond Eskenazi, Malcolm J. Rayfield, and Yoram Yakimovsky of Caltech for NASA's Jet Propulsion Laboratory. For further information, Circle 14 on the TSP Request Card. NPO-14282

Eliminating Clutter in Synthetic-Aperture Radar

A diffusion technique reduces clutter noise in a coherent SAR image signal without degrading its resolution.

NASA's Jet Propulsion Laboratory, Pasadena, California

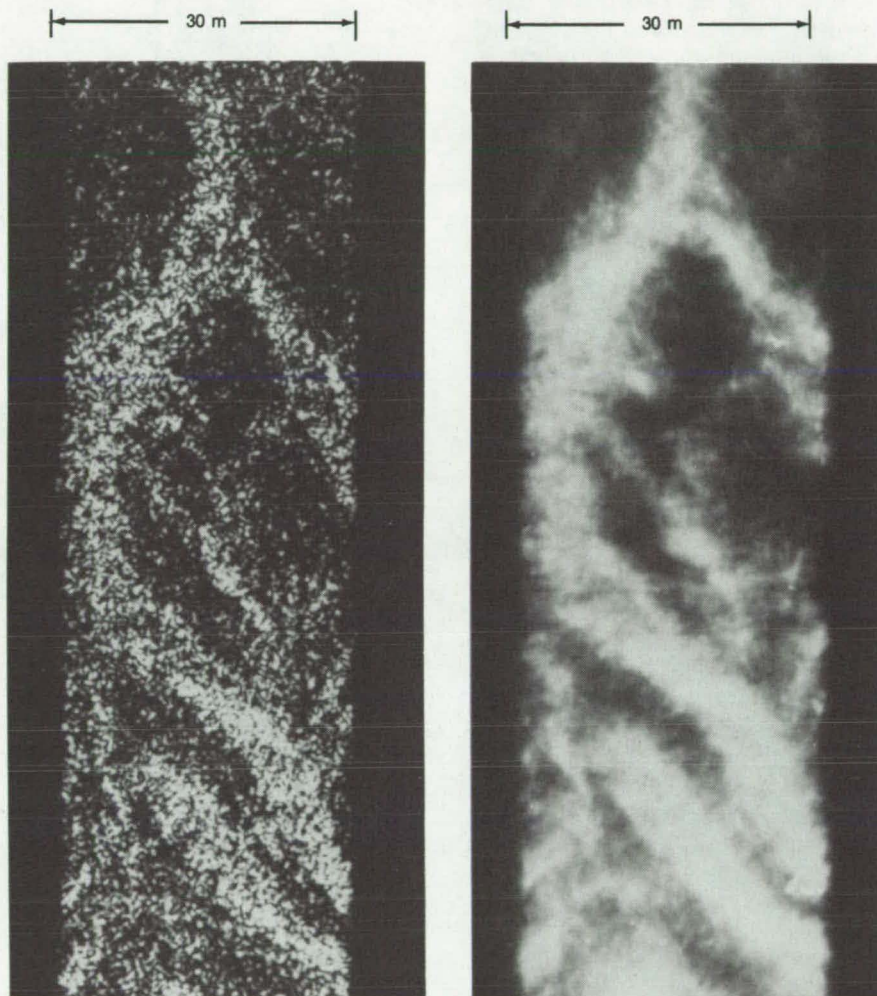
Clutter in synthetic-aperture radar (SAR) images can be greatly reduced by a correlator that introduces time-varying white noise into an image signal, then re-forms the image.

SAR, which employs a small antenna moving in relation to a target to produce the effect of a large antenna, processes the image signal coherently. Like laser imaging systems, which use coherent radiation to form an image, SAR's suffer from the problem of speckling—regions of out-of-phase radiation caused by inhomogeneities such as roughness on the target. In SAR, speckling appears as clutter on the recording film.

The new correlator uses an electronic version of a technique long known in laser imaging to reduce speckling: a moving diffuser is introduced in the image plane of an image-forming lens, and a second lens (which must have lower resolution than the first) re-form the image. Virtually all the speckling is absent in the reformed image. In the SAR correlator, the time-varying white noise is analogous to the moving diffuser in a laser system, and a wide-impulse-response circuit corresponds to the low resolution lens.

The conventional way of reducing speckle in SAR's is to add images obtained from "looks" with different portions of the radar bandwidth. This method is only partly effective, however, because resolution is lost at the narrower Doppler bandwidth used for each independent look. The correlator, in contrast, sacrifices hardly any resolution. The new technique makes radar-mapped terrain features more obvious (see figure). It also has potential application in holographic microscopy.

This work was done by Atul Jain of Caltech for NASA's Jet Propulsion



Both of these **Synthetic-Aperture Radar Images** on film show the same 30-meter-wide stretch of mountainous terrain. The view on the left contains clutter from speckling in the coherent image signal. The view on the right, in which the image signal has been processed by a correlator to reduce clutter, makes terrain features more evident.

Laboratory. For further information, Circle 15 on the TSP Request Card.

This invention is owned by NASA, and a patent application has been filed. Inquiries concerning nonexclu-

sive or exclusive license for its commercial development should be addressed to the Patent Counsel, NASA Resident Legal Office-JPL [see page A8]. Refer to NPO-14035.

Azimuth Correlator for Synthetic Aperture Radar

Azimuth correlation simulates large antenna aperture.

NASA's Jet Propulsion Laboratory, Pasadena, California

Using an azimuth correlator, high azimuthal resolution can be achieved in a synthetic-aperture radar despite a small antenna. The correlator uses charge-coupled-device (CCD) technology to simplify a complex, digital, signal-improvement process. In aircraft or spacecraft, the correlator processes images onboard and in real time to simplify transmission to ground stations.

As shown in Figure 1, radar-range-correlated data samples with real (I) and quadrature (Q) components are transferred to range-line memory elements through a serial-to-parallel converter. Each memory element stores one range line, and the entire memory is organized as N elements cascaded to store sequential range lines. Enough range lines are stored to correspond to the number of points required to correlate over the real aperture in the azimuth dimension.

The last stage of each range-bin memory element is separated from the last stage of the other memory elements by exactly one range line. The outputs of the last stages, taken together, form a complete and unique range bin in the azimuthal dimension at any given time.

When one range line sample is shifted into memory, every other sample moves one stage through the array. As a result, an entirely new set of samples appears at the output stages of the range-line memory elements corresponding to a new azimuthal range bin. This scheme eliminates the need for a high-speed random-access memory.

The azimuthal range bins to be corrected and correlated are automatically read out of the memory in parallel on a range-line sample-by-sample basis. The range-bin readout rate cannot be greater than the range-line sample rate, resulting in the most efficient transfer of data possible. The range bins are next range-migration compensated. This process is precise with no need for interpola-

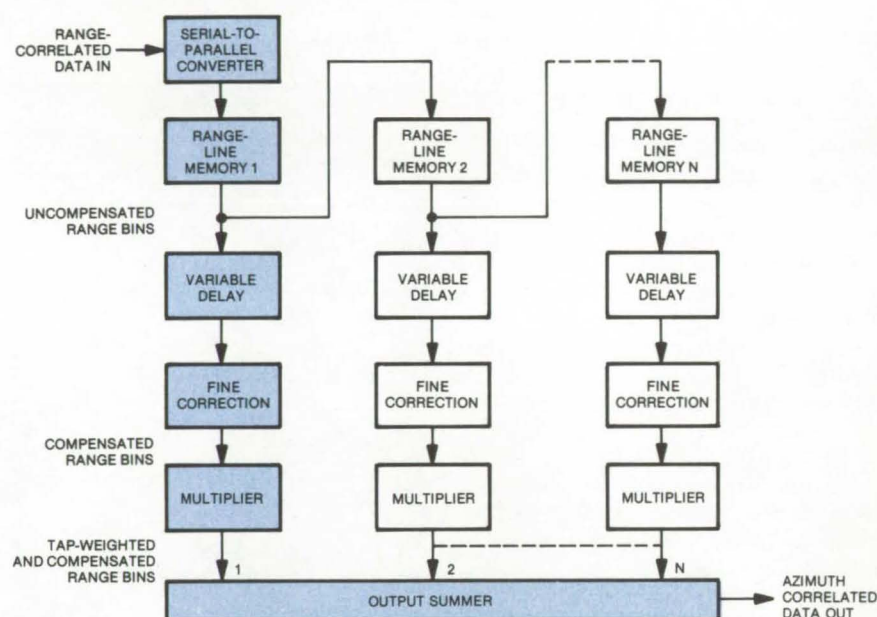


Figure 1. Azimuth Correlator uses a digital processing scheme to retain high azimuthal resolution with a small radar-system antenna. The correlator uses range-line memories to form a range-bin matrix from which range-bins are provided in sequence for real-time image processing.

tion or other methods of approximation.

Figure 2 describes the variable-delay and fine-correction functions. The output of the last stage of each range-line memory element is read into an N-stage register, where N is the maximum number of bins over which migration occurs. In effect, the N-stage registers as a group are storing parallel azimuthal range bins. To compensate for range migration, it is necessary to select the information from any location within each register to form a new range bin for correlation corresponding to the desired correction curve. The net effect is the same as being able to slide every range line in a matrix in either direction through range bins until the desired samples are in the range bin to be correlated.

To avoid interpolation and correct precisely, the curve must be reconstructed within the range bin and effectively resampled at the correct location. This is accomplished using

the $x^{-1} \sin x$ algorithm. If the range line samples in each N-stage register of Figure 2 are convolved with a digitally-sampled $x^{-1} \sin x$ function, the original range-correlated signal is reproduced. However, by shifting the phase of the $x^{-1} \sin x$ signal such that it is sampled at different points, the same range-correlated signal is reproduced following convolution, only it is also sampled at different points corresponding to the phase shift of the $x^{-1} \sin x$ signal. As such, a precise resampling within a range bin may be accomplished to accommodate the desired correction curve.

Range migration correction coefficients from the SAR processor controller electronics positions the $x^{-1} \sin x$ function in each register of each channel at the precise location to accommodate the correction curve. The reproduced signal following convolution is the range-line element from the desired location in the N-stage register properly resampled to cor-

respond precisely to the range-migration correction curve. The net result is, that for every range-line sample shifted into the memory, a fully-compensated azimuthal range bin automatically falls out of the correction stages.

Next each range-bin element of a compensated range bin is weighted by an azimuth reference function coefficient using a digital multiplier. The outputs of each multiplier are then summed to form an image element for each range-bin correlation. The reference function weighting for each range-bin element is fully programmable and is updated from the SAR processor controller electronics to accommodate parameter changes in altitude, velocity, slant range, and the like.

This work was done by Wayne E. Arens of Caltech for NASA's Jet Propulsion Laboratory. For further information, Circle 16 on the TSP Request Card.

This invention has been patented by NASA [U.S. Patent No. 4,132,989]. Inquiries concerning nonexclusive or exclusive license for its commercial development should be addressed to the Patent Counsel, NASA Resident Legal Office-JPL [see page A8]. Refer to NPO-14019.

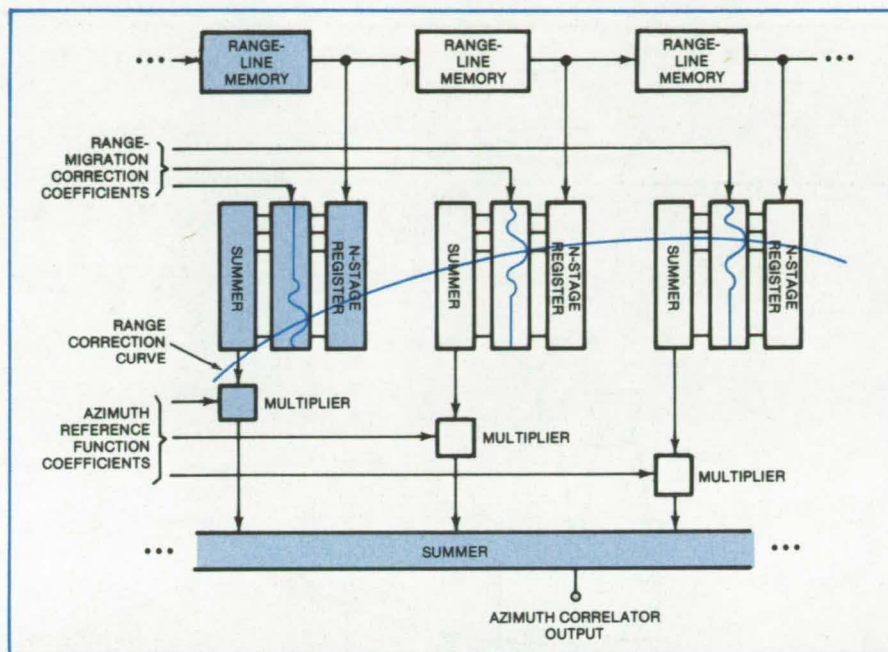


Figure 2. **Variable-Delay and Fine Correction Functions** are initiated by reading the output of the last stage of each range-line memory element into an N-stage register, where N is the maximum number of bins over which migration occurs. Here range migration correction coefficients from the SAR processor controller electronics position the $x^{-1} \sin x$ algorithm in each register of each channel at the precise location to accommodate the correction curve. Thus, for every range-line sample shifted into the memory, a fully-compensated azimuthal range bin automatically falls out of the correction stages.



Signal Separator for Dual-Frequency Antenna

Replacement for dichroic plate reduces noise.

NASA's Jet Propulsion Laboratory, Pasadena, California

A flange in front of one of the horns of a dual-frequency antenna allows the higher frequency to pass, but reflects the lower frequency to the other horn. The flange is about 1.5 meters in diameter and is made of the same material as the horn (copper or aluminum). Because the dimensions of the flange throat are below the dimensions for cutoff of the S-band (or low-frequency) wave, it appears to be solid at that frequency and reflects the S-band signal. However, the flange appears

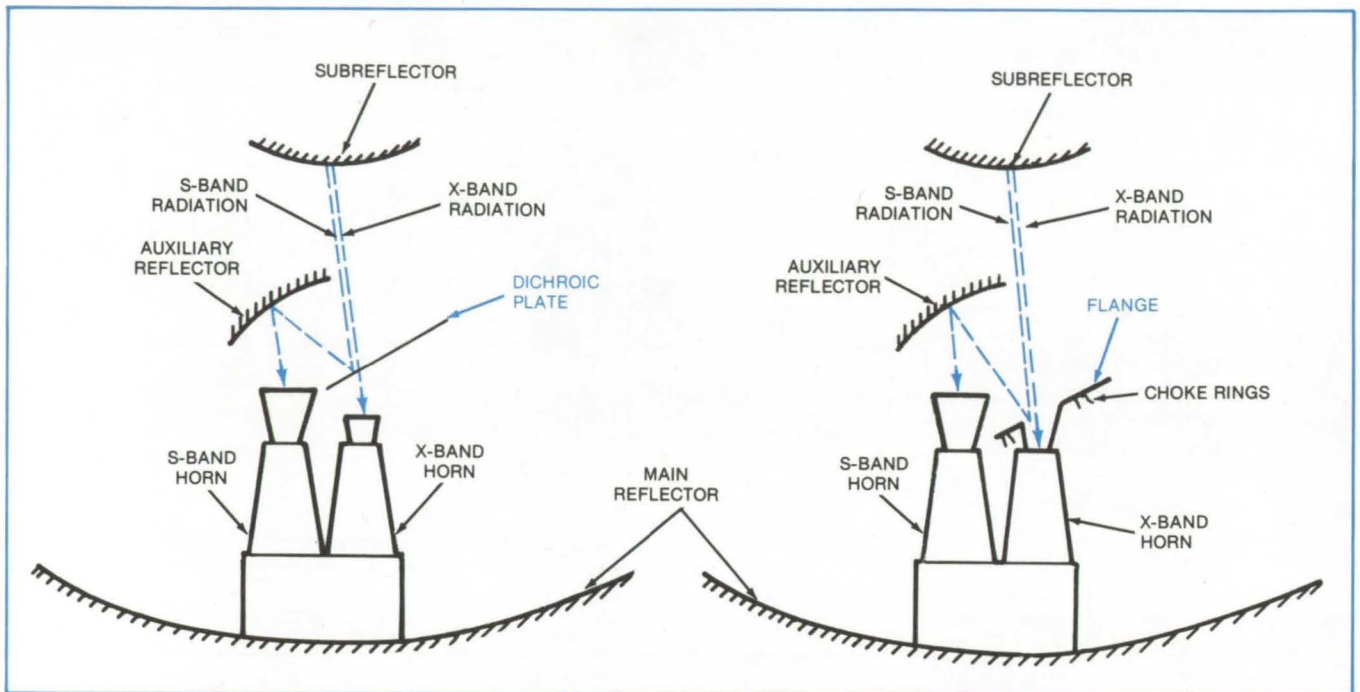
open to the shorter X-band (or high-frequency) wave and admits it to the X-band horn (see figure).

The flange replaces the dichroic plate previously used to separate frequencies in dual-frequency antennas [see "Efficient Dichroic Plate for Microwaves" (GSC-12171) on page 4 of this issue]. Like the flange, a dichroic plate can transmit X-band signals and reflect those at S-band. The dichroic plate, however, must be separately mounted and aligned, and

requires special installation and calibration procedures. The flange, besides being easier to install, is less expensive to fabricate. Most important, the flange reduces the antenna contribution to system noise; whereas, the dichroic plate increases noise temperature by 2 or 3 degrees.

In the dual-frequency antenna, incoming energy at both S- and X-bands received by a 64-meter paraboloid is reflected to a cassegrainian subreflector and then to the flange, which is

(continued on next page)



Dual-Frequency Antenna with flange (right) instead of dichroic plate (left) reduces the contribution of the antenna to system noise because the high-frequency (X-band) signal does not have to pass through the plate medium.

rigidly mounted on the X-band horn at an angle to its axis.

The X-band horn is made just high enough that the S-band short in the flange appears at the horn aperture. Although one side of the flange is shorter than the other because of the flange angle required to reflect S-band signals in the proper direction, this difference

in height does not affect the field pattern of the X-band horn. To improve the flange performance at both low and high frequencies, circular slots called choke rings are cut into the flange surface.

This work was done by Robert W. Hartop of Caltech for NASA's Jet Propulsion Laboratory. For further

information, Circle 17 on the TSP Request Card.

This invention has been patented by NASA [U.S. Patent No. 4,092,648]. Inquiries concerning nonexclusive or exclusive license for its commercial development should be addressed to the Patent Counsel, NASA Resident Legal Office-JPL [see page A8]. Refer to NPO-14022.

Components for an S-Band Communication Subsystem

New S-band communication components include a low-pass filter, a diplexer, and a transmit output filter.

NASA's Jet Propulsion Laboratory, Pasadena, California

A modern RF (radio-frequency) subsystem interconnects two S-band transmitters, two S-band receivers, and two antennas. The subsystem as shown in Figure 1 is capable of connecting either transmitter or either receiver to either antenna while permitting simultaneous operation of a transmitter and a receiver. This is accomplished by the use of RF circulator switches. However, important considerations remain; i.e., to

prevent radiation or the coupling of unwanted transmitter spurious outputs and to provide isolation while the transmitter and receiver operate simultaneously. These functions are accomplished by using newly-developed low-pass-receiver input filters, diplexers, and transmitter output filters.

The subsystem filter-rejection characteristics have been specified out to 35 GHz. In addition to the rejection

and loss specifications, each component carrying the transmitter output power was required to operate at any pressure without breakdown with power levels up to 120 W.

The specifications for the receiver low-pass filter called for a rejection of 30 dB from 10 to 17 GHz and of 50 dB from 17 to 35 GHz. The passband requirements were for minimum loss and minimum VSWR (voltage standing-wave ratio) at a receive frequency of 2.113 GHz.

Two 13-element filters were built and tested. Results have shown that the new filters provided the rejection needed at 10 GHz, exceeding the specification by 8 to 10 dB, but did not meet the 50-dB requirement at 35 GHz. However, these filters provided the rejection in excess of 65 dB at 33.8 GHz, which was the actual target for the 35-GHz requirement. Other filter characteristics included pass-band return loss greater than 22 dB (VSWR less than 1.2/1.0) and the insertion loss of less than 0.1 dB.

The diplexer specifications included a transmitter-to-receiver rejection of 88 dB at a receive frequency of 2.113 GHz and a transmit frequency of 2.295 GHz. The passband requirements had been for minimum loss and minimum VSWR from transmitter or receiver to the antenna. As with the filters, environmental pressure and maximum power requirement had been the same.

A diplexer configuration developed to this specification (see Figure 2) uses no band-pass filters but depends on its diplexing action on the phase properties of the hybrid elements and on the fact that the filters can be made to have nearly-equal phase shifts and reflection coefficients. The hybrids are quadrature types, and the filters are band-rejects centered on the receiver frequency.

The diplexer uses strip-line quadrature hybrids at each end and coaxial band-reject filters between. The hybrids are chemically milled circuits of beryllium copper (silver-plated) between sheets of Teflon and the filters consist of five coaxial stubs coupled to a transverse 50-ohm line. The filter has a 0.1-dB Tchebycheff response and a ripple bandwidth of 140 MHz. This design has been tested and met all the specified requirements.

The design specifications for a transmit output filter called for the rejection of 60 dB for the 4.59- to 8.0-GHz range, 50 dB for the 8.0- to

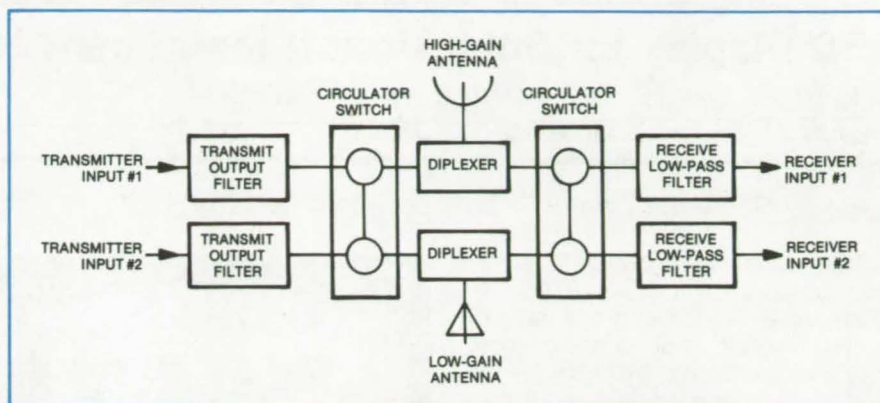


Figure 1. An **S-Band Communication Subsystem** provides the necessary isolation among two transmitters, two receivers, and two antennas. The system uses newly-developed low-pass-receiver filters, diplexers, and transmitter output filters.

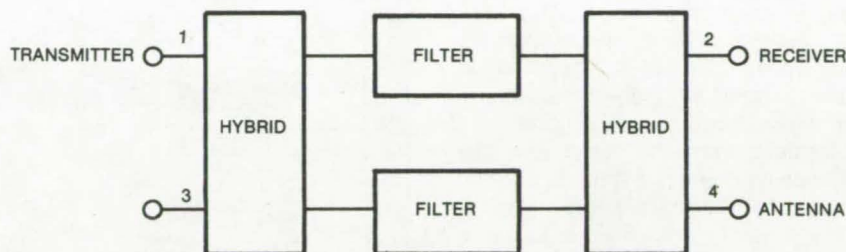


Figure 2. The **Diplexer Configuration** includes two quadrature-type hybrids and two band-reject filters centered on the receiver frequency. Because the transmitter power is divided into two equal parts, each filter has to withstand only one-half the power. The phasing provides for reinforcement of the divided signals to provide full output at the antenna port while exactly cancelling at the receiver port. The desired receive signal at the antenna port is divided by the hybrid, reflected by the band-reject filters, and combined in phase at the receiver input port.

12.0-GHz range, and 30 dB for the 12.0- to 18.0-GHz range. The pass-band requirements called for minimum loss and minimum VSWR at a transmit frequency of 2.295 GHz. The other requirements were the same as for the previous components.

Two filters were built and tested with an input at 134.6 W with no indication of breakdown. Although the filters were slightly deficient between 12 and 15 GHz, they were nevertheless found acceptable in all other areas and were incorporated into the subsystem. The filters have an insertion loss of less than 0.1 dB and a

return loss greater than 23 dB in the operating band.

This work was done by Charles W. Rook of Motorola, Inc., for NASA's Jet Propulsion Laboratory. For further information, Circle 18 on the TSP Request Card.

This invention is owned by NASA, and a patent application has been filed. Inquiries concerning nonexclusive or exclusive license for its commercial development should be addressed to the Patent Counsel, NASA Resident Legal Office-JPL [see page A8]. Refer to NPO-13955.

LED Display for Solo Aircraft Instrument Navigation

Solo pilot's task is made easier through convenient display of landing and navigation data.

Langley Research Center, Hampton, Virginia

The LED display shown in Figure 1 was developed at Langley Research Center to present landing and navigation information to pilots and reduce their workload during solo flights.

Many general-aviation aircraft, including the smaller categories of light aircraft, are equipped with instruments and navigation equipment for instrument-flight-rules (IFR) flight. The workload for solo instrument flight, especially in rough air, can be almost beyond the capability of even an experienced pilot. The pilot's tasks include accurate navigation, chart reading, radio communication with a number of air-traffic control facilities, and the maintaining of precise attitude and trajectory control of the aircraft.

The new LED display includes a paper-tape reader, control circuitry, a digital memory, data latches, and 21 LED alphanumeric displays. A block diagram is shown in Figure 2. On command from the READ pushbutton, a block of 21 characters is read from the paper tape and stored in the digital memory. The control circuitry then reads the memory and distributes the digital data to the individual data storage latches, which are connected to the LED display drivers. Latching the data allows the LED's to operate continuously at their maximum brightnesses. A FWD/REV switch permits the pilot to reverse the direction of the tape reader and retrieve previous instructions. A digital countdown clock/timer conveniently monitors time intervals for precise navigation. The time interval is set with thumbwheel switches, and the count is begun by pushing a button. The time remaining is displayed by an LED, and an alarm can be set to sound at the end of the interval.

Several alternate configurations of the display are possible, including the use of a cassette tape recorder as a more-convenient, higher-capacity data source. Also, data could be transmitted from the airport terminal to the aircraft, where the display electronics would decode and store the instructions for recall by the display. The use

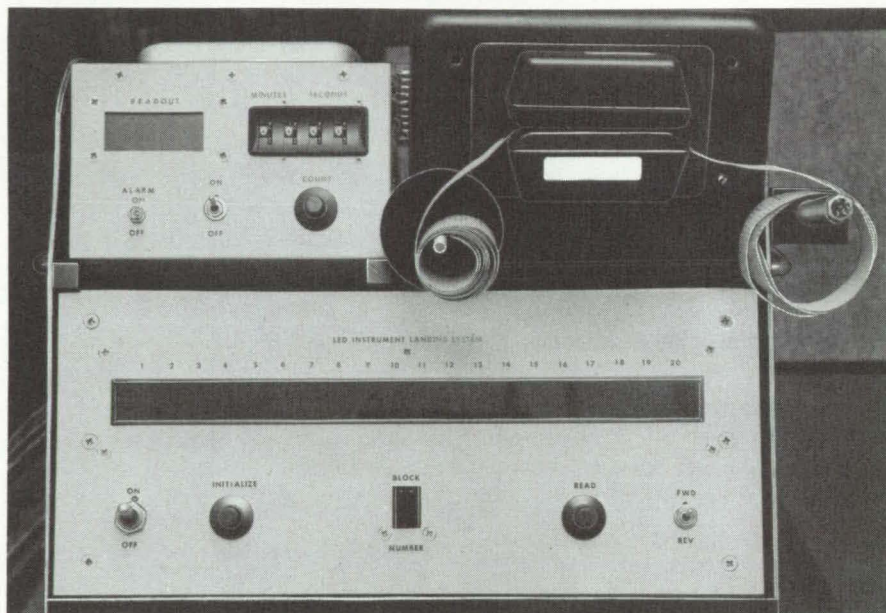


Figure 1. Instrumentation Console With LED Display presents digital landing and navigation data for instrument flight.

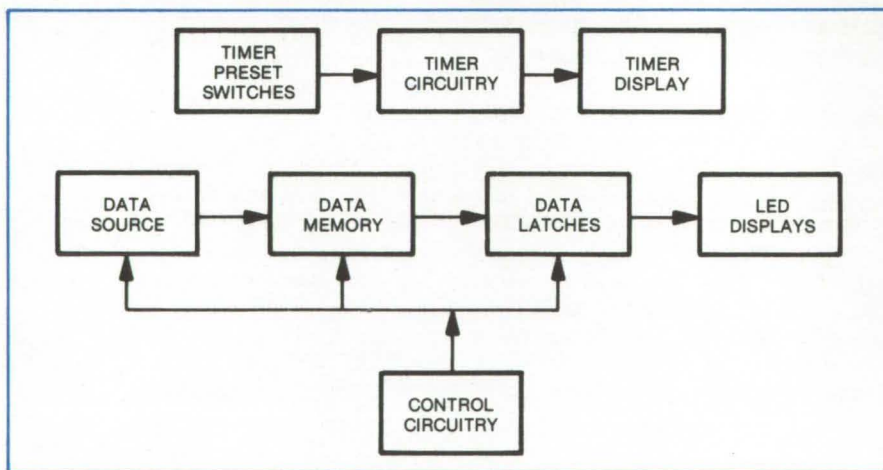


Figure 2. LED Clock-Timer and Data Displays are incorporated in the new instrumentation. The timer is set by a thumbwheel switch and displays the time remaining from the moment of initiation. Navigation data are read from a digital tape (data source) and stored in a memory. Data are stored in individual latches connected to the display to allow continuous operation at maximum brightness.

of LED displays shows promise as a more efficient means of presenting sequential instructions and data, such as course heading, altitude, and radio frequency, to minimize the pilot's workload during solo instrument flight.

This work was done by Roger K.

Crouch, W. Lane Kelly IV, L. J. Lina, and Barry D. Meredith of Langley Research Center. For further information, Circle 19 on the TSP Request Card.

LAR-12292

Cable-Fault Locator

An inexpensive system automatically indicates the location of a short-circuited section of a power cable.

John F. Kennedy Space Center, Florida

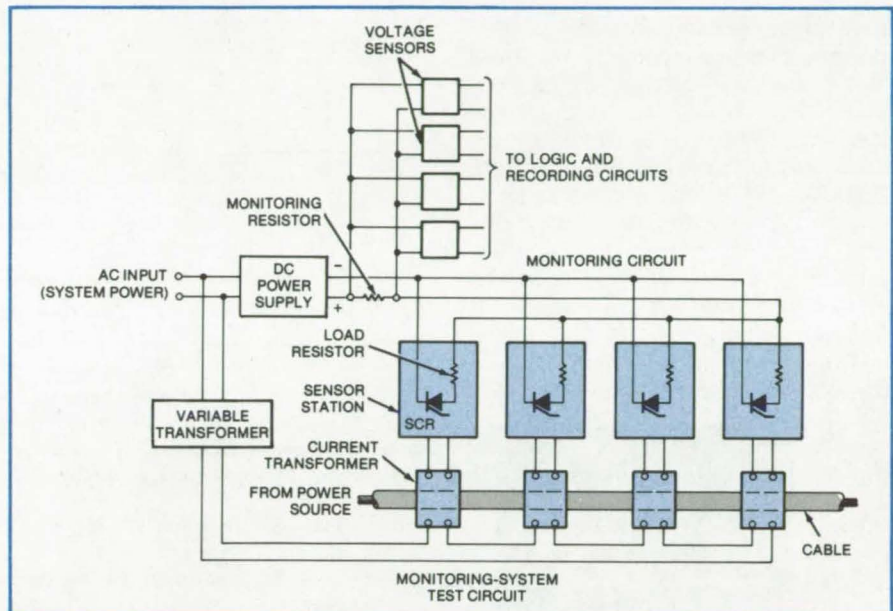
A new fault-monitoring system would instantaneously detect a short circuit in an underground or overhead power cable and display the fault location at a remote monitoring station. A prototype that could monitor a cable with a maximum diameter of 3-1/2 in. (8.89 cm), carrying up to 100 amperes, has been designed.

The simple, potentially inexpensive monitor does not require that the cable be disconnected from its power source or that test signals be applied. Instead, ground-current sensors are installed in manholes or at other selected locations along a cable run (see figure). When a fault occurs, the sensors transmit information about the fault location to the control center. A repair crew can be sent to the location, and the cable can be returned to service with a minimum of downtime.

The high short-circuit current activates all sensors between the power source and the fault. Since the fault will always be between the activated sensor farthest from the power source and the next unactivated sensor, the sensor-status information can be processed by logic circuits to display the location of the affected cable section.

A constant-voltage dc or ac source powers the sensor circuit. At each station, a current transformer encircles all current-carrying conductors in the power cable. The transformer output is applied to the trigger input of a silicon-controlled rectifier (SCR). For normal powerloads, the transformer output is too low to trigger the SCR; however, if there is an unusually high current in the power cable (as would be the case if a fault developed between the cable conductors and ground), the SCR turns on.

Each SCR that is activated places a load resistor in series with a monitoring resistor in the output circuit of the



This **Cable-Fault Monitor** can have many more sensor stations than the four shown here; the larger the number of stations, the more precisely a cable fault can be pinpointed. The variable transformer is included to apply test and calibration signals to the current transformers.

fault monitor. Thus, the voltage across the monitoring resistor will be different for different locations of the fault. Voltage sensors across the monitoring resistor are calibrated to turn on at different voltages. The logic circuitry at the control center processes the voltage sensor signals to determine the location of the faulty section.

The number of sensor stations is limited only by practical considerations of allowable current, voltage, and power in the monitoring circuit. If the monitoring-circuit voltage is increased, more sensors could be installed, but the power dissipated by the SCR load resistors at the sensor stations would also be increased.

A practical fault locator could be powered by a 200-volt ac or dc source. The current in the monitoring resistor would change by 0.05 ampere as each additional sensor is activated.

If the current in the monitoring circuit is limited to 1 ampere, 20 sensor stations can be spaced along a 2-mile (3.2-km) length of cable. The power dissipation in each load resistor is 10 watts, and the circuit would use 12-gage wire.

This work was done by Robert L. Cason and John J. McStay of **Kennedy Space Center** and Andrew P. Heymann, Sr., of Planning Research Corp. For further information, Circle 20 on the TSP Request Card.

This invention has been patented by NASA [U.S. Patent No. 4,110,683]. Inquiries concerning nonexclusive or exclusive license for its commercial development should be addressed to the Patent Counsel, Kennedy Space Center [see page A8]. Refer to KSC-10899.

Cloud-to-Ground Lightning Detector

Device senses electric-field changes and vhf radiation to distinguish cloud-to-ground flashes from cloud-to-cloud flashes.

John F. Kennedy Space Center, Florida

A new lightning detector distinguishes cloud-to-ground strikes from strikes that travel between clouds. The instrument, which is part of the Kennedy Space Center Lightning Detection and Ranging System (LDAR), might also be used as a shutter control for lightning photography or as a control for lightning direction finders. It also could serve as a lightning ground-stroke counter or lightning warning.

The ground-strike detector measures two parameters of the radiation

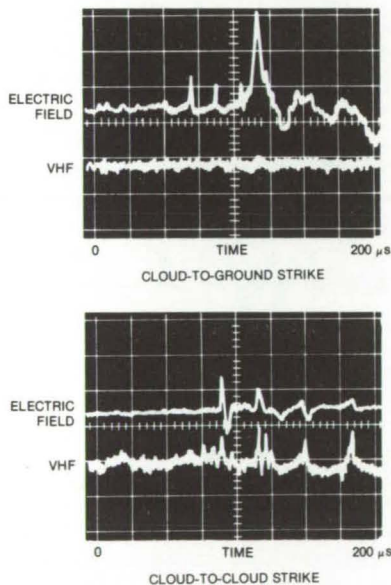


Figure 1. The **Radiation From Lightning Strikes** is shown in these CRT photographs. Note the difference in electric-field characteristic between the upper (cloud-to-ground) and lower (cloud-to-cloud) photos. Also, there is almost no VHF radiation in the cloud-to-ground strike.

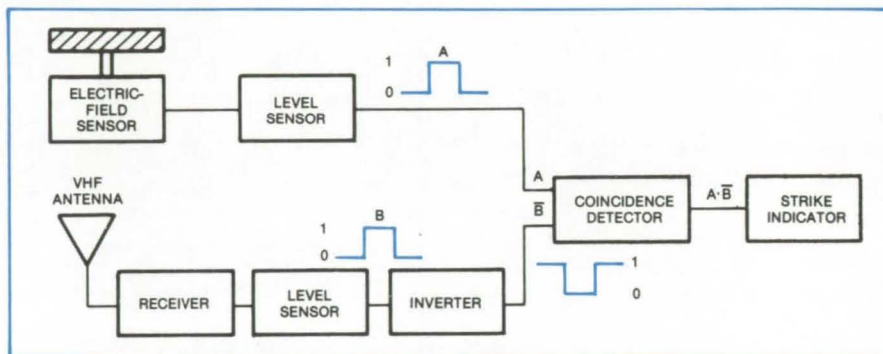


Figure 2. If this **Lightning Detector** senses two coincident pulses, one in the electric-field channel and one in the vhf channel, it assumes that the flash has occurred between clouds. If, however, it senses only an electric-field pulse, it indicates that a ground strike has occurred.

field associated with a flash of lightning:

1. The rate-of-change of the electric field in the 0.01 to 2 MHz frequency range and
2. Electromagnetic radiation in the very-high-frequency (vhf) range between 40 and 50 MHz.

The detector can distinguish the two kinds of lightning because, for cloud-to-ground strikes, there is a large change in the electric-field gradient, and there is minimal vhf radiation. In cloud-to-cloud lightning, there are both negative and positive electric-field changes, and there is appreciable vhf radiation (see Figure 1).

When a strike occurs, an antenna senses the rate-of-change of the electric field (see Figure 2). If the field change is positive and it exceeds a predetermined threshold, a level sensor produces an output for about 2 microseconds.

Concurrently, vhf radiation that is received by another antenna produces

pulses that are fed to a second level sensor. When the pulse level exceeds the predetermined threshold, the sensor generates a second 2-microsecond pulse, which is reversed in polarity by an inverter. If the threshold is not exceeded, the level sensor produces no output.

The pulses from the electric-field channel and from the vhf channel are sent to a pulse coincidence detector that gives an output only when there is an electric-field pulse and there is no vhf pulse. If these conditions are met, the coincidence detector output indicates that a ground strike has occurred.

This work was done by Carl L. Lennon of Kennedy Space Center. No further documentation is available.

Inquiries concerning rights for the commercial use of this invention should be addressed to the Patent Counsel, Kennedy Space Center [see page A8]. Refer to KSC-11099.

Reliable Inverter Systems

Base driver with common-load-current feedback protects paralleled inverter systems from open or short circuits.

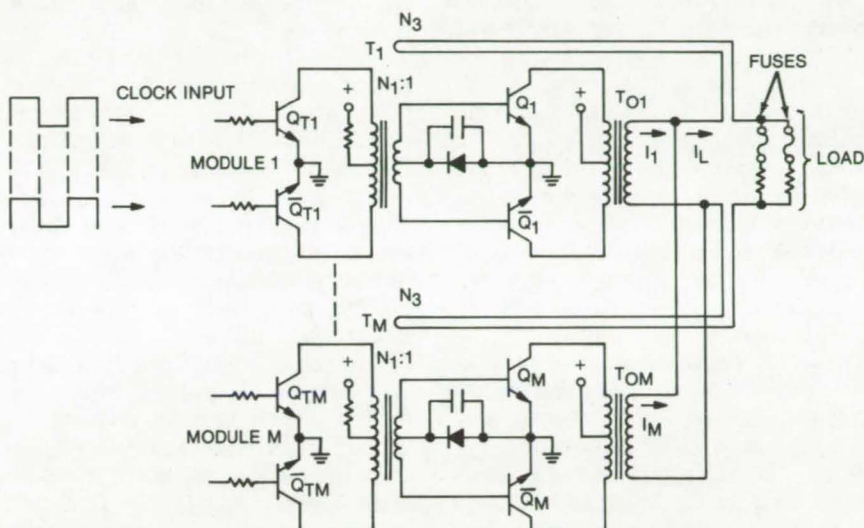
NASA's Jet Propulsion Laboratory, Pasadena, California

Conventional paralleled inverter systems used in power conditioning do not always protect sufficiently against open- or short-circuit faults. Even a circuit that has individual-output-current feedback produces unequal current sharing among power transistors, particularly during turn-on. High current in one power transistor during turn-on may result in transistor failure due to the second-breakdown effect.

An improved feedback arrangement utilizes the common load current derived from all the modules of a paralleled inverter system to control the base drive of each module. This arrangement protects the entire system against open- or short-circuit faults occurring in any of the modules.

The modified base-drive circuit, shown in the figure, incorporates a feedback winding N_3 in the drive transformer of each module. Since this winding feeds the same load current back to the base drive of each module, each power transistor is driven into saturation during an overload condition affecting any of the modules. Therefore, any affected transistor can withstand burnout until the protective fuse operates.

The modified base drive also minimizes the effects of unequal turn-on characteristics in the various power transistors. If Q_1 switches faster than Q_M , current I_1 is larger than current I_M just after turn-on. However, since all transistors are driven by base-



Improved Base Drive for paralleled inverter system uses a feedback winding N_3 in each drive transformer (T_1 through T_M) to apply the same sampling of load current to the base drive of each power transistor. This arrangement protects the inverter system from damage by open or short circuits.

currents of the same magnitude, their output currents equalize quickly.

The circuit also eliminates the total system oscillation that can occur in conventional inverters because of an open circuit in a primary transformer winding. The common feedback signal produced by functioning modules forces the operating frequency of a failed module to coincide with the clock drive so that the module resumes the normal operating frequency in spite of its open circuit.

This work was done by Satoshi Nagano of Caltech for NASA's Jet Propulsion Laboratory. For further information, Circle 21 on the TSP Request Card.

This invention is owned by NASA, and a patent application has been filed. Inquiries concerning nonexclusive or exclusive license for its commercial development should be addressed to the Patent Counsel, NASA Resident Legal Office-JPL [see page A8]. Refer to NPO-14163.

Solar Power Conditioner

A new power conditioner controls the output of a solar array so that excess energy not needed by the load is diverted to charge batteries. The circuit output is standard 110-volt 60-Hz power. It has a dynamic-impedance comparator that automatically determines whether or not the array is delivering its maximum power. (See page 41.)

Eye-Controlled Switch

A new sensor and circuit allow a person to control electronic equipment simply by moving his or her eyes. The device has already been incorporated into an electric-powered wheelchair, where it controls forward and reverse motions, starting and stopping, and steering. Other possible applications are telephone dialing, appliance control, and page turning for the handicapped. (See page 84.)

Microcomputer Helps Evaluate Skin Burns

Skin burns are rapidly diagnosed by a new microcomputer-based system. Multispectral images are interpreted to display a "map" of the burn area. The image is recorded by a silicon-diode-array camera and projected on a color monitor. Other peripherals are a tape drive and an operator's console. (See page 82.)

Monitoring Disaster Areas Via Satellites

Easily-displayed low-cost radar targets signal distress to orbiting satellites.

Langley Research Center, Hampton, Virginia

A proposed technique would use passive radar targets on the ground to communicate distress and/or the extent of damage in a given area. Orbiting satellites equipped with imaging radars operating in a 1- to 10-GHz range could detect these targets and relay the messages to monitoring stations day and night in all weather conditions. Effective medical and evacuation efforts could be carried out successfully around the globe due to this early warning.

The concept involves RF (radio-frequency) reflectors operating in conjunction with satellite-imaging or side-looking radars (synthetic-aperture radars). Targets could be rigid, erectable, and inflatable radar reflectors installed in critical areas. They could be quickly deployed in emergency or might be designed as permanent installations to permit real-time monitoring of potentially dangerous areas. A network of satellites would present a total global coverage several times a day. Major disasters to be monitored could include floods and droughts,

storms, volcanic eruptions, and Earthquakes.

The reflective targets may be deployed in several ways. One of the proposed applications is to install a target array along a river to monitor floods. Each target would be set at a different height. When the water is low, radar detects all the exposed targets. A high waterline may inundate some of the targets, presenting a warning of an oncoming flood until possibly all the targets are inundated.

The same method can be used to monitor floods in low-lying areas during storms and to observe erupting volcanoes for lava flows and ash fallout. In case of volcanoes, some inundated targets are concealed by lava flow, possibly indicating lava flow direction toward populated areas. Earthquakes are monitored by observing set reflector patterns along potential faults.

A second major application is to display a reflector array to present a message or to indicate key places. Since the targets are easy to deploy, they can be used by survivors to signal

distress or to request specific assistance. An important application is to place the targets along the evacuation routes so that alternative exits can be planned in an emergency. Hospitals, communications centers, and other key installations can also be monitored to indicate whether these centers are still operational.

A third major application is to measure rainfall, surface runoff, evaporation, and soil moisture. A specially constructed reflector installed within a formed-concrete waterproof catch basin could be used for this purpose. The reflector is basically a vertical aluminum cylinder resting on a flat plate. The varying water level in the catch basin alters the radar image brightness of the target, which can be used to measure the rain activity in remote locations.

This work was done by Wilford E. Sivertson, Jr., of Langley Research Center. For further information, Circle 22 on the TSP Request Card.
LAR-12344

Simpler Cabling and Power Link for Remote Readouts

Display power and segment data are multiplexed over the same coaxial line.

Goddard Space Flight Center, Greenbelt, Maryland

A nine-digit, seven-segment, light-emitting-diode (LED) display normally requires 63 (9×7) input wires to feed data to each of the segments. Even if the digits are time-division multiplexed, a minimum of 16 (9+7) wires is needed. In either case, the display also requires a sizeable power source for the segment currents. If several remote readouts are to display data from a single, centrally located source, these power and cabling

requirements can be prohibitive in both their complexity and cost.

Most of these problems are eliminated by a system that transmits both the display data and the display power over the same coaxial line (see Figure 1). The data for all 63 segments are transmitted serially and are time-division multiplexed with the power. Thus, only one wire and a return lead are needed, and a single power supply at a central location can service all of the remote displays.

This approach was recently adopted to link several remote readouts with a time standard at Goddard Space Flight Center. In this system, the remote unit displays the day (3 digits), hour (2 digits), minutes (2 digits), and seconds (2 digits) on LED displays. Serial data are transmitted to the remote unit in a pulse-width-modulation (PWM) code, for which a 2-microsecond pulse represents a logic "0" and an 8-microsecond pulse represents a logic "1" (see Figure 2).

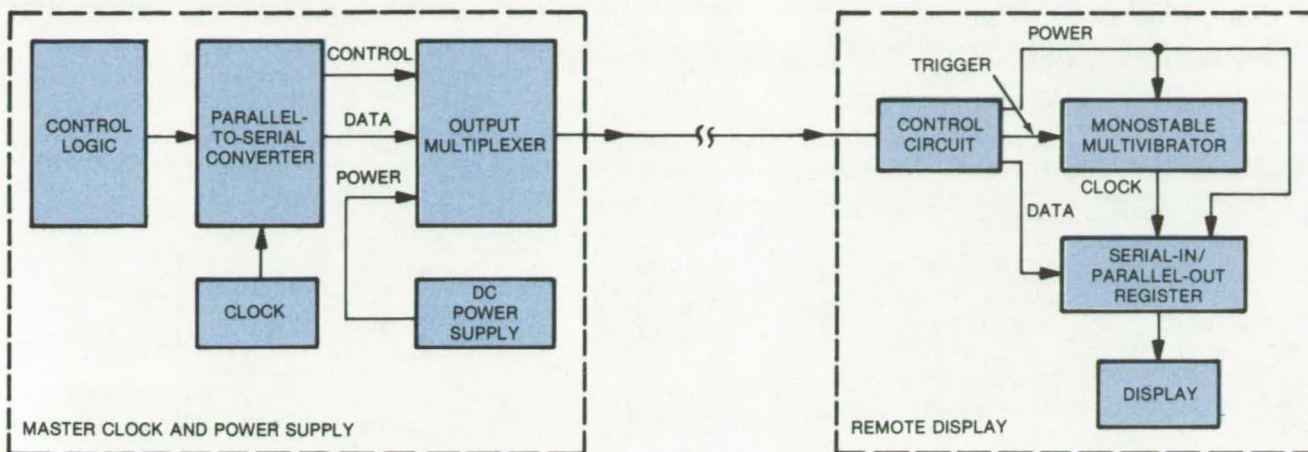


Figure 1. **Time-Counting Circuitry** generates day, hour, minute, and second data as parallel, seven-segment decoded bits. These are converted to pulse-width-modulated serial bits, are time-multiplexed with the power, and transmitted over a single coaxial line to the remote unit.

Data are sent at the beginning of each 1-second cycle. Before transmission begins, dc power is removed from the line, and the voltage drops from the supply level (6 volts) to the true logic level (which is 4 volts in this case). It is held at that level for 51 microseconds to ensure that switching transients have died out. Following this period, data pulses are sent over the line at a bit rate of 100 kilohertz. Data transmission is terminated 689 microseconds after time zero, and the power voltage is restored. The cycle repeats once each second.

At the remote unit, serial-in, parallel-out shift registers store the incoming data. The registers light up the LED segments in the pattern prescribed by the most recent transmission. A monostable multivibrator clocks the registers 5 μ s after the start of each data period. If the incoming signal is low at this point, the datum is recorded as a logic "1"; if the signal is high, it is a logic "0". The incoming dc power charges a capacitor in the remote unit. During the power-off part of the cycle, the capacitor supplies energy to the logic and LED's. (A rechargeable battery could also be used for temporarily

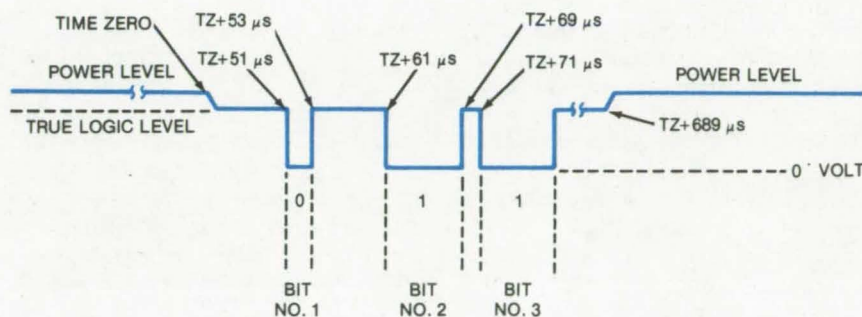


Figure 2. **Data Are Sent** to the remote time indicator as a string of 64 bits (one fill bit and 63 data bits). The bits are pulse-width modulated; a short bit represents a "0", and a longer bit represents a "1". After the data have been received, power is transmitted for the rest of the 1-second multiplex cycle.

energy storage, at some sacrifice of compactness and economy.)

The data stream consists of 64 bits. The first is a fill bit, which is shifted through but not retained. The 63 remaining bits contain the on/off information for each of the seven segments of the nine LED's.

The time standard in the transmitter uses conventional time-counting circuitry that produces 63 parallel, seven-segment decoded outputs. Logic circuitry converts these parallel data into PWM serial data, and the

output circuit multiplexes the data and power for transmission over the coaxial line.

*This work was done by James C. Perry of **Goddard Space Flight Center**. For further information, Circle 23 on the TSP Request Card.*

This invention is owned by NASA, and a patent application has been filed. Inquiries concerning nonexclusive or exclusive license for its commercial development should be addressed to the Patent Counsel, Goddard Space Flight Center [see page A8]. Refer to GSC-12411.

A Closed-Loop Control-Loading System

Correction of dynamic control forces is proposed for flight simulation system.

Langley Research Center, Hampton, Virginia

Many control-loader systems for man-in-the-loop flight simulation that allow for digitally-computed control forces (e.g., forces due to aerodynamic effects or bob weights) provide correct static forces but incorrect dynamic forces. The errors arise from computational delay introduced by the digital process into the continuous control-loader system.

Such a control-loading system was in use on the Langley Differential Maneuvering Simulator (DMS). The DMS realistically simulates two aircraft operating in a differential mode. It consists of two identical fixed-base cockpits and dome projection systems. Each projection system consists of a sky/Earth projector and a target-image generator and projector. The cockpits include typical instrumentation, G-suits, programable buffet mechanisms, and programable control forces. Although the programable control forces are a small part of the overall system, they play a large role in providing the pilot with kinesthetic cues.

Each cockpit is equipped with programable, hydraulic control-loading servos in all three axes. The system can be programmed for preset nonlinear spring gradients, damping, friction, breakout, dead band, and electric stops. Each axis also has inputs for computer-generated forces that are a function of the aircraft dynamic situation. These forces, which are due to aerodynamic effects, bob weights, and the like, are programed in the central digital computer along with the two aircraft models, the relative geometry, and the projection drive equations.

During continued use, it became standard practice to adjust the hardware damping in the pitch axis to well above the value specified for critical damping whenever computer-generated spring gradients or bob weight dynamics were employed. This was necessary to maintain a critically damped system and, in some cases, to

avoid instability. In order to understand the reasons for this increase in required damping, a linear analysis using sampled-data theory was carried out.

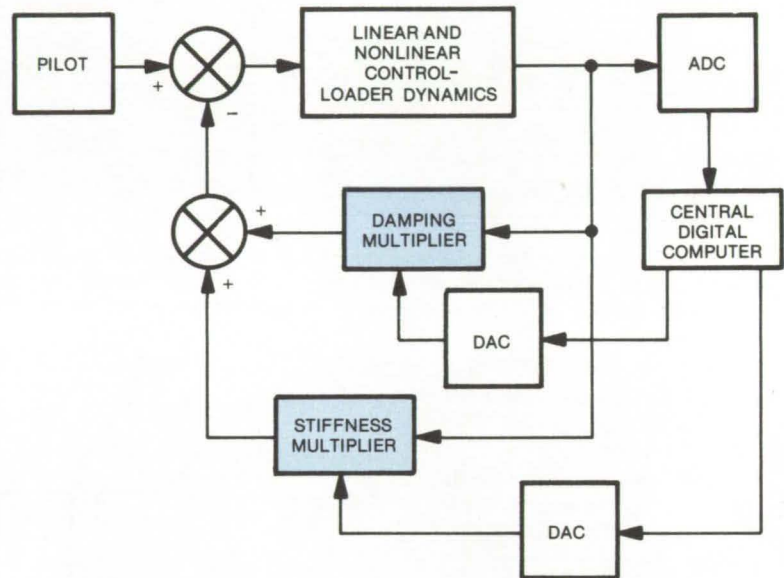
A sampled-data model that accounts for the effects of the central digital simulation computer on the response of the analog control-loader system has been developed and successfully validated. The model includes the representation of a linear control-loader servo with digital feedback of spring gradient forces and, if desired, bob weight forces and actuator lag. The recursive-equation solution of this model was validated with a hybrid simulation of a linear control-loader servo with digital gradient force feedback only and also with the DMS control force system as used in actual flight simulation, both with and without bob weight effects.

Model analysis revealed that errors introduced by force feedback through the digital computer are manifested, in terms of a second-order system, in a reduction in damping and, more signifi-

cantly, in frequency. The revelation of this frequency error and the possible effect of this error on pilot performance in simulated flight have led to a new implementation of control-loader hardware.

The impact of the digital delay is alleviated by the inclusion of two analog multipliers in the feedback loops of the continuous hardware, as shown in the figure. Since the multiplications are carried out in the continuous domain, the lags in the gradients and damping due to the digital computer do not affect the system frequency and damping adversely.

This work was done by Billy R. Ashworth and Russell V. Parrish of **Langley Research Center**. Further information may be found in NASA TN D-8371 [N77-16020], "The Effect of Digital Computing on the Performance of a Closed-Loop Control-Loading System," a copy of which may be obtained at cost from the North Carolina Science & Technology Research Center [see page A7]. LAR-12167

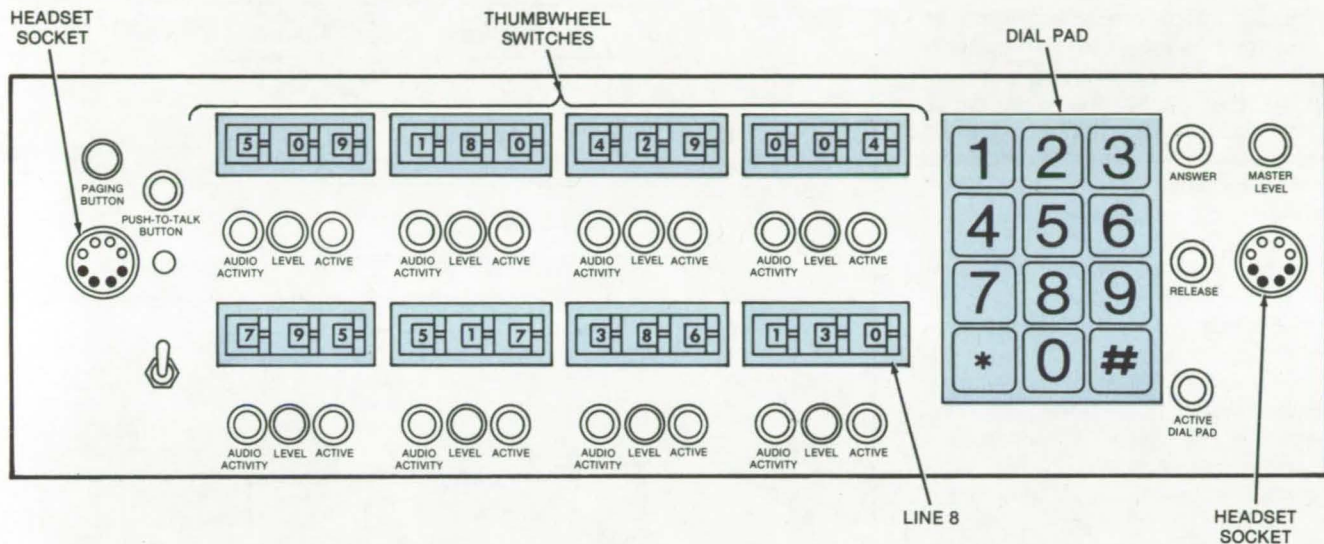


Control Loader and its central digital computer incorporate two analog multipliers in the feedback loops to prevent the computer from adversely affecting system frequency and damping.

A Telephone Multiline Signaling System

Single telephones may be connected to a number of telephone lines.

John F. Kennedy Space Center, Florida



This **Console for the Proposed Telephone Multiline Signaling System** can connect a user to up to eight telephone lines for monitoring and/or conferences. Signals from the console are transmitted via a common signal pair to a central switching computer that interconnects the requested calls.

A proposed telephone signaling system interconnects users of from one up to eight telephone lines in a network. The system is very useful in coordinating activities in large plants and installations. It permits spontaneous conferences, paging, and monitoring from key locations.

Each user has a console with eight selector switches: each switch is a set of three thumbwheels for dialing a three-digit number. Associated with each switch is an audio-activity light, a volume-level knob, and an active button. The audio-activity light flashes when there is audio on the selected line, the volume control permits separate adjustment on each channel, and the active button is depressed for talking on the particular channel.

Each console also includes an active-dial-pad button. The button is depressed to make a point-to-point call by keying in the desired number on the tone pad. These calls are terminated by depressing the release button. Incoming calls are answered by depressing the answer button. All of the point-to-point calls are handled only over line eight on the console. Line-eight activity is preempted for incoming or outgoing point-to-point

calls. After a point-to-point call is terminated, line eight is automatically returned to the net number on the thumbwheel display.

Other panel features include a master level to control volume simultaneously on all channels, sockets for two headsets, a paging button, a headset push-to-talk button, and a toggle switch to stop audible ringing. When both headsets are removed, the instrument turns off automatically.

The entire system is designed with logic circuits. When the thumbwheel switches are manipulated, electrical signals are generated and fed to a bank of AND gates, a group of channel gates, and a command gate. The banks of AND gates include one bank per switch deck. Three banks in this instance are used, one representing units, another tens, and a third hundreds.

The information dialed in the thumbwheel switch requesting a particular line is fed to the AND gates and is subsequently transferred to an encoder. The encoder converts the signals into touch-tone pairs, which are transmitted over a single line pair to a dual-tone multifrequency decoder that converts the signals into binary

electrical signals. These are input to the central switching computer.

Simultaneously, the signals are also fed to a group of channel gates corresponding to the channel on the onsite console. This indicates to the system center the channel to which the particular telephone line is to be connected.

The signals generated by the thumbwheel switch as well as by other pushbuttons are also used to gate command signals through the encoder and decoder logic circuits. These are used to instruct the system computer about specific services, such as talking as well as listening over a particular line.

This work was done by Pierce C. Toole of Kennedy Space Center and Jerry L. Belt, Reams Goodloe, and Donald B. Leiniger of Planning Research Corp. For further information, Circle 24 on the TSP Request Card.

This invention is owned by NASA, and a patent application has been filed. Inquiries concerning nonexclusive or exclusive license for its commercial development should be addressed to the Patent Counsel, Kennedy Space Center [see page A8]. Refer to KSC-11023.

Fader and Ramp Shaper Replace Linear Filters

Switching transients can be suppressed without phase or transport lag or attenuation.

Lyndon B. Johnson Space Center, Houston, Texas

Linear filters are often used to immunize servocontrol systems against abrupt changes in drive signals that might otherwise cause transients and instability. In certain critical loops, however, the additional processing delay caused by the filters may produce an unacceptable phase shift and transport lag.

Rather than decreasing the controller bandwidth with linear filters, it is possible to suppress the objectionable switching transients with signal-shaping circuits that convert large, abrupt inputs into smaller segments that can be handled within the response range of the system. The individual segments are implemented in a train of consecutive execution cycles until the entire input signal has been processed. These techniques, which have been applied in the development and simulation of the Space Shuttle control system, can be optimized to introduce no attenuation, transport delay, or phase lags in the new output signal. They also require fewer computations than linear filters to accomplish the same stabilization.

Two designs that use these techniques have been developed: One, a digital "fader" circuit, smooths the output developed when its input is suddenly switched, by gradually engaging the new level over a specified time interval; the second circuit, a "ramp shaper," interfaces a low-rate processor with a higher rate processor by dividing the output of the slower loop into increments that are processed over interim cycles of the faster processor. The circuits differ in their application but are similar in their operation.

The fader can be implemented by the design shown in Figure 1. Once the enable signal (T) is set, the fader will operate over the number of cycles defined by NFADZ (an integer). At the

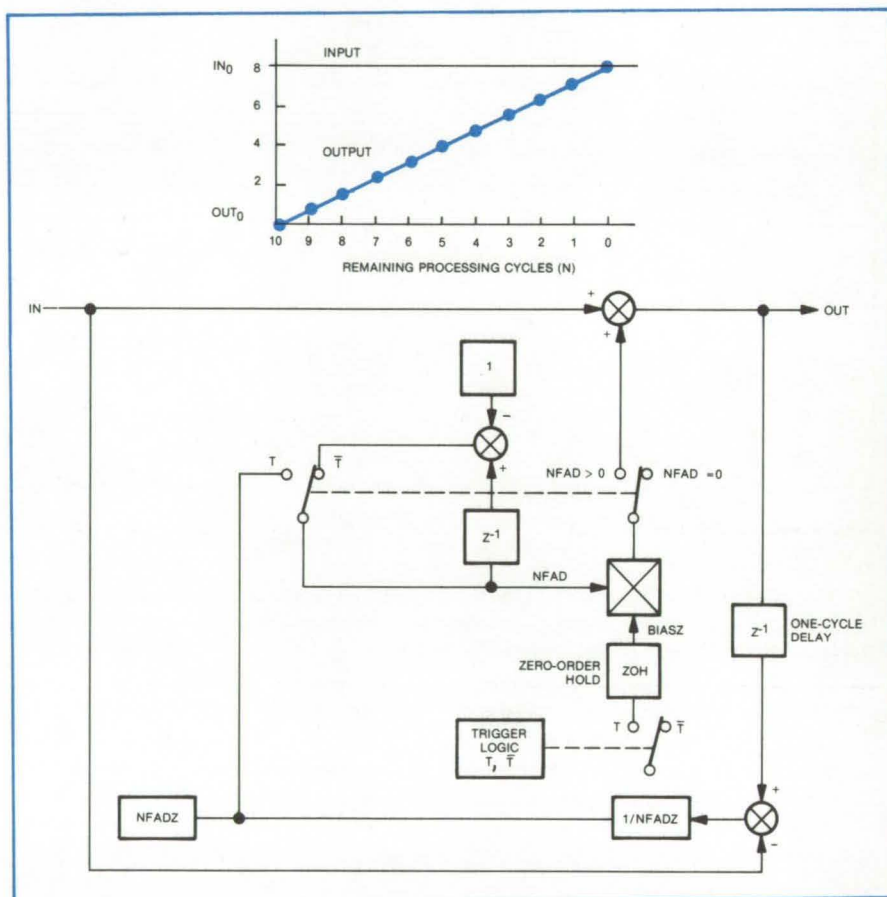


Figure 1. The **Fader Circuit** gradually engages a new input signal in a series of increments over a specified time interval. At the end of the interval, the signal has been transferred to the output without attenuation, and transients and instabilities that might have been introduced by abrupt switching have been prevented.

end of each cycle, the fader output (OUT) is given by the equation

$$OUT = IN + \frac{N}{N_0} (OUT_0 - IN_0)$$

where N_0 is the total number of required cycles, N is the number of cycles remaining, and $OUT_0 - IN_0$ is the difference between the values of the old and new inputs at the time of switching. The graph in Figure 1 shows a typical fader output.

The ramp shaper, shown in Figure 2, divides the low-rate sample into an integral number of equal-magnitude

increments that are defined by the ratio of the low-to-high processing times and distributes the change over consecutive increments. Operation is governed by the equation

$$OUT_n = OUT_1 = o(-) + \frac{n}{n_{max}} (IN - OUT_1 = o(-))$$

A typical output for the case

$$n_{max} = \frac{t_{slow}}{t_{fast}} = 6$$

is shown in the graph.

Both of the functions can be refined by perceiving sampled data that

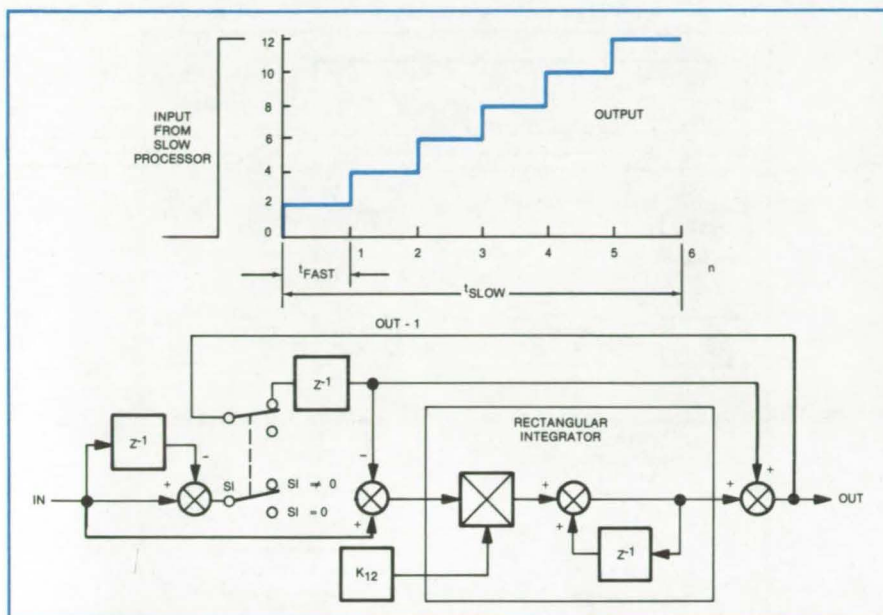


Figure 2. The **Ramp Shaper** divides the input from a low-rate processor (t_{slow} processing time) into increments that are each processed within a cycle period (t_{fast}) of a fast processor.

require no preconditioning for further processing and by computing the optimum number of fader cycles or optimum signal increment for remp-shaping compatible with system stability. Ideally, zero phase-shift capability could be reached through these computations.

This work was done by Thomas A. Robinson of Honeywell Inc. for Johnson Space Center. For further information, Circle 25 on the TSP Request Card.
MSC-16115



Optical Memories in Digital Computing

Potential uses of
multiport optical memories

Marshall Space Flight Center, Alabama

High-capacity optical memories with a relatively-high data-transfer rate and multiport simultaneous-access capability may serve as the basis for new computer architectures. Several computer structures that might profitably use such a memory are: (a) a simultaneous record-access system, (b) a simultaneously-shared memory computer system, and (c) a parallel digital processing structure.

Figure 1 shows the proposed application of a high-capacity optical memory in a simultaneous record-access system. This application involves the storage of vast quantities of records of information, such as libraries, insurance data, medical data, seismic data, criminal data, defense data, tax information, patent records, telephone numbers, stock market information, and the like. Data are stored in page format in the optical memory. The data requirements of each terminal are, in some cases, low enough to have one memory port feed several terminals through a multiplexer.

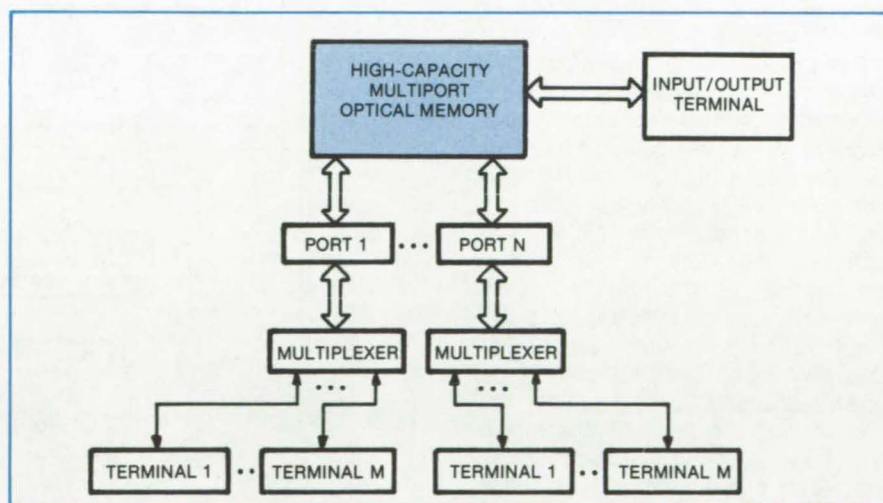


Figure 1. **Record-Access System** incorporates a high-capacity optical memory. Data are stored in the memory in page format. Access to any page is through a cathode-ray-tube (CRT) terminal connected through one of the memory access ports.

There are tradeoffs between port speed, multiplexer speed, and the number of ports. The most effective system would match the total number of users at one port to an economical multiplexer such that the average access time for any user is reason-

able (about 1 min). This access time, divided by the number of users per port, fixes the multiplexer speed and memory-access time per page.

The user terminals are normally applied in the read-only mode and are
(continued on next page)

not allowed to perform write operations to memory. Writing is introduced through the input terminal through a separate memory port.

Figure 2 illustrates the simultaneously-shared-memory computer system. It is essentially the same as most current time-sharing structures. Several users are allowed access to a processing unit. Primary memory is allocated, and user programs are executed independently of the multiport secondary, if possible. Calls to special application programs and large blocks of data are obtained by swapping the data in and out from the multiport memory.

Since swapping of information between memories is a common problem in time-sharing systems, the potential access ease and speed of moving pages in and out of the optical memory is a definite improvement. Some of the parameters needed to characterize such a system are a number of bits per page, the number of pages, the number of ports, access time, primary memory size, write protection scheme, and division of the operating system between the primary memory and the multiport memory.

Figure 3 shows the computer structure for parallel processing. This arrangement is important in applications requiring an enormous number of computations.

The proposed structure is based on a single bus that allows this module to function independently of the other processors and the multiport memory. Each minicomputer (module) is connected to multiport memory through a port and a page memory buffer. This buffer is then tied to the bus for transferring to the processor and other memory units. Transfers between modules are made on an outer bus connecting each module.

An alternate configuration that places the control of all processors under one computer is also proposed. Instructions are kept in the optical memory and fetched by the control computer. Characteristic parameters of both systems are the number of bits per page, the number of pages, the number of ports, page transfer rates, bus transfer rates, and the types of synchronization signals.

This work was done by C. O. Alford

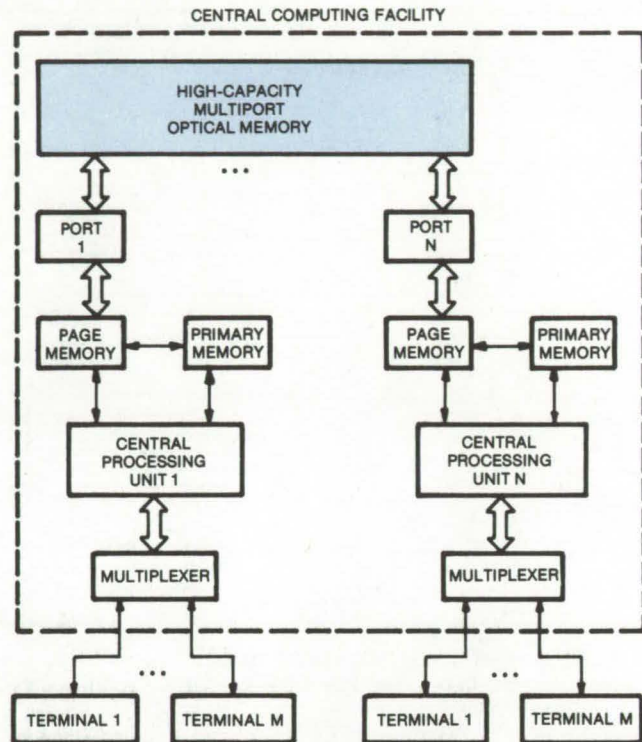


Figure 2. This **Simultaneously-Shared Memory Computer System** uses secondary multiport optical memory as a backing-store mass memory device. Its multiport structure makes it equivalent to several disk drives, and its transport rate is superior to disk systems.

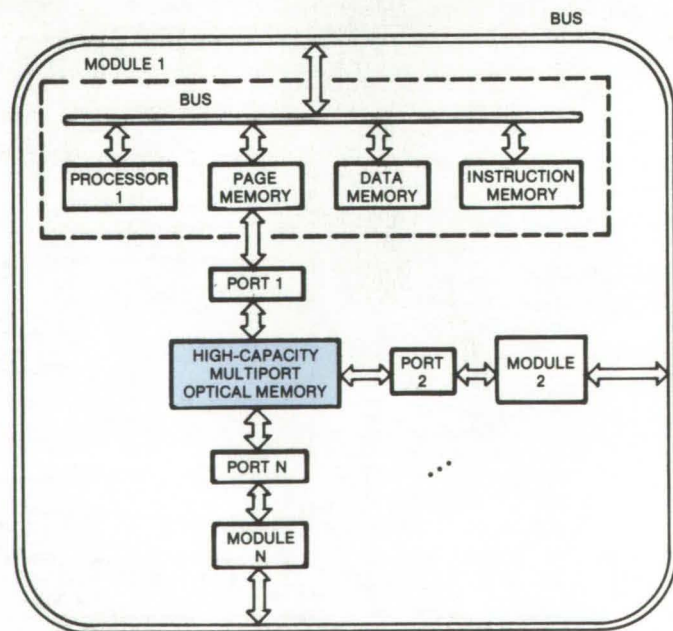
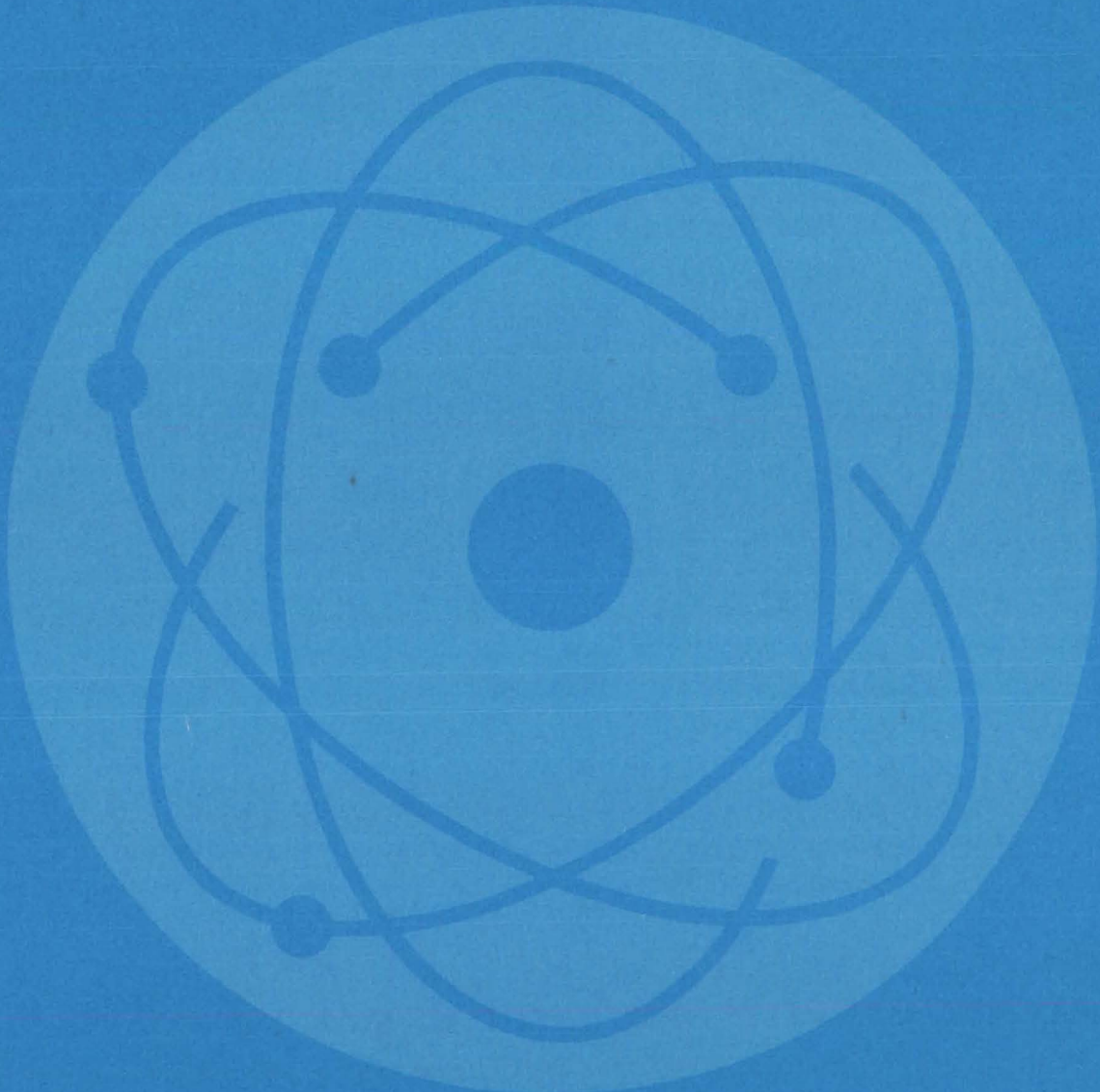


Figure 3. A **Computer Structure for Parallel Processing** is based on a single bus. The configuration has a number of minicomputers (modules) where each minicomputer contains its own processor, data source, and instruction memory.

and T. K. Gaylord of Georgia Institute of Technology for **Marshall Space Flight Center**. For further informa-

tion, Circle 26 on the TSP Request Card.
MFS-23897

Physical Sciences



Hardware, Techniques, and Processes

- 39 Solar-Powered Pump
- 40 Transparent Solar Cell Modules
- 41 Solar Power Conditioner
- 42 Sun Tracker for Clear or Cloudy Weather
- 43 Assembling Solar-Cell Arrays
- 44 Variable-Shape Solar-Energy Concentrator
- 45 All-Electric Gas Detector
- 46 Low-Noise Spectrophone
- 47 Improved Coal-Slurry Pipeline
- 48 Fuel Gas From Biodigestion
- 49 Optically Coupling Tunable Diode Lasers
- 50 Improved Flight-Simulator Viewing Lens
- 51 Projection Optics for a Laser Velocimeter
- 51 A Chevron Beam-Splitter Interferometer
- 52 Optical System for Multispectral Scanner
- 54 Marine Chlorophyll a Analysis
- 55 Production of Large-Area Electrets

Books and Reports

- 57 Theory of Back-Surface-Field Solar Cells
- 57 Rankine-Cycle Solar-Cooling Systems
- 58 Rankine-Cycle Heating and Cooling Systems
- 58 Design Information for Solar-Heating Systems
- 58 Solar-Heating System — Performance Tests
- 59 Performance Test for a Solar Water Heater
- 59 Air Solar Collector — Installation Package
- 59 Static Load Testing of a Liquid Solar Collector
- 59 Liquid Solar Collector — Performance Evaluation
- 60 Weathering of a Liquid-Filled Solar Collector
- 60 Design of a Concentrating Solar Collector
- 60 Concentrating Solar Collector — Performance Tests
- 61 Controller for Solar Heating — Design Package
- 61 Cost Analysis of Hot-Air Solar-Heating Systems
- 62 Solar Energy for Industrial Process Heat
- 62 An Annotated Energy Bibliography
- 63 Analysis of Aperture Antenna Radiation Pattern

Computer Programs

- 63 Analysis of Building Heating and Cooling

Solar-Powered Pump

Steam, generated in a concentrating solar collector, drives this pump for solar-heating systems.

Marshall Space Flight Center, Alabama

Solar-heating systems normally require a certain amount of electrical energy to operate a mechanical pump in the collector loop. By using the steam-operated pump shown in the figure, however, the collector flow can also be solar powered, since solar energy can be harnessed to generate steam.

The steam-powered pump operates on a pressurize/condense/refill cycle, with water or water/glycol as the working fluid (the same fluid as in the main collector loop). Tests have shown that the pump generates a pressure head of up to 50 ft (15.2 m), with an average head of 25 ft (7.6 m); it can supply a flow rate of up to 10 gal/min (38 l/min).

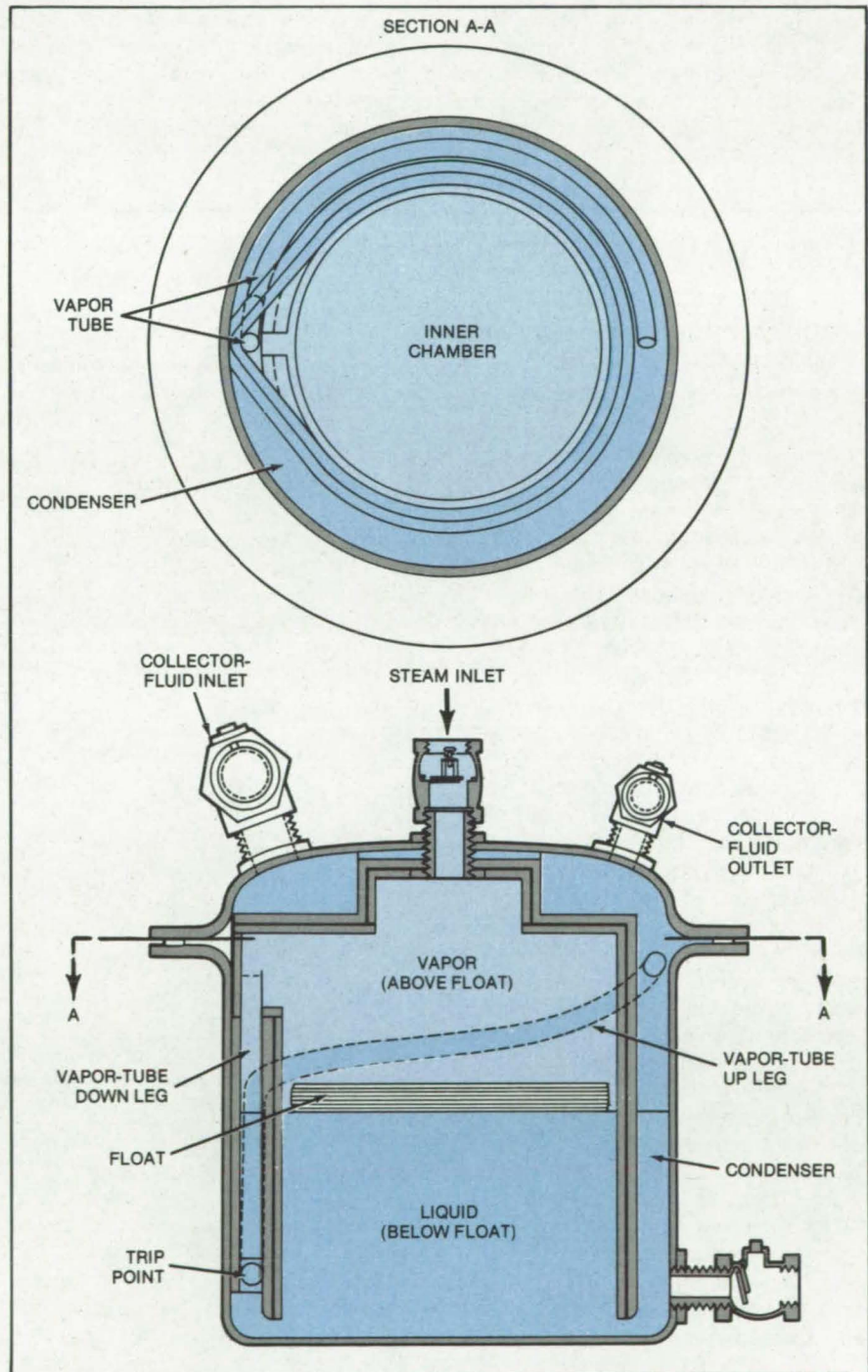
A concentrating solar collector, separate from the main collector, is installed along with the pump. The concentrator may be tracking or nontracking, but it should be capable of delivering vapor at 124° C (for a 40-percent glycol/water working fluid and a 25-ft head).

As shown in the figure, the pump housing is a 22-quart (21-l) cast-aluminum pressure cooker. Attached to the cover of the 13 in. (33 cm) in diameter vessel are inlet and outlet check valves for the collector fluid and a steam-supply fitting. Replacement water is added to the collector through a check valve located at the base of the pressure cooker.

An inner cylinder of steel, covered on both sides with cork and measuring roughly 9 in. (23 cm) in diameter and 11 in. (28 cm) in depth, is mounted on the cover of the cooker. Attached to the inner cylinder is a serpentine vapor tube made out of copper tubing. The down leg of the tube (in the inner chamber) is insulated by the cork wall of the cylinder.

The lowest point of the vapor tube marks the "trip" point of the pump cycle. Beyond that point, the tube leads up to discharge in the pump condenser section (between the inner chamber and the outer wall). An insulated, round float rides on top of the fluid in the inner cylinder.

(continued on next page)



This **Steam-Operated Pump** can be powered with solar energy (by generating steam in a concentrating solar collector). Steam forces the liquid down in the inner chamber, up the condenser, and through the outlet valve. When steam in the vapor tube reaches the trip point, it flows into the condenser, causing a pressure drop that draws in fluid to refill the pump.

When the pump starts operating, it is completely full of the fluid to be pumped. Steam from the concentrating collector enters at the top and begins to fill the central chamber. As the steam comes in, it forces the float and the liquid level down. (The liquid level in the down leg of the vapor tube stays even with the inside level of liquid.) As more steam enters, the level falls further, and liquid is pumped out of the outlet check valve in equal volume to the volume of the steam vapor in the pump.

When the liquid level reaches the bottom of the vapor tube, steam gets by the trip point and rushes up to the tube outlet in the pump condenser section. Along the way it starts to condense, since the uninsulated up leg of the tube is cooler than the vapor. As the pressure falls (because of the rapid condensation that is taking place), there is a very rapid refilling of the inner and outer chambers, which drives the remaining vapor out of the vapor tube to the condenser. Liquid rushes in through the inlet check valve to re-

place the vapor as it is condensed. This entire action (the suction stroke) takes only about three seconds, so that the refilling is done before much vapor can enter the pump.

This work was done by Calmac Manufacturing Co. for **Marshall Space Flight Center**. For further information, Circle 27 on the TSP Request Card.
MFS-23996

Transparent Solar Cell Modules

New materials make solar-cell modules more cost effective.

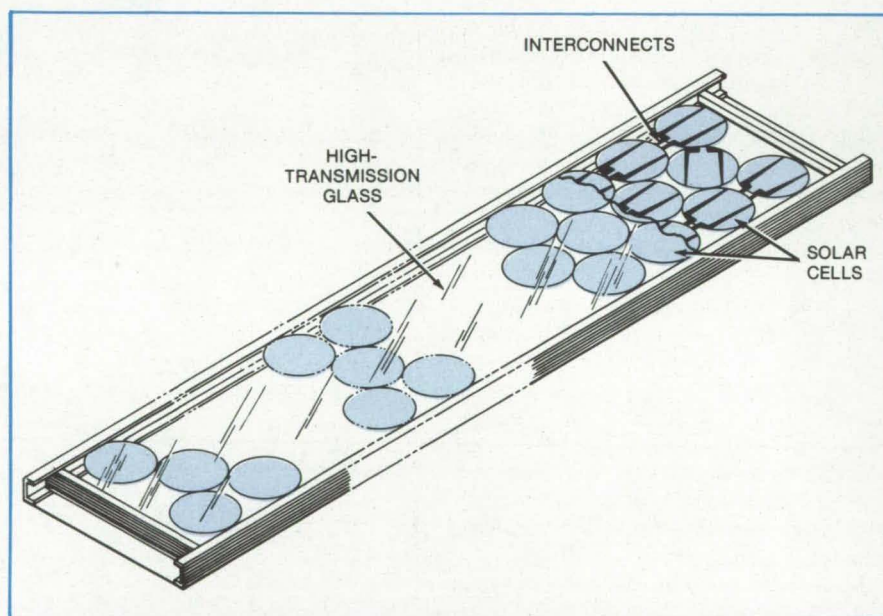
NASA's Jet Propulsion Laboratory, Pasadena, California

A recently modified solar-cell module can deliver about 25 percent more power per unit area (9.84 percent efficiency based on cell area at 60° C and 100 mW/cm² flux) than earlier designs. The new design is suited for automatic production and costs less per unit watt to produce.

Among the major improvements in the design are the use of high-transmission glass, high-transmission adhesive, and vacuum assembly. The module (see figure) is built on a planar support panel made from glass that is very transparent to solar radiation.

A number of circularly-shaped solar cells are bonded to the support panel by a transparent bonding adhesive. Each cell is a silicon wafer with a surface layer defining a pn junction near one face of the cell. The cells are interconnected in series via a number of electrical interconnects.

Module efficiency is improved because of two factors. One, the use of high-transmission components such as glass and adhesive permits more solar energy to reach the cells. The second benefit from the high-transmission components is heat dissipation. This is augmented with circularly-shaped cells that leave larger gaps for the unused heat energy to escape



High-Efficiency, Low-Cost, Solar Module uses high-transmission glass and adhesives. This allows more solar power to reach the cell structure and increases heat dissipation, reducing the cell temperature to more efficient performance levels.

through. Prototype modules have been operated at temperatures about 15° C less than usual for this type of array which by itself increases power output by about 6 percent.

This work was done by Gene J. Antonides, Paul A. Dillard, Walter M. Fritz, and Dan R. Lott of Lockheed Missiles & Space Co., Inc., for **NASA's Jet Propulsion Laboratory**.

For further information, Circle 28 on the TSP Request Card.

This invention is owned by NASA, and a patent application has been filed. Inquiries concerning nonexclusive or exclusive license for its commercial development should be addressed to the Patent Counsel, NASA Resident Legal Office-JPL [see page A8]. Refer to NPO-14304.

Solar Power Conditioner

System converts solar energy to ac power and diverts excess solar power to charge batteries.

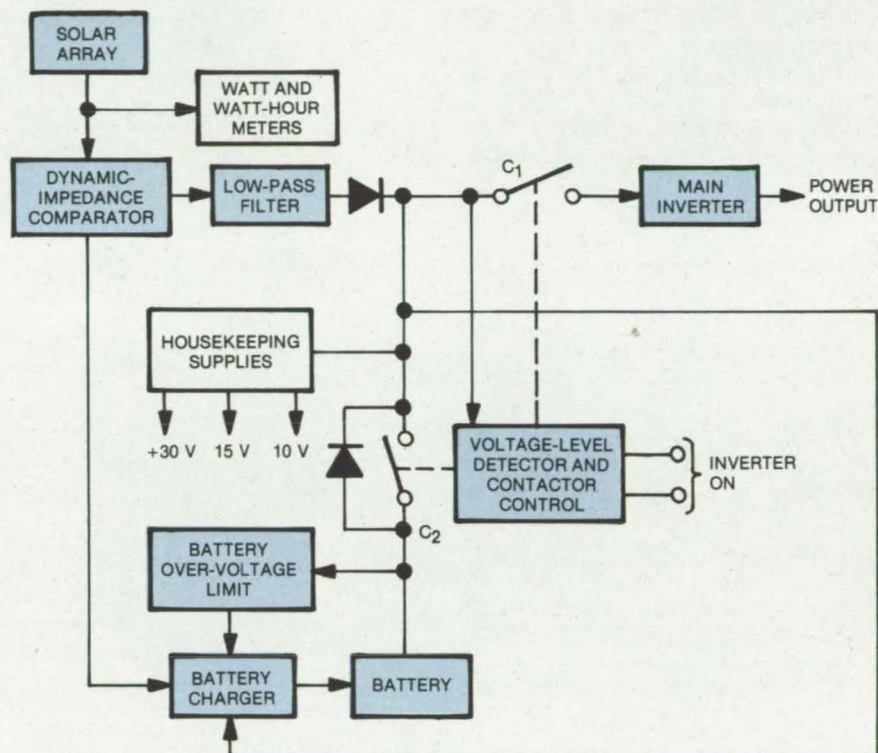
NASA's Jet Propulsion Laboratory, Pasadena, California

An efficient power-conditioning circuit controls the output of a solar-cell array so that excess energy not needed by the load is diverted to charge batteries for reserve power. The batteries are used as back up when sufficient Sunlight is not available. The system generates standard 110-volt 60-Hz power.

The conditioner (see figure) has been installed in a house trailer, where it supplies 3 kW of electric power to operate electronic instrumentation and test equipment. It is designed to utilize the maximum power available from the solar array. The array furnishes power to the trailer loads through the main inverter; excess power is used to charge the battery. The input (dc) voltage to the main inverter ranges from 130 to 275 Vdc.

A dynamic-impedance comparator measures and compares the resistive part of the dynamic impedance to the static resistance of the solar array. An error signal from the comparator controls the charge current to the battery. When the resistive component is equal to the static resistance, the array is delivering its maximum power output, and the comparator generates a zero error signal. Under this condition, no energy is diverted to the battery charger. A positive error signal indicates an excess of available solar power that can be used for battery charging, and a negative error signal indicates that the load has exceeded the maximum power point. To prevent battery damage from overcharging, an overvoltage limiter cuts off the charging current when the battery voltage reaches 170 volts.

A voltage-level detector and contactor-control circuit measures the dc input to the main inverter and determines which of the following power-supply situations should prevail:



This **Power-Conditioning System** combines solar power and battery power in various modes, depending on power availability and demand.

- The solar array supplies all the power.
- The solar array and the battery supply the power.
- The battery supplies all the power.
- The solar array feeds only the battery, and no power is delivered to the main inverter.

For example, if the input voltage drops to 130 volts, contactor C₁ opens, and contactor C₂ closes. The solar array then delivers whatever power it can generate directly to the battery, and no power is delivered to the main inverter. If the voltage-level detector at the inverter input senses a voltage above 130 volts, contact 1 closes, and contact 2 opens; and power is derived from the array or the

battery, whichever is at a higher voltage.

The "housekeeping" supplies that furnish power to the control circuits of the 3-kW system consume minimal energy. The dynamic-impedance converter, for example, requires only 1.5 to 4.5 W, depending on the solar array current. The main inverter consumes about 100 W and the battery charger consumes 45 to 190 W.

This work was done by Larry Jan, Neil Johnson, Siegfried Lindena, Colonel W. T. McLyman, and Joe N. Solario of Caltech for **NASA's Jet Propulsion Laboratory**. For further information, Circle 29 on the TSP Request Card.
NPO-14356

Sun Tracker for Clear or Cloudy Weather

Solar collectors can be continuously oriented for maximum insolation.

Marshall Space Flight Center, Alabama

A new Sun tracker follows the Sun across the sky even when there are obscuring clouds or haze. Designed to orient solar collectors so that they absorb the maximum possible Sunlight, the system is superior to many previous trackers in that it is not "fooled" by bright clouds, by a hole in the cloud cover, or by other atmospheric conditions. Moreover, it does not reset to the east each time the Sun is obscured.

In its normal operating mode, the tracker follows the Sun to within 0.25° of arc. When the Sun is hidden (by clouds for example), the system follows an estimated Sun position that is accurate to within about $\pm 5^\circ$ over a full day. In this mode, the tracker is driven at a speed tuned to the rotation rate of the Earth. When the Sun reappears, it is automatically reacquired, and tracking continues. At the end of the day, the tracker returns to its starting position, pointing toward the east, to await a new Sunrise.

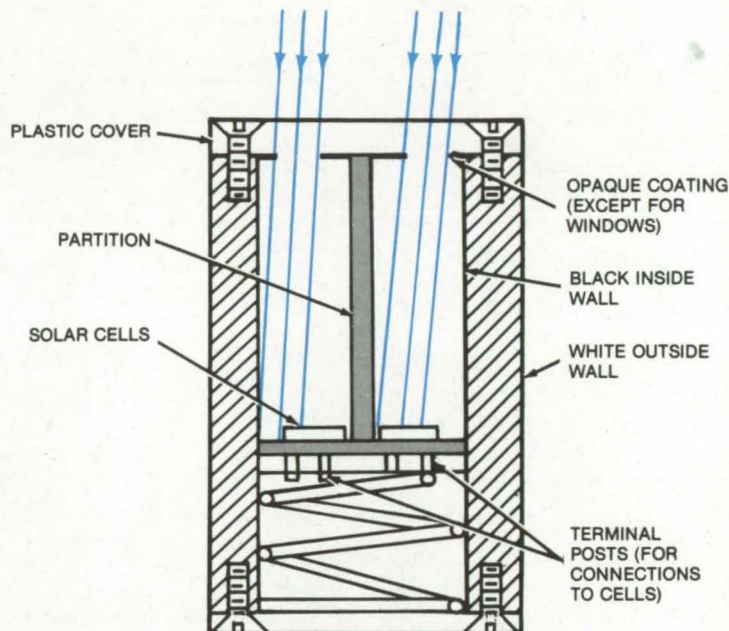


Figure 1. This **Sun Sensor Module** has two solar cells separated by a north/south-oriented partition. The interior of the module is black to absorb scattered light and to ensure that only direct Sunlight illuminates the cells. The exterior is white to reduce solar heating.

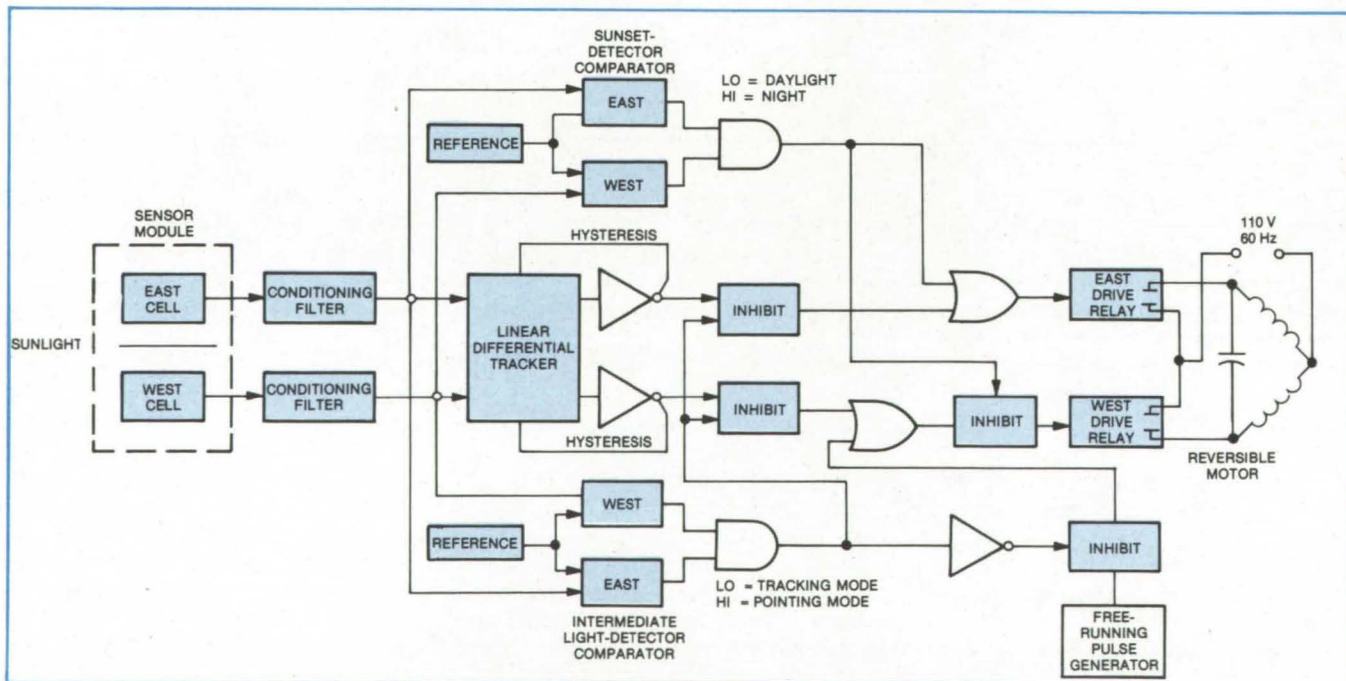


Figure 2. The **Electronic Circuitry for the Sun Tracker** first converts the current outputs of the sensor cells to voltages proportional to illumination, via the conditioning filters. The Sunset detector comparators reset the sensor module toward the east at night. The intermediate light-detector comparators determine when the Sun is obscured by clouds and switch the system to the pointing mode, with a rate based on the Earth's rotation.

The improved features, as compared to an earlier system that is replaced, are a result of the narrower field-of-view of its Sun sensor (see Figure 1). The sensor consists of two 0.5- by 1.0-centimeter silicon solar cells positioned on each side of a partition (oriented in the north/south direction). Windows over the cells are positioned so that when the sensor is centered on the Sun, exactly half the area of each cell is in direct sunlight, and the other half of each is in shadow.

As the Sun moves westward, the exposed area of the cell on the west side of the partition increases, and exposed area of the cell on the east side decreases. The current from each cell is proportional to the exposed area and

the light flux on that area. The system electronics (Figure 2) compare the signals from the cells; and when their difference exceeds a threshold value, the circuit actuates a motor that rotates the cells until their outputs are once again equal.

When a cloud covers the Sun, the output from either or both cells drops, signaling the circuitry to change to an automatic pointing mode of operation instead of a tracking mode. The circuitry no longer accepts the cell output; instead it connects a pulse generator to the motor. The pulses rotate the motor at a rate corresponding to the Earth's rotation, and the sensor continues to point to the Sun. When the Sun comes out again, it will be well

within the acquisition angle of the sensor, and the cells resume control.

When the Sun disappears below the horizon, the output of both cells drops sharply. The circuitry senses this, inhibits its tracking modes, and signals the motor to turn the sensor to its eastward-looking position until dawn.

This work was done by Donale R. Scott and Paul R. White of Marshall Space Flight Center. For further information, Circle 30 on the TSP Request Card.

Inquiries concerning rights for the commercial use of this invention should be addressed to the Patent Counsel, Marshall Space Flight Center [see page A8]. Refer to MFS-23999.

Assembling Solar-Cell Arrays

Fast and economical machine automatically attaches silicon cells to a printed-circuit film.

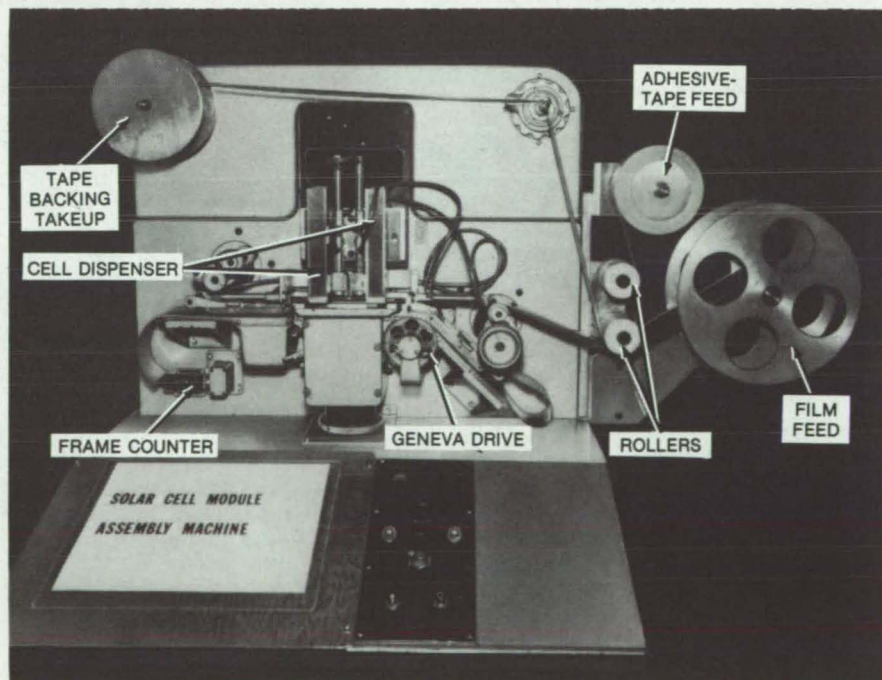
NASA's Jet Propulsion Laboratory, Pasadena, California

A new machine automatically attaches solar cells to a flexible film substrate. The machine can rapidly and inexpensively assemble large numbers of cells for solar panels. A prototype model attaches 250 cells per minute to a continuous film wound from a spool. Further development is expected to boost the rate to 1,000 cells per minute.

The machine uses a Geneva mechanism to move the film in steps, as is done in movie cameras and projectors. (In fact, a film editor was modified to make the prototype.) Since the film is stationary at the moment a cell is dispensed and attached, the difficulties of assembling cells on a moving substrate are avoided.

Edge-perforated film, 70 millimeters wide (made from a material such as Kapton), is fed from a reel into the machine. The edge perforations mesh with a sprocket on the Geneva movement (see figure). Simultaneously, double-faced adhesive tape is fed from another reel and is led with the film over a roller, which presses the tape onto the film. The tape backing is led to a takeup reel as it is removed from the tape.

(continued on next page)



This demonstration model of a **Solar-Cell Assembly Machine** is an adaptation of a 70-millimeter movie film editor. The lamp housing is replaced by the solar-cell dispenser. The machine is run in reverse (the film is pushed rather than pulled) so that the film can make the sharp bend around the Geneva drive sprocket before the solar cells are attached to it.

Each of two vertical chambers holds 500 silicon solar cells over the film path ("Sunny" side up). When the film is stationary, an air-piston-driven slide pushes one cell from each chamber, a vacuum plunger picks it up, and another air piston presses it against the adhesive tape on the film. The slide and vacuum plunger are withdrawn, the film is moved to its next stop position, and the cycle is repeated. The piston and plunger actions are synchronized with the Geneva movement by a set of cam-operated valves. Variable orifices in the air lines make it possible to control the response time of the pistons.

Electrical connections between the cells and conductors can be made by laser welding or soldering. Laser techniques, however, appear to be the only methods fast enough to keep up with the cell attachment operation. Successful welds have been made by using a 0.7-micron ruby laser.

The prototype dispenses cells measuring 2 by 4 by 0.03 centimeters. Cells as thin as 0.005 centimeter can be handled in the machine if they are assembled with a cover glass. To increase the speed of the machine, the slide and plunger actuators can be converted from air or vacuum devices to positive-acting mechanical linkages, and the cell-dispensing structure can be made more rigid.

This work was done by Joseph T. Bloch, Randolph T. Hanger, and Frank W. Nichols of The Boeing Aerospace Co. for **NASA's Jet Propulsion Laboratory**. For further information, Circle 31 on the TSP Request Card.

[See related article, "Automated Solar-Cell-Array Assembly Machine" (NPO-13652), on page 206 of NASA Tech Briefs, Vol. 3, No. 2.]

Inquiries concerning rights for the commercial use of this invention should be addressed to the Patent Counsel, NASA Resident Legal Office-JPL [see page A8]. Refer to NPO-14416.

Variable-Shape Solar-Energy Concentrator

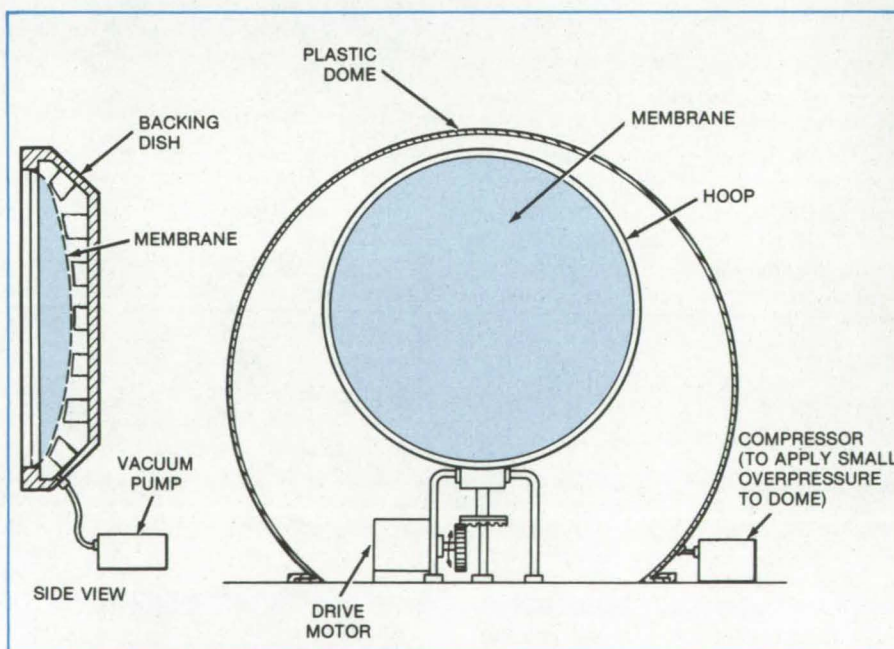
A lightweight, low-cost, tracking solar concentrator would be fabricated out of a polymeric-film membrane and "pulled" into shape by pressure loading.

NASA's Jet Propulsion Laboratory, Pasadena, California

In a proposed low-cost, three-dimensional, tracking solar concentrator, a stretched aluminized membrane is supported on a lightweight hoop and enclosed in a lightweight transparent plastic dome that protects it from the elements. Since the membrane concentrator would be considerably lighter than conventional rigid concentrators, it could be driven by a relatively-inexpensive, low-power tracking mechanism.

As shown in the figure, the aluminized (polymeric-film) membrane is supported by a hoop that is fastened to a lightweight backing dish. The dish and membrane enclose a sealed volume, and a vacuum can be drawn in this volume to change the membrane shape. The aluminized reflecting surface can be adjusted to a parabolic contour, or to other shapes, by differential pressure loading. The loading is varied either by fabricating a membrane with a nonuniform radial-thickness distribution and applying uniform pressure or a nonuniform pressure distribution can be applied by adding distributed weights to a membrane of uniform thickness.

To create a parabolic shape, the loading should be uniform on a unit



This **Lightweight Solar Concentrator** would be fabricated from a flexible polymeric-film membrane. The membrane shape is controlled by differential pressure loading. Fine adjustments to the shape could be made by mounting electrets or magnets on the membrane and applying electric or magnetic fields.

area of a plane perpendicular to the axis of the parabola. Local curvature corrections can be made by placing electrets or magnetic materials near

selected locations on the convex undersurface of the film and applying electric or magnetic fields to "pull" the membrane into the desired shape.

Although the unit has yet to be constructed and tested, its relatively simple design and potential for low-cost fabrication and operation indicate that the concept warrants further development.

This work was done by Charles G. Miller of Caltech and Jens H. Pohl of California Polytechnic State University, of San Luis Obispo, California for **NASA's Jet Propulsion Laboratory**. For further information, Circle 32 on the TSP Request Card.

This invention has been patented by NASA [U.S. Patent No. 4,046,462]. Inquiries concerning nonexclusive or exclusive license for its commercial development should be addressed to the Patent Counsel, NASA Resident Legal Office-JPL [see page A8]. Refer to NPO-13736.

All-Electric Gas Detector

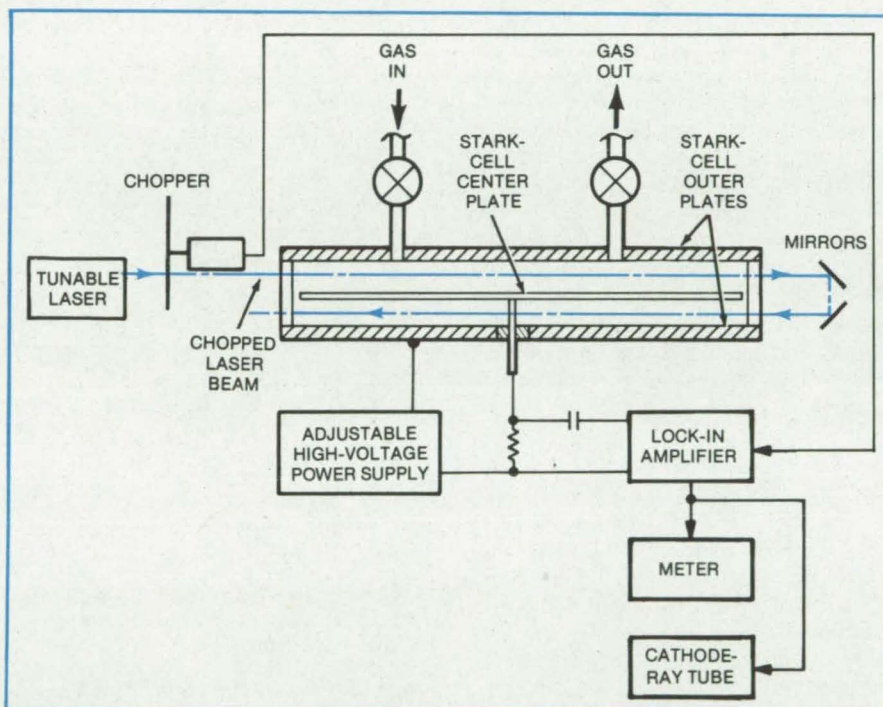
Instrument identifies gases by measuring pressure-induced voltage change.

NASA's Jet Propulsion Laboratory, Pasadena, California

An optoacoustic gas detector is modified to operate with electric signals. Unlike previous detectors of this type, the new device does not require gas-pressure sensing via a microphone. The use of electrical signals is simpler and more reliable than acoustic signals. Electronic detection eliminates a delicate electro-mechanical transducer and the microphone and the gas volume is also reduced, increasing the sensitivity. The instrument can detect water vapor, atmospheric fluorocarbons, and certain nitrous and nitric compounds that indicate the presence of explosives.

A chopped laser beam (see figure) is directed into the device, which consists basically of a chamber with a Stark-cell detector containing a gas specimen. A pressure change results when the gas specimen has a spectral absorption line within the laser bandwidth. The sample can thus be identified by the laser frequency and the magnitude of the electric field required to bring the absorption line into resonance with that frequency. An electric field, using a high voltage (about 1,000 V), is set up between the plates of the Stark Cell (a center plate and two outer plates). The voltage is adjustable so that the gas absorption wavelength can be brought into coincidence with the laser spectrum.

When absorption occurs, the gas heats, causing pressure and density changes. This changes the dielectric



Gas Detector Employs a Stark Cell, modified so that voltage changes on the cell can be measured directly as an indication of absorption by a gas. Previously, a sound transducer was used to measure the pressure change created by absorption.

constant of the gas by a minute amount and, in turn, changes the capacity of the electrode arrangement. The capacity change induces a change in voltage across a resistor, which is detected by a lock-in amplifier synchronized with the laser chopper wheel. The amplifier square-wave output — proportional to the

absorption of the gas — is displayed on a cathode-ray tube and read out on a voltmeter.

This work was done by Jack S. Margolis of Caltech for **NASA's Jet Propulsion Laboratory**. For further information, Circle 33 on the TSP Request Card. NPO-14341

Low-Noise Spectrophone

Noise is reduced, increasing the sensitivity of new spectrophone.

NASA's Jet Propulsion Laboratory, Pasadena, California

A new spectrophone operates at lower noise levels and thus detects trace amounts of gases with greater sensitivity. The spectrophone uses a continuous laser beam instead of the usual chopped laser beam. When a chopped beam enters a spectrophone chamber, the chamber windows continually heat up and cool down in response to the laser pulses. These heating and cooling cycles create pressure pulses, causing background noise that can mask the pulses produced by absorption of the specimen gas in the chamber. With continuous-beam operation this pressure noise is eliminated, since the temperature of the windows remains constant.

To reduce noise further, the voltage on the Stark-cell plates is held constant. The spurious acoustic signal generated by a varying electric field is thereby eliminated. Some form of modulation is still required, however, so that the specimen gas can interact with the laser beam. Two alternative modulation schemes can be used in the new spectrophone.

The laser beam can be polarization-modulated by a rotating half-wave plate positioned between the laser and the chamber (Figure 1). The plate is turned by a motor so that the polarization changes cyclically at an acoustic frequency.

An alternative is to modulate the polarization of the electric field in the Stark cell. An additional set of plates is positioned orthogonally to the original plates (Figure 2). The voltage on the additional set of plates is in phase quadrature with the voltage applied to the original set of plates. An acoustic-frequency sine wave in quadrature on the two sets of plates creates a rotating, constant-magnitude electric

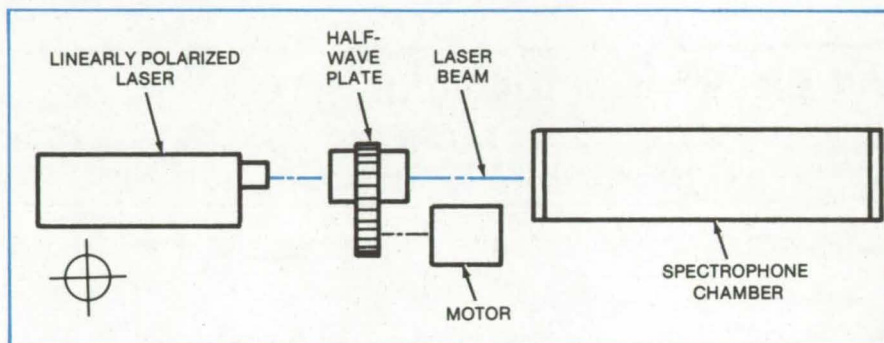


Figure 1. The **Polarization of a Laser Beam** is modulated by a motor-driven half-wave plate interposed between the laser source and the test chamber.

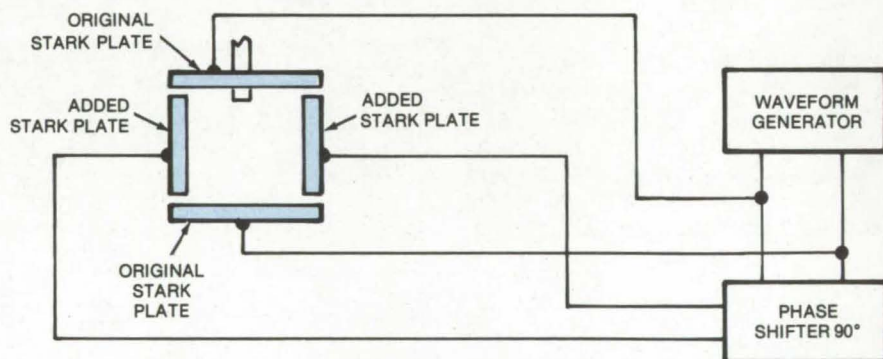


Figure 2. The **Polarization of an Electric Field** is modulated by adding a set of plates, the voltage of which is in quadrature to that on the original plates of the Stark cell, shown here in cross section.

field. As the field rotates, the absorption of the gas is modulated into and out of the coincidence with the laser wavelength.

Neither of the two modulation methods produces abrupt changes in the chamber, since there are no on and off states. Background noise therefore is effectively eliminated. [See related article, "Improved Spectrophone" (NPO-14143), on page 187 of NASA Tech Briefs, Vol. 3, No. 2.]

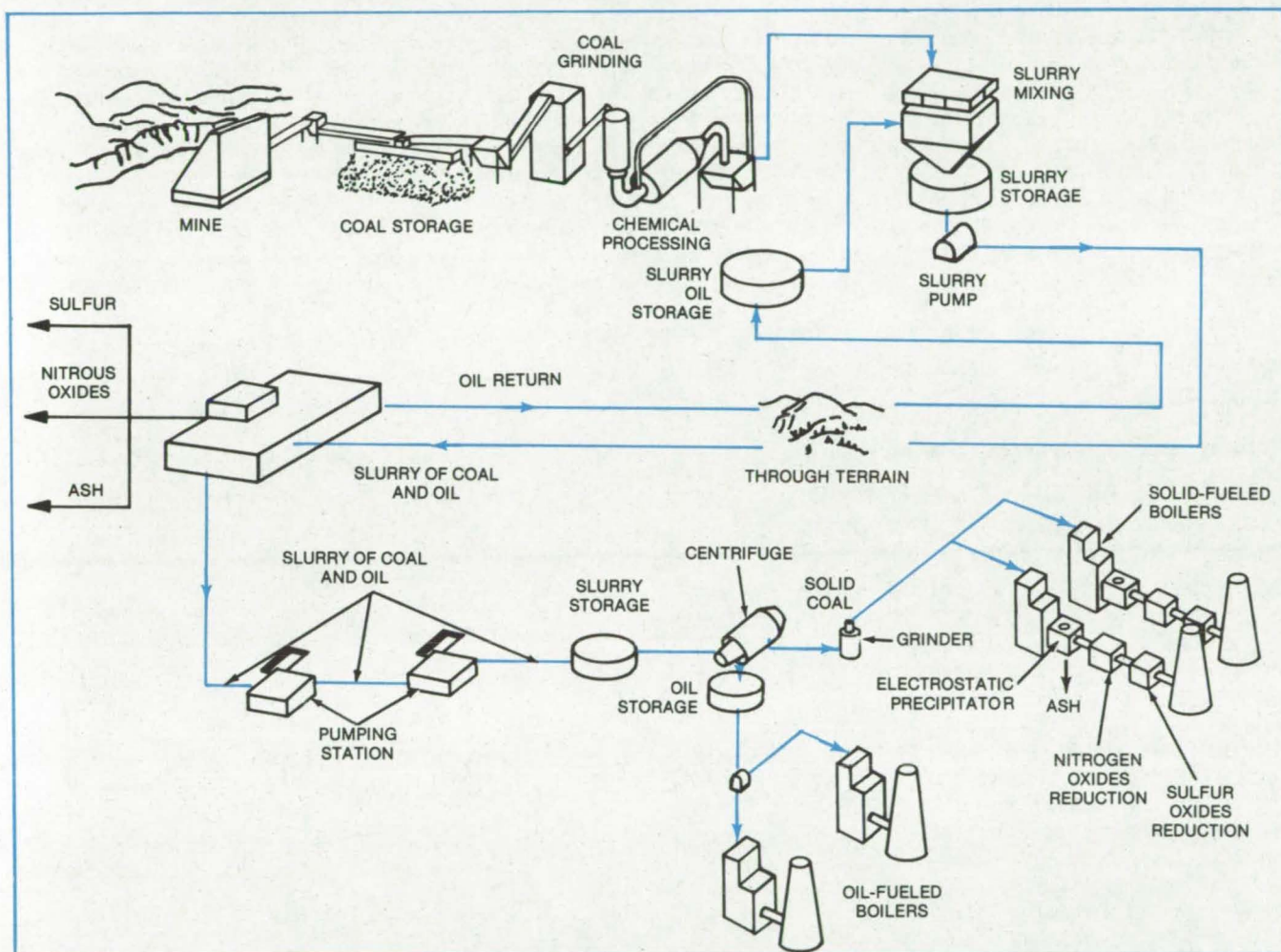
This work was done by Michael J. Kavaya and Jack S. Margolis of Caltech for NASA's Jet Propulsion Laboratory. For further information, Circle 34 on the TSP Request Card.

This invention is owned by NASA, and a patent application has been filed. Inquiries concerning nonexclusive or exclusive license for its commercial development should be addressed to the Patent Counsel, NASA Resident Legal Office-JPL [see page A8]. Refer to NPO-14362.

Improved Coal-Slurry Pipeline

System would move coal to power-generating stations in an oil slurry, removing pollutants en route.

NASA's Jet Propulsion Laboratory, Pasadena, California



A **High-Strength Steel Pipeline** carries a hot mixture of powdered coal and coal-derived oil to an electric-power-generating station. The slurry is processed along the way to remove pollutants and to recycle part of the oil.

In a novel scheme for transporting coal from the mine to distant power-generating stations, powdered coal and coal-derived oil move through a pipeline as a nonaqueous slurry. During the journey through the pipeline (at temperatures between 300° and 400° C), solvation of the coal takes place, increasing the quantity of liquid and decreasing the amount of solid. A portion of the oil is removed for recycling at an intermediate station, and the remaining slurry is processed to remove sulfur, ash, and

nitrogen. At the end of the line, the slurry is separated into its liquid and solid components, which are burned in separate facilities.

This scheme does not have the severe particle-size limitations that exist in anticipated coal/water-slurry pipelines. In the latter, large particles could settle in the pipeline and eventually clog it, and too-small particles would not be easily separated by centrifuging at the end of the line. Moreover, since both the coal-derived oil and solid coal are used as

fuels, there is no inefficient water-separation step at the end of the pipeline in the new method. The environmental hazards associated with removing water from a location where it is needed, transporting it, and disposing of it as waste water at a distant location are also eliminated.

The proposed coal-transport scheme is diagrammed in the figure. At the mine, the coal is ground to a powder. A small portion of the powdered coal is converted by conventional chemical processing to

(continued on next page)

amines, such as ethylene diamine and 1,6-hexane diamine, which act as surfactants to assist in matching the coal and solvent solubility characteristics. Powdered coal, amines, and coal-derived oil are mixed, heated to 300° to 400° C, and pumped away from the mine through the pipeline. It is anticipated that a pipe about 18 to 24 inches (45 to 61 cm) in diameter would be sufficient.

As the slurry moves through the pipe, as much as 70 percent of the powdered coal is liquefied under the influence of heat, pressure, the oil medium, and the amine surfactants. (The ground in which the pipeline is buried insulates the slurry, retaining heat.)

At an intermediate point about 100 miles (161 km) from the mine, the

slurry is passed through a separation system in which about 30 to 50 percent of its oil content is removed and returned to the mine through a parallel pipeline. The recycled oil is added to new ground coal and fed into the slurry pipeline again. At the intermediate processing station the nonrecycled slurry is processed to reduce its ash, sulfur, and nitrogen content. The slurry, which consists of about 40 percent liquid coal and 60 percent coal solids at that point, is reheated and pumped through another pipeline to the power station, which may be as much as 2,000 miles away.

At the end of the line, the slurry is separated by centrifuging into an oil fraction and a coal-slurry fraction containing both liquid and solid coal in suspension. If necessary, the oil

fraction is processed further to reduce ash, sulfur, and fixed nitrogen content to a point at which the oil can be burned in a boiler without special pollution-control equipment.

The coal-slurry fraction is burned in boilers that do have pollution-control equipment. These coal-slurry-fired boilers furnish the baseload energy output, and the "clean" oil-fired boiler is operated for peakloads. With this strategy, the coal burning generates a minimum amount of pollution, yet capital investment in pollution-control equipment is minimized.

This work was done by Warren L. Dowler of Caltech for NASA's Jet Propulsion Laboratory. For further information, Circle 35 on the TSP Request Card.
NPO-14425

Fuel Gas From Biodigestion

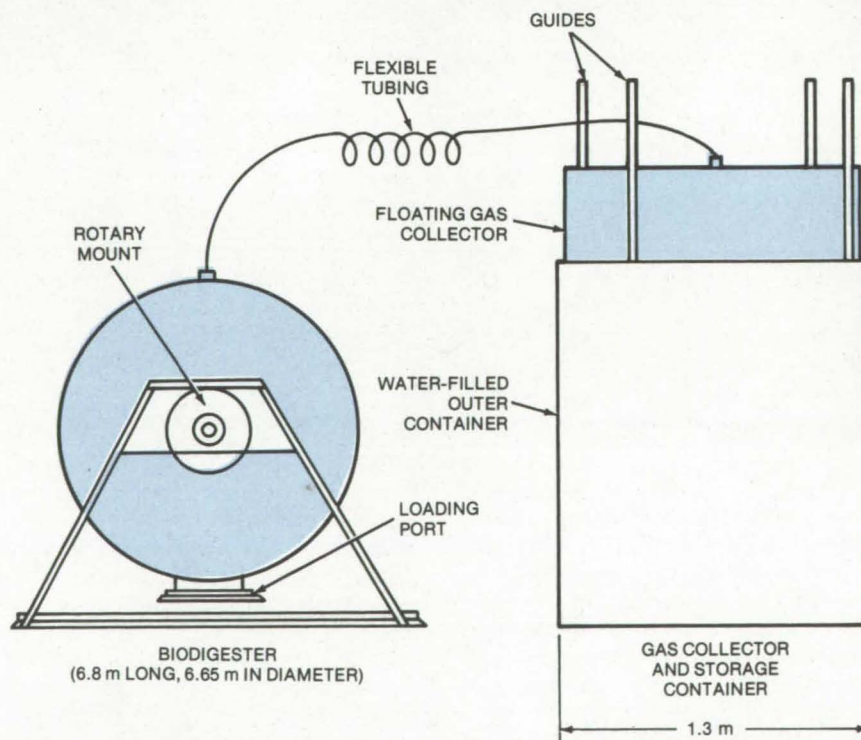
Easy-to-operate apparatus generates methane for household consumption.

Marshall Space Flight Center, Alabama

The apparatus shown in the figure produces fuel gas by anaerobic bacterial digestion of organic matter, such as aquatic vegetation. It includes a simple, safe gas collector for short-term storage, and it generates enough gas (primarily methane) for individual or home consumption. One of its primary advantages over previous designs is a built-in, manually operated agitator that allows the vegetation to be mixed periodically to accelerate gas production.

Already developed and successfully tested is as a prototype, the biodigester consists of a 1,000-gallon (3,786-l) cylindrical container mounted on rotary bearings. For loading, the container is rotated manually so that its large port is upright. Grass clippings, leaves, and other vegetation are dumped into the port. The port is bolted tight, and the container is rotated until the port is at the bottom. In this position, the port is below the surface of the mixture, and air cannot leak through it and interfere with the anaerobic digestion process.

The evolved gas gathers at the top of the container and passes through a



Fuel Gas Is Generated for Individual or Home Consumption by anaerobic bacterial digestion of vegetation in a rotary container. The evolved gas feeds through a coiled tube to a floating collector in a water-filled barrel, at the rate of about 100 to 200 liters per day.

small flexible tube into the storage collector. Three stationary bars mounted inside the tank stir the mixture when the container is rocked back and forth. Thus, one can agitate the mixture without opening the container and releasing gas.

The gas collector is a large inverted canister in a water-filled barrel. As gas flows into the collector, the canister rises (floating on the water) to accommodate the gas. The water prevents the gas from escaping, and vertical guides keep the floating canister from

swaying or tipping over. The back pressure from the filled canister is not sufficient to upset the digestion process.

The process produces gas at the greatest rate at a temperature of 36° C, although temperatures 5° C above or below this value do not seriously affect the process. When the outside air temperature falls below 31° C, heated water can be circulated through the interior of the digester. Possible heat sources are gas from the biodigester itself or from a solar

collector. The basic design can be adapted easily to larger systems.

This work was done by Rebecca C. McDonald and B. C. Wolverton of the National Space Tech. Laboratory for Marshall Space Flight Center. For further information, Circle 36 on the TSP Request Card.

Inquiries concerning rights for the commercial use of this invention should be addressed to the Patent Counsel, Marshall Space Flight Center [see page A8]. Refer to MFS-23957.

Optically Coupling Tunable Diode Lasers

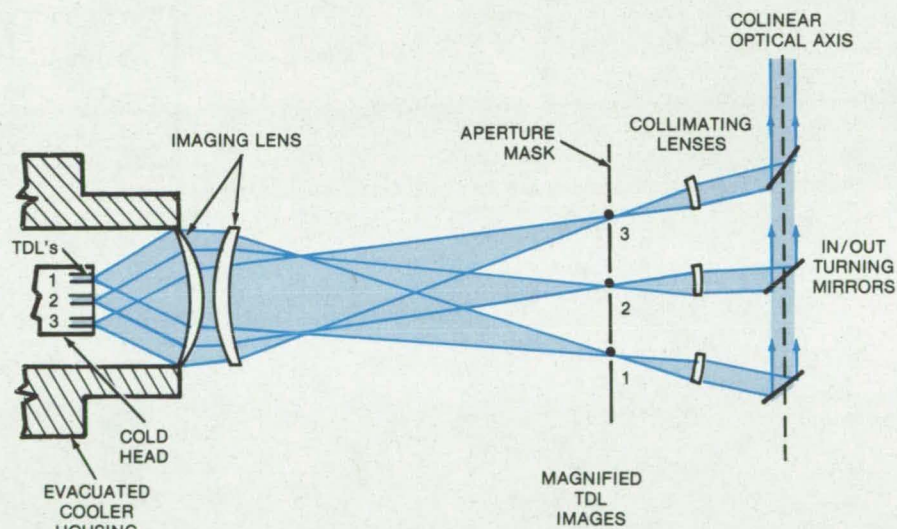
A set of mirrors and lenses to generate multiple tunable laser outputs

Langley Research Center, Hampton, Virginia

Spectroscopes that use tunable diode lasers (TDL's) as far-infrared light sources often require multiple TDL's to cover a wavelength range unavailable from the single laser. A proposed optical-coupling using lenses and mirrors can combine separate TDL outputs and expand the wavelength range. The proposed method uses a single cooler housing and requires no moving parts within the cooler assembly.

An earlier scheme for obtaining multiple laser outputs from a single cooler housing incorporated a rotating cold head supporting a number of TDL's. In this complex mechanical design, each laser is rotated into position within the cooler head in an evacuated low-temperature environment.

The proposed approach shown in the figure is a package of three TDL's, separated by approximately 5 mm. These are imaged external to the cooler by a pair of germanium meniscus lenses that will accommodate both the laser separation and the divergent (approximately F/1, F being the F-number) wave front from the individual lasers. The emerging beams are individually collimated and superimposed onto a common optical axis by turning mirrors oriented at the proper angles. The collimated outputs



This **Optical Coupling Arrangement** produces multiple TDL outputs from a single cold head. A set of lenses and mirrors will replace a complex mechanical system used for the same purpose.

from the three lasers are colinear for interfacing with other optics in the system. A single beam can be selected from the multiple output by inserting or removing the turning mirrors and an aperture mask in the image plane.

The limit to the number of TDL's that can be handled in this manner depends upon the packaging of the

laser array and the numerical aperture of the imaging lens. With the system illustrated, an F/0.7 first lens is required to gather the radiation from each TDL.

This work was done by D. M. Robinson and C. W. Rowland of Langley Research Center. No further documentation is available. LAR-12438

Improved Flight-Simulator Viewing Lens

Three-element plastic lens system reduces chromatic aberration and distortion.

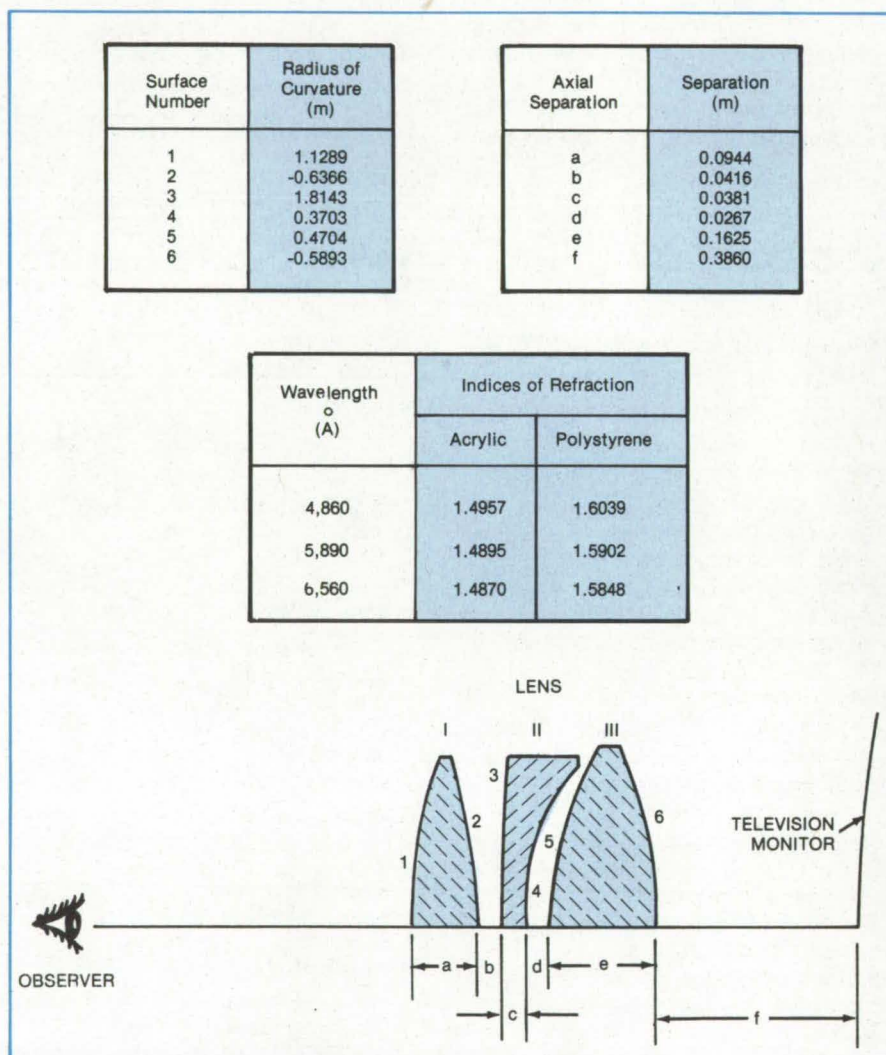
Langley Research Center, Hampton, Virginia

Many flight simulators have been using one of two systems to transmit a visual display to the simulator pilot. The in-line system consists of one or more lenses placed between the observer and a source of image information, which is usually a television monitor. The non-in-line type of system consists of a spherical mirror and a beam splitter placed between the television monitor and the observer. Although the non-in-line system has better optical characteristics, it is heavier, larger, and generally costs more. A single aspheric lens may be used as an alternate to the multiple-lens in-line system, but the cost is also high.

The in-line systems have been developed with arrays of two, three, and four lenses. These arrangements produced images with significant distortion and lateral chromatic aberration. Chromatic aberration was one of the principal causes of poor resolution found in most in-line systems. Distortion presents false visual cues to the pilot of a flight simulator and thereby may create adverse results.

An improved lens system, consisting of three plastic elements, is shown in the illustration. Lenses I and III are made of acrylic plastic, and lens II is made of polystyrene. Lens design parameters are also shown in the illustration. The advantage of this triplet design over the previous in-line approaches is a reduction of both distortion and lateral chromatic aberration, especially at large field angles.

This work was done by William M. Kahlbaum, Jr., of Langley Research Center. Further information may be found in NASA TP-1066 "Analysis and Design of Refractive Virtual Image System," a copy of which may be



The **Triplet Lens** uses two double-convex lenses made of acrylic for the front and rear elements and a polystyrene single-concave, single-convex lens for the middle element.

obtained at cost from North Carolina Science & Technology Research Center [see page A7].

This invention is owned by NASA, and a patent application has been

filed. Inquiries concerning nonexclusive or exclusive license for its commercial development should be addressed to the Patent Counsel, Langley Research Center [see page A8]. Refer to LAR-12251.

Projection Optics for a Laser Velocimeter

Afocal optics make the scanning volume independent of focus position.

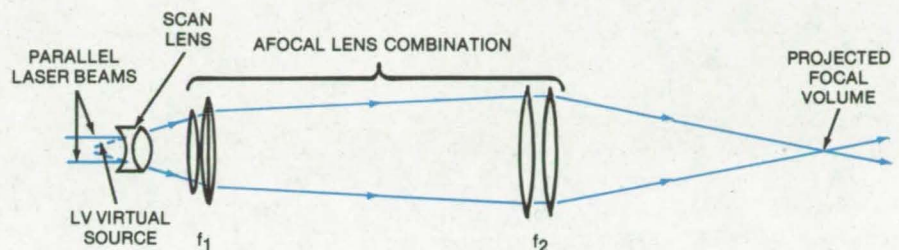
Langley Research Center, Hampton, Virginia

Novel projection optics for a laser velocimeter (LV) scan a constant focal volume over the entire focus-position range. The optics thus simplify LV measurements over large flow fields (such as those encountered in wind tunnels) by eliminating calibrations required when the focal volume varies with position.

The heart of the projection optics (see figure) is a two-lens afocal combination, often found in telescopes. The lenses are separated by a distance equal to the sum of their focal lengths, making their net magnification equal to the ratio of the focal lengths (f_2/f_1) and independent of the object distance. This constant magnification, when applied to the intersecting laser beams of the LV, results in a constant cross-beam intersection angle and constant focal-volume dimensions.

The afocal combination projects light from parallel laser beams into the flow field, where the beams intersect to form the sampling volume. The position of the volume in the flow field is changed by moving a scan lens along the optical axis.

The image produced by the scan lens can be either real or virtual and is usually located within the focal length



A Two-Lens Afocal Combination projects light from two laser beams into a sampling volume in the flow field. The focus is moved in the flow by changing the position of the scan lens, but the volume remains constant.

of the first lens in the afocal pair. The virtual image of this first lens becomes the object for the second lens, which forms the final image in the flow field.

The location of the projected LV focus depends on the position of the scan lens. The range of the focus is equal to the translation range of the movable lens, multiplied by the square of the magnification of the afocal lens combination (hence, the desirability of having the magnification independent of object position).

The afocal projection optics are currently being used in a backscatter LV, in which the optical path of the transmitted laser beams is also the path of the backscattered radiation. In

this system, the afocal combination gives a constant collection cone for the backscattered light. If a flat backscatter collector is placed between the parallel laser beams, its projected area on the scan lens corresponds to an exit pupil. This exit pupil is magnified or reduced for the corresponding movement of the scan lens, so that the collecting cone is constant.

This work was done by David B. Rhodes of Langley Research Center. No further documentation is available.

Inquiries concerning rights for the commercial use of this invention should be addressed to the Patent Counsel, Langley Research Center [see page A8]. Refer to LAR-12328.



A Chevron Beam-Splitter Interferometer

An interferometer allows for small errors in alignment.

NASA's Jet Propulsion Laboratory, Pasadena, California

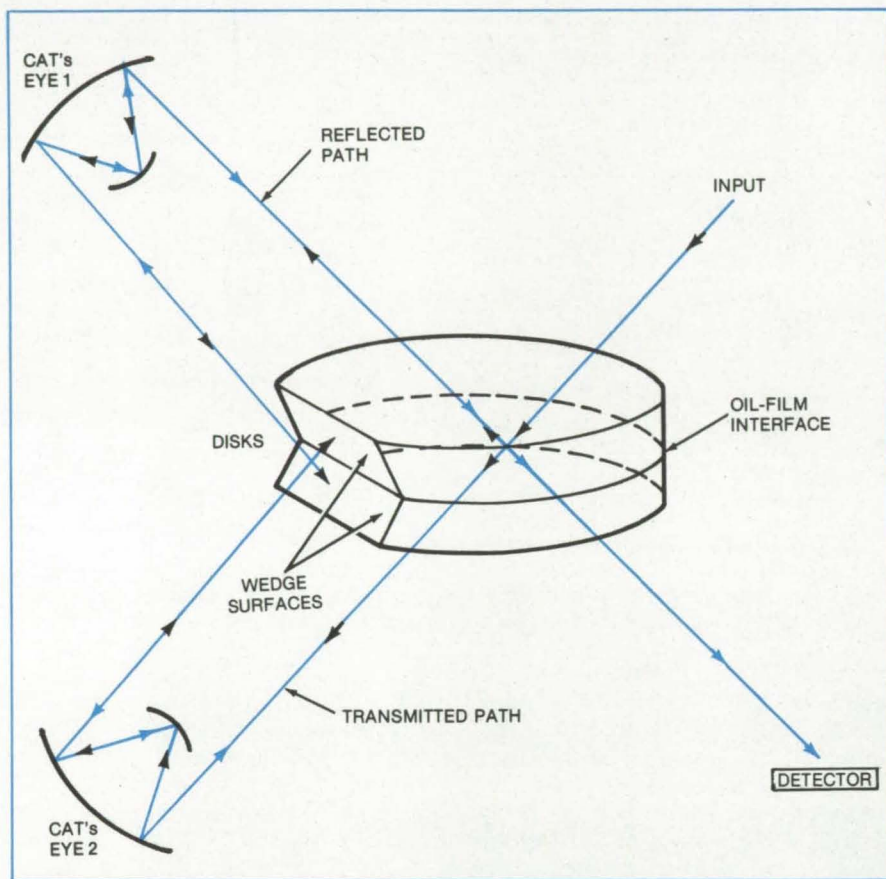
A new double-pass, chevron beam-splitter interferometer is fully tilt compensated. It includes a wedge-shaped beam splitter and compensator that remove channeling effects and permit optical phase tuning. This arrangement is wavelength independent and allows small errors in alignment that are not tolerated in Michelson, Mach-Zender, or Sagnac interferometers.

The device is therefore useful in experiments where background vibrations affect conventional interferometers.

The interferometer shown has two wedged disks to avoid channeling in the spectrum. A beam generated from the source strikes the interface and is split into reflected and transmitted paths. The reflected beam is directed

by a cat's-eye to the lower reflecting surface of the wedge. It is then reflected back along the same path through the cat's-eye and the beam-splitter pair to the detector. The transmitted beam similarly passes through a second cat's-eye to the upper wedge surface and returns along its initial path to the beam-splitter interface where it is reflected

(continued on next page)



A **Chevron Beam-Splitter Interferometer** incorporates a wedge-shaped beam splitter and compensator. All surfaces except for the beam splitter are servocontrolled. Transmission through the device is not wavelength dependent due to a monomolecular film of oil between the upper and lower halves of the beam splitter. The device is tolerant to background vibration because of tilt compensation.

from the bottom of the upper half to combine with the first beam and then goes into the detector.

The interface between the upper and lower halves of the beam splitter has a monomolecular coating of an optically compatible oil. This layer is thinner than 1 wavelength of light transmitted or reflected through the device, which results in wavelength-independent operation.

Because of the new configuration, the source beam impinges error-free on the detector independently of the beam-splitter tilt, up to a limit set by the dimension of the reflecting surfaces of the wedge. Any rotation of the beam in its first pass through the cat's-eye is simply compensated for by a corresponding opposite rotation that results in exact recombination of the re-reflected path.

This work was done by James B. Breckinridge of Caltech for **NASA's Jet Propulsion Laboratory**. For further information, Circle 37 on the TSP Request Card.

This invention is owned by NASA, and a patent application has been filed. Inquiries concerning nonexclusive or exclusive license for its commercial development should be addressed to the Patent Counsel, NASA Resident Legal Office-JPL [see page A8]. Refer to NPO-14502.

Optical System for Multispectral Scanner

Data on eight spectral bands are measured simultaneously by a compact, efficient, versatile airborne system.

Lyndon B. Johnson Space Center, Houston, Texas

An optical system developed for a NASA multispectral scanner circumvents many of the problems associated with previous systems. Designed for scanning eight spectral bands simultaneously from an aircraft at a variety of speeds and altitudes, it is efficient, compact, reliable, and easy to align.

The optical arrangement is shown in Figure 1. Radiant energy from the ground scene is reflected from a rotating mirror into the primary parabolic reflector and then is focused on a

field stop that limits the instantaneous field-of-view. The energy passing through the field stop is collimated by a second parabolic mirror and then is reflected out of the telescope by a flat folding mirror. This collimated beam is directed to a dichroic filter that reflects energy at short wavelengths (from about 0.4 to 4 μm) and transmits energy at longer wavelengths (from about 6 to 14 μm).

The reflected short-wavelength (SWL) energy is dispersed by a double-prism spectrometer and fo-

cused onto a seven-element detector array by a triplet lens. Spectral coverage and band limits are set, in the conventional manner, by the location and size of the detectors in the array (see Figure 2). The detectors for the first four bands are silicon, the next two are germanium, and the seventh is indium arsenide; all are thermoelectrically cooled to 195 K.

The long-wavelength (LWL) energy that is transmitted through the dichroic filter is filtered by a 10.4- to 12.5- μm filter and then focused on the detector

by a germanium lens. The detector is mercury/cadmium/telluride, liquid-nitrogen cooled to 77 K.

This system combines standard optical components to meet system requirements in a relatively simple and straightforward manner.

- The collimating and folding mirror arrangement offers three advantages: (1) It collimates both the SWL and LWL channels; (2) being reflective, it eliminates chromatic aberration effects; and (3) it reduces the effective focal length of the telescope, which reduces the size of the optical components that follow.

- The spectrometer contains two synthetic sapphire prisms as dispersive elements. Sapphire was chosen because it has high dispersion and transmission over the required spectral range of 0.45 to 2.35 μm . A grating would not have provided sufficient efficiency over the wide spectral range.

- The effective focal length of the optical system is approximately 10 inches (25.4 cm) for the SWL channels and 7.2 inches (18.3 cm) for the LWL channel. This relatively-short focal length reduces the size of the detectors and optical system. Noise, which is proportional to detector area, is less with a smaller detector.

- Band limits for the long-wavelength band can be easily controlled because the band-limiting filter is in a collimated beam.

Alignment of the system is aided by the modularity of the optical system. A baffle is required around the flat folding mirror and the collimating mirror to prevent light from reaching the detectors from outside of the instantaneous field-of-view.

Variable flying conditions are compensated for by a variable-speed motor that drives the 45° scan mirror. Two blackbody reference sources are sampled once during each scan for LWL calibration. A tungsten lamp illuminates an integrating sphere that fills the aperture once per scan as a reference for the SWL bands. Flight tests confirm the effectiveness of this optical system.

This work was done by Roy C.

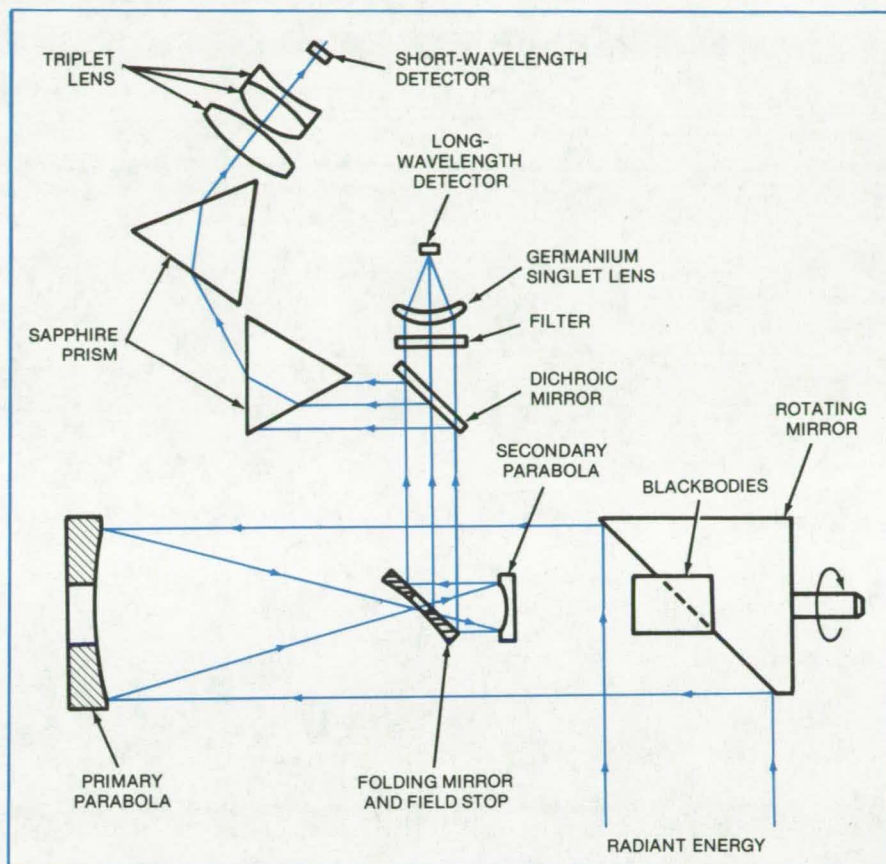


Figure 1. The **Optical System** for a multispectral scanner is shown here. Seven short-wavelength bands and one broad infrared band are detected simultaneously. The instantaneous field-of-view is 2.5 milliradians, the scan angle is 100°, and the scan speed is variable from 600 to 6,000 rpm.

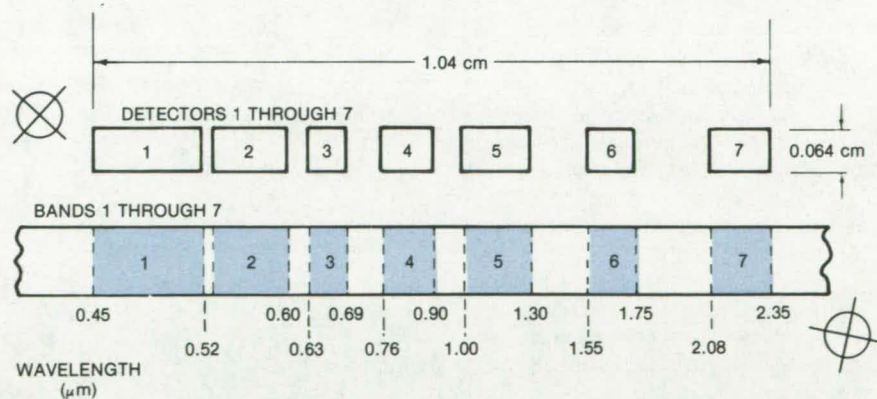


Figure 2. **Seven Spectral Bands** are detected in the short-wavelength portion of the scanner optical system. They are determined by the geometry of the detector array placed in the spectrum dispersed by the prisms.

Stokes of Johnson Space Center and N. G. Koch of Lockheed Electronics Co. For further information, Circle 38 on the TSP Request Card.

Inquiries concerning rights for the commercial use of this invention should be addressed to the Patent Counsel, Johnson Space Center [see page A8]. Refer to MSC-18255.

Marine Chlorophyll a Analysis

Quantitative distribution maps of coastal zones are prepared by regression analysis of sea-truth data and data collected by aircraft multispectral scanners.

Langley Research Center, Hampton, Virginia

Chlorophyll a is an important environmental parameter for monitoring water quality, nutrient loads, and pollution effects in coastal zones. High chlorophyll a concentrations usually occur in areas that have high nutrient inflows from sources such as sewage treatment plants and industrial wastes. High chlorophyll a levels and associated eutrophication of water bodies limit their usefulness for recreation, water supplies, and other purposes. High chlorophyll a levels or "blooms" and the resultant secondary pollution also deplete oxygen concentrations, leading to upsets of the ecological balance in water systems. Low chlorophyll a concentrations may be due to the addition of toxic substances from industrial wastes or other sources. Thus, either abnormally high or low concentrations of chlorophyll a may indicate pollutant inputs or effects.

Remote sensing with its wide spatial coverage and synoptic view provides an opportunity to assess distribution of water quality parameters such as chlorophyll a and uncover information not readily available by other means. In addition, remote sensing as a nonintrusive technique may provide useful information for monitoring and enforcing pollution practices. Experiments with aircraft multispectral scanners over the turbid James River in Virginia and the New York Bight ocean area indicate that statistically-significant quantitative relationships exist between remotely sensed data and onsite chlorophyll a measurements in these environmentally different areas. Data collected in the visible and near-infrared spectral ranges were used in the analysis. Changes in chlorophyll a concentrations give unique spectral responses compared with those for other water quality parameters. Also, calibrated regression equations from the analysis were used to map quantitative distributions of suspended sediment and other parameters of interest.

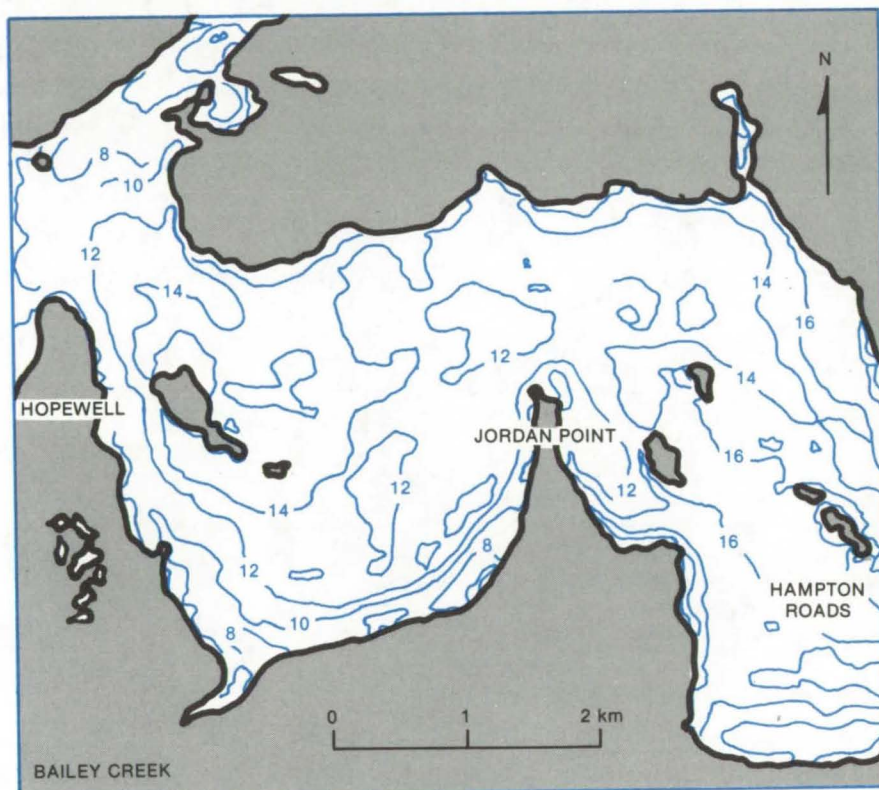


Figure 1. James River Chlorophyll a Concentrations shown on the color contour lines are in milligrams per cubic meter. Of particular interest is the Bailey Creek area in the lower left corner. Bailey Creek is a source of sewage-plant and industrial effluents, and its lower chlorophyll a content is probably due to toxic materials.

Remotely sensed data were collected with multispectral scanners on-board aircraft in conjunction with sea-truth measurements taken from boats or by helicopter over the two areas of the Atlantic Coastal Zone. In both experiments sea-truth measurements were made within about 2 hours of the remote sensor overpass. These sea-truth measurements included chlorophyll a concentrations and other water quality parameters. Statistical stepwise regression analysis was used to determine calibrated regression equations for quantitatively relating sea-truth measurements to remotely sensed data.

The concentration distributions of water quality parameters were mapped quantitatively from the regression equations. For each water quality parameter, concentrations were determined for each pixel. This field of data was smoothed to remove local spectral and spatial noise features, and a contour map was developed by a computerized plotting routine. Quantitative distributions of chlorophyll a in the James River near Hopewell, Virginia, and in the New York Bight apex are shown in Figures 1 and 2, respectively. Sea-truth measurements (not shown) were taken throughout both areas.

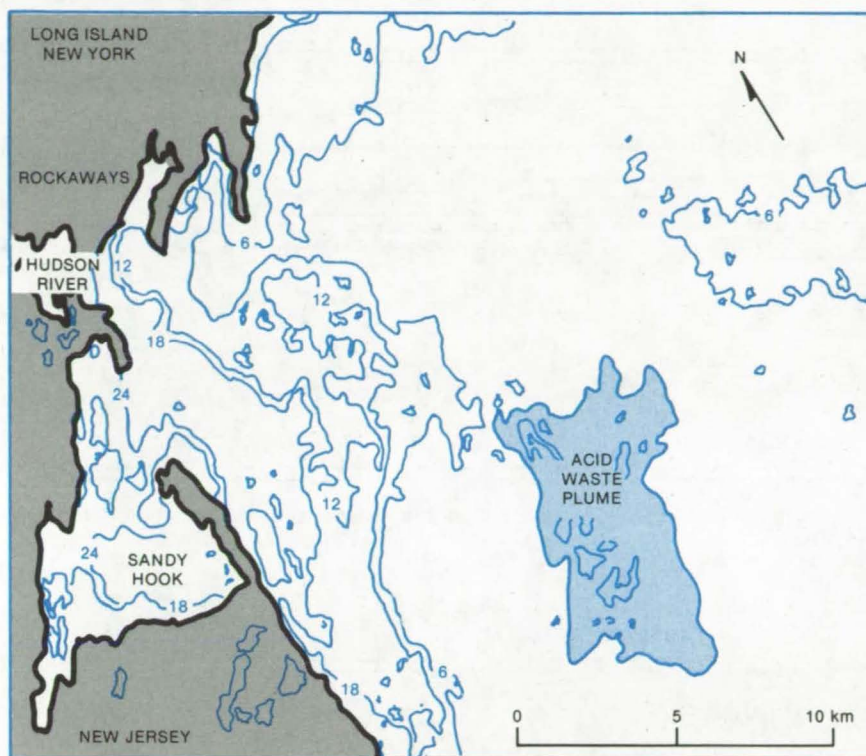


Figure 2. The New York Bight Apex was also the subject of remotely-sensed chlorophyll a determinations. Note the high concentrations (mg/m^3) in the near-shore areas and in the Hudson River plume as it flows into the New York Bight. The acid waste plume mapped in the lower right is shown distinctly because of its anomalous characteristics.

Results of the experiments indicate that concurrently-collected sea-truth measurements may be used to calibrate remotely-sensed multispectral scanner data. The same calibration technique, statistical stepwise regression analysis, was used in both experiments to identify and incorporate significant bands of multispectral scanner data into regression equations that quantitatively related remotely sensed data to water quality parameters, such as chlorophyll a and suspended sediment, and these regression equations were further used quantitatively to map synoptic distributions of chlorophyll a in the remotely sensed scenes.

This work was done by Robert W. Johnson of Langley Research Center. For further information, Circle 39 on the TSP Request Card.

Additional documentation, NASA TP-1021 [N78-13628] "Quantitative Analysis of Aircraft Multispectral Scanner Data and Mapping of Water Quality Parameters in the James River in Virginia," may be obtained [prepayment required] from the North Carolina Science & Technology Research Center [see page A7]. LAR-12293



Production of Large-Area Electrets

Charge-injection methods for low-cost production of homocharged electrets

Marshall Space Flight Center, Alabama

Two new methods are proposed for producing electrets, which are permanently-polarized dielectric materials analogous to magnets. Electrets are used in filters, dust mops, dustcloths, air-conditioning systems, carpet sweepers, and other devices for attracting dust. Both of the new methods could speed up production and reduce the costs for homocharged large-area electrets. Conventional methods are slower and are based on the decay of heterocharged electrets into the homocharged type, which

may take from several hours to several months.

In one approach (see Figure 1), a continuous roll of dielectric material is passed through a standard heating unit. Some polymeric dielectrics may be used that can withstand the high heat. Alternately, inorganic materials, such as mica, gadolinium molybdate, and fused quartz, are also suitable. As the dielectric is passed through the heater, it is heated to its electret Curie point. From the heater it is then passed over a heated metal plate.

Located above the plate is a wire-brush corona electrode connected to a high-voltage dc supply (0 to 20 kV).

Plasma produced from the discharged corona is injected into the heated dielectric material closely below the electrode. Before the finished material reaches the takeup spool, it is cooled by either an airstream or a cold-water metallic plate followed by a fan (optional). The resulting material with the "frozen-in" charge becomes a homocharged electret.

(continued on next page)

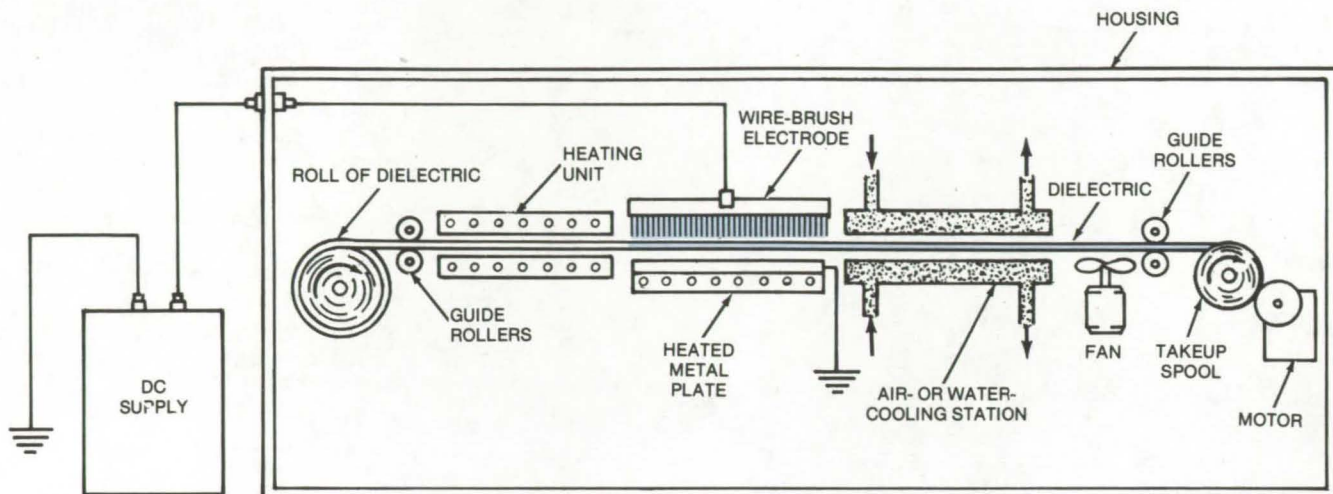


Figure 1. **Injected-Charge Method** of producing an electret is based on moving a continuous roll of dielectric material through heating, corona-discharge, and cooling stages. The dielectric is heated to its electret Curie point before plasma is injected into the material.

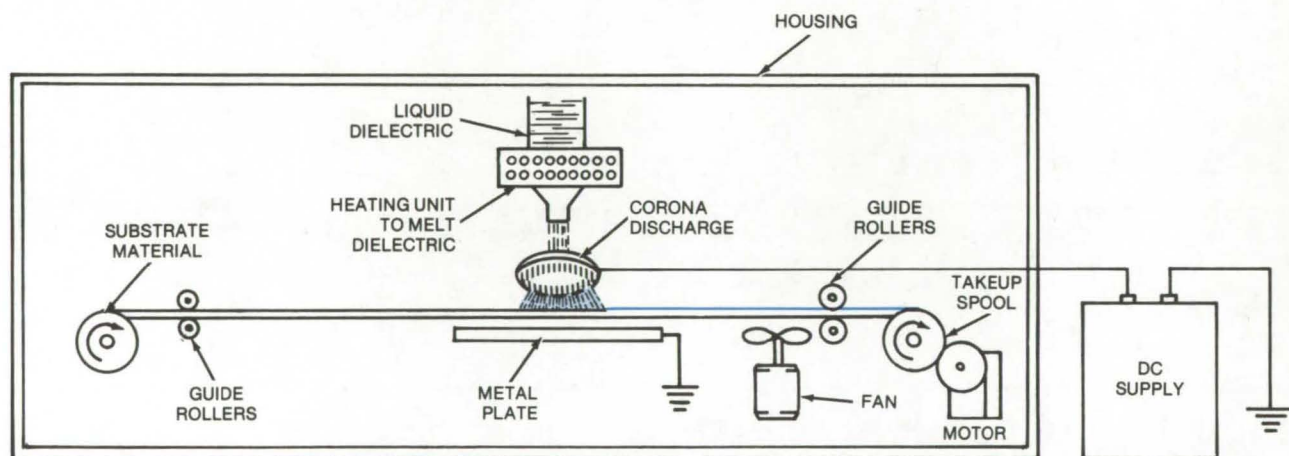


Figure 2. **Dielectric-Spray Method** produces a homocharged electret on a suitable substrate (e.g., cloth or paper). The spray is exposed to corona discharge before it is deposited on the substrate. After cooling, the electret is peeled off the substrate for use.

A second approach shown in Figure 2, utilizes a dielectric mist or spray to inject a charge onto a substrate material. The mist can be any suitable dielectric material that is liquid at room temperature or can be heated to a molten state. The substrate may be paper, cloth, or conventional dielectric material.

As the substrate is reeled between the spray gun and the grounded metal

plate, the dielectric spray or mist is dispersed in the substrate. Simultaneously a corona discharge is applied to the spray before it reaches the substrate. The substrate with the deposited material is cooled before reaching the takeup spool. When the process is finished, the homocharged electret is peeled off the substrate for use.

This work was done by P. K. C. Pillai, Edward Shriver, and Orville

Weaver of **Marshall Space Flight Center**. For further information, Circle 40 on the TSP Request Card.

This invention is owned by NASA, and a patent application has been filed. Inquiries concerning nonexclusive or exclusive license for its commercial development should be addressed to the Patent Counsel, Marshall Space Flight Center [see page A8]. Refer to MFS-23186.

Books and Reports

These reports, studies, and handbooks are available from NASA as Technical Support Packages (TSP's) when a Request Card number is cited; otherwise they are available from one of NASA's Industrial Application Centers or the National Technical Information Service.

Theory of Back-Surface-Field Solar Cells

The performance of these two-junction devices is superior to conventional unijunction cells.

A new report describes a simple, concise theory of back-surface-field (BSF) solar cells (npp⁺ junctions) based on Shockley's depletion-layer approximation. By also assuming uniform doping, the electrical characteristics of BSF cells as a function of relevant parameters (e.g., cell thickness and diffusion lengths) may be determined with a minimum of computer run time. The superior performance of BSF cells as compared to conventional np junction cells is explained on the basis of two effects: (1) The sharing of the applied voltage among two junctions (np and pp⁺) decreases the cell dark current, and (2) the reflection of minority carriers by the built-in field of the pp⁺ junction increases the short-circuit current. The theory predicts an increase in open-circuit voltage with a decrease in cell thickness. Although the short-circuit current decreases, the efficiency of the cell is virtually unchanged if its thickness is reduced from 200 to 50 microns. Thus, it may be possible to fabricate lighter cells without sacrificing power output. Moreover, the amount of raw silicon needed and problems associated with depositing the silicon film may also be reduced.

The theory is based on some simple assumptions:

1. That for low-level injection, Shockley's depletion-layer theory is applicable;

2. That the electron current of the base is reflected by the pp⁺ junction; and
3. That any externally applied voltage is shared between the np and pp⁺ junctions.

The first assumption makes it possible to linearize the theory and thereby to simplify computer runs. Assumption (2) results in the increased short-circuit current, and the decrease in dark current is a result of assumption (3).

The report evaluates the hole, electron, and photon-induced contributions to the current density for both conventional and BSF solar cells. These are integrated over all wavelengths for an assumed value of photon flux to predict the I-V characteristics of the device. All input parameters in the calculations are defined and tabulated. The results clearly show the superior performance of BSF cells. Where comparison with experiment is made, the agreement is good.

This work was done by Oldwig Von Roos of Caltech for NASA's Jet Propulsion Laboratory. To obtain a copy of the report, Circle 41 on the TSP Request Card.
NPO-14451

Rankine-Cycle Solar-Cooling Systems

A summary of three developmental systems

A new report reviews progress made by three contractors to Marshall Space Flight Center and the Department of Energy in developing Rankine-cycle machines for solar cooling. The report is part of a larger program for the development of solar heating and cooling systems and the demonstration and testing of commercially available equipment. The Rankine-cycle machines are being developed independently by AiResearch Manufacturing Company (Torrance, California); General Electric Company (Philadelphia, Pennsylvania); and Honeywell

Inc. (Minneapolis, Minnesota). These systems were selected from among a group of proposals that represent current technology in this field.

Three Rankine-cycle cooling systems developed by AiResearch Manufacturing Company have capacities of 2.7, 22.7, and 68.2 metric tons. Each operates as a closed-cycle heat pump in which solar energy is used to power a turbine that drives the compressor in the refrigerator loop. The systems also operate in a heating mode by using the collected solar energy to heat the refrigerant and electrical energy to operate a motor on the same shaft as the compressor.

Cooling systems with capacities of 2.7 and 9 metric tons are under development by General Electric Company. These also use a heat pump, but they have a configuration different than the AiResearch systems. A vapor compressor is mated with an efficient, vertically mounted expander in a hermetically sealed package. An electric motor drives the compressor when solar energy is not available. The expander is a low-speed, two-stage, multivane rotary device that is connected to the compressor by an overrunning magnetic-drive clutch assembly.

Honeywell Inc. is developing a family of heating and cooling units with capacities of 2.7, 22.7, 45.4, and 68.2 metric tons. These systems include a generator to produce electric power directly from solar energy. They consist of (1) a solar collector loop that interferes with a thermal-energy storage loop through a tube-and-shell heat exchanger, (2) a Rankine-cycle boiler and engine, and (3) a motor/generator and water chiller. Operational tests have been completed on the 22.7-metric-ton system, and the data are included in the report.

This work was done by Hoyt M. Weathers of Marshall Space Flight Center. To obtain a copy of the report, "Rankine Cycle Machines for Solar Cooling," Circle 42 on the TSP Request Card.
MFS-25094



Rankine-Cycle Heating and Cooling Systems

A report on the design of solar-powered heating/cooling systems

A 173-page report includes detailed drawings, performance data, equipment specifications, and other information pertinent to the design of solar-heating and cooling systems based on the Rankine heat-pump cycle. Systems ranging from 80-kBTU-per-hour (84×10^6 J/h) heating and 3-ton (26×10^3 N) cooling capacities to 800-kBTU per hour (840×10^6 J/h) and 25 tons (224×10^3 N) are in the preliminary design stages for eventual construction and installation in single-family residences and commercial buildings.

The basic system is a reversible vapor-compression heat pump that is driven in the cooling mode by a Rankine power loop and, in the heating mode, by a variable-speed electric motor. The heating/cooling systems differ from similar heating-only systems in the arrangement of the heat-pump subsystem and in the addition of a cooling tower that serves as a heat sink for cooling the mode.

In the heating mode, the cooling tower is inactive. In the cooling mode, the heat pump uses thermal energy from a solar-energy storage tank as the primary source of power. Since the installation sites have not yet been selected, only limited work has been done at the overall system level, and the report primarily considers refinements of the various subsystems. Most of the activity is concerned with design of the heat pump.

Topics covered include:

- heat-pump subsystem (overall design),
- turbomachine/motor,
- motor control,
- system control,
- heat-pump heat exchangers,
- cooling tower, and
- refrigerant pump.

An appendix presents detailed data on the measured heat-transfer and pressure drop for the refrigerant evaporating in a finned-tube coil heat

exchanger, one of three kinds of heat-transfer surfaces studied. The performance characteristics of all three are compared in the main body of the report.

This work was done by AiResearch Manufacturing Co. for Marshall Space Flight Center. To obtain a copy of the report, "Preliminary Design Package for Solar Heating and Cooling Systems," Circle 43 on the TSP Request Card. MFS-23998

Design Information for Solar-Heating Systems

Report includes a hazards analysis, quality-control information, and a training program for installation contractors.

A new report contains preliminary design information for two solar-heating and hot-water systems that are presently under development. The systems are similar, except for differences in the thermal storage-tank configurations. The basic system consists of a flat-plate solar collector that uses a paraffinic heat-transfer fluid, a water-filled thermal-energy storage tank (with a collector-fluid/water heat exchanger), a liquid/air heat exchanger to generate hot air for space heating, a water/water heat exchanger (in the thermal storage tank) to heat domestic hot water, and auxiliary electric heaters to supply backup heat.

In one system, a 1,500-gal (5,680-l) concrete container is the thermal-energy storage tank. It is insulated with 2 in. (5.1 cm) of urethane foam and is buried. Heat is transferred in a composite flat-plate heat exchanger, located within the tank. The other system has an all-steel tank with an integral plate/coil heat exchanger. This tank is also insulated with urethane foam. It is installed within the building being heated.

In addition to describing the systems (there are 23 pages of design drawings), the report discusses quality control during fabrication, special

tooling needed, a hazards analysis, and a preliminary training program for installation contractors.

This work was done by Colt, Inc., for Marshall Space Flight Center. To obtain a copy of the report, "Preliminary Design Package for Solar Heating and Hot Water System," Circle 44 on the TSP Request Card. MFS-25097

Solar-Heating System — Performance Tests

Tests verify its suitability for field installation in single family dwellings.

A 126-page report describes comprehensive performance tests of a complete solar-powered space and hot-water heating system for small single-family dwellings. Design and performance specifications for this system are outlined in "Solar-Heating System" (MFS-25022) on page 522 of *NASA Tech Briefs*, Vol. 3, No. 4.

Air is the collector fluid in this stand-alone, prepackaged, modular system. Its major components include the collector, a pebble-bed thermal-storage bin, a hot-water preheat tank, heat exchangers, dampers, and a control system. Performance tests were carried out on each of the sub-components and on the complete system. The results were compared with the vendors' predicted performance. Overall system operation was verified without exposing any significant problems. It was judged suitable for field installation and can supply 48.2 percent of a total annual space-heating and hot-water load of 59.63×10^6 Btu (62.9×10^9 J), projected to conditions at a site in Clinton, Mississippi.

The report includes a detailed description of the test procedures and a discussion of the results. A 76-page appendix contains the test data.

This work was done by the Federal Systems Division of IBM Corp. for Marshall Space Flight Center. To obtain a copy of the report, "SIMS Prototype System 4 — Performance Test Report," Circle 45 on the TSP Request Card. MFS-25116

Performance Test for a Solar Water Heater

Test procedure for a domestic solar-powered hot-water system

Two new reports describe the procedures and results of performance tests on a solar-powered hot-water system. The system contains a single-glazed flat-plate collector and an 82-gallon (310-liter) domestic water heater as the storage vessel. A 5.3-gal/min (20.7-l/min) pump, operated by a differential temperature controller, circulates water through the collector and storage vessel. The solar water heater is a "dump" system: It automatically drains the water if its temperature drops close to the freezing point.

The performance test determines:

- The amount of energy collected by the system;
- The amount of energy delivered to the household by the solar source;
- The power required to operate the system and maintain the proper tank temperature (the tank contains a 3-kilowatt electric heater as a standby energy source);
- Overall system efficiency; and
- Temperature distribution (stratification) in the tank.

The report lists the equipment needed for the performance test. Data from this instrumentation are recorded on magnetic tape. After the test, the data are processed by computer, and performance plots are drawn automatically.

The report presents equations and the definitions of terms for the calculation of collector efficiency, solar energy available, solar energy collected, hot-water load, total electrical energy (the sum of energy consumed by the standby heater and the pump), and heat-transfer coefficient of the hot-water tank.

The initial phase of testing is described in the first of the two reports referenced at the end of this article. Performance data are tabulated for 27 representative daily tests conducted over a 9-month period in the other report. The system efficiency is approximately 25 percent in both the initial and long-range phases of testing.

This work was done by the Solar Energy Systems Division of Wyle Laboratories for Marshall Space Flight Center. To obtain copies of the reports, "LARGO Hot Water System Thermal Performance Test Report" and "LARGO Hot Water System Long Range Thermal Performance Test Report — Addendum," Circle 46 on the TSP Request Card. MFS-25114

Air Solar Collector — Installation Package

Includes operating and assembly instructions

A nine-page installation package for an air solar collector contains a parts list, operating and assembly instructions, and performance specifications. A schematic of the collector is also included.

The 147- by 103-in. (3.73- by 2.62-m) collector consists of 72 cylindrical airflow tubes, each of which surrounds and is concentric with 1 of 72 return tubes. The tube assemblies are manifolded together at one end. Air is forced through the annular space between the tubes and back through the return tubes at a nominal flow rate of between 8 and 12 lb/h (3.6 and 5.4 kg/h) per square foot (0.092 m²) of collector area. With the tube elements removed, the structure weighs 80 lb (36 kg); when the elements are installed, it weighs 300 lb (136 kg).

Thermocouples are installed at the flow inlet and flow outlet for generating signals to the control logic of the solar heating system. One of these is an overtemperature sensor that turns off the fan when the temperature exceeds 450° F (232° C). In a stagnation mode, the collector can withstand temperatures up to 600° F (316° C).

This work was done by Owens-Illinois, Inc., for Marshall Space Flight Center. To obtain a copy of the installation package, "Installation Package for Sunpak Solar Collectors," Circle 47 on the TSP Request Card.

Inquiries concerning rights for the commercial use of this invention should be addressed to the Patent Counsel, Marshall Space Flight Center [see page A8]. Refer to MFS-25031.

Static Load Testing of a Liquid Solar Collector

Checks for susceptibility to leakage and other damage

The flat-plate liquid solar collector described in "Thermal Performance of a Flat-Plate Liquid Solar Collector" (MFS-23890), on page 217 of NASA Tech Briefs, Vol. 3, No. 2, has been subjected to static pressure loads and then examined for leakage and other damage. The results of these tests are summarized in the report referenced at the end of this article.

Six static pressure loads between 10 and 120 lb/ft² (479 and 5,746 N/m²) were applied by using a special load frame filled with water to various depths. The water pressure was transferred to the collector glazing surface through a flexible diaphragm. After each pressure application, the collector was flushed and checked for leaks. None were found for the specified range of applied loads.

This work was done by the Solar Energy Systems Division of Wyle Laboratories for Marshall Space Flight Center. To obtain a copy of the report, "Libbey-Owens-Ford Solar Collector Static Load Test," Circle 48 on the TSP Request Card. MFS-25115

Liquid Solar Collector — Performance Evaluation

Report contains a detailed analysis of raw data.

Thermal performance tests and measurements of the incident-angle modifier and transient response of the liquid solar collector referenced in "Design and Installation of a Flat-Plate Solar Collector" (MFS-25010), on page 523 of NASA Tech Briefs, Vol. 3, No. 4, and "Liquid Solar Collector — Performance Tests" (MFS-25082), on page 524 of that issue are summarized in a 25-page report.

The flat-plate collector has a time constant of 1 minute and 44 seconds; its thermal efficiency ranges between about 20 and 60 percent, depending on the test conditions. Incident-angle modifier values are between 0.95 and

(continued on next page)



1.0 for incident angles of 60°, 50°, 40°, 30°, and 0°.

The report includes tabulations of raw data, graphs, and discussion of the analysis of the measurements. Test conditions, test equipment, and data-acquisition instrumentation are described. The measurements were taken by using the Marshall Space Flight Center solar simulator.

This work was done by the Solar Energy Systems Division of Wyle Laboratories for Marshall Space Flight Center. To obtain a copy of the report, "Thermal Performance Evaluation of The Calmac (Liquid) Solar Collector," Circle 49 on the TSP Request Card.

MFS-25090

Weathering of a Liquid-Filled Solar Collector

Thermal performance was evaluated before and after 15-1/2 months of natural weathering.

A new report describes the procedures and results of tests for the effects of weathering on a flat-plate liquid solar collector. Thermal performance was measured before and after natural weathering for 15-1/2 months by using the Marshall Space Flight solar simulator. [See "Solar Simulator Test Facility" (MFS-23972), on page 507 of *NASA Tech Briefs*, Vol. 3, No. 4.]

The tested collector has a steel absorber plate coated with black chrome (emissivity 0.12, absorptivity 0.95). Copper flow tubes are bonded to the upper surface of the plate. It is covered by a double layer of tempered glass. The collector dimensions are 3 by 3 ft by 6-1/2 in. (0.91 by 1.8 by 0.17 m).

Following weathering, the collector absorber plate was found to be slightly discolored. The thermal performance was measured according to the National Bureau of Standards recommended approach: Collector efficiency was plotted against a parameter U : the inlet-to-ambient temperature differential divided by the incident radiation flux.

A comparison of the before-and-after efficiency curves indicated a change in the ordinate intercept but no change in slope. This implies no change in the collector heat-loss coefficient, but it does show a change in the absorptivity.

This work was done by Wyle Laboratories for Marshall Space Flight Center. To obtain a copy of the report, "Long-Term Weathering Effects on The Thermal Performance of The Lenox/Honeywell [Liquid] Solar Collector," Circle 50 on the TSP Request Card.

MFS-25113

Design of a Concentrating Solar Collector

Includes over 200 pages of drawings and specifications

The design package for the concentrating solar collector referenced in "Concentrating Solar Collector — Installation Package" (MFS-25068) on page 524 of *NASA Tech Briefs*, Vol. 3, No. 4 is now available. The bulk of the 217-page package is a detailed set of design drawings and parts lists for all components and subcomponents of the system (including its tracking drive).

A water/glycol solution is the working fluid for this concentrating collector. It has a galvanized steel housing, a copper absorber tube, and fiberglass insulation. Four modified Fresnel prismatic lenses in the collector cover, with a total area of 43 ft² (4.0 m²), give a concentration ratio of 10 to 1. Two or more panels can be ganged to form a collector array.

The tracking drive has a bidirectional motor controlled by photocells and supporting circuitry. It points the collector at the Sun in daylight and resets to the east at night to await the next Sunrise.

Fluid temperatures up to 240° F (115° C) are generated in the collector. When used for heating, it will supply 1,242 Btu/ft²-d (14.1x10⁶ J/m²-d) at an inlet fluid temperature of 105° F (65° C). This performance is for noon solar flux of 316 Btu/h-ft² (998 J/s-m²), an average ambient

temperature of 50° F (10° C), and zero wind velocity. The "application" section of the package describes the collector in detail, and a section devoted to performance specifications is also included.

This work was done by Northrup, Inc., for Marshall Space Flight Center. To obtain a copy of the package, "Design Package for Concentrating Solar Collector Panels," Circle 51 on the TSP Request Card.

MFS-25098

Concentrating Solar Collector — Performance Tests

An evaluation of collector thermal performance, incident-angle modifier, and transient response.

The concentrating solar collector described in "Concentrating Solar Collector — Installation Package" (MFS-25068), on page 524 of *NASA Tech Briefs*, Vol. 3, No. 4, has been tested, using the Marshall Space Flight Center solar simulator. Collector thermal performance, transient behavior, and incident-angle behavior were evaluated. A 25-page report that summarizes the test results may be obtained by requesting the Technical Support Package referenced at the end of this article.

In accord with the National Bureau of Standards recommended approach, collector efficiency is measured by measuring the insolation and the entry and exit temperatures of the transfer liquids. Efficiency is plotted as a function of a parameter $\tau = (t_i - t_a)/I$, where t_i and t_a are the inlet and ambient temperatures, respectively, and I is the incident solar flux. The efficiency (based on aperture area) varied between 30 and 55 percent.

The collector time constant is the time required, once the insolation drops to zero, for the inlet/outlet temperature difference to drop to 0.368 of its original value. It was measured to be 2 minutes and 2 seconds.

An outdoor, movable rack was used in the incident-angle modifier tests.

The collector was adjusted so that the incident radiation angles were 0°, 20°, 30°, 38°, and 46° with respect to the normal to the collector surface. The efficiency for the off angles was measured and related to the efficiency for normal incidence by using standard techniques.

This work was done by the Solar Energy Systems Division of Wyle Laboratories for Marshall Space Flight Center. To obtain a copy of the report, "Indoor Test For Thermal Performance Evaluation on The Northrup Concentrating Solar Collector," Circle 52 on the TSP Request Card. MFS-25086

Controller for Solar Heating — Design Package

A 54-page brochure contains performance specifications and detailed drawings for two new instruments: (1) a differential controller and (2) a temperature monitor for solar-powered water-heating systems. Included in the package are schematics, wiring diagrams, test procedures, and parts lists. The information should be of interest to architects, engineers, and others involved in the design and installation of solar-heating systems.

The solid-state controller is a differential thermostat that monitors the temperature in the collector and in the hot-water storage tank of the solar-heating system. It switches on when the collector temperature exceeds the storage temperature by a preset limit [typically 20° F (11.1° C)]. In the on condition, the input voltage (either 120 or 24 Vac) is delivered at output terminals for the control of pumps in the collector loop.

The controller is used with either air or water temperature probes containing matched thermistors in metal housings. The probes are electrically connected to the controller package through high-temperature-resistant cables. Tracking accuracy is $\pm 5^\circ$ F ($\pm 2.7^\circ$ C) over the operating temperature range between -40° and +300° F (-40° and +149° C).

The temperature monitor, also a solid-state device, senses the indoor, outdoor, and storage temperatures and shows them on a 3-digit liquid-crystal display (with a plus or a minus sign). Linear diodes that operate over

the range -40° to +199° F (-40° to +111° C) are the temperature sensors. A thermostat generates signals to control the solar- and backup-heating systems. Three light-emitting diodes indicate the mode of operation: solar collecting, solar distribution, or backup heating.

A 4- by 4- by 3-1/2-in. (10- by 10- by 9-cm) package houses the controller module. Its weight is 2 lb (0.9 kg), the same as that of the temperature monitor.

This work was done by the Solar Control Corp. for Marshall Space Flight Center. To obtain a copy of the package "Solar Control Design Package," Circle 53 on the TSP Request Card. MFS-25009

Cost Analysis of Hot-Air Solar-Heating Systems

An analysis based on experience with two operational test sites

A study of two operational test sites (Huntsville, Alabama, and Carlsbad, New Mexico) has furnished estimates of actual costs and potential cost savings of new and retrofit hot-air solar-heating and hot-water systems for single-family dwellings. The results of the study are presented in a 29-page report that is now available. Also included in the report is a description of innovative design concepts that have been tested, and which offer potential cost savings.

The study first considered the procurement, installation, and maintenance costs of the test sites and then made production cost estimates and identified potential savings based on a cost-reduction design study. The quantities of systems assumed for the production estimates are based on a goal of 2.5 million solar-heated homes by 1985. It was assumed that the system being evaluated would account for 40 percent of that market.

The estimates were broken down into five categories:

- **Cost of the Prototype**, including actual costs and expected costs added by contractors;
- **Projected Mass-Production Costs of the Prototype** without design changes;

- **Projected Mass-Production Cost of an Improved Prototype**, including savings incurred by using different materials, construction methods, and design techniques to produce essentially the same system;

- **The Cost Equivalent** expected to be incurred by the "average" American homeowner in 1985 if he were to install the test system; and

- **Innovative Design Concepts** that reduce costs, including imaginative design and construction concepts.

In connection with this last category, three tested cost-effective designs are discussed:

1. The use of the home framing structure for transmitting and distributing the heated air: In this concept, the rafters form a plenum for the collector panels and for returning solar-heated air to wall plenum chambers that replace the conventional ductwork needed in a hot-air solar-assisted system. Manifolding is completely eliminated since it is an integral part of the framing structure, and heat is transmitted at the periphery of the building where it can be effectively used for radiation heating or vented into selected rooms.
2. An integrated core module concept that offers the advantages of a standardized, prepackaged unit for many home-structure designs: It employs only one air handler and one hot-water tank; a simplified control system and control logic permit the use of fewer dampers and fewer controls. This unit could be preassembled or mass-produced and transported (minus heat-storage-bed rocks and collector glass) to the installation site for final assembly.
3. A "full-standing" prepackaged module, adaptable for retrofit applications

Other possible design economies, not evaluated in the report, are mentioned.

This work was done by Billy J. Hawkins and Rodney D. Stewart of Marshall Space Flight Center. To obtain a copy of the report, "Cost Analysis of New and Retrofit Hot-Air Type Solar Assisted Heating Systems," Circle 54 on the TSP Request Card. MFS-25092



Solar Energy for Industrial Process Heat

Solar energy can supplant fossil fuels in industrial processes, such as milk processing.

Solar energy can furnish much of the heat needed for milk processing, with large savings in expenditures for oil and gas. Moreover, Sunlight can ensure an adequate, readily available source of process heat — an important advantage in processing a highly perishable product in an era of uncertain fossil-fuel supplies.

These are some of the findings of a study of the potential for solar-energy usage by the dairy industry in California, a \$1-billion-per-year business of which 5 percent is spent on energy. The study was part of a larger survey of the potential application of solar energy to the industrial, agricultural, and commercial sectors.

The identification of those near-term applications for solar energy in California with the greatest energy-displacement potential was the objective of the survey. Correspondingly, the largest energy users were identified and ranked according to their thermal-energy consumption. Processes were screened for those with requirements under 350° F (176° C) and under 212° F (100° C). These moderate- and low-temperature processes have the greatest potential for direct changeover to solar energy in the near term. The under-212° F category accounted for roughly 2 percent of total California energy consumption in 1975; the under-350° F category accounted for about 10 percent. Thus, the potential for energy and cost savings is substantial.

Several industries were studied in detail. The milk-processing industry was an example of an industry with relatively high potential for solar energy. Milk enters a processing plant in large tank trucks that pick up milk daily from farms. The milk is transferred into large 30,000- to 50,000-gallon (113.5- to 189.2-m³) storage tanks, where it is mixed and stored at 40° F (4.4° C). It is then subjected to a flash pasteurization process in which it is held at a temperature of 161.5° F

(71.9° C) for 7 seconds. The milk is cooled immediately, and the heat it gives up is used to warm the incoming milk. The product is packaged and stored for delivery to retail outlet. The entire process, from the entry of raw milk to packaging and delivery, takes about 24 hours.

The facilities and equipment with which the milk comes in contact are cleaned with water or steam at 160° to 180° F (71.1° to 82.2° C). The large storage tanks are cleaned every 72 hours. Steam is the prime medium for process heating and cooling and for cleaning. Much, if not all, the steam necessary for these purposes can be supplied by solar energy.

The ease of conversion to solar energy depends on the age of the processing plant. In older plants, the amount of clear, unobstructed roof area available for solar collectors is considerably less than in new plants. In addition, the roof structure in older plants may require strengthening to support a collector assembly. These physical limitations in no way preclude conversion to solar energy in older plants, but they may limit the amount of solar energy that can be collected and thus limit the amount of fossil-fuel energy that can be "displaced." Nevertheless, there is a stronger incentive to convert older plants because they are much less efficient in their use of energy than newer ones; for a given processed-milk output, an older plant may consume twice as much energy as a new plant.

The climate in the dairy industry is favorable to conversion to solar energy. Firms communicate and exchange technical information with each other, and their managements are generally receptive to new ideas. In addition, the industry is sensitive to public pressure because it receives support for milk prices from public funds. Thus it would benefit from the "goodwill" engendered by installing a fuel-conserving, nonpolluting energy system such as solar energy.

Many of the conclusions regarding the dairy industry apply as well to other industries that employ thermal-energy processes at temperatures under 350° F. Because of the capital investment, most solar-energy applications are not economically attractive today without government support. There are factors other than

initial cost, however, that affect decisions on conversion to solar energy. Certainly, a successful demonstration of the economic and technical feasibility of solar energy would help to stimulate more widespread acceptance.

This work was done by Rosalyn H. Barbieri and Donna L. Pivrotto of Caltech for NASA's Jet Propulsion Laboratory. To obtain a copy of the study report, Circle 55 on the TSP Request Card.
NPO-14498

An Annotated Energy Bibliography

Contains approximately
10,000 references

A comprehensive, annotated compilation of books, journals, periodicals, and reports on energy and energy-related topics is now available. This bibliography contains approximately 10,000 technical and nontechnical references from bibliographic and other sources dated January 1975 through May 1977.

The references are arranged by date with the latest works first; each item includes an abstract or summary of the document, its publication date, author(s), and accession number (if available). The 22 major subject headings and numerous subheadings are grouped as follows:

- **Energy and Power.** General; Resources, Supply/Demand, and Forecasting; Research and Development; Policy, Legislation, and Regulation; Environment; Consumption, Conservation, and Economics; Analysis, System, and Modeling; and Information Sources and Documentation.
- **Energy and Power Sources.** General; Fossil Fuels; Hydrogen and Other Fuels; Liquid/Solid Wastes and Biomass; Waste Heat Utilization; Nuclear; Geothermal; Solar; Wind; Ocean/Water; Magnetohydrodynamic and Electrohydrodynamic Generators; Electric Power Engineering; Automotive Power Plants and Energy Storage.

This report was compiled by Sandra J. Blow of Langley Research Center. Further information may be found in

NASA TM-74765 [N77-28577] and TM-74764 [N77-28578], "An Annotated Energy Bibliography," Volumes 1 and 2, Appendix 2, copies of which may be obtained at cost from the North Carolina Science and Technology Research Center[see page A7].
LAR-12488

Analysis of Aperture Antenna Radiation Pattern

Analysis technique and application to transmission through layered dielectric

A report, "The Principal Plane Radiation Pattern of a Dielectric Covered Aperture Near an Edge," presents an analysis of the radiation pattern produced by an aperture antenna transmitting through a layered dielectric material. The analysis was developed as an aid in predicting the behavior of the Space Shuttle K_u-band antenna, which is contained within the thermal-protection structure (TPS) of the vehicle just aft of the reinforced carbon nose cap. The antenna transmits through the TPS, but surface

waves trapped in the TPS are diffracted by the discontinuity at the junction between TPS and nose cap; and it was feared that this diffraction might cause a ripple in the far-field radiation pattern of the antenna.

The analysis shows, however, that the diffraction is not a serious problem. The properties of the TPS surface are such that the edge scattering function vanishes in the radiation equations.

The report also describes a computer program developed to compute radiation patterns on the basis of the analysis. The program provides a listing of all the allowed surface-wave propagation modes, with data on the characteristics of each mode. In addition, the program prints out the amplitude and phase of the far-field radiated power for a variety of observation angles. These data are given for two conditions: (1) with the TPS edge removed to an infinite distance and (2) for each edge distance specified in the input.

The analysis is treated as three independent parts. First, the TPS is assumed to extend to infinity in the transverse directions, and the primary radiation pattern of the aperture and

the field distribution in the TPS are calculated, using Fourier-transform analysis. Second, the effect of the attenuating layer on the propagation of the trapped modes is treated, for a semi-infinite geometry, with the excitation produced by a specified surface-current distribution in a certain plane, chosen to give the same magnetic-field distribution as that obtained for the infinite TPS configuration of the first part of the analysis. Third, the field distribution at the edge is broken down into its individual modes, and the diffracted wave for each mode is obtained.

Summing the direct radiation from the aperture (from part 1) and the diffracted radiation for each of the surface-wave modes at the discontinuity gives the total radiation pattern for the antenna in the principal plane.

This work was done by Richard Herskind, Edward Sayre, John E. Trousdale, and Jerrold Yos of the Systems Division of Avco Corp. for Johnson Space Center. To obtain a copy of the report, Circle 85 on the TSP Request Card.
MSC-16246



Computer Programs

These programs may be obtained at very reasonable cost from COSMIC, a facility sponsored by NASA to make new programs available to the public. For information on program price, size, and availability, circle the reference letter on the COSMIC Request Card in this issue.

Analysis of Building Heating and Cooling

Thermal model of buildings helps find most economical systems.

Heating and cooling systems can be tailored to meet the actual requirements of a building by using the JPL Energy Conservation Program (ECP). Significant energy costs can be saved

with this inexpensive-to-run program that accurately simulates the thermal performance of a building.

Before energy costs became such an important factor, heating and cooling equipment were generally selected based on the weather during a peak summer or winter hour. The result was usually oversized equipment, which not only takes up more space but is less efficient and more costly to run than optimally sized systems.

The ECP gives the design engineer both a methodology and an easy-to-use computer program for simulating hourly thermal characteristics over a full year for individually characterized zones within the building. Input data are from readily available sources, and the program is simplified to keep the computational cost low enough for repeated analyses of many design approaches. Even with these advantages, the computational error is less than 10

percent, which is very reasonable for engineering purposes and a vast improvement over older techniques.

The Energy Consumption Program calculates the energy requirements of a building in three major steps:

1. heat losses and gains to an enclosure are computed;
2. heating and cooling loads (as imposed inside the fan/coil units, or air-handlers) are determined; and
3. the energy inputs to all primary components are found.

For heat loss and gain calculations, the weather data required are dry-bulb temperature, cloud cover, and wind speed. Heat Transmission through walls and roofs are based on the "total equivalent temperature difference" method, where the effects of outside air temperature and solar radiation are combined in a simple calculation. Local solar-radiation values are based on the known ASHRAE model, with

(continued on next page)

cloud-cover factors used to modify the hourly radiation values to yield the local and site-specific values. The "air change method" is used to calculate the infiltration and exfiltration heat loss or gain instead of the "crack method." The effects of opening and closing doors or windows and other air leakage are averaged, assuming a fixed outside-air change rate. The computation of heat loss or gain then follows, assuming quasi-steady-state conditions.

Both internal and external heating loads are calculated. The internal heat load in a zone is composed of heat gain from people and equipment (incandescent and fluorescent lights, electronic and mechanical equipment, and sources such as process heat and kitchen equipment). Each load is calculated on an hourly basis for two types of days: a standard working weekday and an average weekend or holiday day. The number of people occupying the zone, miscellaneous heat loads,

and the wattage of equipment are input for every hour of the two types of day. The architecture and construction are incorporated by data including orientation, latitude, elevation, wall areas, glass areas, space volume, physical dimensions, exterior-surface solar absorptivity, and cross-sectional descriptions of walls and roofs. Shading from overhangs, projections, and adjacent buildings is used to attenuate the incident solar radiation and the heat transmission to exterior walls. As an energy-saving option, time clocks to control the operation of fan/coil units may be included in the load calculation. Nine types of fan/coil arrangement have been incorporated into ECP.

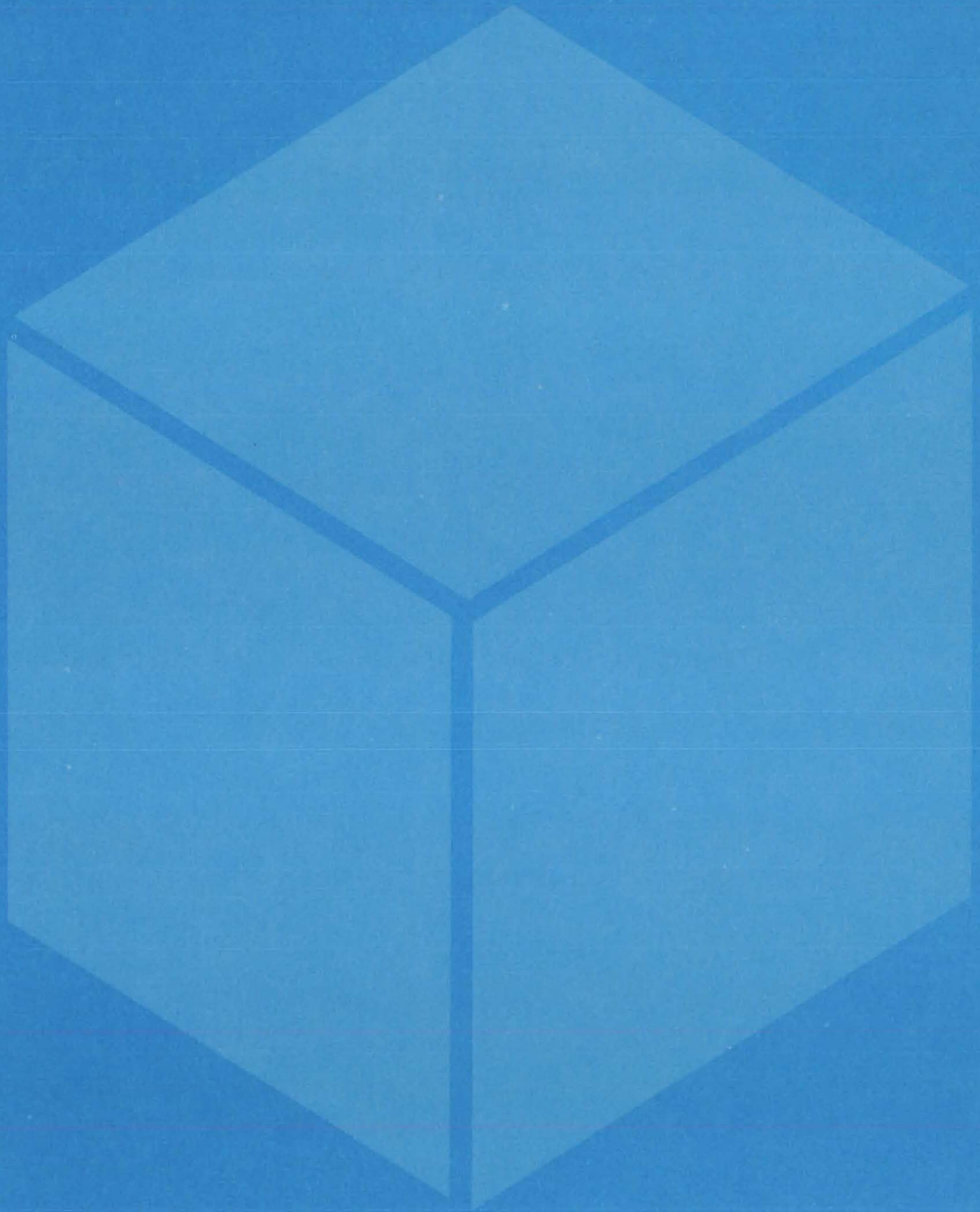
To determine the energy requirements of components, one must specify the type of heating or reheating systems (electric, gas-fired, or heat pump), the arrangement of fan/coil units with respect to compressor or chilling units, and compressor stages

and size. The energy consumed by auxiliary equipment that does not affect the heating and cooling loads (such as air-handler fans, pumps, and external lights) is calculated from rated capacity and total hours of operation. Finally, the unit cost of thermal and electric energy as purchased from a utility or as generated on site is used to compute the monthly and yearly cost of energy.

The ECP is written in FORTRAN V and has been implemented on a UNIVAC 1108 with a central memory requirement of approximately 32K of 36-bit words.

This program was written by Victor W. Chai, Sandra Higgins, Fikry L. Lansing, Floyd W. Stoller, and Douglas M. Strain of Caltech for NASA's Jet Propulsion Laboratory. For further information, Circle A on the COSMIC Request Card.
NPO-14683

Materials



Hardware, Techniques, and Processes

- 67 "Self-Packaging" Desiccant
- 68 Irradiation Pretreatment for Coal Desulfurization
- 69 Fluidized Coal Combustion
- 69 Soda Ash Removes Sulfur from Fuels
- 70 A Continuous Silicon-Coating Facility
- 71 Silicon Tetrachloride Spray Feeder
- 72 A Reactor for More Efficient Solar Cells
- 73 Chemical-Vapor-Deposition Reactor
- 74 Silicon Source for Vacuum Deposition
- 75 Low-Absorptance Porcelain-on-Aluminum Coating
- 76 Burning Crude Oil Without Pollution
- 77 Continuous Sterilization of Plumbing Systems

Books and Reports

- 78 Controlled Metal-Film Deposition on Alumina Substrates

"Self-Packaging" Desiccant

A water-soluble filler in a permeable rubber envelope absorbs large quantities of moisture without becoming gummy or corrosive.

NASA's Jet Propulsion Laboratory, Pasadena, California

A new desiccant absorbs large quantities of water without becoming sticky or releasing corrosive agents. Possible applications include the protection from moisture of electronic components, optical instruments, pharmaceuticals, and chemicals.

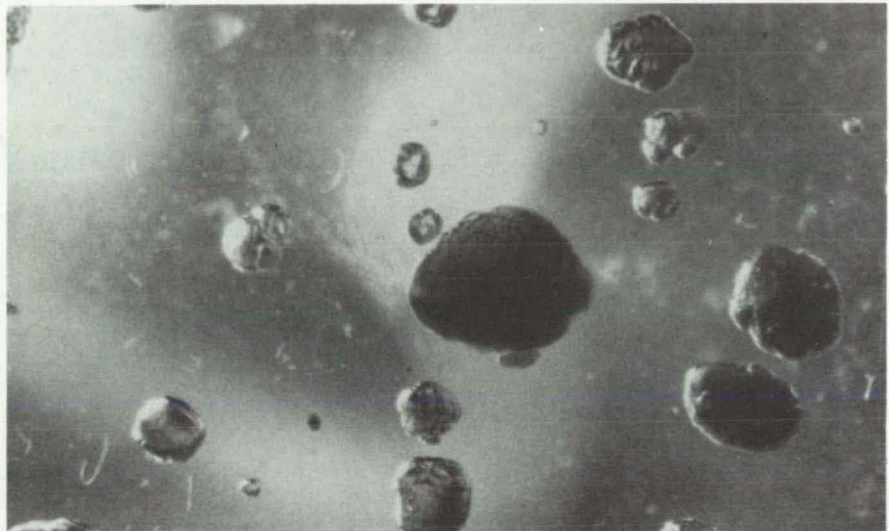
The new desiccant consists of a water-soluble filler contained in a water-permeable elastomeric matrix. The composition can be molded into virtually any shape. For example, it can be formed as a thin film for lining the walls of a container, or, it can be formed as an insert for a screw-on cap.

Calcium chloride, potassium acetate, or other low-cost material can serve as the water-soluble filler for the desiccant. The elastomer can be a natural or synthetic rubber. Silicone rubber is a good choice because its transparency makes it possible to observe the extent of water absorption by the filler. Foam materials such as polyurethane are also suitable.

Under osmotic pressure, moisture diffuses into the elastomer and is absorbed by the filler particles. The particles form pockets and grow in size as they absorb more moisture (see figure). When the filler has absorbed its full capacity, it can be regenerated by heating to drive off the absorbed moisture.

When compared with commonly used desiccants, the filled elastomer has some important advantages. Calcium chloride alone, for example, turns into a gummy, corrosive paste as it absorbs water. Although an insoluble desiccant such as silica gel does not become gummy, it absorbs water only on its surface and thus has a smaller capacity than water-soluble salts. Moreover, some gels absorb only water vapor and may disintegrate if they come in contact with liquid water.

In laboratory experiments, a filled-elastomer desiccant was made by milling 20 percent by weight of a water-soluble salt with rubber. Vulcanization of the milled mixture produced a rubber sheet with solid filler.



Particles of Water-Soluble Salt in a Transparent Silicone Elastomer, shown here greatly magnified, form pockets as the salt dissolves in water that diffuses into the elastomer (top). After prolonged exposure, the pockets assume a spherical shape (bottom).

The experiments have shown that the more water-soluble the filler is, the greater is the diffusion of water into it and the more water it holds. Particle size is also an important factor. For a given filler material, diffusion is faster for smaller particle sizes; and, the higher the filler content of the

elastomer, the higher the diffusion rate and the greater the amount of water absorbed.

This work was done by Robert F. Fedors of Caltech for NASA's Jet Propulsion Laboratory. For further information, Circle 56 on the TSP Request Card.
NPO-14354



Irradiation Pretreatment for Coal Desulfurization

Irradiating coal prior to conventional solvent desulfurization could improve sulfur extraction.

NASA's Jet Propulsion Laboratory, Pasadena, California

Before coal can be used for power generation, it should contain less than 0.7 percent by weight of sulfur. Although sulfur that is physically attached (mostly pyritic sulfur) can be easily separated by crushing, pulverization, or other mechanical process,

chemically bonded sulfur (mostly organic sulfur attached directly or indirectly to the polyaromatic rings) is more difficult to remove.

Current techniques for chemical desulfurization, such as hydrosulfurization and solvent extraction, are

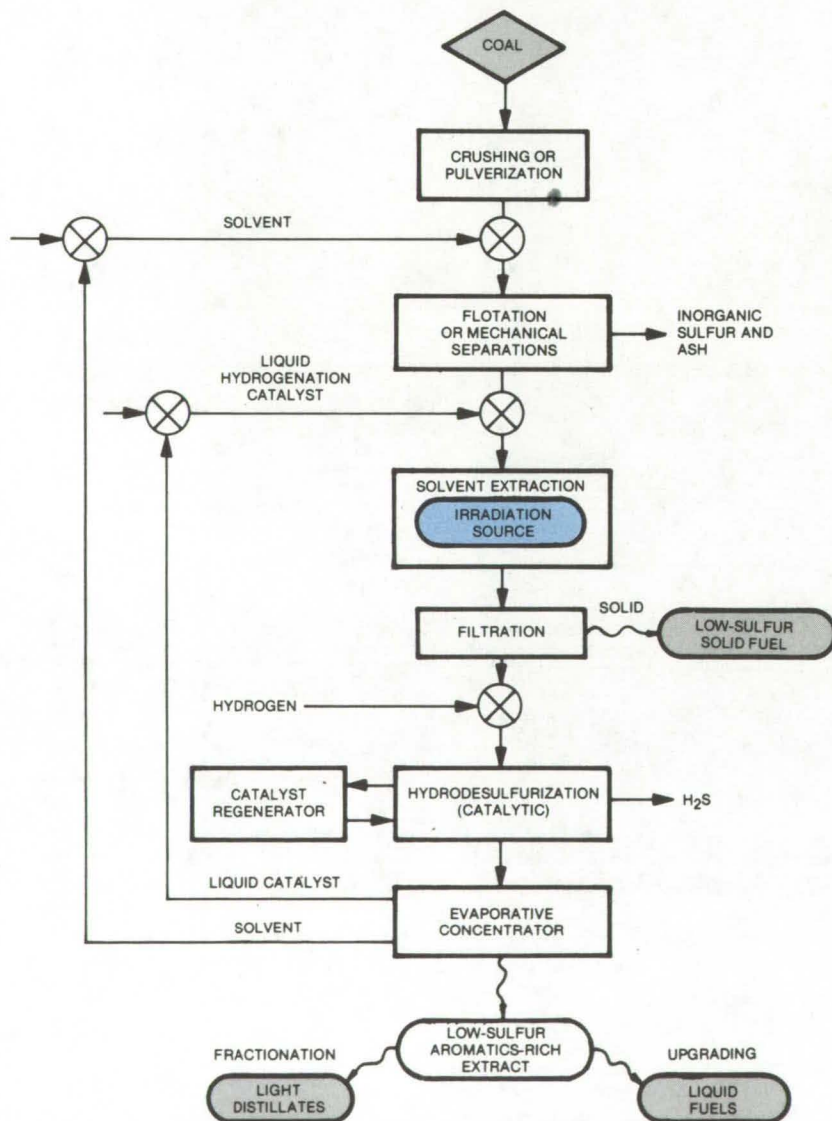
expensive and consume considerable energy. However, a proposed new radiation pretreatment could lower the costs of conventional solvent extraction and hydrotreatment.

In the new process (see figure) highly-penetrating nuclear radiation (β - and γ -radiation) would selectively cleave the carbon/sulfur bonds in the polyaromatic coal structure, while leaving the stronger carbon/carbon bonds intact. It is conjectured that the formation of free radicals under irradiation would lower the energy barrier to chain scission by the coal solvent. The sulfur-bearing fragments detached this way would be more easily dissolved in heavy aromatic solvents, increasing the total extraction. By using radioactive wastes from nuclear powerplants as the irradiation source, the cost of the pretreatment could be kept relatively low.

In comparison with hydrogen as a desulfurization agent, nuclear radiation has superior penetration capability into the coal network; and, by catalyzing the scission and extraction with hydrogenation agents such as diphenylamines, the sulfur removal could be even further enhanced.

After separating the low-sulfur solids, the extract could be hydrosulfurized by reaction with a gaseous hydrogen stream. The final extract could be either fractionated into light hydrocarbons or further upgraded into liquid fuels, and the solvent and catalysts could be recovered.

This work was done by George C. Hsu of Caltech for NASA's Jet Propulsion Laboratory. For further information, Circle 57 on the TSP Request Card.
NPO-14104



Irradiation Pretreatment to Solvent Extraction of sulfur weakens the energy barrier to desulfurization by breaking carbon/sulfur bonds. The aromatics-rich extract could be hydrosulfurized, fractionated, and upgraded to yield light distillates and liquid fuels.

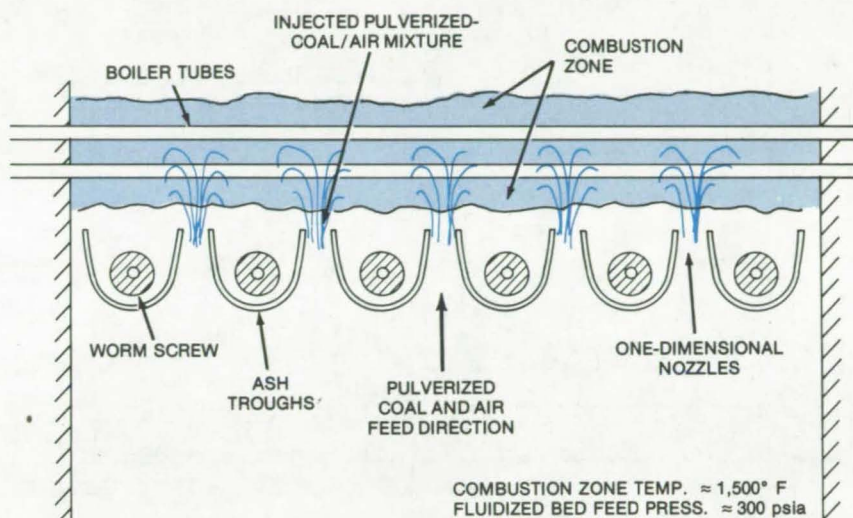
Fluidized Coal Combustion

Fuel-delivery/ash-removal system improves efficiency of coal combustion.

NASA's Jet Propulsion Laboratory, Pasadena, California

A fluidized-bed coal combustion process, in which pulverized coal and limestone are burned in the presence of forced air, may lead to efficient, reliable boilers with low sulfur dioxide and nitrogen oxide emissions. The proposed design includes a one-dimensional channel injector to control the flow of coal/air mixtures to the combustion zone and an ash-removal system scheme to maintain combustion efficiency.

The figure shows a set of one-dimensional channel injectors. The injectors distribute a mixture of pulverized coal and limestone and a stream of incoming air into the combustion zone, which incorporates boiler tubes. As the mixture enters the combustion zone, the nozzle grid assembly sets up downstream vortexes of the air/fuel mixture. The resulting eddies accumulate ash within the concave surfaces of the grid assembly. Ash is removed by worm screws installed in each trough. Excess ash is pulled through a sleeve; the combination of screw pitch and compacted ash in the sleeve prevents pressure loss from the combustion zone. Sufficient ash level is retained above the worm screw to form a natural bed that supports coal during combustion and maintains a



Proposed **Fluidized Coal Combustion** system has one-dimensional injectors to feed pulverized-coal/air mixture into the combustion zone. The grid assembly includes ash troughs with worm screws to remove excess ash from the system.

thermal blanket between the combustion zone and the screw.

The proposed system will operate with combustion zone temperatures of approximately 1,500° F (815° C). The fluidized-bed pressure will be about 300 psia (2.07×10^6 N/m²).

This work was done by Philip I. Moynihan and Donald L. Young of Caltech for **NASA's Jet Propulsion**

Laboratory. For further information, Circle 58 on the TSP Request Card.

This invention is owned by NASA, and a patent application has been filed. Inquiries concerning nonexclusive or exclusive license for its commercial development should be addressed to the Patent Counsel, NASA Resident Legal Office-JPL [see page A8]. Refer to NPO-14273.

Soda Ash Removes Sulfur from Fuels

Soda ash added to coal/oil/water emulsions removes up to 80 percent of the sulfur content.

Goddard Space Flight Center, Greenbelt, Maryland

Tests have shown that adding soda ash (sodium carbonate) to a coal/oil/water emulsion reduces 75 to 80 percent of sulfur dioxide gas emitted during subsequent combustion of the emulsion. This is considerably better than the less than 50-percent reduction typical when limestone is used as the sulfur reducing agent. The process works because soda ash is very soluble in water and can be added to the emulsion in quantities well above that needed to complete the sulfur-remov-

ing reaction.

Three approaches have been suggested: (1) sodium carbonate is dissolved in water in a coal/oil/water emulsion for which the coal/oil/water ratio is from 2:2:1 to 2:2:0.5; (2) an oil/water emulsion with dissolved sodium carbonate is used; and (3) water, containing dissolved sodium carbonate, is directly sprayed into a coal or oil flame.

The emulsion can be formed by ultrasonic agitation, high shear mixing,

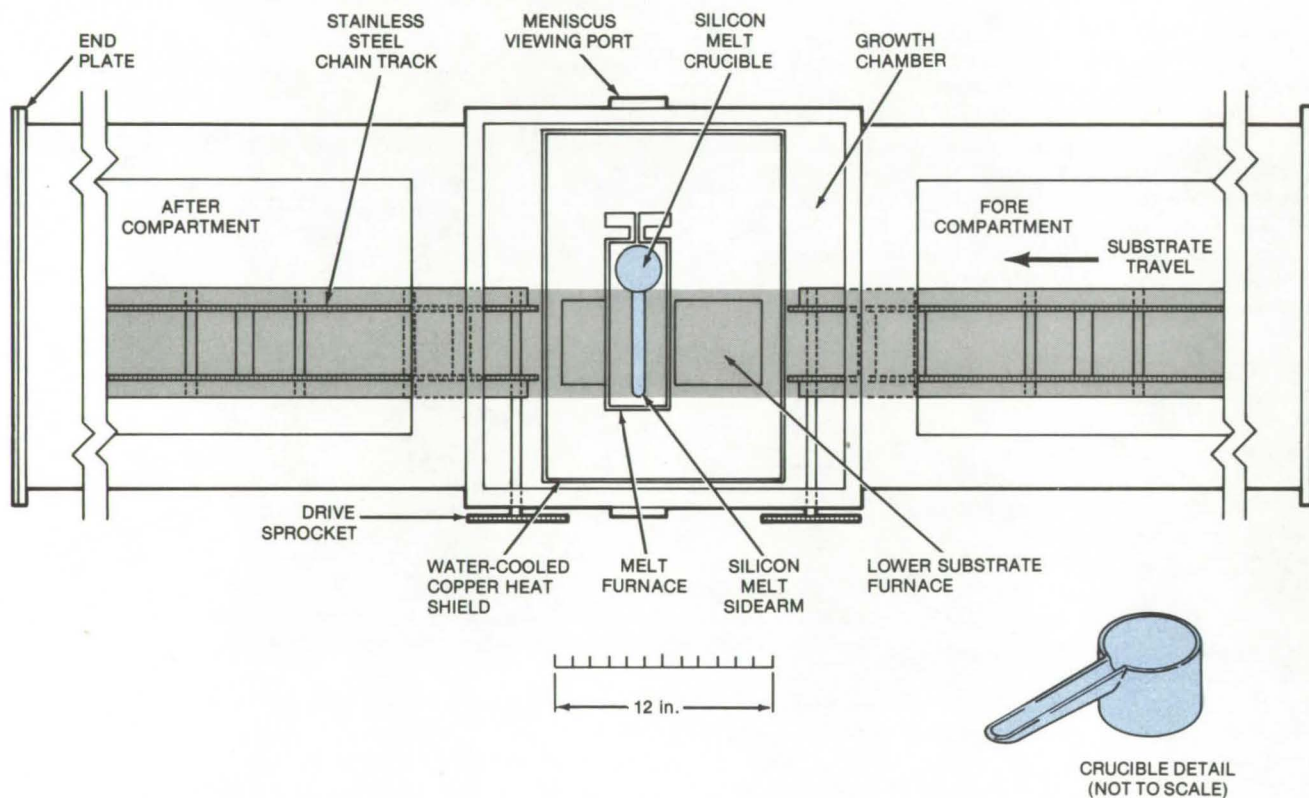
homogenization, or a similar technique. After the combustion process, the sodium sulfate fly ash could be precipitated, and the particles can be disposed of or possibly sold as a commercial product.

This work was done by John Doohar, Sung Moon, and Donald Wright of Adelphi University for **Goddard Space Center**. No further documentation is available.
GSC-12403

A Continuous Silicon-Coating Facility

An automated facility improves efficiency in fabricating solar cells.

NASA's Jet Propulsion Laboratory, Pasadena, California



A **Continuous Silicon-Coating Facility** currently under development will coat graphite-coated ceramic substrates for the production of solar cells. The substrates are coated by brushing against molten silicon supplied to a grooved sidearm. The process reduces contamination that occurs in conventional dip-coating processes, improving material service life.

A continuous silicon-coating facility currently under development will be used to process 100- by 10-cm graphite-coated ceramic substrates for silicon solar cells. The facility is an improvement over the conventional silicon dip-coating method. Its throughput is increased because of reduced contact time between the ceramic and molten silicon. Short contact time reduces melt contamination that is more common in dip coating, due to a longer contact. As a result, minority carrier life in silicon coatings, and thus solar-cell efficiency, is improved.

The continuous coater, as illustrated, will process 100- by 10-cm substrates. Two stainless-steel chain

conveyors deliver and remove the ceramic substrates, with the graphite-coated surface facing down toward the molten silicon. The conveyor speeds can vary to allow coating thicknesses ranging between tenths of mm/s to a number of cm/s. The entire facility, including the growth chamber and the fore and aft chambers, is maintained under an inert-gas atmosphere.

The substrates moving through the growth chamber pass just above a grooved sidearm. Silicon melt contained in the groove forms a meniscus bulging about 3 mm above the arm. The substrates passing above brush against the meniscus, picking up the silicon coating. The silicon is continu-

ously replenished from the crucible. An automatic rod-shaped quartz plunger progressively lowered into the crucible, maintains a constant silicon level in the pick arm. The plunger position may be controlled by using either a linear array of light-sensitive elements to monitor radiation emitted from the silicon meniscus or using a small laser beam that is interrupted when the meniscus is at a proper level.

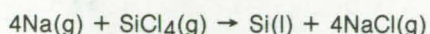
This work was done by Charles Butter and John D. Heaps of Honeywell Inc. for **NASA's Jet Propulsion Laboratory**. For further information, Circle 59 on the TSP Request Card. NPO-14373

Silicon Tetrachloride Spray Feeder

An efficient spray feeder supplies SiCl_4 into a reactor for production of highly pure silicon.

NASA's Jet Propulsion Laboratory, Pasadena, California

A silicon tetrachloride spray-feeder mechanism is incorporated into a high-temperature reactor [see article "A Reactor for More Efficient Solar Cells" (NPO-14381) on page 72 of this issue] for the production of highly pure silicon intended for solar cells. The feeder supplies SiCl_4 as liquid droplets that rapidly vaporize in the high-temperature reaction zone. The reaction in this process (assuming a sodium reductant) is

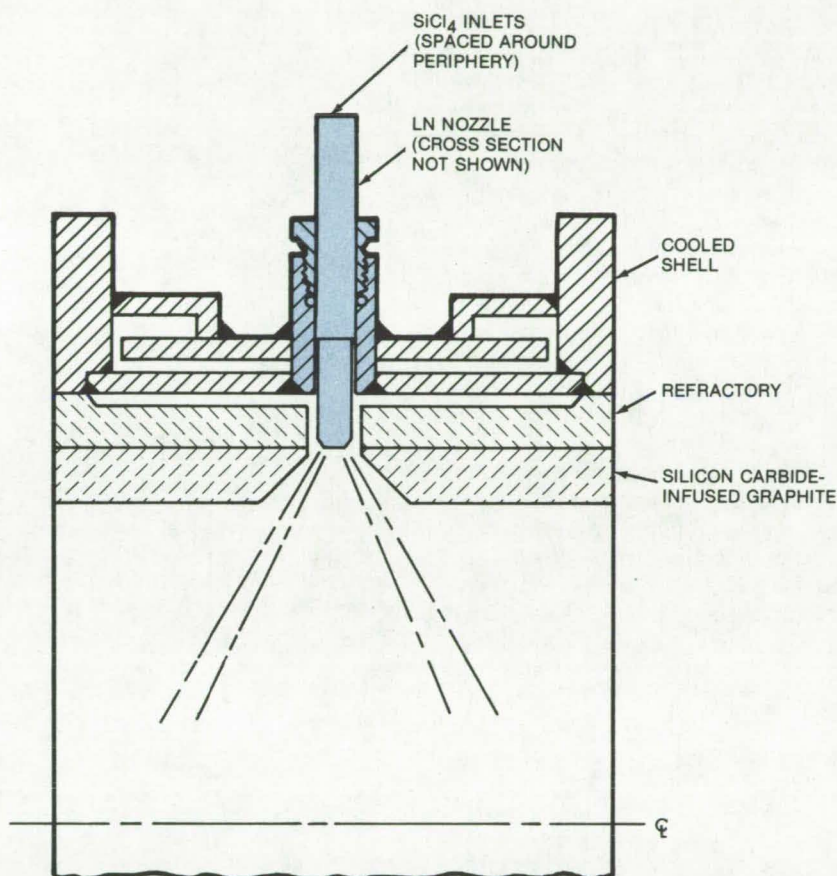


where g and l designate gaseous and liquid phases, respectively.

The liquid feed is more advantageous than gas because liquid is less prone to contamination. Also, liquid spray penetrates the hot reactor gas stream better than a gaseous feed; mixing is superior due to the boiling action of liquid droplets as they vaporize in the hot zone.

The feeder (see figure) consists of a short tubular-shaped water-cooled metal outer shell. Up to 10 equally-spaced, radially-directed spray nozzles (at least 6) are used. Its interior is lined with an inner layer of graphite, which has been infused or coated with silicon carbide or silicon nitride, and an intermediate layer of insulating refractory material such as castable alumina. These inner layers have openings for nozzle extension and feeding.

The spray nozzles may be easily moved in or out to optimize mixing by adjusting a threaded collar. The nozzles are standard hydraulic atomizing types and are selected on the basis of feed-rate requirements, droplet size, spray pattern, and droplet velocity. The nozzle assemblies are quickly and easily replaced as needed. The dispersion angle of the droplet stream does not exceed 90° .



The **Spray-Feeder Assembly** supplies liquid SiCl_4 into a high-temperature reactor designed to produce highly pure silicon for solar cells. A liquid rather than a gas supply is used because the liquid is less prone to contamination and because a more thorough reaction mixture is obtained by deeper-penetrating liquid spray and the vaporizing droplets.

The overall feeder assembly can be easily removed from the line for cleaning and repair. The specially-shaped narrow entry ports prevent excessive cooling of the reactor interior via nozzles that are in contact with the relatively-cool silicon feed.

This work was done by Thomas N. Meyer and Charles B. Wolf of Westinghouse Electric Corp. for **NASA's Jet Propulsion Laboratory.**

For further information, Circle 60 on the TSP Request Card.

This invention is owned by NASA, and a patent application has been filed. Inquiries concerning nonexclusive or exclusive license for its commercial development should be addressed to the Patent Counsel, NASA Resident Legal Office-JPL [see page A8]. Refer to NPO-14382.

A Reactor for More Efficient Solar Cells

An economical approach to production of highly pure silicon

NASA's Jet Propulsion Laboratory, Pasadena, California

A proposed reactor produces highly pure silicon at a relatively high temperature of 2,000 K. The advantage of the approach over conventional, lower temperature methods is that liquid silicon product is more easily separated from its gaseous coproducts. It is therefore possible that high production rates may be obtained in relatively-small reaction chambers, which could include means for separating coproducts and for collecting and casting the liquid silicon into ingots. The conventional processes for producing high-purity silicon are run at temperatures below 1,373 K. These are necessarily multistep due to greater difficulty in separating the liquid coproducts from silicon.

In the reactor a stream of vaporized alkali metal (e.g., sodium, magnesium, or zinc) and a high-temperature

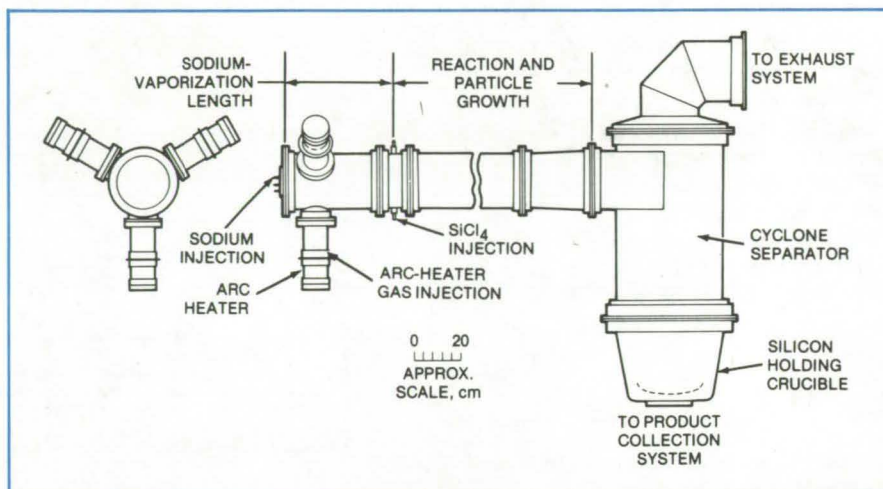


Figure 1. The **New Reactor** is designed for the production of highly pure silicon. The high-temperature process eases the separation between silicon and the coproducts. The products are separated in a cyclone separator. The coproduct gases are vented through the exhaust system, while pure liquid silicon is collected on the bottom.

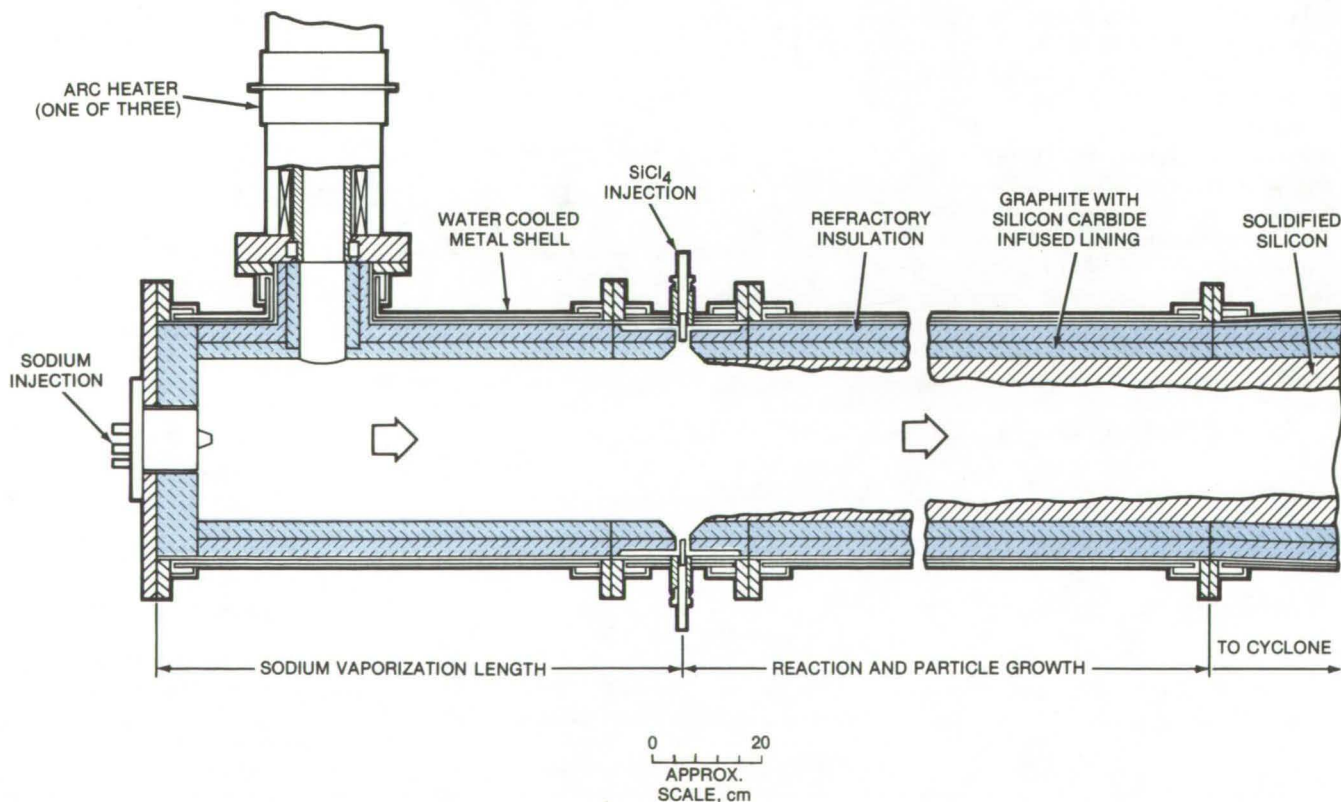
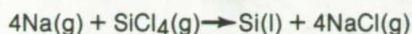


Figure 2. The **Inside Reactor Walls** are heavily insulated by using a refractory outer layer and infused or coated graphite. The heavy insulation limits product contamination.

carrier gas are mixed with a stream of atomized or vaporized silicon tetrachloride. The basic reaction in this process (assuming a sodium reactant) is



where g and l designate gaseous or liquid states. The byproduct salt and the carrier gas can be recycled after the pure silicon has been separated. This process is continuous.

The reactor assembly (see Figure 1) incorporates:

- Three radial arc heaters connected to a common plenum;
 - An upstream sodium injector;
 - A silicon tetrachloride spray-feeder [see the article "Silicon Tetrachloride Spray Feeder" (NPO-14382) on page 71 of this issue] injector assembly;
 - A reaction and particle growth chamber; and
 - A cyclone separator, silicon collector, and effluent withdrawal duct.
- All the components are water cooled by the annular cooling passages.

The interior (see Figure 2) walls of all the components except the arc heaters are lined with an internal layer of refractory insulation. The insulation is covered with graphite and a silicon carbide infused lining.

The three arc heaters connected to the plenum heat the transfer gas, such as a mixture of H_2 plus Ar, which is passed into the plenum at temperatures between 2,000 and 2,200 K. The plenum is about 17 in. (43 cm) in diameter and 40 in. (102 cm) long. The length is a critical design parameter, the 40-in. length being chosen so that all particles less than 100 μm in diameter are vaporized.

A sodium injector connected to the upstream end of the plenum has a sonic gas region to disperse liquid sodium droplets less than 100 μm in diameter. These droplets are completely vaporized when they are mixed with the high-temperature arc-heater gas. A separate temperature control keeps the sodium hot enough to remain a liquid.

The silicon tetrachloride is fed in through short, water-cooled tubes at the downstream end of the plenum.

Ten radially-directed hydraulic atomizing nozzles disperse the silicon tetrachloride droplets, which vaporize very rapidly in the hot gas stream.

The reaction rates of gaseous sodium and gaseous silicon tetrachloride are extremely rapid. Thus most of the reactor length is utilized for silicon-particle droplet growth, which takes place by diffusion and agglomeration and is enhanced by the turbulence of the gas stream. The actual length of the reaction zone may vary depending on mass flow rates. The proposed reactor uses two sections 3 ft (91 cm) long.

The product silicon is separated from its coproduct in a cylindrically-shaped cyclone separator. The cyclone collects all particles larger than 6 μm in diameter. A crucible bolted to the bottom of the cyclone collects the molten silicon, which is removed for subsequent processing.

This work was done by Maurice G. Fey, Thomas N. Meyer, and Charles B. Wolf of Westinghouse Electric Corp. for NASA's Jet Propulsion Laboratory. For further information, Circle 61 on the TSP Request Card. NPO-14381

Chemical-Vapor-Deposition Reactor

Improved reactor reduces nucleation and formation of solid reaction products and purging time between gases.

NASA's Jet Propulsion Laboratory, Pasadena, California

An improved chemical-vapor-deposition reactor utilizes multiple stacked sample trays compactly arranged in the path of horizontally-channeled reactant-gas streams. This efficient design more rapidly deposits a film on substrates and reduces gas and energy consumption. Because there are no dead spots to trap the reactive gases, the reactor may be purged quickly before another gas is introduced for multilayer film deposition.

Uniformly-spaced inlet quartz (Figure 1) slabs establish 1- to 3-mm laminar flow zones for gas entering the reactor. Arranged as an extension of the inlet slabs is a stack of substrate boats (sample holders) positioned in the central reactor zone. The boats are close to the spaced inlet slabs so that the gas-flow pattern is retained in the deposition zone. The central zone is heated by a conventional electrical or RF frequency heater. A single dust collector at the exit of the reactor traps residual reaction products.

The entire unit is housed in a cylindrical quartz tube designed for low-pressure evacuation. A removable cap and venting outlet facilitate removal of the sample boat and dust collector for cleaning.

An optional, rectangular quartz tube can be used as an internal housing surrounding the slab inlet zone and the central zone (substrate boats). This housing reduces the volume of the reaction gas necessary for film deposition, and thus saves on gas consumption.

(continued on next page)



The operating procedure is similar to that of a conventional reactor. Any appropriate reactive-gas mixture may be used, one example being organic silane 0.003 to 0.80 weight percent, oxygen 0.01 to 10 weight percent, and the balance nitrogen. Once the substrate trays are loaded inside (see Figure 2) the dust collector reinserted, and the chamber evacuated, the heaters are activated. When the temperature reaches a predetermined level (normally between 300° and 1,100° C), the reactive gas is admitted at a small positive pressure, the flow rate being monitored by gas flowmeters. The substrates are then exposed to the laminar gas flow for a designated time period.

In multilayer film deposition, the initial gas is shut off, the system is purged with inert gas, and a second gas is introduced. The process may be repeated to obtain the necessary multilayer configuration.

Only a relatively short deposition zone need be heated. This localization reduces energy consumption and the possibility of contamination from the reactor walls.

This work was done by Shy-Shiun Chern of Caltech for **NASA's Jet Propulsion Laboratory**. For further information, Circle 62 on the TSP Request Card.

Inquiries concerning rights for the commercial use of this invention should be addressed to the Patent Counsel, NASA Resident Legal Office-JPL [see page A8]. Refer to NPO-14137.

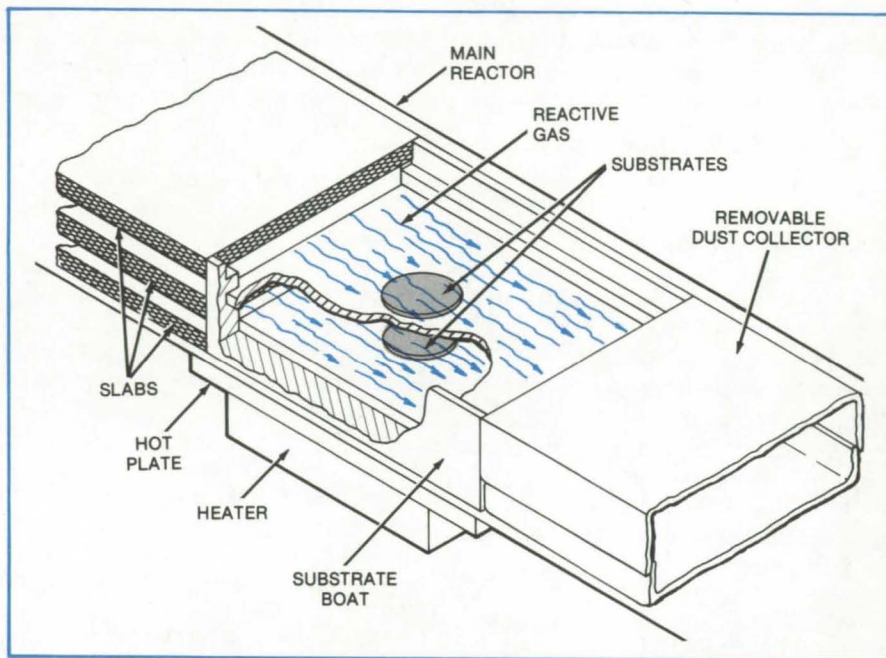


Figure 1. **Chemical-Vapor-Deposition Reactor** features horizontally-stacked quartz slabs that establish laminar flow zones for the incoming reactive gas. The result is reduced gas consumption and more rapid deposition. Power consumption is also reduced, due to shortened deposition zone.

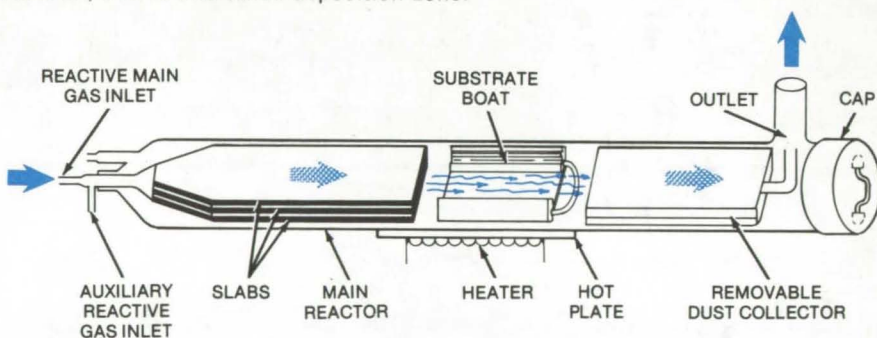


Figure 2. **The New Reactor** operates similarly to a conventional unit. Reactive gas is passed over the substrates for a designated period of time. This illustration shows the substrate boats in place with reactive gas flowing through the deposition zone.

Silicon Source for Vacuum Deposition

A source with two independent silicon filaments

Langley Research Center, Hampton, Virginia

A silicon source for ultra-high-vacuum deposition incorporates several improvements over conventional silicon sources. Two independent silicon filaments represent the major improvement. Not only is the deposition faster and more uniform upon

large substrates but p and n types of silicon may be deposited simultaneously. Another improvement is the water-cooled copper shield that also serves as mounting structure. The entire assembly may be constructed outside the vacuum system and in-

serted through a standard opening flange 2-3/4 in. (6.98 cm) in diameter. A complex power supply, generating high starting voltages and high currents, is unnecessary.

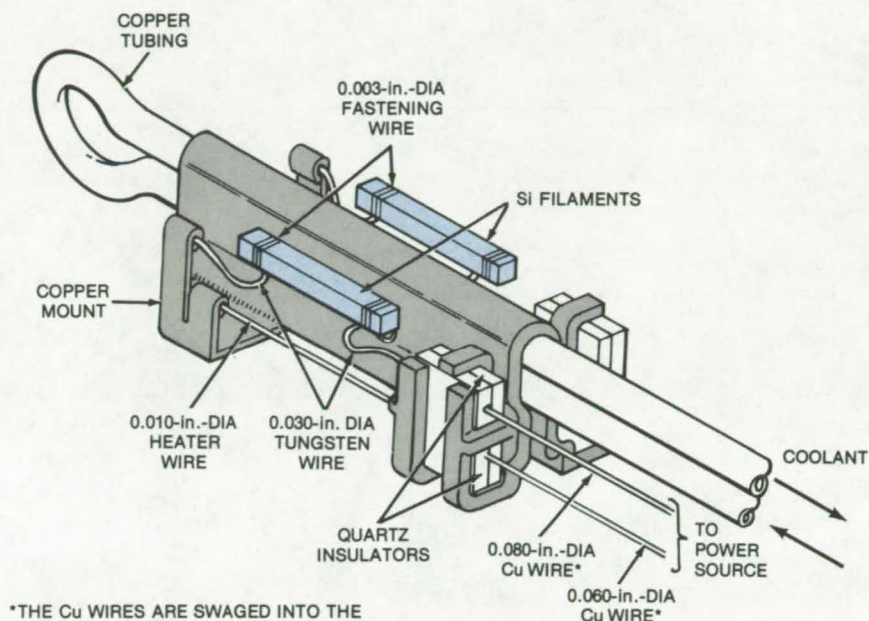
The silicon filaments (see figure) are 0.2 by 0.1 by 3 cm. A looped and

ground tungsten wire 0.030 in. (0.076 cm) in diameter serves as an electrical contact to the filament. It is laid on the silicon on both ends and wrapped tightly to it by means of a 0.003-in. (0.0076-cm) tungsten wire held in tension. A tungsten heater wire 0.01 in. (0.025 cm) in diameter is parallel with the silicon and about 0.32 cm away from it.

The copper mount/cooling assembly is used as an electrical contact common to all the tungsten and silicon filaments. The electrical leads at the other end of the filaments are retained by quartz insulating blocks, the blocks being held by fingers extending from the copper shield.

Initially, a current of 6 to 7 A is applied through the tungsten filament while a 1-A current at 20 V is applied across the silicon filament. After a minute or two, as the silicon heats up, the voltage across it drops, and the tungsten is turned off. The silicon runs at a current of about 15 A, at a voltage of 12 V, during the deposition process.

Tests have shown that the new source deposits evaporated silicon onto a substrate 1 cm away at a rate of 2 $\mu\text{m}/\text{h}$. The pressure during the evaporation process ranges between 1.5×10^{-10} to 3.5×10^{-10} torr.



An Improved Silicon Source for ultra-high-vacuum evaporation uses two independent silicon filaments. Silicon is deposited faster and more uniformly on substrates, and p and n types of silicon may be deposited simultaneously. An efficient water-cooled copper shield supports and cools the structure and isolates the two filaments.

This work was done by G. W. Racette and D. J. Rutecki of General Electric Co. for Langley Research

Center. For further information, Circle 63 on the TSP Request Card. LAR-12356

Low-Absorptance Porcelain-on-Aluminum Coating

A solar absorptance of 0.22 is obtained for a porcelain thermal-control coating.

Marshall Space Flight Center, Alabama

A new porcelain coating for aluminum sheet and foil has a low solar absorptance. Although the coating is specially formulated, it is applied by standard commercial methods. Originally developed to keep space satellites from overheating under the intense rays of the Sun, the coating has an absorptance of only 0.22, substantially less than the 0.31 absorptance of commercial porcelain-enameled aluminum. Moreover, its absorptance is stable, changing only by 0.03 after 1,000 hours of exposure to simulated Sunlight.

The porcelain resists hostile environments on Earth as well as in space: It is unaffected by high humidity; coated

panels at 542° C can be plunged into water at 21° C with no adverse effects; and the porcelain can be cleaned with ordinary solvents.

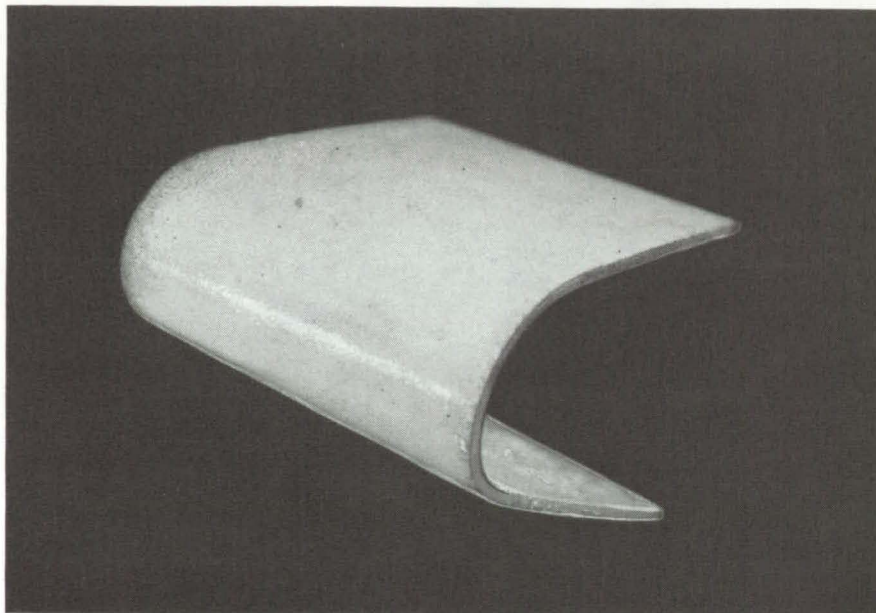
The low absorptance at solar-radiation wavelengths between 0.28 and 2.5 micrometers is obtained by combining pigment particles having a high index of refraction with a glass "host" medium having a low index of refraction; the volume of the host is large in comparison to that of the pigment.

A mixture of two ground-glass frits is the starting material. One frit, which later becomes the host, consists primarily of oxides of sodium, lithium, and silicon (but no titanium). The other frit contains dissolved titania (TiO_2), which later precipitates as a white pigment.

A small amount of free titania is added to the mixture to encourage pigmentation. The amount is small compared to that used in commercial processes, which yield a relatively high-absorptance porcelain.

The mixture is applied to the aluminum and fired at 538° C for 210 to 360 seconds. The shorter firing time results in a lower absorptance value because less pigment dissolves in the host glass. However, the firing time must be long enough to encapsulate completely the pigment particles in the host; otherwise, the absorptance will increase during long solar exposures. The constituents and their proportions in the porcelain formulation can be

(continued on next page)



A **Low-Absorptance Porcelain Coating** adheres to a sheet of aluminum alloy even when the sheet is turned around a 180° bend. The aluminum sheet thickness is 1.0 millimeter (magnified 2.3X); the coating is 0.13 mm in thickness.

varied to obtain the required frit solubility, viscosity, and thermal index of expansion. The properties of various compositions studied during the development of the low-absorptance coating may be obtained by requesting the Technical Support Package referenced at the end of the article.

The low-absorptance porcelain adheres well on types 6061, 6062, and 6063 aluminum alloys (see figure). Postporcelainization heat treatments, such as quenching and aging to produce maximum alloy strength, do not harm the coating.

This work was done by Hyman Leggett of Hughes Aircraft Co. for **Marshall Space Flight Center**. For further information, Circle 64 on the TSP Request Card.

Inquiries concerning rights for the commercial use of this invention should be addressed to the Patent Counsel, Marshall Space Flight Center [see page A8]. Refer to MFS-23879.

Burning Crude Oil Without Pollution

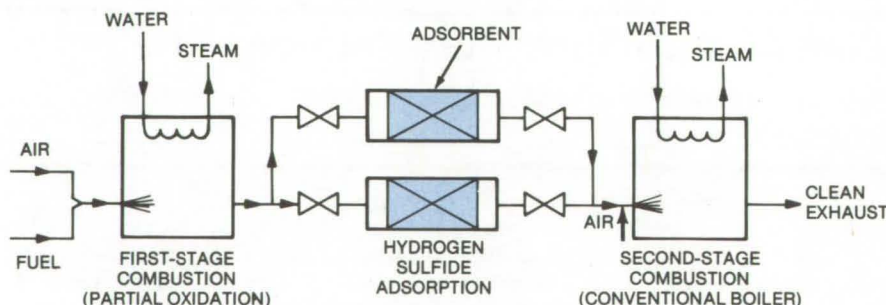
Steam for secondary oil recovery can be generated at the well without violating clean-air standards.

NASA's Jet Propulsion Laboratory, Pasadena, California

Crude oil can be burned at drilling sites by a new two-stage combustion process without producing pollution. The new process makes it possible for oil drillers to conform to increasingly strict federal and state clean-air standards without installing costly equipment for removing sulfur dioxide from flue gases or transporting refined oil to the site.

Secondary recovery of oil is thus more economical with the new process. The oil remaining in a well after conventional oil removal can be obtained by injecting steam — generated by burning on-site crude oil — into the well.

The new process removes sulfur from the crude oil before it is converted to corrosive sulfur dioxide. In the first stage of the process, the dewatered crude oil is partially oxidized at a high fuel-to-air ratio — about 10 or 11 to 1, by weight. This first-stage combustion is carried out at a relatively low temperature, the precise value depending on the



In the **Two-Stage Combustion of Crude Oil**, with hydrogen sulfide removal between stages, the first stage converts sulfur content to hydrogen sulfide, which can be removed easily and economically by metal oxide adsorbents. The adsorption process yields clean fuel for the second combustion stage. The metal sulfides formed in the adsorbent can be regenerated to metal oxides by heat.

characteristics of the petroleum. Virtually all the sulfur in the fuel reacts with hydrogen to form hydrogen sulfide.

The exhaust from the first combustion stage is completely converted to a low-Btu gas. This exhaust is passed through a "scrubber" containing inexpensive metal oxides with a high

affinity for hydrogen sulfide: lime (calcium oxide), iron oxide, or zinc oxide, for example (see figure). The oxides adsorb the hydrogen sulfide in the first-stage exhaust, producing a "clean" fuel composed primarily of methane, hydrogen, and carbon monoxide.

This clean fuel is burned in the second stage and yields water and carbon dioxide as the combustion products, but no sulfur oxides.

In both combustion stages, the flame temperature stays below

2,700° F (1,500° C), the temperature at which nitrogen oxides form. Thus atmospheric nitrogen is not converted to pollutants.

This work was done by John Houseman of Caltech for NASA's Jet

Propulsion Laboratory. For further information, Circle 65 on the TSP Request Card.
NPO-14344

Continuous Sterilization of Plumbing Systems

An ETO/Freon 12 humidifier allows online disinfection of plumbing.

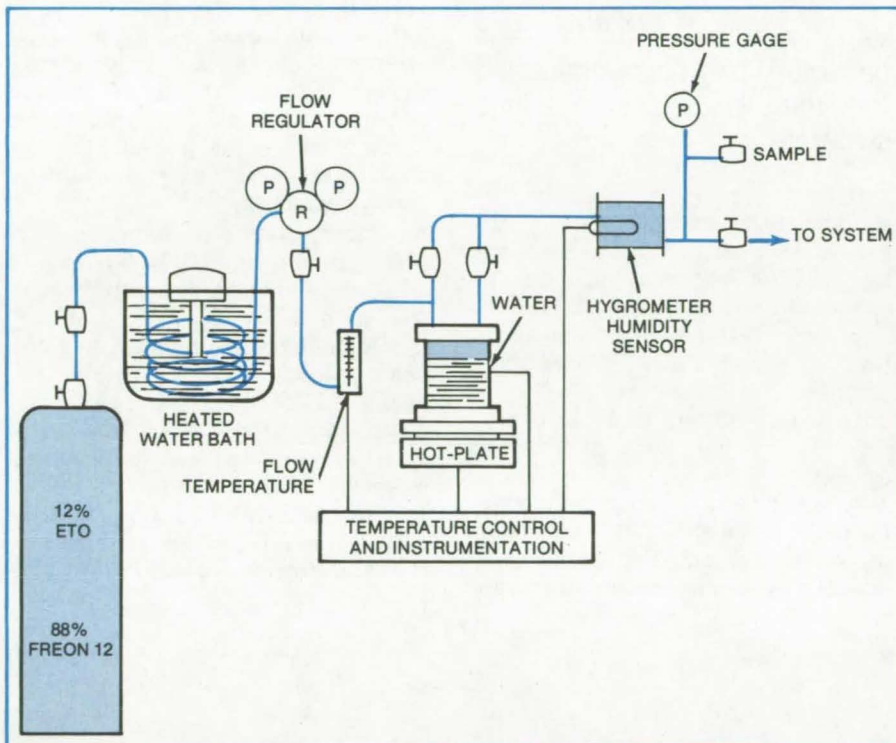
John F. Kennedy Space Center, Florida

The continuous sterilization of plumbing, such as in hospitals, clinics, and biological testing laboratories, is possible with an ethylene oxide/Freon 12 (ETO/F-12) humidifier, originally developed to sterilize potable water systems aboard the Space Shuttle. To be an effective sterilant, the gas mixture must be humidified to between 40 and 80 percent relative humidity. Previously, ethylene oxide has been used mainly for batch sterilization, in which objects are disinfected in an autoclave. However, this is not practical when the continuous disinfection of larger systems is required.

Two methods for humidifying ETO/F-12 were investigated during development of a prototype system. The first approach, bubbling the gas through water, was abandoned after it was discovered that the humidity of the product stream could not be accurately controlled.

In the second, successful approach, ETO gas is passed over the water surface. The relative humidity of the sterilant can be precisely adjusted by varying the temperature (and hence the vapor pressure) of the water. Distilled or deionized water was used in the humidifier to minimize hydrolysis of the ETO.

As shown in the figure, ETO/F-12 liquid from a storage cylinder is first passed through a copper coil immersed in a water bath at 95° F (35° C), to vaporize the mixture. After flowing through a pressure regulator and a flowmeter, the gas is injected into the humidifier, parallel to the water surface. The inlet flow nozzle is configured to inject the gas with a swirling action so that it does not impinge directly on the stainless-steel container wall. From the humidifier,



This **Prototype Ethylene Oxide/Freon 12 Humidifier** can be attached to a plumbing system (such as for potable water) for online sterilization of the plumbing.

the gas flows through a hygrometer humidity sensor (optional) and into the system to be sterilized.

In laboratory studies, the gas was injected at flow rates between 0.2 and 1.0 stdft³/min (0.005 and 0.03 stdm³/min) at pressures of 20, 22.5, and 25 psig (0.13×10⁶, 0.15×10⁶, and 0.17×10⁶ N/m²). Satisfactory humidity readings were obtained at all flow rates and pressures with the humidifier water temperature at 105° or 110° F (41° or 43° C).

Various scrubber solutions for removing ETO from a gas stream were also studied. A three-stage scrubber

containing 0.1M H₂SO₄ at a pressure approximately 2 psig (0.01×10⁶ N/m²) lower than the pressure of the incoming gas effectively removes ETO for a 1-hour flow time at 0.2 stdft³/min and 20 psig. Gas chromatographic analysis of the scrubber effluent gas showed the ETO concentration to be below the 100-ppm detection limit.

This work was done by Coleman J. Bryan, Clyde V. Moyers, and Edward E. Wright, Jr., of Kennedy Space Center. For further information, Circle 66 on the TSP Request Card.
KSC-11085

Books and Reports

These reports, studies, and handbooks are available from NASA as Technical Support Packages (TSP's) when a Request Card number is cited; otherwise they are available from one of NASA's Industrial Application Centers or the National Technical Information Service.

Controlled Metal-Film Deposition on Alumina Substrates

Vapor growth of small iron and palladium particles on alumina for the study of catalytic systems

Refractory oxides such as magnesia, spinels, and alumina (Al_2O_3) are extensively used in thin-film electronics (i.e., for silicon-on-sapphire devices) and in the chemical industry as support materials for metal catalysts. The preparation of well-characterized particulate metal deposits on these substrates is a basic prerequisite for the study of catalytic systems.

A recent investigation of the preparation, nucleation, and controlled growth of particulate deposits (palladium and iron) on electron-transpar-

ent alumina substrates is presented in a new report. The results indicate that characteristic properties of the metal deposits (such as particle density, size distribution, and orientation) are strongly dependent on the cleanliness, phase, and crystallographic orientation of the alumina substrate. Thus, the study concludes, these properties may be reproducibly controlled by adjusting the substrate characteristics and vapor-deposition conditions.

In the studies, amorphous alumina substrate films were installed in a transmission electron microscope equipped with a special ultrahigh-vacuum specimen chamber. The substrate temperature, the metal vapor flux, and the residual gas environment could be regulated within the chamber during deposition.

Clean crystalline alumina surfaces were prepared in situ by high-temperature annealing of the amorphous films. The surface crystallinity and phase were determined by the maximum annealing temperature (T_a). For example, a T_a of 950°C resulted in fine-polycrystalline $\eta\text{-Al}_2\text{O}_3$. At $T_a \approx 1,100^\circ\text{C}$, a phase transformation to $\delta\text{-Al}_2\text{O}_3$ occurs, and at $T_a \approx 1,200^\circ\text{C}$, very coarse-crystalline $\delta\text{-Al}_2\text{O}_3$ consisting of nearly perfect large single-crystal regions is created. Stereo and

replica electron microscopy were used to check the morphology of the substrate films.

The metal-vapor deposition followed heat treatment of the alumina within minutes after the desired substrate temperature was established. Different substrate temperatures, in conjunction with a constant flux of 1 to 2 A/min, determined the degree of supersaturation during the deposition. Background pressure was in the mid 10^{-9} -torr range (although background pressures an order of magnitude higher did not substantially influence the results).

The report contains a thorough discussion of the effects of substrate morphology on the properties of the vapor deposits. It was found, for example, that when higher substrate-annealing temperatures were used (giving a coarse, more perfect crystalline phase), the palladium metal deposit was more uniform. Also, significant epitaxial trends that are of interest in catalytic applications were observed in the Fe/alumina system.

This work was done by Eal H. Lee, R. Dale Moorhead, and Helmet Poppa of Ames Research Center. To obtain a copy of the report, Circle 67 on the TSP Request Card.
ARC-11214

Life Sciences



Hardware, Techniques, and Processes

- 81 High-Resolution Echocardiography
- 82 Microcomputer Helps Evaluate Skin Burns
- 83 Artificial Limb Connector
- 84 Eye-Controlled Switch

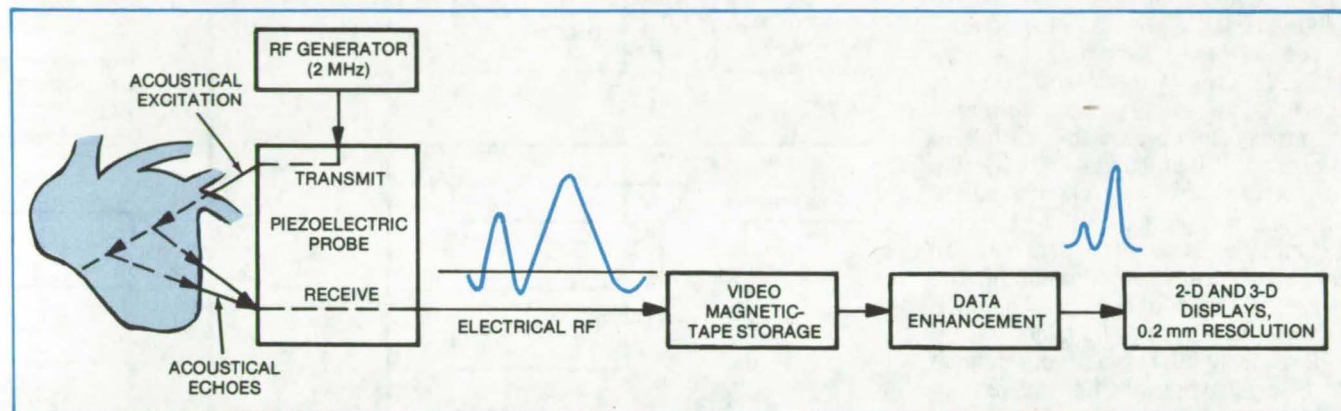
Books and Reports

- 85 Identification of Micro-organisms

High-Resolution Echocardiography

Computer processing of ultrasonic signals enhances 2-D or 3-D heart-image resolution by a factor of 10.

NASA's Jet Propulsion Laboratory, Pasadena, California



Images of the Heart that are constructed by a computerized data-enhancement system avoid rectification and filtration of echo signals and thus retain the fine details of heart structure. Data-enhancement systems of the future will use charge-coupled devices (CDD's) in place of the magnetic-tape storage, to speed up data processing.

Ultrasonic echoes reflected from the heart can be analyzed by a computer to resolve details as small as 0.2 millimeter. It is thus possible to determine whether small blood vessels around the heart are blocked — an impossible task with conventional echocardiography systems, which are limited to 2-millimeter resolution.

The new high-resolution computer-aided ultrasound system, unlike X-ray systems, does not expose the patient to harmful radiation and is noninvasive, requiring no injection of dyes into the heart arteries by catheters.

The new system provides two- and three-dimensional images of the beating heart from many angles. It is thus possible to observe whether the heart wall is moving normally and to diagnose such conditions as myocardial infarct and ischemia (manifested by dead muscle tissue and noncontracting muscle tissue, respectively). Changes in volume, mass, and shape can be seen.

Any of a variety of commercial ultrasound generating and transducing equipment can be used in the system, in combination with computer programs for data enhancement like

those used for communications, radar, sonar, and seismic data reduction.

In typical ultrasound equipment, piezoelectric crystal transducers — which convert radio-frequency electrical energy to acoustic waves — are contained in a probe that is aimed at the heart. In some equipment, the ultrasound is transmitted and the reflections from the heart are received on the same transducers. In other equipment, the signal is transmitted by one transducer and received by another.

In conventional echocardiography systems, the received signal is rectified and subjected to severe low-pass filtering. In the process, two or more closely spaced echoes can be combined so that they appear as a single pulse (see figure) — hence details of the heart structure are lost.

In the new system, however, the received signal in its raw, unrectified, unfiltered form is recorded on magnetic video tape. These data are processed by computer and restructured into a series of sharp pulses instead of a string of merging, undelineated waves.

Echoes are collected from a variety of viewing angles. For example, the probe is pointed toward the heart from the diaphragm area under the bottom rib and from various locations between the ribs. The results are synthesized into a single image that is displayed on a graphical printout or a TV tube. The two- or three-dimensional reconstruction sharpens the features of the image and removes "ghosts."

In its present form, the system requires a considerable amount of time to produce an image. Almost instantaneous, real-time observations can be made if an array of charge-coupled devices (CCD's) is substituted for the magnetic tape. The CCD's can preprocess the data at high speed and feed a microprocessor. Logic circuitry to perform a similar function has already been developed for synthetic aperture radar.

This work was done by Robert Nathan of Caltech for NASA's Jet Propulsion Laboratory. For further information, Circle 68 on the TSP Request Card.
NPO-14349



Microcomputer Helps Evaluate Skin Burns

Microcomputer analysis of the reflectances of skin tissue can help diagnose severe burns.

NASA's Jet Propulsion Laboratory, Pasadena, California

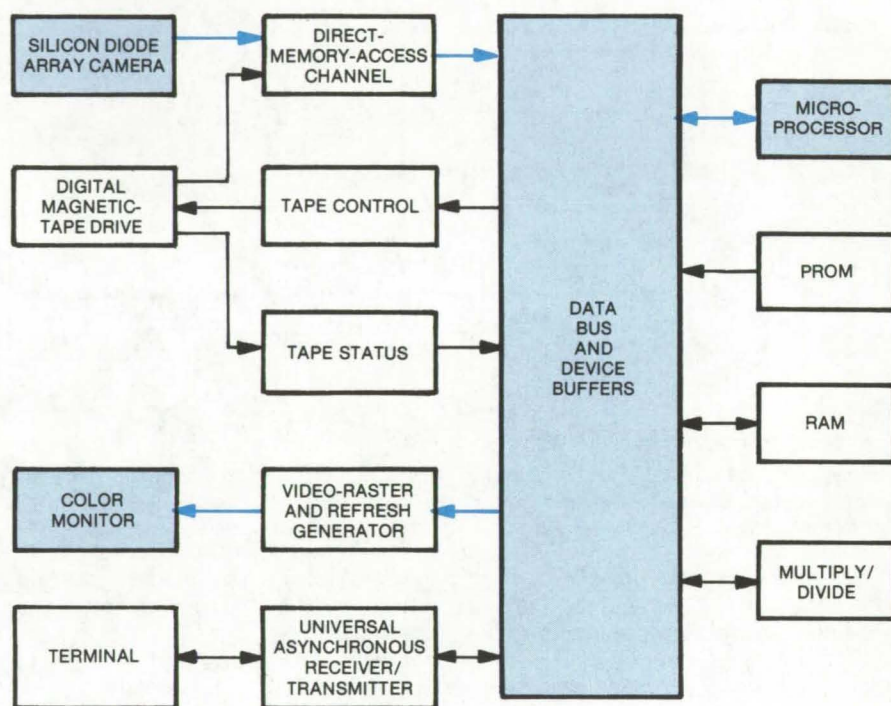
The speeded-up analysis of burns, made possible by a new microprocessor-based system, makes more effective clinical treatment possible. Multispectral imaging of the burn area is rapidly interpreted by a microprocessor that produces a display map of full- and partial-thickness burns. This information allows the physician to remove the exact thickness of burned skin early in the treatment. The result is reduced risks of infection, scarring, and loss-of-function.

Previously it has been very difficult to distinguish between full- and partial-skin-thickness burns. The physician's personal experience may be the only guide, and the actual extent of the burn may reveal itself only weeks after treatment. The removal of too little tissue delays healing, but excising too much tissue eliminates healthy skin that is needed to repair the damage.

Infrared and visible-wavelength photography (particularly in the red and green bands) has been useful in the diagnosis of skin-burn depth. All three frequency bands show characteristic reflectances from viable and damaged skin. Each characteristic varies independently with the degree of the burn and the progress of healing.

In the new system (see figure), television diode array sensors (each with a spectral filter covering the frequency band of interest) measure the reflectances in the red, green, and infrared from the burned area. This forms three separate images of the area in 64 shades of gray.

The images are then processed by the computer to form new images representing the ratios of the optical densities in the three spectral bands.



Microprocessor-Controlled Burn Analyzer interprets reflectance data (as gathered by the camera) to generate color-coded video images that show the variations in burn depth over the affected area. Reflectances are measured in the infrared, red, and green frequency bands.

From previous and continuing experiments, it is known that these differences can be correlated with burn depth. The new images are color-coded in the primary colors and are combined on a video monitor for direct observation. In this scheme, a deep, full-thickness injury appears yellow or white, a shallow, full-thickness injury shows up reddish, and areas with a partial-thickness burn show blue. By using other light wavelengths in the analysis, the system may also find

uses in the evaluation of skin disorders, including cancer.

This work was done by Victor J. Anselmo and Terrence H. Reilly of Caltech for **NASA's Jet Propulsion Laboratory**. For further information, Circle 69 on the TSP Request Card.

Inquiries concerning rights for the commercial use of this invention should be addressed to the Patent Counsel, NASA Resident Legal Office-JPL [see page A8]. Refer to NPO-14402.

Artificial Limb Connector

Flexible shaft improves seal of skin around the percutaneous sleeve used with bone-fixation prosthetic connector.

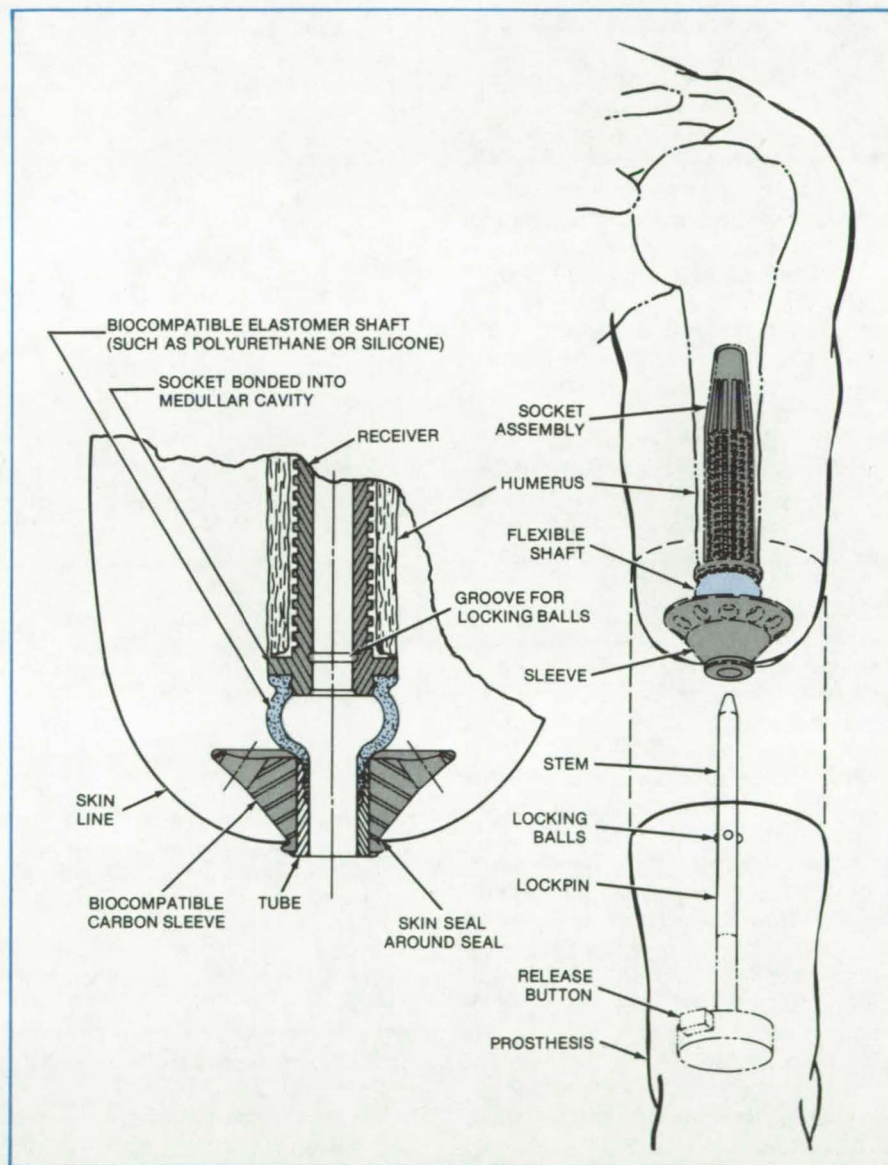
John F. Kennedy Space Center, Florida

Recently, prostheses have become much more sophisticated, incorporating electronic equipment and servomotors to produce more-natural limb movement. The latest technology has also been utilized to improve on the connector for attaching the artificial limbs to amputees' stumps.

In cooperation with NASA, the Rancho Los Amigos Hospital of Downey, California, has been active in developing various prosthetic improvements. One of such improvements resulted in the prosthesis being quickly connected and disconnected to the bone within the amputees' stump. [See NASA Tech Brief B74-10183 (KSC-10833) for details.] This original bone-fixation connector had a percutaneous sleeve rigidly attached to a bone-implanted receiver, which received a ball lockpin or stem for attaching the prosthesis to the stump. This arrangement, however, restricted the movement of the stump skin in relation to the bone within the stump.

A new flexible connector (see figure) gives the skin the freedom needed to self-adjust to promote the healing of the flesh and to relieve skin stresses while maintaining a skin seal surrounding the implanted percutaneous sleeve. This connector comprises a flexible bellows or hollow shaft made of biocompatible silicone or similar material. The flexible shaft has one end attached to the bone-implanted receiver and the other end attached to the percutaneous sleeve.

After surgically implanting the socket assembly (receiver, flexible shaft, and percutaneous sleeve) in the amputee's stump, the skin will seal itself around the high-purity-carbon percutaneous sleeve. With the ball lockpin on the prosthesis extended through the percutaneous sleeve and inserted in the bone-implanted receiver, the flexible shaft will allow the sleeve to move or float with the skin relative to the receiver and bone without breaking between the skin and the sleeve.



An Artificial Arm [or Leg] is secured to an implanted receiver by a lock pin. The flexible shaft accommodates changes in stump shape without disturbing the skin seal around the sleeve.

This improved artificial limb connector is applicable to either an arm or a leg prosthesis.

This work was done by Charles W. Bright and Lester J. Owens of Kennedy Space Center and Vert Mooney and James B. Reswick of Rancho Los Amigos Hospital. For further information, Circle 70 on the

TSP Request Card.

This invention is owned by NASA, and a patent application has been filed. Inquiries concerning nonexclusive or exclusive license for its commercial development should be addressed to the Patent Counsel, Kennedy Space Center [see page A8]. Refer to KSC-11069.

Eye-Controlled Switch

Eye movements start and stop an electric wheelchair, direct it forward and backward, and steer it.

Marshall Space Flight Center, Alabama

A new eye-motion sensor and an electronic circuit allow an electric wheelchair to be controlled by eye movements alone. The user moves his or her eyes to the upper left corner to start or stop the wheelchair and to the upper right to turn the chair to the left or right. Originally developed for astronauts as a means of controlling a spacecraft during the high-g forces of a launch, the device could be adapted to allow handicapped people to use eye movement to dial telephones, turn pages, and control appliances.

A small lamp in the sensor directs a low-intensity beam at the eye, and a photocell adjacent to the lamp catches the reflected beam. One lamp/photocell combination is mounted on each earpiece of a standard eyeglass frame (see Figure 1) so that the beams are directed at the upper outside eyelid areas when the wearer is looking straight ahead. If the sensor is aimed properly, the user can blink or look ahead, upward, to the right, or to the left without affecting the control circuit. Since the white of the eye (the sclera) has about the same reflectance as the eyelid, it will not change the sensor output if it is illuminated by the lamp. If, however, the wearer intentionally directs the eyes to the upper right or left, so that an iris intersects one of the beams, the light reflected to the corresponding photocell is reduced (since the iris has lower reflectance than either the sclera or the eyelid), and the change in photocell current actuates a switch. The lamps and photocells are connected by braided wires to a control box (Figure 2) on the battery-powered wheelchair.

The left eye controls the forward and reverse motions of the wheelchair according to a forward/off/reverse/off cycle. The user looks to the upper left to turn the wheelchair motor on in the forward direction; the next glance

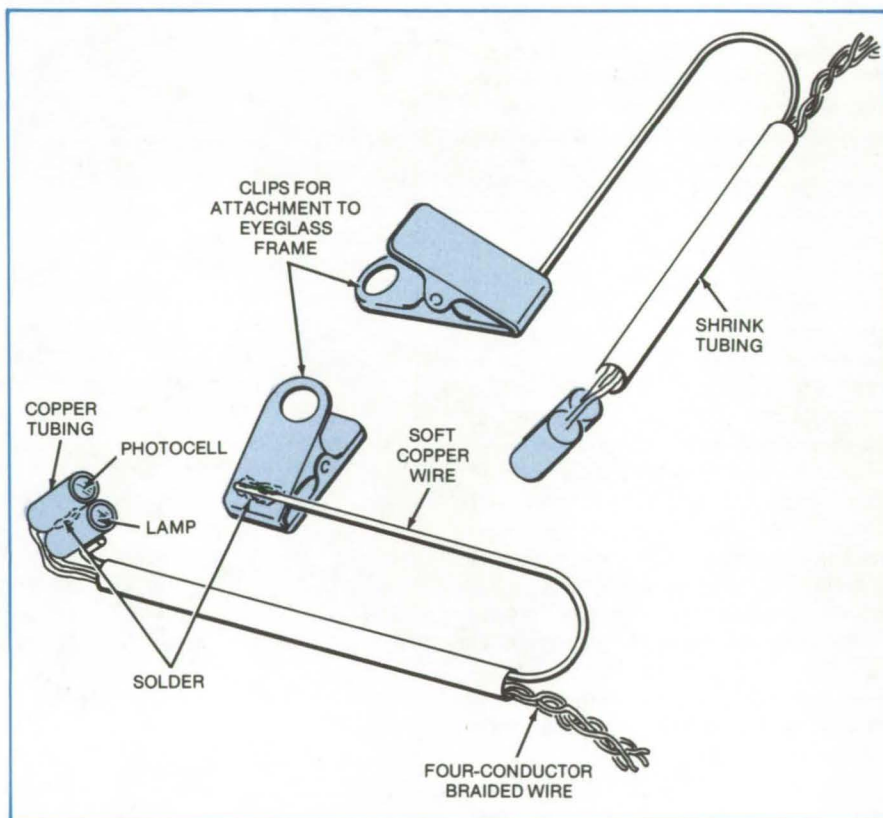


Figure 1. These **Eye-Movement Sensors** for wheelchair control are clipped to standard eyeglass frames. Each lamp/photocell combination is aimed at the upper outside corner of one of the user's eyes. The control circuit sensitivity is adjusted for the reflectivity of the user's eyes.

at the upper left turns the motor off; another glance reverses the motor; and a fourth glance turns it off again. Additional eye movements repeat the cycle.

The circuit can be set for forward-only movement if the user so wishes. If the left photocell is activated to forward and then to stop in rapid succession, the circuit will bypass the reverse/stop portion of the cycle.

The right eye steers the wheelchair. A glance at the sensor at the upper right turns the chair to the right and another glance turns it to the left. Unlike the forward/reverse circuit,

however, the left/right electronics are nonlatching. The steering wheels revert to straight-ahead motion as soon as the user stops looking at the sensor. The wheels can be turned even when the wheelchair drive motor is off; thus the chair can be jogged into tight spaces.

For safety, the control circuit requires that the user give a control command at periodic intervals with either the left or the right eye. Thus, if the user becomes unconscious or the circuit malfunctions, the wheelchair will stop automatically after an interval adjustable from 3 to 15 seconds.



Figure 2. The **Control Box** houses the logic that operates the wheelchair drive motors. Controls for gain adjustment and setting of the delay time are located on the top and side panels, respectively.

This work was done by G. L. Walker and B. G. Weaver of Hayes International Corp. for **Marshall Space Flight Center**. For further information, Circle 71 on the TSP Request Card.
MFS-25091

Books and Reports

These reports, studies, and handbooks are available from NASA as Technical Support Packages (TSP's) when a Request Card number is cited; otherwise they are available from one of NASA's Industrial Application Centers or the National Technical Information Service.

Identification of Micro-organisms

A comprehensive manual of standardized laboratory procedures

A 170-page manual presents detailed laboratory procedures for conducting microbiological and immunological evaluations of samples taken from human subjects. Developed as an outgrowth of preflight and postflight

microbiological analyses of spaceflight crewmen, the standardized procedures should be useful to researchers and clinicians in laboratories, hospitals, and other biological test facilities. Included in the manual are procedures for identifying aerobic and microaerophilic bacteria, yeast and yeastlike organisms, and filamentous fungi.

Both United States and Soviet scientists contributed to the development of the procedures and to the compilation of the manual. The two countries have been actively pursuing research in this area since the beginning of their manned spaceflight programs. Prior to the joint Apollo/Soyuz flight in the summer of 1975, the U.S. and U.S.S.R. agreed to conduct a cooperative biological experiment using samples collected from the cosmonauts, astronauts, and areas of the Apollo and Soyuz spacecraft. Standardized procedures were

developed to correlate test results obtained by scientists in both countries and to enable comparison of the results with those obtained in earlier spaceflights.

The manual includes materials lists, instructions for identification tests, expected test reactions, and charts for correlating the test results with expected results involving particular micro-organisms. The 14 major chapters are:

1. Introduction and General Identification Schema
2. Identification of Gram-Positive Cocci
3. Identification of Gram-Negative Cocci
4. Identification of Spore-Forming Gram-Positive Rods
5. Identification of Non-Spore-Forming Gram-Positive Rods
6. Identification of Lactose-Positive Gram-Negative Rods

(continued on next page)



7. Identification of Lactose-Negative Gram-Negative Rods
8. Identification of Yeast and Yeast-like Organisms
9. Identification of Filamentous Fungi
10. Bacteriophage Typing of *Staphylococcus aureus*
11. *Staphylococcus* Sensitivity to Antibiotics
12. Immunological Studies With Blood
13. Immunological and Biochemical Studies With Salivary Parotid Fluid
14. List and Formulas for Nutrient Media and Reagents

Chapter 2, on the identification of gram-positive cocci, lists 18 reagents and culture media (such items as heart-infusion agar, rabbit plasma, and ammonia are needed). A branching flow diagram illustrates the sequence of tests to be followed according to the reactions of the unknown cocci.

In this scheme, the first test is to inoculate heart-infusion agar with the test sample. If this culture produces the enzyme catalase, the sample is subjected to a prescribed sequence of tests (e.g., glucose decomposition and the determination of coagulase and phosphatase); if the culture produces no catalase, it is given a different series of tests (e.g., bile resistance and ring precipitation.) The flow diagram thus represents a process of elimination by which the unknown can be identified as pneumococci, monococci, or any of a variety of species of *Staphylococcus* or *Streptococcus*. Step-by-step instructions for each test are given.

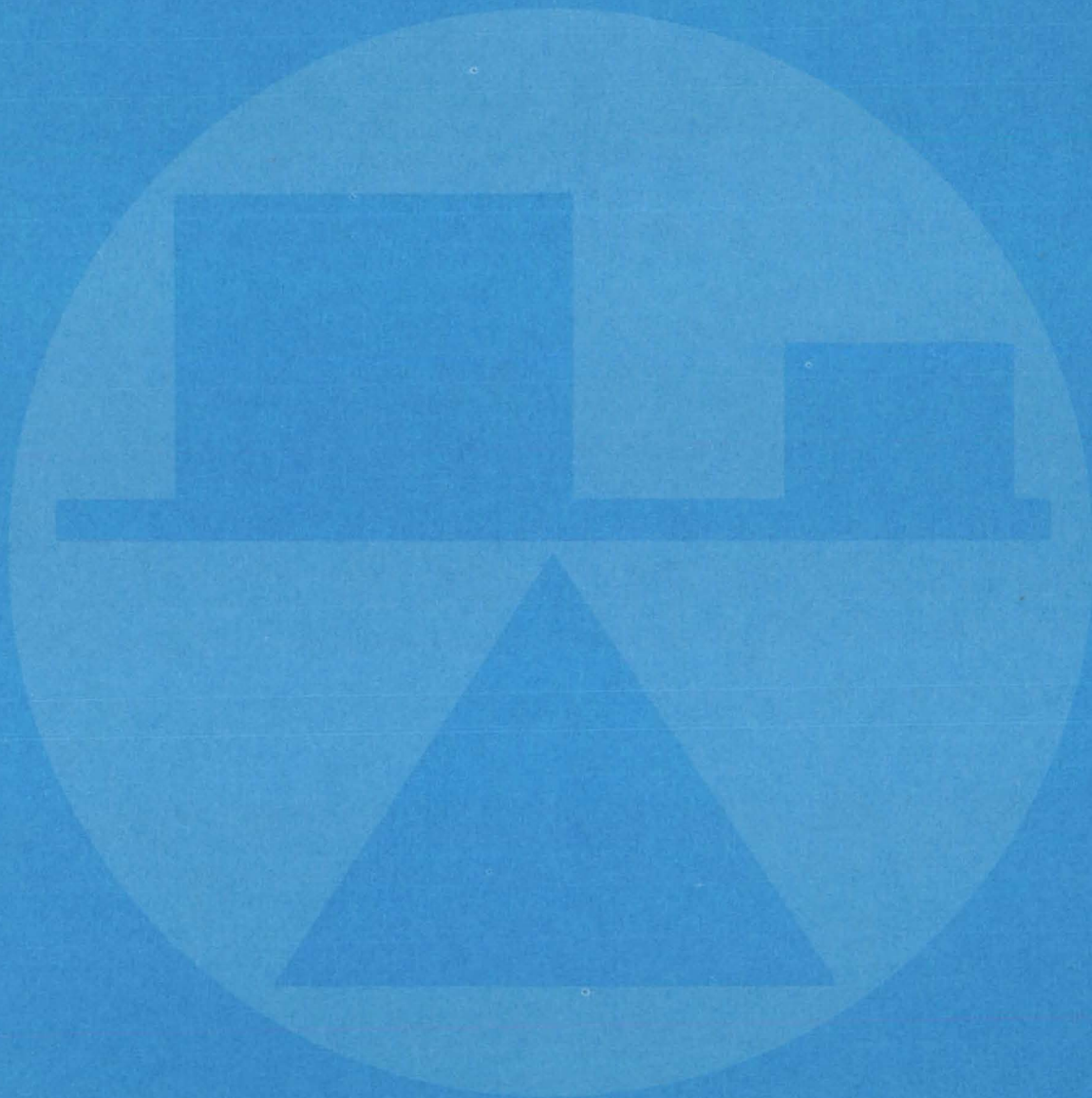
Chapter 10 describes methods for typing *Staphylococcus aureus*, using bacteriophages. Methods for measuring the sensitivity to antibiotics of isolated *Staphylococcus* strains, described in Chapter 11, were used to measure changes in sensitivity after space flights.

Chapters 12 and 13, covering procedures for immunological and biochemical studies of the blood and saliva of crewmembers, present methods for assessing the effects of microbes on astronauts and cosmonauts during space missions by tests made before and after a flight.

The last chapter gives standardized "recipes" for 89 culture media and 36 reagents. When a specific material is required, a source is specified in the test procedure.

This manual was edited by Gerald R. Taylor of Johnson Space Center and S. N. Zaloguev of the U.S.S.R. Ministry of Health. It is identified as NASA TM-58185 [N78-29725], "Methods for Microbiological and Immunological Studies of Space Flight Crews" [\$9.00]. A copy may be purchased [prepayment required] from the National Technical Information Service, Springfield, Virginia 22151.
MSC-18358

Mechanics



Hardware, Techniques, and Processes

- 89 Containerless High-Temperature Calorimeter
- 90 Obtaining an Electrical Output From a Mechanical Flowmeter
- 91 Differential Oil Flow Meter
- 92 Bidirectional Fluid-Flow Monitor
- 92 Electrical Indication of Airflow Rate
- 93 Nondestructive Pull Tester
- 94 Push Test for Stitch Welds
- 95 Checking Weld Penetration
- 95 Ultrasonic Grating Checks Electron-Beam Welds
- 96 Accurate Measurements of Mass and Center of Mass
- 98 Measuring Resistance or Conductance of Insulators
- 99 Laser Alinement of Large Assemblies
- 100 Measuring the Thickness of Plastic Films
- 100 Troubleshooting Plated-Wire Memories
- 102 Determination of Total Surface Reflectivity
- 103 Characterizing Glass Frits for Slurries
- 103 Test-Configuration Identifiers
- 104 Antitheft Container for Instruments
- 105 Extending the Range of Leak Detectors
- 106 Attaching Strain Transducers to Fragile Materials
- 106 Audible Monitor for Electroplating
- 107 Inspecting Cracks in Foam Insulation
- 108 Measuring Insulation Thickness
- 109 Burn-Test Apparatus for Fiber Composites

Books and Reports

- 110 Measuring Moisture in the Atmosphere
- 110 Friction Coefficients of PTFE Bearing Liner

Computer Programs

- 110 Aircraft Mission Analysis
- 111 Dynamic Simulation and Stability Analysis
- 112 Goddard Trajectory Determination
- 113 Minicomputer Version of SPAR
- 113 Hinge-Connected Rigid Bodies
- 114 Centroids, Moments, and Radii of Gyration

Containerless High-Temperature Calorimeter

Samples are heated by electron bombardment in a calorimeter that measures many high-temperature properties.

Marshall Space Flight Center, Alabama

In a new high-temperature calorimeter constructed at Marshall Space Flight Center, contamination to samples is kept to a minimum by suspending them from a wire in a vacuum chamber. The calorimeter can help to determine the phase diagrams and other properties of reactive metals and alloys, including materials containing the transition elements or rare-earth elements.

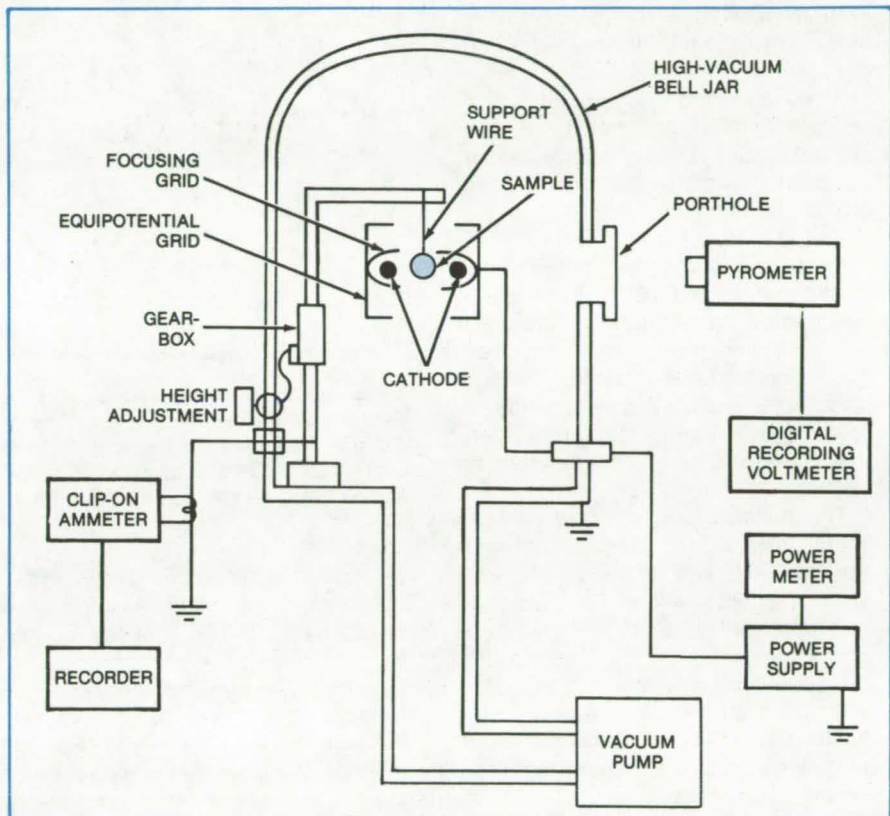
The calorimeter operates from 1,000° to 3,600° C yet it consumes less than 100 watts at temperatures less than 2,500° C. Various sample shapes, such as wires, disks, spheres, rods, or irregular bodies, can be accommodated, and only about 100 milligrams of sample are needed for accurate measurements.

The sample, encircled by a cathode filament, is heated by electron bombardment (see figure). To reduce contamination from the wire support, the wire is made of the sample material or of one of the sample constituents. The sample is attached to the wire by spot welding or by a mortar slot cut into the sample.

The cathode filament is held at a high negative voltage and is heated to incandescence by an external power supply. Since the sample is connected to ground through its support wire, electrons emitted by the cathode strike it with high energy, thereby heating it. A collimating grid around the cathode ensures that the electrons impinge on the sample from all directions to heat it uniformly.

Power delivered to the sample is controlled by adjusting the supply voltage and by raising or lowering the sample in the heater assembly. The power is measured by monitoring the voltage and the current. Temperature is measured by a pyrometer that views the sample through a porthole.

At thermal equilibrium, the power into the sample is balanced by the heat loss due to radiation. Thus, the emissivity can be calculated from the



A Metal Sample Is Suspended within a cathode ring and focusing grid. The sample is grounded by a connection through the supporting wire and bar, and it is heated by electron bombardment. The position of the sample in the ring can be changed by signals to the gearbox on the sample support bar.

readings of the heating-power voltmeter, the clip-on ammeter, and the pyrometer. This approach can be used to measure the emissivity of both the solid and liquid phases of the sample.

Once the emissivity is known, the specific heat of the solid sample can be determined by slowly heating it and measuring its rate of temperature change and the power it absorbs. The melting temperature can be determined by observing the temperature at which melting begins or at which there is a sudden step in the rate of temperature change. If the composition of the alloy is known from chemical analysis, the high-temperature equilibrium phase diagram can

be determined by measurements on samples of various compositions.

The heat of fusion of the metal or alloy can be found by measuring the sample mass and the energy input as melting takes place; surface tension can be calculated by measuring the critical mass of a drop released from the molten material.

This work was done by Lewis L. Lacy, Daniel B. Nisen, and Michael B. Robinson of Marshall Space Flight Center. For further information, Circle 72 on the TSP Request Card.

Inquiries concerning rights for the commercial use of this invention should be addressed to the Patent Counsel, Marshall Space Flight Center [see page A8]. Refer to MFS-23923.



Obtaining an Electrical Output From a Mechanical Flowmeter

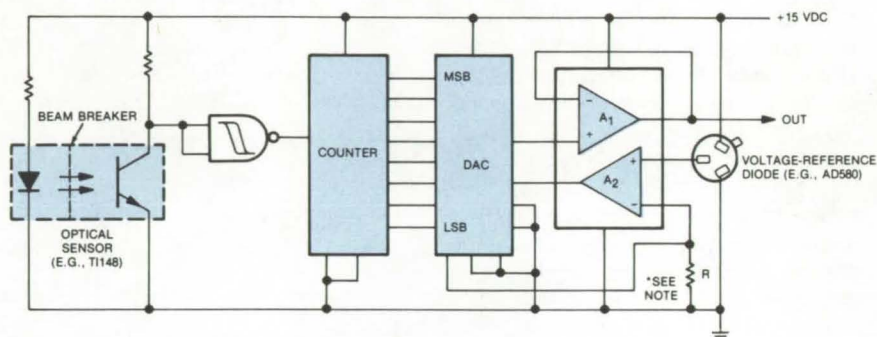
Circuit derives analog signals from the mechanical readout of a conventional, water, gas, fuel-oil, or power meter.

Marshall Space Flight Center, Alabama

With minimal modification to the meter itself, the mechanical readout of a water, gas, fuel-oil, or power meter can be converted to an analog signal, suitable for online processing. The conversion circuit uses an optical sensor, low-power counting electronics, a one-chip digital-to-analog converter, and an operational amplifier. It can be assembled on a single printed-circuit card and mounted, with a minimum of downtime, on a meter that is already in service. When compared with conventional purchased electronic flow sensors, this approach is simpler and less costly, particularly if the flow system already has a meter with a mechanical readout installed in it.

The basic circuit is shown in the figure. The optical sensor is a light-emitting diode and phototransistor in a single package. When the beam is interrupted, it turns off the transistor, which sends a clock pulse to the counter input. (The pulse is inverted and buffered by a Schmitt-trigger NAND gate.) The counter output keeps a running total of the number of pulses recorded by the sensor, and a DAC generates an analog voltage that corresponds to the counter total. This voltage is fed to the circuit output through a voltage follower.

The beam breaker for each meter application is a simple modification of the meter mechanical readout. For



*NOTE: R IS CHOSEN TO SET OUTPUT VOLTAGE RANGE

A Flowmeter Mechanical Readout is adapted to interrupt the light beam of an optical sensor, and the sensor output is processed by this circuit. Each interruption registers a count, and the total number of counts is converted to an analog signal. Typical counters that might be used are the CD4020 or CD4040; the DAC could be the AD7530; and an LM358 could be the output amplifier. Equivalent circuits could also be used.

example, the rotor disk of a standard watt-hour meter normally has one or more holes punched in it (for use during calibration). The beam breaker can thus be made by installing the optical sensor so that one of the holes crosses the beam as the disk rotates. For fuel-oil or gas flowmeters, the beam breaker can ride on the rotary output shaft of the meter; and for many conventional water flowmeters, the meter output can be magnetically linked to a beam breaker.

The range and sensitivity of these conversion circuits are determined by the particular counter and DAC used. By using a counter with more stages,

the range can be increased. The number of bits of the converter must of course be compatible with the counter output. Errors in the electronics are less than one incremental step in output; the error in the mechanical meter itself ultimately limits the accuracy of the analog signal.

This work was done by William T. Powers of **Marshall Space Flight Center**. For further information, Circle 73 on the TSP Request Card.

Inquiries concerning rights for the commercial use of this invention should be addressed to the Patent Counsel, Marshall Space Flight Center [see page A8]. Refer to MFS-23958.

Precision Leveling of Large Machinery

The precise leveling of large structures is possible with a tool originally developed to level massive antennas. It consists of an electronic level and an orthogonal bubble level. A movable counterweight stabilizes the instrument as it is being read. Its dimensions are determined by the size of the item to be leveled. (See page 130.)

Volume-Change Indicator for Molding Plastics

A mechanical device monitors the volume of a plastic charge during compression/displacement molding. Two rotating disks that are driven by mandrels in the molding apparatus measure the displacements of the force and balance rams. By watching the disks, the operator can better control the pressure and temperature of the charge. (See page 122.)

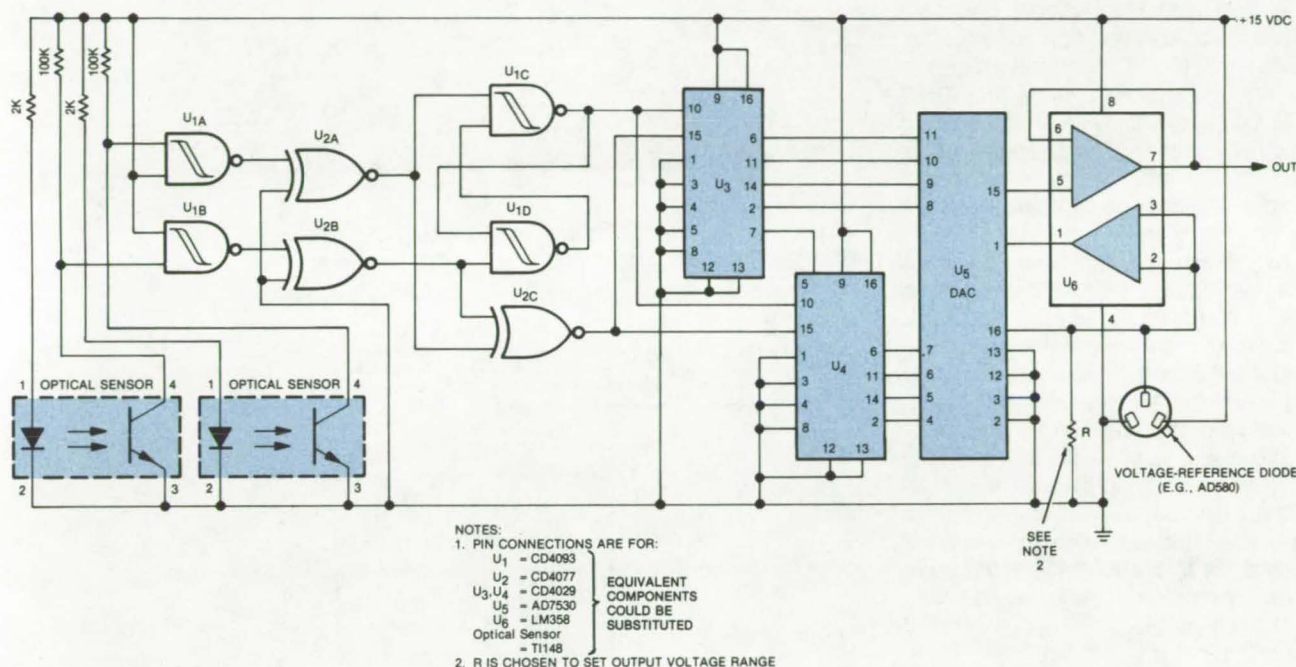
Low-Noise Spectrophone

A new optoacoustic gas analyzer has lower noise and greater sensitivity than previous designs. The laser is operated in the CW mode rather than chopped, reducing temperature changes in the windows. To modulate the absorption, the beam is polarization-modulated, or orthogonal sets of Stark plates rotate the field polarization. (See page 46.)

Differential Oil Flowmeter

A simple circuit monitors fuel consumption by an oil-fired furnace or water heater.

Marshall Space Flight Center, Alabama



In this **Differential Oil-Flow Sensing Circuit**, up/down counters U₃ and U₄ accumulate the difference in flow through two sensors as an 8-bit count output. U₅ converts the count to an analog voltage. The sensors are conventional oil flowmeters with mechanical readouts, but the output shafts are modified with beam breakers that interrupt the light beams in the optical sensors.

The difference in the oil flow volume through two mechanical flowmeters is converted to an analog signal by the simple and inexpensive circuit shown in the figure. As with the absolute flowmeter described in the previous article, the differential circuit can be adapted to monitor the flow of other physical quantities (e.g., power, gas, and water). Moreover, it can be implemented with only minor changes to two conventional oil flowmeters that have mechanical readouts.

The circuit could be used to measure the fuel consumed by an oil-fired furnace or water heater. One flow sensor would be installed in the oil feedline and the other in the return line. An analog output that represents the feed flow less the return flow is generated by the circuit. In a prototype that has been built and tested, the output is 0 to

5 volts dc for a differential flow of 0 to 128 gallons (0 to 484 l).

The oil flow sensors in the prototype are commercially available units with a response range of from 1/20 to 10 gal/h (0.19 to 39 l/h). Each has a reciprocating piston that drives a rotary output shaft. The shaft carries an interrupter that cuts across the light beam in an optical sensor.

As shown in the figure, each optical sensor is a light-emitting-diode/photo-transistor combination. When the light beam of either sensor is interrupted, it generates a pulse at the output of U_{2A} or U_{2B}, and, unless the pulses from both sensors occur simultaneously, a pulse also appears at the output of U_{2C}.

The output of U_{2C} clocks 4-bit up/down counters U₃ and U₄. A latch formed by U_{1C} and U_{1D} determines

whether U₃ and U₄ are in the up mode or the down mode; pulses from optical sensor 1 clock the counters up, and pulses from sensor 2 clock them down. Thus, U₃ and U₄ register the accumulating difference in the number of pulses from the sensors, which is a measure of the differential oil flow. The 8-bit count total of U₃ and U₄ is converted to an analog voltage by digital-to-analog converter U₅. Dual op-amp U₆ and associated circuitry set the output voltage range.

This work was done by William T. Powers of **Marshall Space Flight Center**. For further information, Circle 74 on the TSP Request Card.

Inquiries concerning rights for the commercial use of this invention should be addressed to the Patent Counsel, Marshall Space Flight Center [see page A8]. Refer to MFS-23959.

Bidirectional Fluid-Flow Monitor

A simple, inexpensive monitor detects flows as slow as 0.1 gal/min.

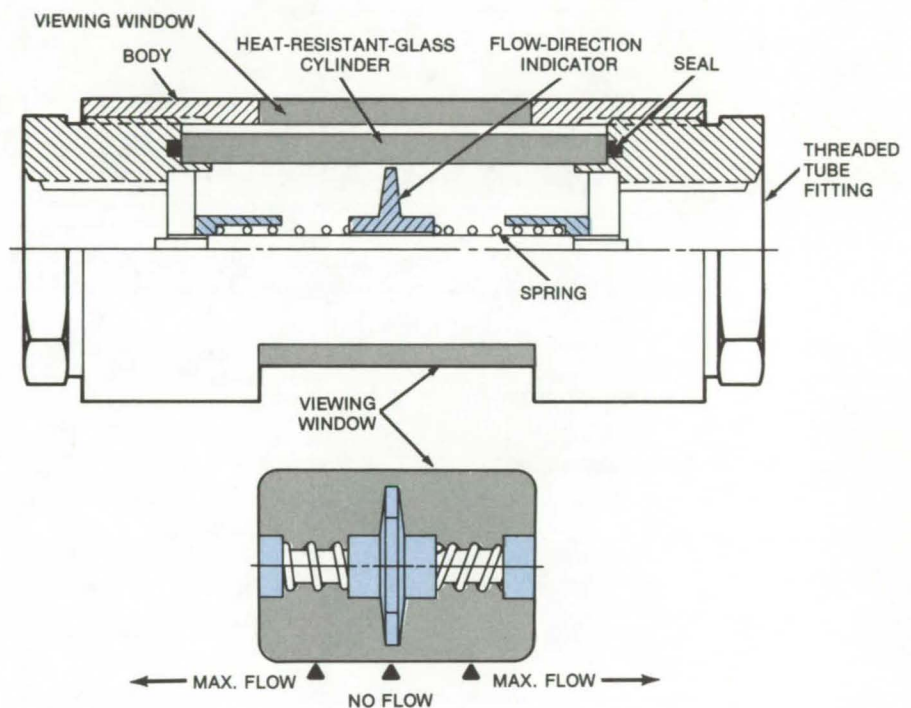
Lyndon B. Johnson Space Center, Houston, Texas

A proposed bidirectional fluid-flow monitor would detect flow rates as low as 0.1 gal/min (0.4 l/min.). It would operate at temperatures up to 350° F (177° C) and at pressures to 500 psig (3.6×10^6 N/m²). The monitor shows "no flow" and "maximum flow" conditions and approximately indicates intermediate flow rates.

As shown in the illustration, the monitor consists of a disk riding on a shaft with balancing springs that push against the sides of the disk. The pressure of the flowing fluid displaces the disk by an amount that is a measure of the flow rate.

The disk and shaft are housed in a heat-resistant glass cylinder enclosed within a metallic body. The sides of the body are fitted with viewing windows. Tube threads at the ends of the body allow the monitor to be installed in line with the flow pipe. The orientation of the monitor is not critical.

The balancing springs are calibrated such that the disk aligns with NO FLOW or MAX. FLOW decals when either of those flow conditions prevails. The monitor is intended for applications in which the flow rates range between 0.1 and 15 gal/min (0.4 and 57 l/min), the pressures can reach 500 psig, and the temperature ranges between -65° and 350° F (-54° and 177° C).



This **Bidirectional Fluid-Flow Monitor** has a disk indicator riding on a shaft to show maximum flow or no flow. The indicator is held by balanced springs on each side and responds to flows as low as 0.1 gal/min.

This work was done by Salvador L. Barajas of Rockwell International Corp. for Johnson Space Center. No further documentation is available. MSC-16762

Electrical Indication of Airflow Rate

Temperature and power sensors allow automatic collection of airflow data for online processing.

Marshall Space Flight Center, Alabama

A method for measuring airflow rate produces electrical outputs that can be used directly by an automatic data-logging system. Developed for the evaluation of solar hot-air collectors, it is an adaptation of a gas-flow measurement technique originally developed by C.C. Thomas in 1911.

Previously, airflow in the collector duct was determined by measuring the pressure head with a manometer. The measurements were used in manual calculations of the air velocity and flow rate. An enormous amount of such data must be collected in a typical collector design evaluation.

With the new method, a minicomputer can collect raw data for online processing. The method relies on temperature measurements, which are easily converted to electrical signals, rather than on manometer column indications.

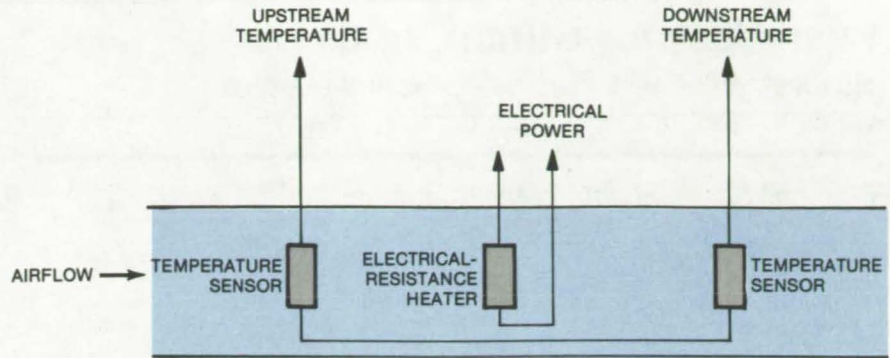
Two temperature sensors are placed in the air duct, one upstream from the other, and a small electrical resistance heater is positioned between them (see figure). This arrangement generates signals representing the upstream and downstream temperatures and the power consumed in the resistance heater.

The minicomputer calculates the airflow (q) in cubic feet per minute according to the equation

$$q = \frac{3.823P}{t_2 - t_1}$$

where P is the heater power, t_2 is the downstream temperature, and t_1 is the upstream temperature. The proportionality constant is determined by inserting the known value of the heat capacity of air in Thomas' original equation.

The temperature sensors used in the collector studies are thermopiles, which produce a voltage directly pro-



Airflow Is Computed from electrical signals representing upstream and downstream temperatures and the electrical power transferred to the air from the heater. Each thermopile temperature sensor is distributed over the cross-sectional area of the duct.

portional to temperature. The power sensor is a Hall-effect transducer.

This work was done by Charles Murrish of Life Sciences Engineering for **Marshall Space Flight Center**. For further information, Circle 75 on the TSP Request Card.

Inquiries concerning rights for the commercial use of this invention should be addressed to the Patent Counsel, Marshall Space Flight Center [see page A8]. Refer to MFS-23873.

Nondestructive Pull Tester

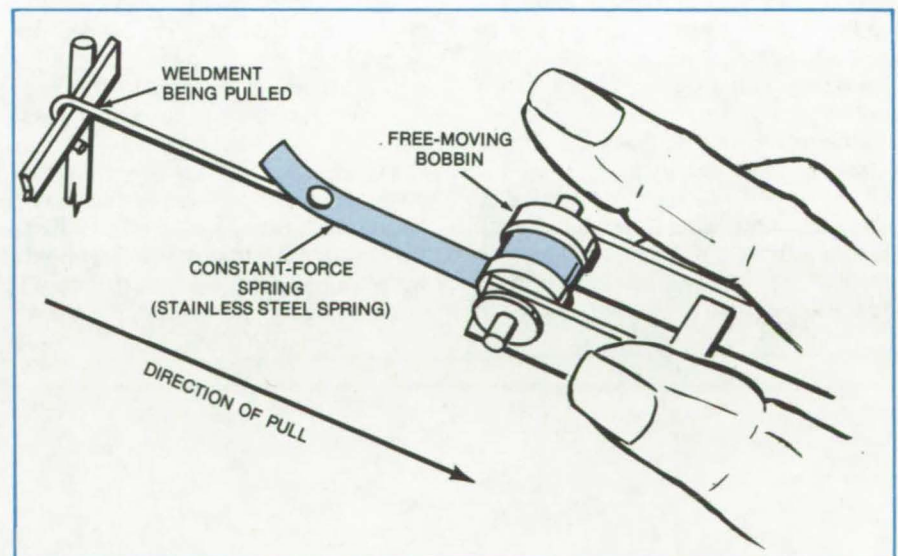
Quality control of welded electric wires is improved with an easy-to-use tool.

Lyndon B. Johnson Space Center, Houston, Texas

Improperly-welded electrical connections cannot always be identified by electrical-continuity tests. The compression of a wire against a contact in preparation for welding may ensure temporary continuity even though the connection has not actually been welded.

The simple handtool shown in the figure applies a small, constant pull force to the weldment (typically less than one-twentieth the force required to pull a weld apart). It can thus be used to find unwelded or partly welded wires without damaging good welds. In one application, the force applied by the tool is 0.5 pound (2.2 N).

The tool is a strip of stainless-steel spring wound around a free-moving bobbin. A hook at the end of the spring engages the wire to be tested and pulls it with a constant force as one pulls the tool away from the wire. After the weld is tested, the spring rewinds itself around the bobbin.



As the **User Pulls This Weld Tester**, a flat stainless-steel spring unreels, applying a small constant force to the weld.

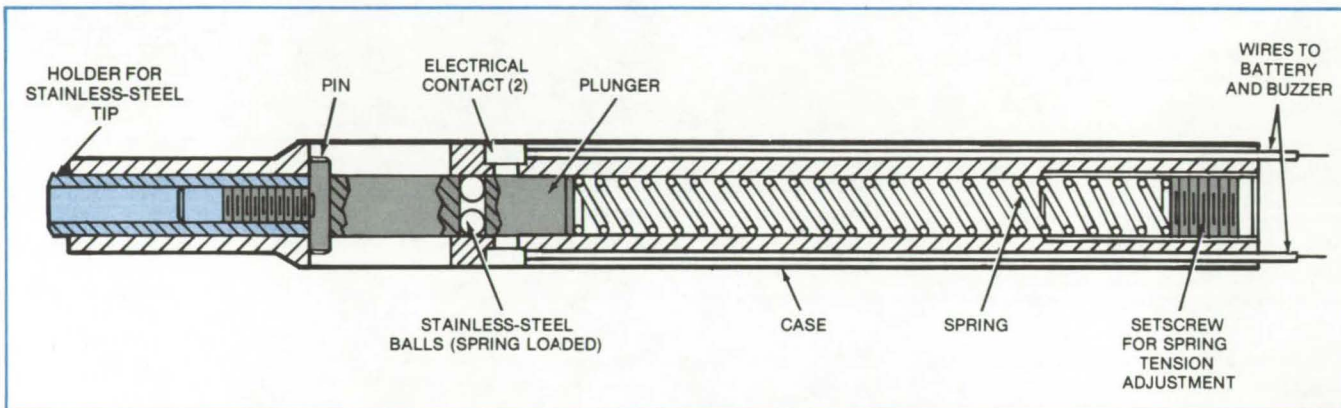
This work was done by Alfred Levy of Hughes Aircraft Co. for **Johnson**

Space Center. No further documentation is available. MSC-18329

Push Test for Stitch Welds

Nondestructive test identifies poor and marginal welds without harming good ones.

Marshall Space Flight Center, Alabama



The **Push-Tester Case** encloses a spring and plunger. A pair of wires connects the tester to a battery and buzzer. When the tip of the tester is exerting a force of 7 pounds on a stitch weld, the balls in the plunger complete the circuit between electrical contacts in the case, and the buzzer sounds.

Weak or otherwise defective stitch welds, in which insulated nickel wires are welded to stainless-steel terminals on the back planes of electronic equipment, have hampered the assembly of control electronics for the Space Shuttle. However, stitch welds can now be tested nondestructively with the aid of a small, pencil-like tool that applies a low, predetermined force to individual welds. The new tool makes it possible to test such welds as soon as they have been made and to correct them if necessary.

The tool is held so that its stainless-steel tip (see figure) pushes on the weld junction in a direction normal to the axis of the wire. The user pushes the tool against the junction, and an audible signal sounds when the force reaches exactly 7 pounds (31 N). In the

Shuttle weld tests, the 7-pound force was enough to open defective welds, yet light enough to not damage good welds.

The tool operates by closing an external circuit when the 7-pound force is attained. The tip pushes a nonconductive plunger against a 7-pound (force) spring that, when compressed, aligns steel balls in the plunger with contacts in the outer case. This closes the circuit to an external battery and buzzer. The sound indicates that the weld has been subjected to the required test force.

In a comparison test, the push tool helped detect poor welds that would otherwise have gone unnoticed (until they failed catastrophically). Ten welds were made at each of eight different voltage settings, covering the range

from cold to hot welds. Of these 80 welds, 26 were found to be defective by the 7-pound push test. The welds that passed the test were subjected to destructive pull and peel testing; all were found good except for a single marginal weld. In a control group of 80 welds made under the same conditions but not push-tested, 21 welds were found to be bad or marginal by pull and peel testing.

This work was done by Charles J. Torborg of Honeywell Inc. for Marshall Space Flight Center. For further information, Circle 76 on the TSP Request Card.

Inquiries concerning rights for the commercial use of this invention should be addressed to the Patent Counsel, [see page A8]. Refer to MFS-25027.

Checking Weld Penetration

A fused wire in the weld root area verifies proper penetration in electron-beam-welded joints.

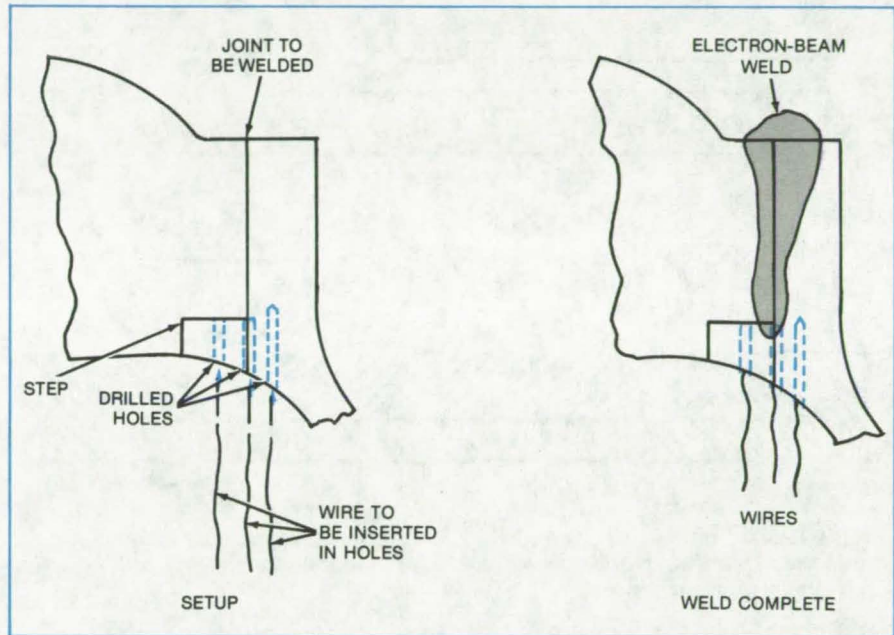
Marshall Space Flight Center, Alabama

A simple wire-insertion verifies weld penetration in electron-beam-welded joints. The method could be used in automotive, aircraft, and machinery manufacturing when electron-beam welds cannot be inspected ultrasonically.

Before the workpiece is welded, one or more sets of at least three holes each are drilled in the root area of the joint (see figure). One hole of the set is drilled precisely at the joint, and the others are drilled on either side. The holes are parallel to the plane of the joint, and they extend to the required level of weld penetration. A wire that is preferably composed of the same alloy as the workpiece is inserted in each hole.

After welding is completed, the wires are inspected: If the center wire is fused, the weld root is at the required depth. However, if the electron beam is slightly off track, one of the side wires will be fused, and the side on which the fused wire is located indicates the direction of mistrack.

In a particular application, possible defects that could be introduced by either the hole or the fused wire should be considered before adopting this inspection procedure.



The **Electron-Beam Weld** has penetrated to the proper depth if only the center wire is fused. The beam is misaligned if the left or right wire is fused.

*This work was done by D. I. Macfarlane of Rockwell International Corp. for **Marshall Space Flight Center**. No further documentation is available.*

Inquiries concerning rights for the commercial use of this invention should be addressed to the Patent Counsel, Marshall Space Flight Center [see page A8]. Refer to MFS-19395.



Ultrasonic Grating Checks Electron-Beam Welds

A simple inspection method checks that the weld penetrates to the root area of the joint.

Marshall Space Flight Center, Alabama

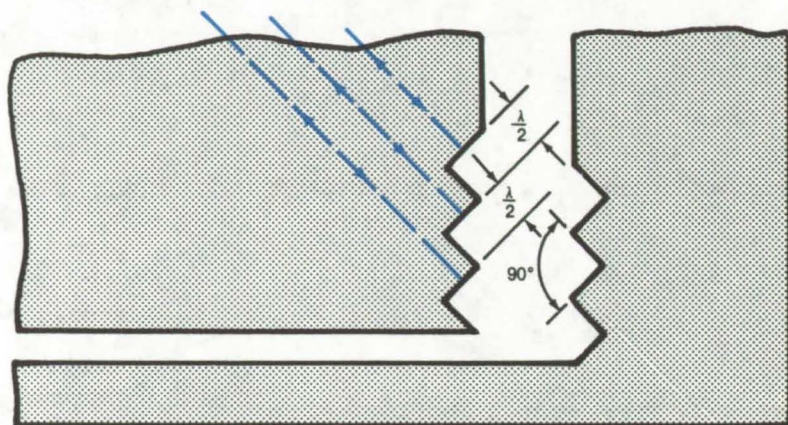
Obtaining satisfactory weld penetration is critical in electron-beam welding. However, if the weldment is a right-angle joint or other blind configuration, visual inspection is impossible, and a nondestructive remote-sensing method must be adopted to check that the weld has penetrated to the root area.

One such remote-inspection technique, shown in the figure, was recently developed for checking welded components in the Space Shuttle main engine. In this approach, several small steps are machined in the root area, forming a grating that strongly reflects ultrasonic waves from a nearby transducer. If the weld reaches

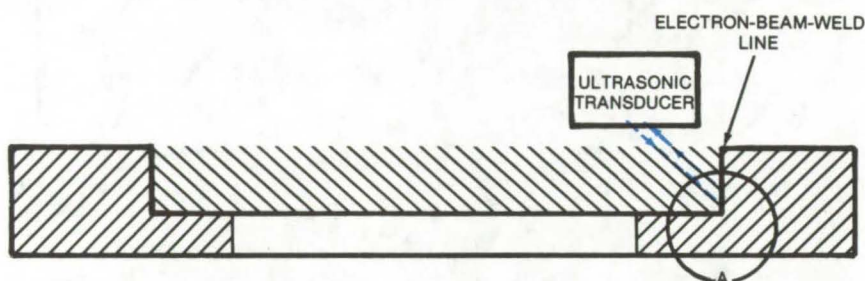
the root, it upsets the ultrasonic echo and indicates a successful weld. If not, the continuing echo is an indication of a faulty weld. The method is simple, easy to apply, and requires the removal of only a small amount of material from the surfaces of the joint.

As shown, the grating steps are matching right-angle notches in the

(continued on next page)



DETAIL A



An **Ultrasonic Grating** strongly reflects sound waves from the root area of a joint to be electron-beam welded. If the weld penetrates to the root, it upsets the grating, indicating a successful weld.

joint surfaces. The step height is one-half of the ultrasonic wavelength. Thus, the waves reflected from adjacent steps are displaced in phase by one full wavelength, and they arrive in phase at the detector to give a strong resonance. For the example shown, the ultrasonic frequency is 5 MHz, and the step height (calculated using the velocity of sound in the material) is 0.01 in. (0.02 cm).

This work was done by Hugh A. Mitchell of Rockwell International Corp. for **Marshall Space Flight Center**. No further documentation is available.

Inquiries concerning rights for the commercial use of this invention should be addressed to the Patent Counsel, Marshall Space Flight Center [see page A8]. Refer to MFS-19422.

Accurate Measurements of Mass and Center of Mass

A procedure used for spacecraft is accurate to within 0.01 percent.

NASA's Jet Propulsion Laboratory, Pasadena, California

Regardless of its shape, an object can be measured for the mass and the center of mass with high accuracy by a method that eliminates errors in alignment, leveling, and calibration. The method, which was originally developed to determine the mass and the center of mass of the Voyager spacecraft, could be applied to scientific instruments, recorded turntables, flywheels, and other devices that require precise balance. For the 750-kilogram Voyager, the mass was determined to an accuracy of 0.01 percent, and the center of mass was located to within 0.14 millimeter.

Mass and the center of mass are determined by measurements on three load cells that support the object in a test fixture (see figure). The

object rests on an adapter ring and load plate, and the load cells support the plate at the apexes of an equilateral triangle. The three cells rest on a common turntable.

After a set of load-cell readings is recorded, the turntable (with cells) is rotated through 120° with respect to the object, and another set of readings is taken. A third set of load-cell readings is recorded after the turntable has been rotated through another 120°. This procedure accounts for load-cell calibration errors and the effect of nonparallelism of the top and bottom planes of the load-cell turntable.

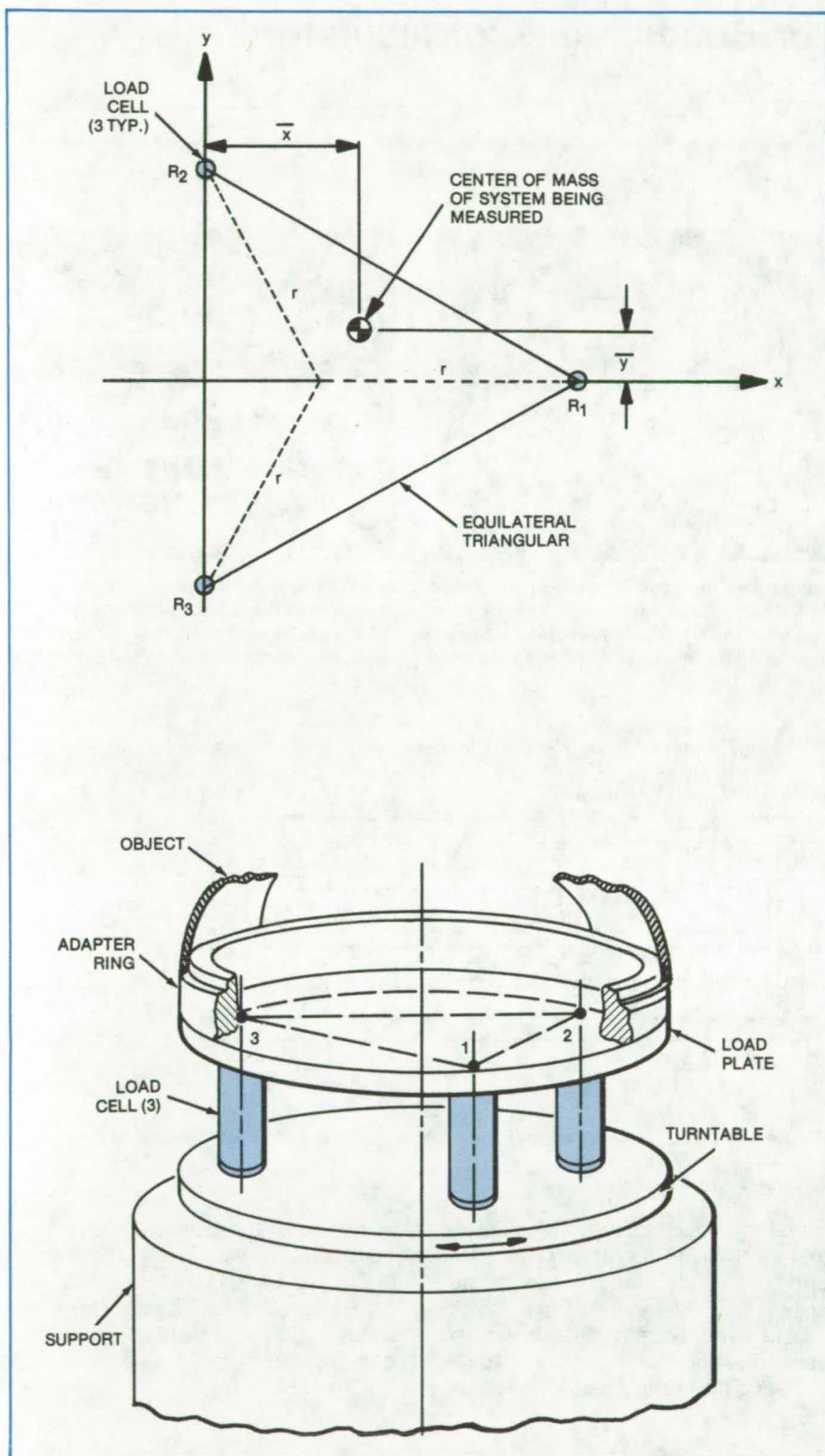
Three more sets of load-cell readings are taken after the object has been rotated by 180° with respect to

the load plate. As before, the turntable is rotated by 120° with respect to the object before each set of data is taken. This step eliminates ground-plane tilt error and any errors in the concentricity of the load plate and fixture ring.

For each of the six sets of load-cell readings, values of the x and y projections of the object center of mass (including the adapter ring and load plate) on the lower surface of the load plate can be calculated from the equations

$$x = \frac{3r}{2} \frac{R_1}{W}$$

$$y = \frac{\sqrt{3}}{2} r \frac{R_2 - R_3}{W}$$



For **Measurements of Mass and the Center of Mass**, an object is rigidly mounted on a plate supported by three load cells (in color). Load-cell readings are recorded, and the turntable is twice rotated by 120° to take two additional sets of measurements. Then the object is rotated by 180° , and the procedure is repeated. Equations and the computer program for determining the mass and the center of mass from these measurements are discussed in the text.

In these expressions, R_1 , R_2 , and R_3 are the reactions (measured in kilograms) at the load cells due to the mass W of the object, and r is the distance from the equilateral triangle centroid to its apex, as shown in the figure. A value for the object (plus support) mass can be obtained by simply adding the three reaction forces.

The values of x , y , and W are then averaged over the six sets of readings to determine the center-of-mass coordinates (\bar{x} and \bar{y}) and mass (W). Then, the known geometry and mass of the fixture are accounted for to give the center of mass and mass of the object.

This method eliminates all alignment, leveling, and load-cell calibration errors for the lateral center-of-mass determination. It permits a statistical best fit of the measurement data. An associated data reduction computer program has been written to implement this method. This method and the data reduction computer program compute the mass and center of mass of the object being measured, along with the associated standard deviations.

For the Voyager measurements, the load-cell range was 1,000 kilograms, and the resolution of the load-cell readout was 0.05 kilogram. The maximum error of the load-cell calibration was 0.1 percent, and the load cells were positioned to within 0.05 millimeter.

This work was done by Edwin Y. Chow and Marc R. Trubert of Caltech for **NASA's Jet Propulsion Laboratory**. Further information may be found in NASA CR-156130 [N78-20177], "A Highly Accurate Method for the Determination of Mass and Center of Mass of a Spacecraft" [\$5.25]. A copy may be purchased [prepayment required] from the National Technical Information Service, Springfield, Virginia 22151. NPO-14428



Measuring Resistance or Conductance of Insulators

A three-electrode fixture rapidly measures the resistance of insulators.

Lyndon B. Johnson Space Center, Houston, Texas

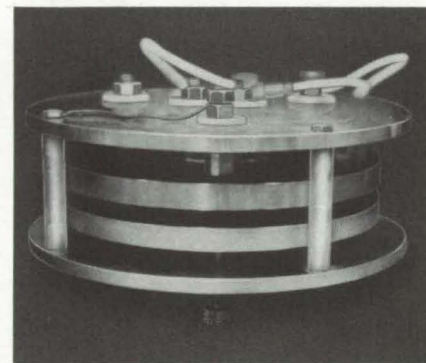
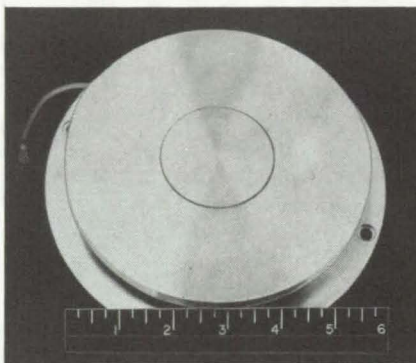
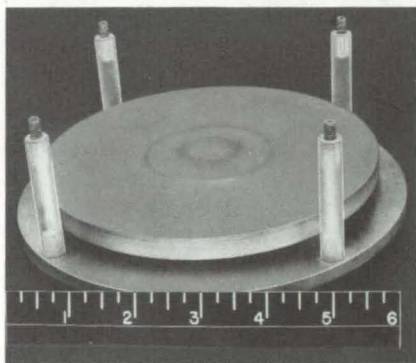


Figure 1. This **Three-Electrode Fixture** is used in measuring the resistance or conductance of insulating materials. The baseplate supports an unguarded electrode, as shown in the photograph at the left; the top electrode shown in the center photo consists of two parts: a guarded electrode in the center surrounded by a guard electrode; the assembled fixture is shown at the right. This fixture accommodates specimens up to 3 inches in diameter; a different top electrode (not shown) accommodates specimens up to 6 inches in diameter.

The measurement of dc resistance or conductance of insulators such as plastics or rubber requires a stable fixture for holding electrodes against the test specimen. For maximum utility, the fixture should also be able to accommodate different sample shapes. The ASTM (American Society for Testing Materials) standard D-257 for resistance measurement, while effective, is a rather slow procedure that uses mercury electrodes. Thus, it is not very suitable for rapid quality-control or production testing of large quantities.

For many applications, the portable three-electrode fixture shown in Figure 1 gives the required accuracy with substantially less labor and expense than previous methods. This fixture, which is used for inspection, verification, and qualification tests of insulating materials in the Space Shuttle program, includes three electrodes (one guard electrode, one guarded electrode, and one unguarded elec-

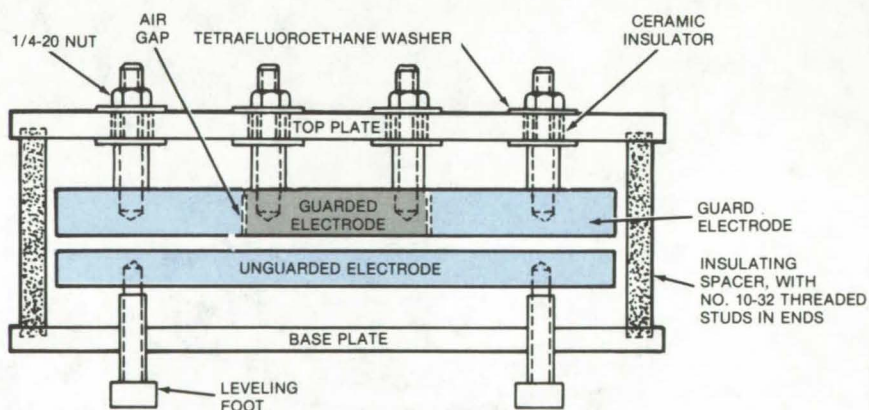


Figure 2. **Partial Cross Sectional View** shows how the three electrodes are attached to the top and base plates.

trode). It accommodates specimens that are 3 in. (7.6 cm) or 6 in. (15.2 cm) in diameter, and it can be adjusted for different sample thicknesses. The plane of the unguarded base electrode can be changed by adjusting the leveling feet (Figure 2) to

accommodate samples that have nonparallel surfaces.

This work was done by Harry S. May of Rockwell International Corp. for Johnson Space Center. No further documentation is available.
MSC-18132

Laser Alinement of Large Assemblies

A laser tiltmeter saves time and costs in assembling large structures.

Lyndon B. Johnson Space Center, Houston, Texas

An electronically-leveled laser instrument simplifies the alinement of large structures. This system is operated from a single alinement reference tower. Earlier methods have used autocollimators requiring two expensive towers.

The new instrument incorporates a special tiltmeter-controlled, laser alinement transit (Figure 1). The

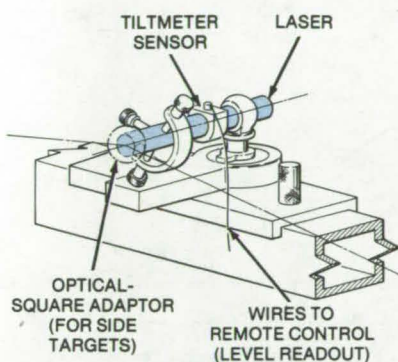


Figure 1. **Laser Alinement Transit** is equipped with a tiltmeter sensor and an optical square (not shown). This instrument is placed at various points on the alinement tower to check the alinement of parts on large assemblies. Instrument alinement readings are taken from central monitoring station.

transit is placed at one of the alinement points on the tower as illustrated in the example of NASA's Space Shuttle assembly (Figure 2). The transit then is alined parallel to the fuselage centerline by rotating an optical square attachment on the laser to line up with the fixed side targets.

The entire alinement procedure is monitored at the central control station. There, one readout instrument monitors the tiltmeter level while the other produces a continuous digital display to show the beam centering on the target. The latter shows both vertical and horizontal displacements from the line of sight. Feedback to this display is generated by "quad-cell" photosensitive targets placed on each subassembly. Level position of the laser beams from electronic side targets is also monitored at this station.

The new system utilizes a single, low-level quad-cell, fixed-target station to permit the calibration of each

laser instrument before it is installed in the tower. After setting the zero reading of the level to the center of the electronic readout swing (due to continuous basic structural movement), two fixed quad-cell side targets and an optical square on the laser gun are used to verify the level alinement of the instrument. After calibration, the instrument is moved to its line-of-sight tower station. The electronic level then is used in conjunction with the optical square and the fixed side targets to set the beam on the line of sight. Once calibrated, the instrument can be easily moved from station to station without affecting the electronic level.

This work was done by William S. Cazares and Delmer D. Kern of Rockwell International Corp. for **Johnson Space Center**. For further information, Circle 77 on the TSP Request Card.
MSC-19346

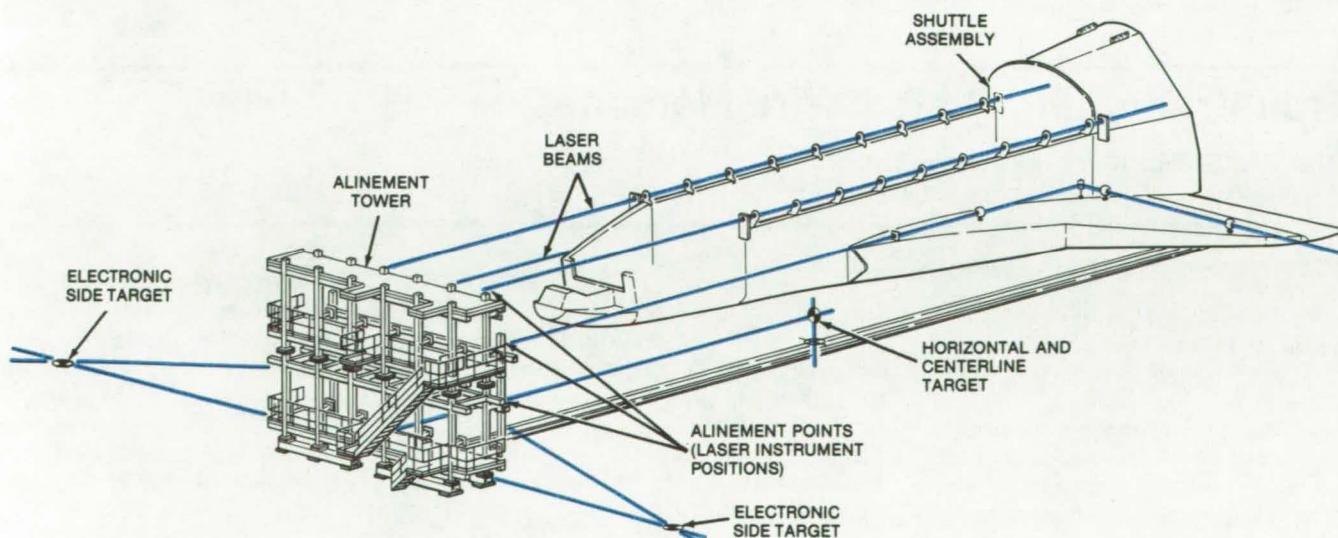


Figure 2. A **Laser Alinement System** is shown in use on NASA's Space Shuttle subassembly alinement. This system can be effectively utilized in aircraft and shipbuilding assemblies.

Measuring the Thickness of Plastic Films

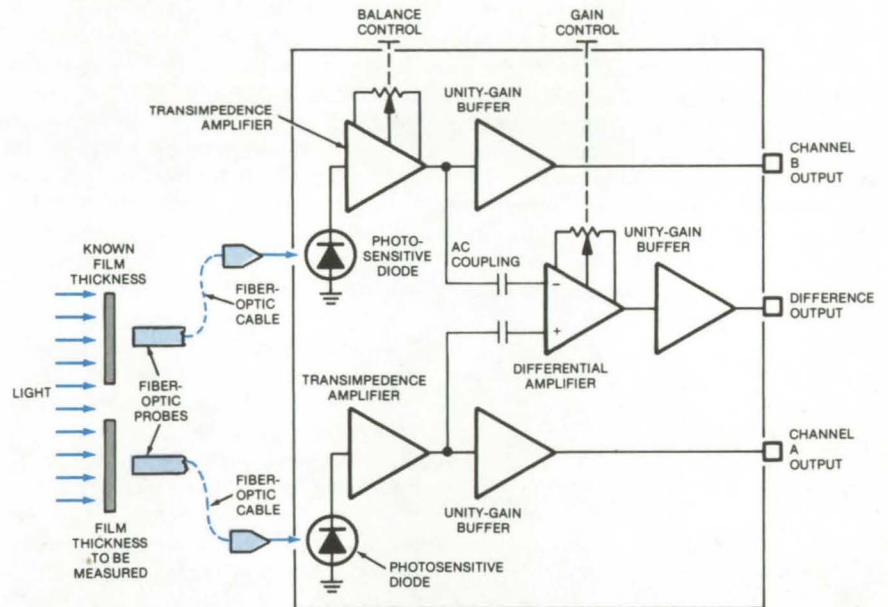
A new instrument monitors thickness by measuring the attenuation of light as it passes through the film.

Ames Research Center, Moffett Field, California

An optical instrument measures the thickness of translucent and transparent sheets in the thickness range from about 2 to 8 microns. It can resolve thickness variations over areas as small as 8 square millimeters.

As shown in the figure, the thickness monitor measures the attenuation of light passing through the film, which, according to Beer's law, is proportional to the thickness. A light source illuminates one side of the film, and a fiber-optic probe on the other side picks up the transmitted light. At the same time, a second probe picks up the light transmitted through a film of known thickness. Electronic circuitry compares the intensity of light from the two probes and generates a signal proportional to the thickness difference (see figure).

In a thickness monitor developed to evaluate polymer films for a solar "sail," the fiber-optic cables are 3.2 millimeters in diameter and 1 meter long. Since the cables are flexible, they can be moved back and forth to scan a large sheet. In addition, the circuitry can be operated in either a single-beam or a double-beam mode, and its output can be viewed on an oscilloscope or strip-chart recorder. In tests



This **Film-Thickness Monitor** compares signals from light passing through known and unknown film thicknesses. The difference in signal strengths represents the thickness of the unknown and can be displayed on an oscilloscope or strip-chart recorder.

on transparent and translucent polyimide films 2.2 to 7.6 micrometers thick, the measured thicknesses agreed with the known thicknesses to within 25 percent.

This work was done by Kevin C. Donohoe and Theodore Wydeven, Jr., of Ames Research Center. No further documentation is available.
ARC-11219

Troubleshooting Plated-Wire Memories

Reflected electrical pulses reveal flaws without disassembly of the memory system.

Marshall Space Flight Center, Alabama

Faults in plated-wire memories can be identified and located by an adaptation of time-domain reflectometry (TDR), a technique widely used to pinpoint faults in telephone lines. Until now, it was usually necessary to disassemble the memory and probe its interconnecting cables, printed circuits,

and solder connections for open circuits or short circuits. With TDR, the troubleshooting is done from outside the memory system by applying electrical pulses and analyzing their reflections. Intermittent faults are much easier to find because the memory system is not disturbed by probing or disassembly.

Plated-wire memories, in which data are stored on copper wires plated with magnetic material, offer fast response, low power consumption, and resistance to radiation. Because the data-storage elements are long wires resembling transmission lines, they are suitable for TDR.

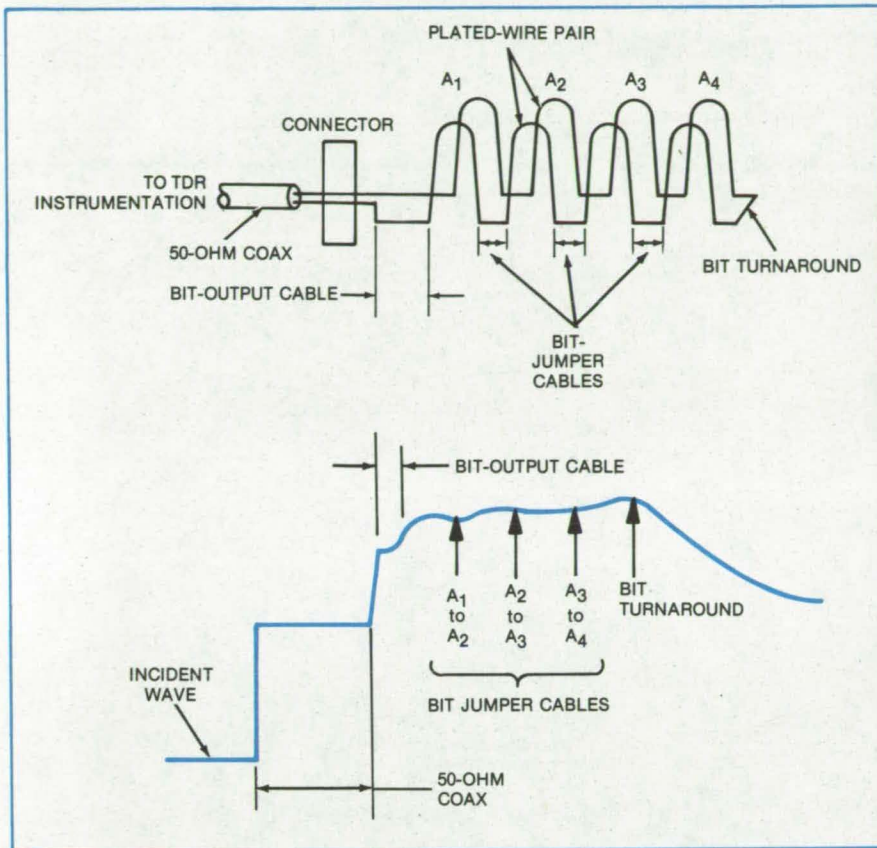


Figure 1. The **Pattern of the Waveform** reflected from a normal plated-wire memory stack correlates with details of the stack structure.

The basic instrumentation for TDR consists of a fast-rise-time step generator, which applies voltage steps to a memory wire, and a high-speed sampling oscilloscope, which displays the reflections created by impedance mismatches along the wire. The shape and magnitude of the reflected wave indicate the nature and degree of an impedance mismatch. The time for the reflected wave to return to the instrumentation indicates the location of the mismatch. The method is remarkably sensitive; impedance mismatches as small as a few percent are discernible.

Although plated-wire memories vary widely in size and shape, they contain hairpinlike sense lines plated in tunnels in memory boards. The TDR wave reflected by such a memory "stack" can be related to points in the stack structure (Figure 1). For example, the reflection waveform on the TDR oscilloscope first rises to a level established by the 50-ohm coaxial cable connection from the TDR instrumentation. At the connector to the memory, the impedance

rises sharply, and the corresponding reflection appears in the waveform. The oscilloscope trace remains at the slightly-varying high level of the plated wire until bit turnaround of the memory stack sends reflections, at which point the trace gradually returns to the level of the 50-ohm connecting cable.

The waveforms produced by faulty memory stacks are markedly different from the normal waveform (Figure 2). A short circuit appears as a sharp drop in the waveform, and an open circuit appears as a pronounced rise. In both cases, the point at which the waveform deviates corresponds to the location of the fault in the memory stack.

It is important to use a good-quality connecting cable that has a constant impedance. A mismatch in the test cable can distort the waveform and make it difficult to interpret. In examining a waveform on the oscilloscope, superposition of a waveform from a good stack helps to make subtle mismatches more obvious (see Figure 2).

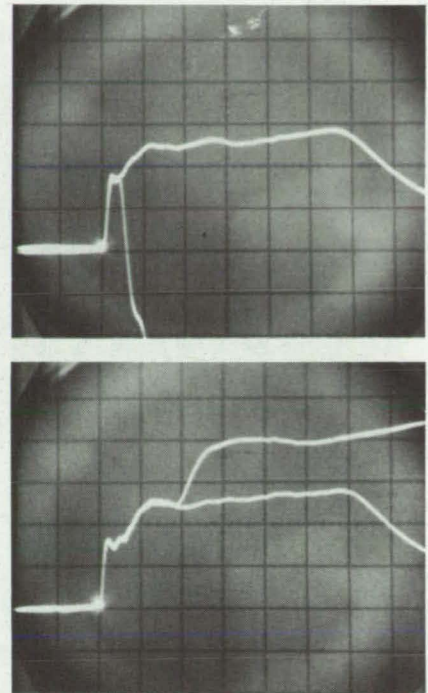


Figure 2. **Reflections From Faults**, superimposed on a normal waveform, reveal the nature and location of the faults. The short circuit illustrated in the oscilloscope trace at the top apparently is located at loop A₁ of Figure 1, whereas the open circuit in the trace on the bottom is located at loop A₂.

This work was done by Clyde M. Baker, Thomas M. Bright, and Robert C. Constable of Honeywell Inc. for Marshall Space Flight Center. For further information, Circle 78 on the TSP Request Card.

Inquiries concerning rights for the commercial use of this invention should be addressed to the Patent Counsel, Marshall Space Flight Center [see page A8]. Refer to MFS-23903.



Determination of Total Surface Reflectivity

Instrumentation and data analysis
techniques to determine total reflectivity

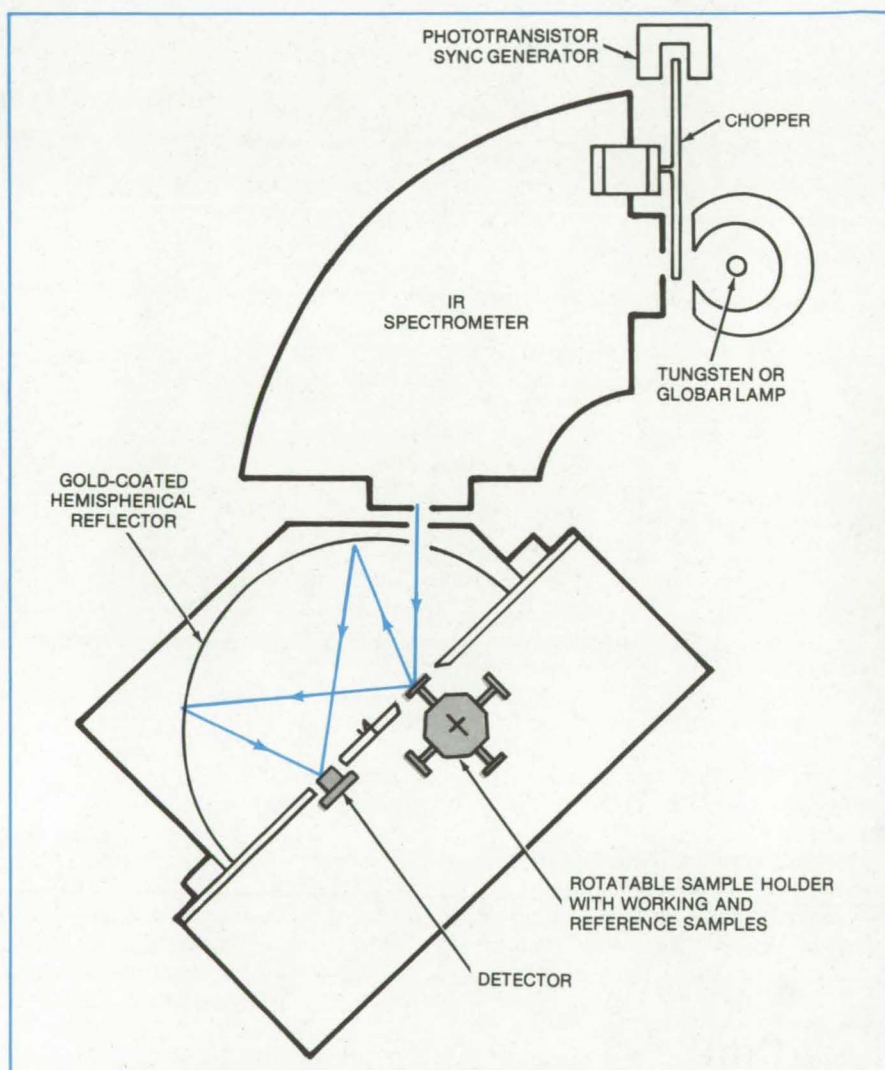
Marshall Space Flight Center, Alabama

Conventional measurements of surface reflectivity are relatively accurate for specular surfaces. However, large errors can occur when measuring the surfaces exhibiting both specular and diffuse reflectances — for example, a microscopically faceted surface with both types of reflectances in a proportion that varies with the inclination and size of the facets and with the direction of incident light. A similar example is a dusty mirror that reflects both diffusely and specularly.

A recently proposed method of measuring total reflectance employs a relatively inexpensive reflectometer (see figure) with a gold-coated hemispherical reflector. The light sources may be a tungsten lamp for the visible region or a Globar lamp for the infrared (IR). A beam chopper is also incorporated with phototransistor sync-signal generator for synchronous detection of the light signal. The chopped IR beam is dispersed with a salt prism spectrometer covering a wavelength range of from 0.6 to 20 μm .

The chopped dispersed beam enters the gold-coated hemispherical reflector and is reflected by a sample or reference surface mounted on an indexed rotating holder. The holder carries four disk-shaped samples and positions each sample at a point off the hemisphere center and near a diametral plane. The reflected light is focused onto a 1-mm² triglycine-sulfate detector located at an optically conjugate point.

The sample holder contains two samples under investigation and two carefully-prepared reference disks. The diffuse-reflectance reference disk has an MgO surface. The second is a gold-coated glass disk that serves as a specular-reflectance standard. The reflectometer is adjusted so that: (1) readings for both the gold and MgO samples are independent of the holder on which the sample is mounted, and (2) mirror and detector positionings are such that readings do not depend on small deviations of the sample-



Proposed Reflectometer for the measurement of diffuse and specular reflectances uses a rotatable sample holder with working and standard samples. A gold disk serves as a specular-reflectance reference, and an MgO-coated disk serves as a diffuse-reflectance standard. Reflectances are computed from the relative light intensities measured and data on the collection efficiency of the detector.

holder shaft angle about index points.

The detector records light intensities reflected from the sample surfaces. Reflectivities of the sample surfaces are obtained from the recorded intensities and by knowing the detector collection efficiency for both specular and diffuse components. The mathematical relationship can be solved either by hand or by computer.

This work was done by Donald J. DeSmet, Andrew J. Jason, and Albert C. Parr of the University of Alabama for Marshall Space Flight Center. For further information, Circle 79 on the TSP Request Card.

Inquiries concerning rights for the commercial use of this invention should be addressed to the Patent Counsel, Marshall Space Flight Center [see page A8]. Refer to MFS-25024.

Characterizing Glass Frits for Slurries

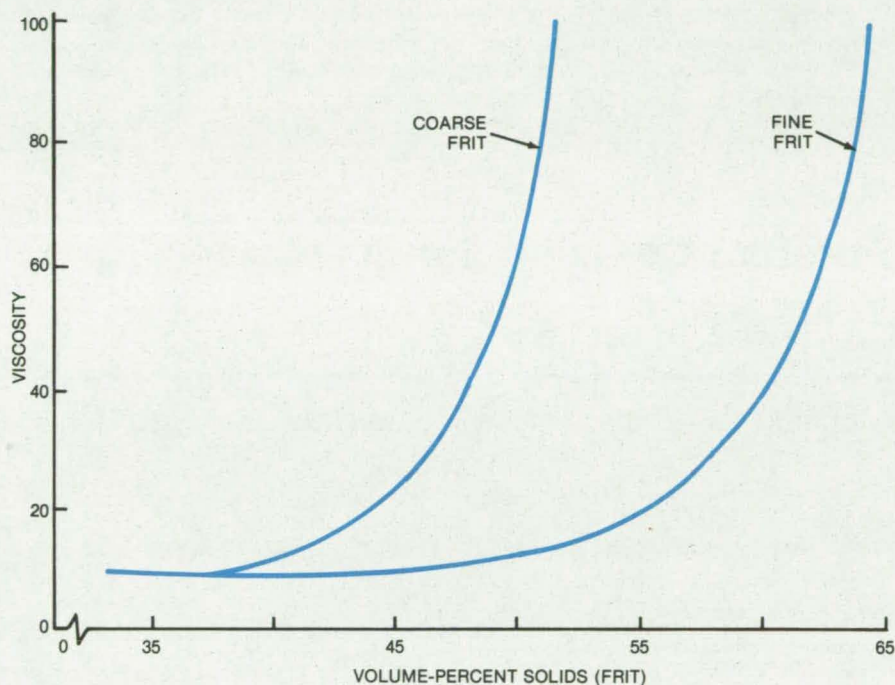
Solids content of ceramic-coating mixture can be optimized as the result of one simple measurement.

Lyndon B. Johnson Space Center, Houston, Texas

Glass-frit slurries can now be mixed with consistently reproducible properties, even from different batches of glass frit, using a new technique for characterizing the frit. When a slurry is used to make high-temperature ceramic coatings, glazes, and the like, the application rate, coating uniformity, and freedom from defects depend on having the proper viscosity. However, various batches of frit may have quite different particle-size distributions and therefore require different quantities of liquid for a given viscosity (see figure). In the absence of a simple characterization of the frit, trial-and-error mixing of each slurry is necessary.

The new test technique measures one quantity that determines the integrated properties of the frit for combination with a given liquid. This quantity, the "liquid absorption," is the amount of the given liquid that must be added to 5 grams of frit powder to make a flowable mix. The flow point is readily distinguishable and definitive.

The liquid absorption determines the particle packing factor or volume percent of particles present in the mix at the flow point. Curves can be prepared that show the viscosity of a slurry as a function of the percent solids for frits with various liquid absorptions; thus one measurement of a frit sample al-



The **Viscosity of a Slurry** depends on its glass-frit content and on the particle-size distribution of the frit. A given curve on this graph is characterized by the "liquid absorption" measurement of the frit.

lows reliable preparation of a slurry with any desired viscosity.

This work was done by Harry N. Nakano of Lockheed Missiles & Space

Co., Inc., for Johnson Space Center. For further information, Circle 80 on the TSP Request Card. MSC-18322



Test-Configuration Identifiers

An organized approach to identifying test configurations for large complex systems

John F. Kennedy Space Center, Florida

A new report that describes a systematic approach for establishing and identifying test configurations for the Space Shuttle will be useful to those testing other complex systems (e.g., submarines, aircraft, air traffic controllers).

Like any large system, the Shuttle is tested at several stages in its development; subassemblies are tested first, and eventually the entire system is

operationally tested. The Shuttle test system is a distributed computer system, which allows a great deal of interaction within a totally synchronized environment.

For the shuttle, four major considerations influencing test configurations are:

1. **The Test Site.** This is the physical location of the test article. Four sites are possible for Shuttle test-

ing, including the Orbiter processing facility, the external tank checkout facility, and two mobile launch pads.

2. **The Test Article.** This is any major component of a particular Shuttle vehicle. Major elements include the Orbiter vehicle, solid rocket boosters, main engines, and external tank.

(continued on next page)

3. *Data Communications.* There are six pulse-code-modulation links to the Orbiter, a launch data bus (which operates in both directions), and ground-support equipment for synchronized physical and electrical support for test and launch. These communications links are for issuing test instructions and measuring test results.
4. *Control Site.* The test control site is the physical location of the control and monitoring station [firing room 1 and firing room 2 in the launch

control center (LCC)]. For this application, the control site is a interactive distributed computer system.

Typical constraints that must be followed in setting up a test configuration are that the configuration demand no more data links than the number of processors available in a firing room; and when elements are tested simultaneously, scheduling of test sites and communications links must not overlap.

By a careful identification of vari-

ables and constraints, 55 allowable test configurations were identified and labeled with "Test Configuration Identifiers" (TCID's), letter codes that identify the configuration. The TCID's accommodate single-site, simultaneous-site, and multiple test configurations.

This work was done by W. D. Sumrall of IBM Corp. for Kennedy Space Center. To obtain a copy of the report, Circle 81 on the TSP Request Card.
KSC-11087

Antitheft Container for Instruments

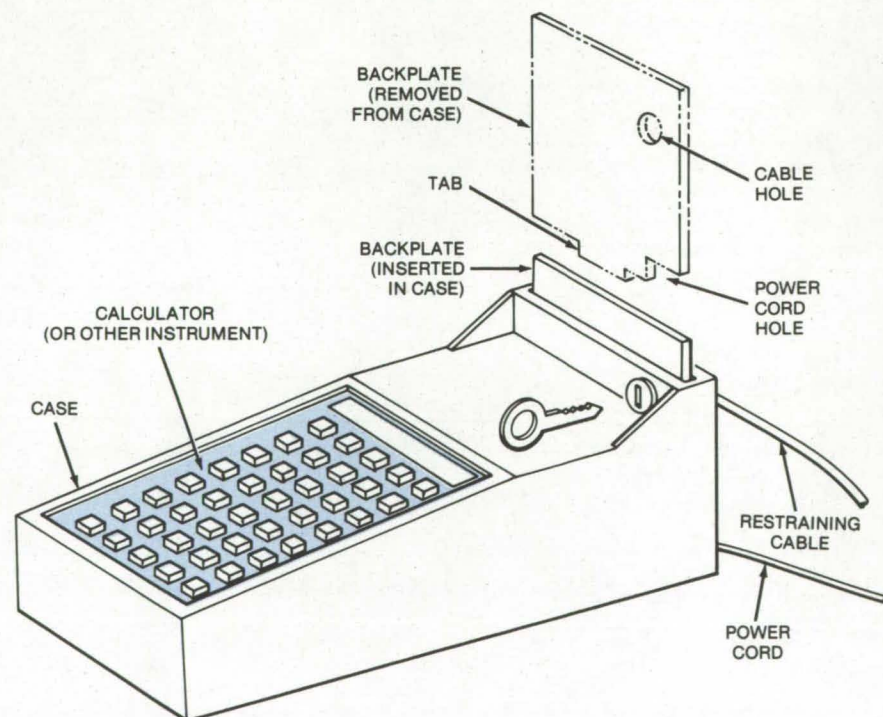
A secure case for small instruments of various sizes.

Goddard Space Flight Center, Greenbelt, Maryland

The thefts of calculators, voltmeters, portable computers, and other small instruments are prevented by placing them in a case that allows the instrument to be used but makes it difficult to remove it. As shown in the figure, the container has an open top so that the calculator keys or other controls are accessible and the readout is visible. The case is restrained by a cable attached to its backplate and secured to a wall, column, desk, or counter. A lock on the backplate is opened to release the cable.

The backplate has a tab at its bottom and holes for the restraining cable and a power cord. After the instrument has been placed in the case, the plate is pushed into a slot until the tab engages a groove in the base of the case. The restraining cable is inserted through the hole in the backplate and into the lock. The backplate cannot be pried open at the power-cord hole without also damaging the instrument in the case.

Although many instrument manufacturers furnish locking devices with their products, most are intended for specific models. An advantage of the new antitheft case is that it can be built in just a few sizes to accommodate many different instruments. Another advantage is that no holes or other modifications have to be made to the instrument itself. Holes can be punched in the backplate of the case,



The Calculator Case Is Restrained by a cable inserted through the backplate and into a lock.

however, for electrical connections to other instruments, such as printers or display devices. Holes can also be punched in the bottom of the case to let cooling air circulate around the instrument. For even greater security, the case lock can also engage the desk or countertop.

This work was done by James J. Kerley, Jr., of Goddard Space Flight

Center. For further information, Circle 82 on the TSP Request Card.

This invention is owned by NASA, and a patent application has been filed. Inquiries concerning nonexclusive or exclusive license for its commercial development should be addressed to the Patent Counsel, Goddard Space Flight Center [see page A8]. Refer to GSC-12399.

Extending the Range of Leak Detectors

With a simple pressure-gage calibration, a mass-spectrometer leak detector can measure leakage rates up to 300 times greater than its normal limit.

Marshall Space Flight Center, Alabama

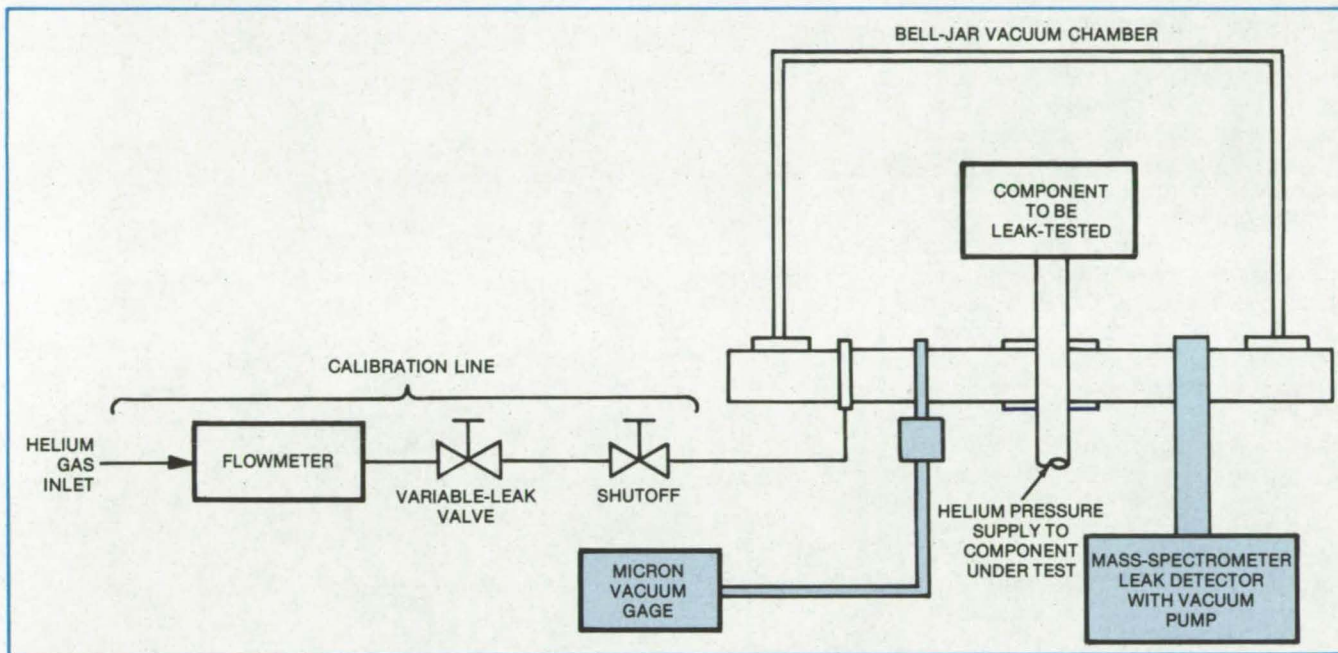


Figure 1. The vacuum pump in this **Mass-Spectrometer Leak Detector** displaces a constant volume, independent of pressure over its working range. Thus, a vacuum gage can be calibrated to measure leakage rates above the normal range of the spectrometer.

Helium leakage rates below about $0.0005 \text{ stdcm}^3/\text{s}$ are readily measured by conventional mass-spectrometer leak detectors. Occasionally, however, it is necessary to determine faster leakage rates that are out of the range of conventional mass spectrometers. Higher range spectrometers are available, but they are costly and are not found in most laboratories.

Leakage rates in the range from 0.0005 to $114 \text{ stdcm}^3/\text{s}$ can be measured, however, by properly calibrating the pressure gage in the mass-spectrometer vacuum system. This approach utilizes the constant-volume displacement characteristic of a mechanical vacuum pump. At steady state, the pump continually removes a constant volume of gas from the vacuum chamber (Figure 1), and this displacement is independent of pressure over the normal working range of from 0 to 100 microns. Since helium leaks into the chamber at a constant

rate and is being removed at a constant rate by the pump, the steady-state chamber pressure rises in proportion to the leakage rate. Thus, the reading on a micron vacuum gage in the chamber is a measure of the leakage rate.

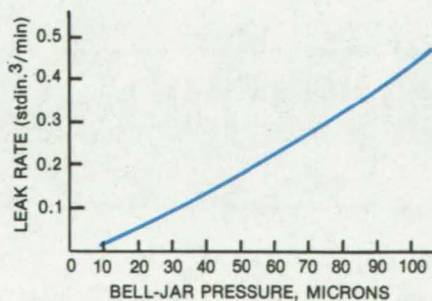


Figure 2. The **Calibration Curve** of leakage rate versus vacuum-gage reading is nearly linear. The slight curvature in the upper range is caused by back pressure from the vacuum chamber.

The system is calibrated to establish a curve of leakage rate versus micron level by letting helium into the chamber at a known rate and recording the pressure (Figure 2). The accuracy of the measurement depends on the accuracy of the micron gage, which is typically ± 5 percent.

The calibration should be carried out at the component test temperature to eliminate outgassing effects in the chamber. Of course, the leakage of the vacuum system must be extremely small for the calibration to be valid; and to reduce outgassing by newly assembled parts, the system should be pumped for at least 48 hours before it is calibrated.

This work was done by M. E. Burr of Rockwell International Corp. for Marshall Space Flight Center. For further information, Circle 83 on the TSP Request Card.
MFS-19411

Attaching Strain Transducers to Fragile Materials

An A-shaped clamp prevents damage to thin, brittle specimens.

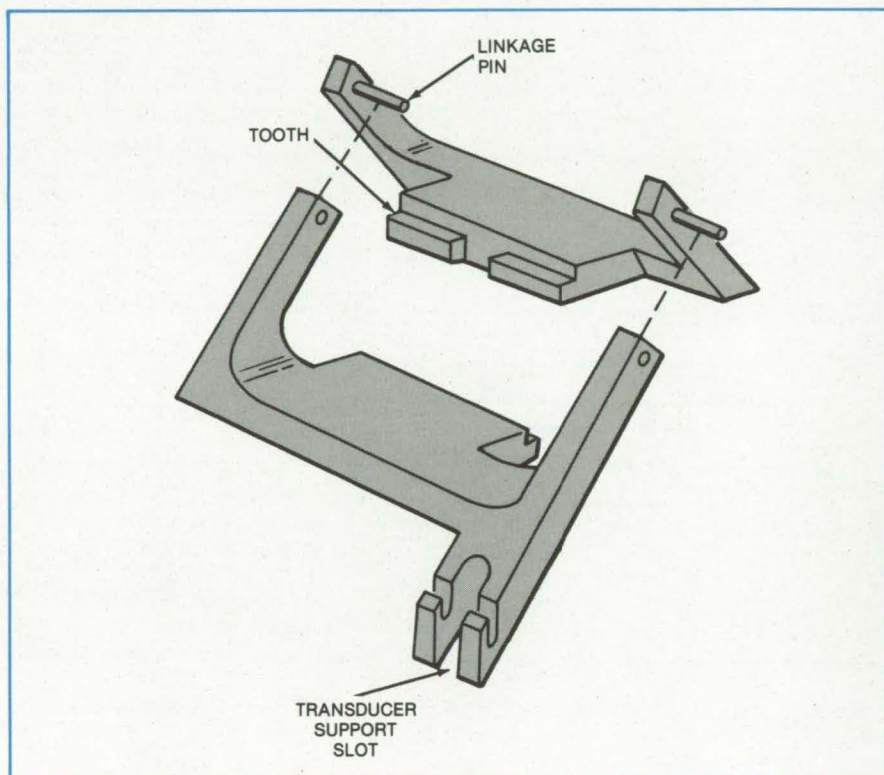
Lyndon B. Johnson Space Center, Houston, Texas

A simple clamp gently holds brittle or fragile strips during high-temperature stress/strain testing. The clamp also supports a displacement transducer away from the heated zone, and it defines reference points for the strain measurement on the specimen surface. Unlike rigidly attached supports, the new clamp prevents the specimen from cracking due to unequal thermal expansion between it and the holder. Moreover, the clamping force is constant over the wide range of temperatures encountered in the test.

The clamp is assembled from two components (see figure). The components form an A-bar that pivots about the linkage pins at its apex. The teeth on the two members rest against opposite sides of the specimen.

The clamping force is increased by the weight of the transducer, which hangs from slots on opposite sides of the A-bar. The geometry and dimensions of the clamp determine the force on the specimen. For stress/strain measurements, it is desirable to clamp the specimen firmly but with minimum stress. Thus the device illustrated has a rather large moment arm from the teeth to the pivot pin.

This work was done by Michael F. Duggan of Lockheed Missiles & Space Co., Inc. for Johnson Space Center. No further documentation is available. MSC-16580



This **Clamp for Thin, Brittle Strips** consists of two parts that link together by pins. The teeth gently clamp the sides of a test specimen (not shown). A strain transducer can be supported from the slots in the clamp. The holder was originally developed to test ceramic glazes on samples of silica used for surface insulation on the Space Shuttle.

Audible Monitor for Electroplating

"No buzzer" indicates early problem in electroplating.

Marshall Space Flight Center, Alabama

A buzzer connected to a magnetic switch serves as an indicator when a part is properly immersed into an electroplating bath. As the part is lowered into the bath, the buzzer sounds, indicating that current flows through the part. If the current is cut off accidentally, the buzzer stops — a

warning that the part must be removed and refinished before plating is resumed, otherwise the plating will not stick. The buzzer operates only during the initial stage of the electroplating process.

The indicator (see figure) is a coil with magnetic switch and a buzzer.

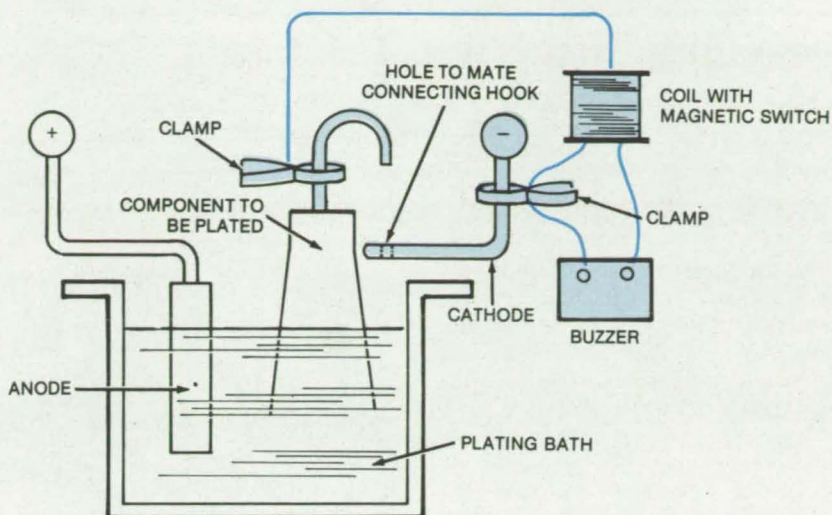
One end is clamped to the part to be plated (in this case the connecting hook); the other is connected to the cathode of the electroplating system.

As the component is lowered into the bath, current flows between the anode and cathode via the clamp holding the connecting hook. This

current closes the magnetic switch that activates the buzzer. The buzzer sound indicates that the component is connected and that current flows through it. The buzzer continues to sound until the component is lowered to the point where the connecting hook mates with the hole in the cathode terminal. Direct connection with the cathode shunts the coil, shutting off the buzzer.

The indicator can prevent unnecessary waste of electrical energy and labor, and is easier to monitor than pilot lights, which need constant visual attention.

This work was done by Eugene A. Burowick of Rockwell International Corp. for **Marshall Space Flight Center**. For further information, Circle 84 on the TSP Request Card. MFS-19333



A Buzzer indicates current flow through a component while it is being submerged into the electroplating bath. No sound indicates no current flow, which means that the component must be removed and refinished before plating is resumed.

Inspecting Cracks in Foam Insulation

A dye solution indicates extent of cracking.

Marshall Space Flight Center, Alabama

The extent of cracking in spray-on foam-insulation (SOFI) samples is determined by the use of a dye solution. The dye penetrates the crack, and when the sample is dissected, the dyed section shows the original crack depth clearly. Trying to determine the crack depth by examining an undyed cross section of foam is difficult because the crack often expands or deepens during the dissection.

The dye solution used is a 0.1-percent solution of methylene blue in denatured ethyl alcohol. This highly

visible solution penetrates cracks completely and evaporates quickly. The dye is injected by a large (14-gage) hypodermic needle across the crack on the foam surface. When the solvent evaporates, the sample is dissected, and the blue dye shows the depth and extent of the cracking. Thus, subsurface cracks and delaminations from the substrate are clearly indicated.

The technique is suitable for any plastic-foam sample subjected to structural or environmental tests. A nondestructive method is possible by

the use of an X-ray opaque solution instead of the dye solutions. The X-rays of the foam cross section will then reveal the extent of any cracks. A similar approach can be used with low-energy radioactive tracers to follow cracks or by an electroless plating solution to metallize crack surfaces for X-rays.

This work was done by Larry W. Cambell and Gustave K. Jung of Martin Marietta Corp. for **Marshall Space Flight Center**. No further documentation is available. MFS-23799

All-Electric Gas Detector

A new instrument identifies gases by detecting changes in the dielectric constant due to the absorption of laser radiation. Potentially simpler and more reliable than conventional optoacoustic analyzers, the instrument requires no pressure transducer or microphone. It can detect water vapor, fluorocarbons, and nitrogen compounds that indicate the presence of explosives.

(See page 45.)

Projection Optics for a Laser Velocimeter

Novel projection optics for a laser velocimeter eliminate tedious calibrations by scanning a constant focal volume over the entire focus-position range. The heart of the optics is a two-lens afocal combination, for which the net magnification is independent of the object distance. The optics can be used with either forward-scatter or backscatter laser velocimeters.

(See page 51.)

Inexpensive Land-Use Maps Extracted From Satellite Data

Land-use maps can be drawn inexpensively and accurately by a method that interprets satellite photographs. Areas that have similar textures on the image are blocked out on a transparent overlay and are assigned a land-use category according to prescribed guidelines. In tests, the procedure evaluated land use with an accuracy of 74 percent.

(See page 150.)

Measuring Insulation Thickness

An easily calibrated eddy-current meter measures the thickness of thermal insulation on metal substrates.

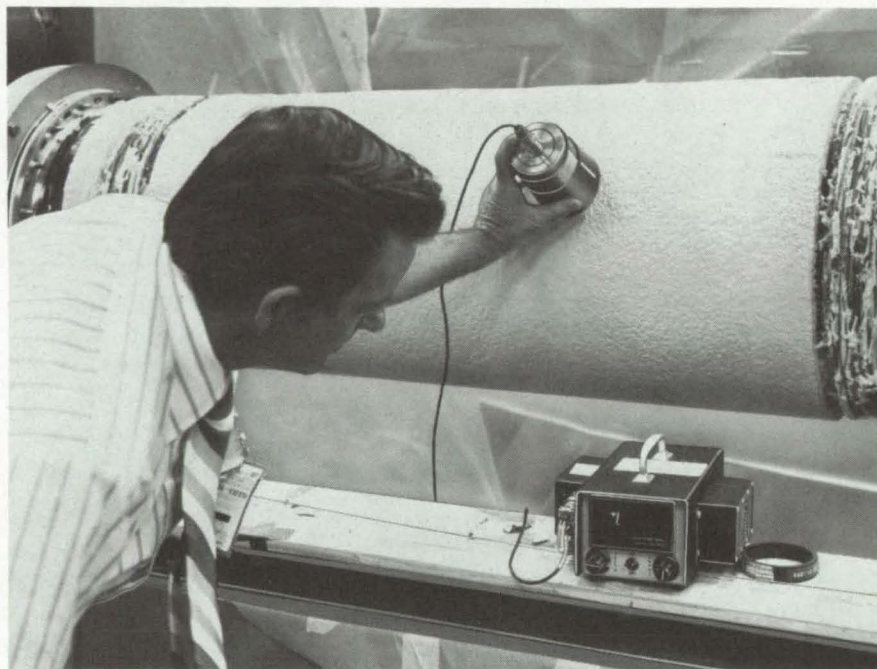
Marshall Space Flight Center, Alabama

The thickness of foam insulation on pipes or flat surfaces can be measured by a commercial eddy-current meter that has been calibrated with specially designed adapters (see figure). The adapted meter is also suitable for determining the thickness of other nonconductive materials on conductive substrates; for example, the thickness of fiberglass parts for boats or automobiles can be measured while the parts are still in the mold.

With the new technique, it is not necessary to have the meter specially calibrated by the manufacturer. Instead, one can adjust the instrument as often as necessary for each situation and substrate metal. The technique is particularly useful for sprayed-on insulation. With spraying, it is not always possible to apply insulation uniformly, but it is nevertheless necessary to ensure that the insulation thickness is adequate.

The eddy-current meter is calibrated on bare metal of the same type that serves as a substrate for the insulation. First, the zero point is established: An adapter is placed over the meter probe to position it 0.200 inch (0.508 cm) above the bare metal, and a knob is adjusted so that the meter indicates zero voltage. (The zero adapter can be used on both flat and cylindrical surfaces; for the cylinders, a V-groove in the adapter aligns the probe with the centerline of a pipe or similarly curved object.)

Next, the full-scale meter reading is established: Another adapter is placed over the zero adapter, the probe is placed on the bare metal, and a knob is adjusted so that the meter indicates



The **Thickness of Insulation** on a 17-inch (43-cm) pipe is measured with an eddy-current meter. The probe is being used with the zero adapter and the 1-1/2-inch spacer (see text); thicknesses up to 1-1/2 inches can be measured. The 1/2-inch spacer can be seen next to the meter.

its maximum voltage. One of two adapters is used for this part of the calibration: a short adapter for insulation thicknesses up to 1/2 inch (1.3 cm) or a longer one for thicknesses up to 1-1/2 inches (3.8 cm). For thicknesses up to 2 inches (5.1 cm) the two adapters can be combined. Calibrating for maximum voltage indication at 1/2, 1-1/2, or 2 inches allows the user to take full advantage of the precision of the instrument in the lower thickness ranges.

This calibration is based on the assumption that the voltage indication

is linear with respect to insulation thickness. Thus, a highly-linear eddy-current meter must be used.

*This work was done by D. M. Munn of Martin Marietta Corp. for **Marshall Space Flight Center**. For further information, Circle 86 on the TSP Request Card.*

Inquiries concerning rights for the commercial use of this invention should be addressed to the Patent Counsel, Marshall Space Flight Center [see page A8]. Refer to MFS-23798.

Burn-Test Apparatus for Fiber Composites

A metal grid and electric lamp make more-sensitive burn-test apparatus.

NASA's Jet Propulsion Laboratory, Pasadena, California

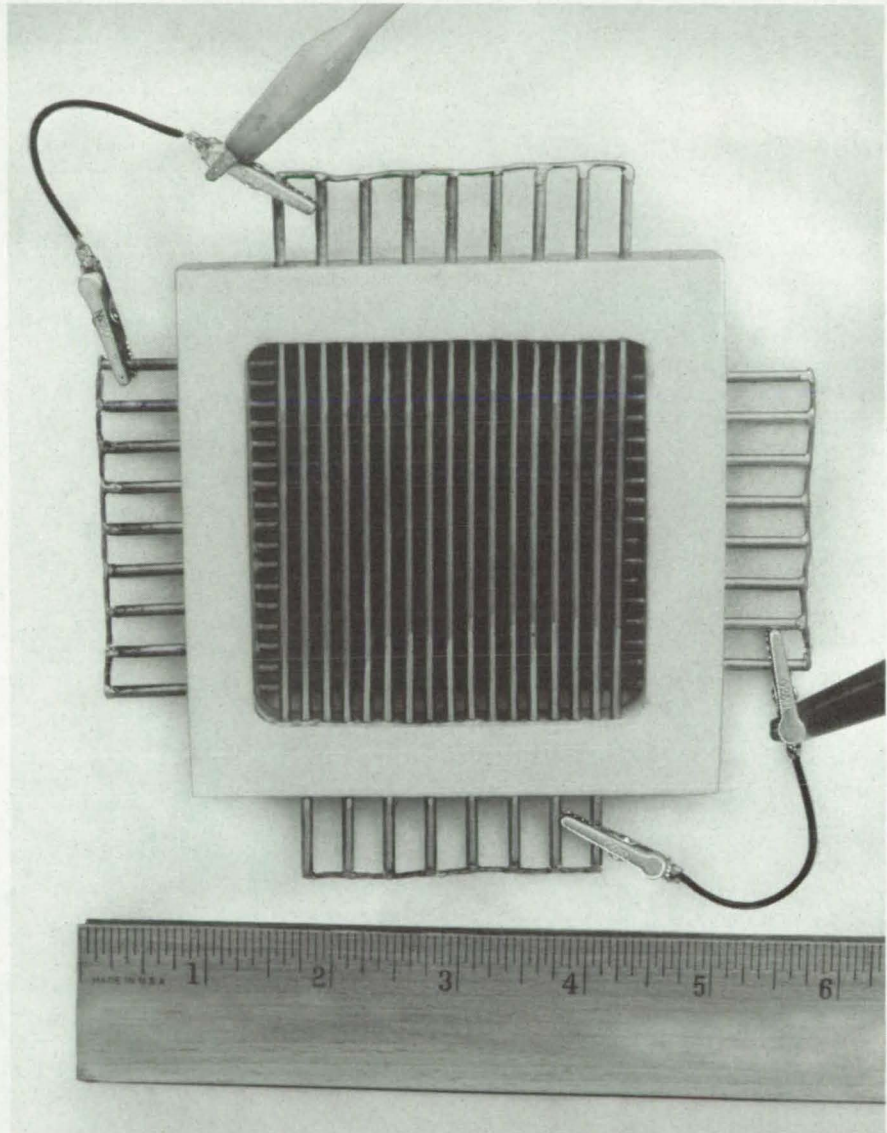
A new burn-test apparatus monitors the release of conductive carbon fibers from a specimen of carbon-reinforced composites exposed to flame. Made simply from conductive metal grid and an indicator lamp, this setup is more sensitive than photographing or physically trapping and counting the fibers, particularly when carbon fiber diameters are under $10\text{ }\mu\text{m}$.

Two mutually-orthogonal brass conductivity grids are spaced $1/16\text{ in.}$ (1.6 mm) apart (see figure). In each grid, adjacent parallel elements are connected to the alternate lamp terminals. With this arrangement the conductive fiber causes a short whenever it contacts two adjacent parallel grids. Fibers passing through the first grid are caught by the second. The lamp lights every time there is a short.

Tests are conducted with the double grid inside a glass chimney. The sample is tested in a funnel so that all the burning products enter the chimney toward the grid.

In a typical test, a fiber composite sample mounted in a mechanically vibrated holder is exposed to propane flame. The test is timed from the start until the lamp lights, indicating the first release of a conductive fiber. The time is recorded for various composites and the composites analyzed to improve their safety. The grid is not sensitive to smoke or any other particles.

This work was done by Warren L. Dowler, James D. Quinn, Kumar N. Ramohalli, and Donald E. Udlock of Caltech for NASA's Jet Propulsion Laboratory. For further information, Circle 87 on the TSP Request Card. NPO-14578



The **Double-Grid Arrangement** incorporates two mutually orthogonal sets of conducting grids. On each grid the adjacent elements are connected to alternate lamp terminals. Conductive fibers from a burning composite sample are trapped in the grids, causing shorts that light a lamp.

Books and Reports

These reports, studies, and handbooks are available from NASA as Technical Support Packages (TSP's) when a Request Card number is cited; otherwise they are available from one of NASA's Industrial Application Centers or the National Technical Information Service.

Measuring Moisture in the Atmosphere

Field and laboratory techniques are surveyed.

A 43-page report describes instruments for measuring moisture in the air. The report categorizes instruments according to sensing method:

- Thermodynamic:** Based on determining simultaneously wet-bulb and dry-bulb temperatures (instruments such as the sling psychrometer and the Assmann psychrometer);
- Hygroscopic:** Based on a dimensional change in a moisture-absorbing material, such as human hair, animal membranes, or natural or synthetic fibers;
- Condensation:** Based on the measurement of the temperature at which moisture in the air forms a dew on a cooled surface;
- Absorption:** Based on the measurement of the mass of moisture absorbed by a desiccant (as in the gravimetric hygrometer) or on the measurement of the change in electrical resistance of lithium chloride effected by moisture absorption (as in the dew cell);
- Diffusion:** Based on the preferential retention of diffused moisture by certain porous materials, such as clay, gelatin, and cellophane; and

•**Optical:** Based on the effect of absorbed moisture on properties such as refractive index or infrared or ultraviolet absorption (spectroscopic hygrometer).

For each category, the report discusses accuracy and response speed and compares advantages and disadvantages.

Meteorological moisture measurements in the field are emphasized, although a section of the report briefly describes methods best suited to measurements in the laboratory. Another section covers methods for measuring the moisture in the upper atmosphere with instruments onboard aircraft and balloons. A list of 17 source documents is included.

This work was done by Dale L. Johnson of Marshall Space Flight Center. Further information may be found in NASA TM-78190 [N78-31405], "Instruments for Measuring the Amount of Moisture in the Air," a copy of which may be obtained at cost from the New England Research Application Center [see page A7]. MFS-25032

Friction Coefficients of PTFE Bearing Liner

New data defining coefficient of friction of PTFE bearing liner as a function of temperature

PTFE (polytetrafluoroethylene) bearing liners are used on thrust-vector attitude-control gimbals of large liquid rocket engines to minimize friction and to extend wear life. At the time of its introduction, no data were

available on frictional characteristics of PTFE under temperature extremes and in vacuum environment. Recently, however, tests were conducted and the data obtained.

Laboratory tests had been conducted and reported on a full-scale model to obtain the coefficient of friction as a function of temperature at bearing-unit pressures in the 12,000- to 15,000-psi (82.8×10^6 - to 103.5×10^6 -N/m²) range. Static and dynamic coefficients of friction as functions of temperature had been obtained. Results show that friction remains essentially unchanged even at cryogenic temperatures.

Tests were also run on reduced-scale hardware to determine the effects of vacuum. Extended periods in a vacuum of 10^{-8} torr posed no problem on the bearing material. Life was unaffected, performance remained consistent, and signs of degradation in the vacuum were not evident. Subsequent full-scale tests run on the PTFE gimbal at a temperature range of -60° to 78° F (-51° to 26° C) confirmed earlier results. The coefficient data again fell within the bands defined by tests on a full scale model.

These reported data can be used as reference by designers of aircraft-control system rod-end bearings, flight-control linkage bearings, wing pivot bearings, and the like, and for bearings used on equipment in polar regions.

This work was done by C. M. Daniels of Rockwell International Corp. for Marshall Space Flight Center. To obtain a copy of the report, Circle 88 on the TSP Request Card. MFS-19389

Computer Programs

These programs may be obtained at very reasonable cost from COSMIC, a facility sponsored by NASA to make new programs available to the public. For information on program price, size, and availability, circle the reference letter on the COSMIC Request Card in this issue.

Aircraft Mission Analysis

Segmented program (NSEG) for low- and high-speed craft

Aircraft missions, from low to hypersonic speeds, can be analyzed rapidly, using the program NSEG. This program employs approximate equations

of motion that vary in form with the type of flight segment. Takeoffs, accelerations, climbs, cruises, descents, decelerations, and landings are considered. There are options for layered-atmosphere and flight-envelope mapping.

Realistic and detailed vehicle characteristics are input for accurate mission analysis, and engine scaling can

be used to fit the design being studied. Several approximate flight-path-optimization capabilities, based on Rutowski energy-like criteria, consider minimum-time or minimum-fuel flight segments and maximum-range segments during climb or descent. Takeoff and landing analysis is based on the Air Force Flight Dynamics Laboratory DATCOM method of modeling high-lift aerodynamics. The user can also supply his own high-lift aerodynamic model.

There are three main atmosphere options:

- the 1962 U.S. Standard atmosphere,
- a stratified atmosphere model, and
- an external atmosphere model supplied by the user.

The stratified atmosphere model requires the input of the number of layers (maximum 25), altitudes, temperatures, and pressures. The mission specification is open ended in that the upper limit on the number of flight segments to be included in a mission profile can be increased with a simple program change. Inputs are vehicle characteristic data, details of the mission, and selection of program options. Output can be printer-generated tabular data or contour plots on a CALCOMP plotter, CRT, or Houston plotter.

NSEG is written in FORTRAN IV and has been implemented on a CDC 6000-series computer with a central memory requirement of approximately 130K octal 60-bit words and is overlaid.

This program was written by D. S. Hauge and H. L. Rosendaal of Aerophysics Research Corp. for Langley Research Center. For further information, Circle C on the COSMIC Request Card.
LAR-12299

Dynamic Simulation and Stability Analysis

Dynamic interaction simulation of actively and passively controlled systems

The Dynamic Interaction Simulation of Controls and Structure (DISCOS) program was developed for the dynamic simulation and stability analysis of passive and actively controlled spacecraft. In the use of DISCOS, the physical system undergoing analysis may be generally described as a cluster on contiguous rigid and flexible

structures (bodies) that model a mechanical system such as a spacecraft. The entire system (spacecraft) or portions of it may be either spinning or nonspinning.

Member bodies of the system may undergo large relative excursions, such as during appendage deployment or controlled antenna motion. The general system of bodies is, by its inherent nature, a feedback system in which inertial forces (such as those due to centrifugal and Coriolis acceleration) and the restoring and damping forces are motion-dependent. The system may possess any user-defined control system in which position and rate errors are actively controlled through the use of reaction control jets, servomotors, or momentum wheels.

Bodies of the system may be interconnected by linear or nonlinear springs and dampers, by a gimbal and slider block mechanism, or by any combination of these. DISCOS can be used to obtain nonlinear and linearized time-domain response, interaction constraint forces, frequency-domain response, and associated system-stability characteristics.

DISCOS is probably the most powerful computational tool to date for the computer simulation of actively-controlled, coupled multi-flexible-body systems. The program is not easy to understand and apply effectively, but is not intended for simple problems. The DISCOS user is expected to have an extensive working knowledge of rigid-body and flexible-body dynamics, finite-element techniques, numerical methods, and frequency-domain analysis. Various possible applications of DISCOS include simulation of the Shuttle payload deployment/retrieval mechanism, antenna deployment, analysis of multispin spacecraft dynamics, and the analysis of the attitude control of large highly flexible satellites.

The overall approach of DISCOS is special in that any member body of the system may be flexible and the system is not restricted to a topological tree configuration. The equations of motion are developed by using the most general form of Lagrange's equations, including auxiliary nonholonomic rheonomic conditions of constraint. Nonlinear, flexible- and rigid-body dynamic coupling effects are accounted

for in unabridged fashion for individual bodies and for the total system.

Elastic deformation can be represented by normal vibration modes or by any adequate series of Rayleigh functions, including "quasi-static" displacement functions. The internally-derived nonlinear equations of motion may be either numerically integrated or numerically linearized by the DISCOS program. Provisions are included for environmental loading of the structure (spacecraft), including solar pressure, gravity gradient, and aerodynamic drag.

Inputs to DISCOS include the topological and geometrical description of the structure under analysis, initial conditions, a control system description, and NASTRAN-derived (or other suitable finite-element program) flexible-body input data. Specialized routines read and preprocess NASTRAN-generated input data and redimension the DISCOS program to minimize core requirements.

Outputs include an extensive list of calculated parameters for each body of the structure, the system state vector and its time derivatives, Euler angles and position coordinates and their time derivatives, control system variables and their time derivatives, and various system parameters at a given simulation time. For linearized system analysis, a frequency-domain analysis of selected system or subsystem transfer functions is possible via Nyquist, Bode, Nichols, and root-locus methods.

This program is written in FORTRAN IV for batch execution and has been implemented on an IBM 360 with a central memory requirement of approximately 1,100K of 8-bit bytes. Use of the DISCOS program requires access to a finite-element structures program such as NASTRAN for the preparation of flexible-body input data. For plotted output an SC 4020 plotting system is required. User-supplied FORTRAN IV subroutines are required for a definition of the control system and the environmental loading conditions for particular problems; extensive discussion is provided, however, to minimize preparation difficulties.

This program was written by Harold P. Frisch of Goddard Space Flight Center. For further information, Circle D on the COSMIC Request Card.

GSC-12422



Goddard Trajectory Determination

Package of programs for R. & D. or mission support

The Goddard Trajectory Determination System (GTDS), a collection of programs designed to support Earth, Lunar, and interplanetary missions, may also be used as a research and development tool. GTDS capabilities cover a wide area of computational requirements for mission support and mission analysis. The software package is a spacecraft communication, command, and tracking system containing eight main programs and numerous subroutines. It has supported research and development in trajectory determination, preflight and postflight analyses, simulation of tracking data, ephemeris generation, and related tasks.

A single GTDS program will satisfy most operational orbit-determination requirements. The various programs can, however, be executed in any sequence by using output from one program as input to a succeeding one. GTDS is capable of providing near-real-time mission support through interactive execution.

One program in the collection, Ephemeris Generation (EPHEM) program, propagates the vehicle state and state partial derivatives from prescribed initial conditions over a given timespan. Several orbital theories allow a choice of precision and efficiency; they range from a first-order analytic theory to precise Cowell numerical integration. The state transition matrix can be generated by analytic approximation or by precision numerical integration of variational equations.

Output is generated for an online printer with the spacecraft state (position and velocity) referenced to the indicated central body. As an option, the output can include the state vectors related to specified non-central bodies. Satellite ephemeris files can also be generated for subsequent use by GTDS and other systems that need satellite ephemeris data.

The Differential Correction (DC) program estimates a set of parameters in a mathematical model of spacecraft motion. These are determined so as to minimize (in a Bayesian weighted least-squares sense) the sum of the squares of the differences between computed and observed trajectory data while simultaneously constraining parameters to satisfy a priori estimates to within a specified uncertainty. Both first- and second-order statistics (mean and covariance matrix) are determined for the estimated parameters.

The Filter (FILTER) program incorporates four sequential estimation algorithms (called Extended Kalman Filter, Modified Extended Kalman Filter, Jazwinski Filter, and Modified Jazwinski Filter) that process each observation to update recursively the spacecraft state at each observation time.

The Early Orbit Determination (EARLYORB) program initially estimates an Earth orbit when there is no a priori estimate available to start a differential correction. The EARLYORB program uses several selected station observations to approximate rapidly an initial estimate for a DC program. As few as six observation measurements can be used to calculate the estimate of the spacecraft state.

The Data Simulation (DATASIM) program computes, at a specified frequency, simulated observations of an Earth-centered or Lunar-centered satellite for given sets of tracking stations and observation intervals. Optionally, random and bias errors can be applied to the observations. Observations can also be modified to account for the effects of atmospheric refraction, antenna mount errors, transponder delays, and light time delays. Observation files resulting from the Data Simulation program run can be used as input for simulations of GTDS mission support operations and for determining station tracking schedules.

The Error Analysis (ANALYSIS) program determines satellite state uncertainties about a given orbit as a function of epoch state uncertainty and observation data uncertainties for a given station-dependent tracking

schedule. This program provides for observation types modeled in the DC program, with design flexibility to model other observation types as the program is expanded.

The Ephemeris Comparison (COMPARE) program compares two ephemerides. The comparison can be specified optionally over a particular arc or over the arc of overlap between ephemerides. The radial, along-track, and crosstrack differences are output in tabular form to the printer. Optionally, printer plots of these differences can also be produced.

The primary function of the Data Management (DATAMGT) program is to retrieve data from the GTDS online data base to create temporary working files of data to be used by other programs in GTDS. In performing this function, the Data Management program operates as a part of the program that will use the working files for a future program execution. In this function, the Data Management program operates as a stand-alone program.

The Permanent File Report Generation (FILERPT) program produces reports describing the data and models existing in the GTDS online data base and SLP Ephemeris Files. At the user's option, summary or complete reports can be obtained from each file. Information concerning observations, station positions, astrodynamic constants, potential fields, integration coefficients, and other data files are obtainable.

The GTDS programs are written in FORTRAN IV and have been implemented on an IBM 360 operating under OS. Core requirements for execution of the various programs depend on the types of data being processed but should seldom exceed 490K for batch processing and 600K for interactive processing. An IBM 2250 graphics-display device is required for the interactive use of the GTDS programs.

This program was written by Bernard Dixon of Goddard Space Flight Center. For further information, Circle E on the COSMIC Request Card.
GSC-11946

Minicomputer Version of SPAR

Structural performance analysis and redesign program for minicomputers

SPAR (Structural Performance Analysis and Redesign Program) has now been implemented on minicomputers. Because of its efficiency in solving large structures problems on UNIVAC 1108 and CDC CYBER computers, SPAR was converted at Langley Research Center to run on practically any minicomputer with 64K (16-bit words) of memory. The features of the original program, described in an earlier issue of *NASA Tech Briefs* (Vol. 3, No. 2, p. 270), are retained in the new minicomputer version.

SPAR is a powerful tool for efficiently solving a wide range of finite-element structural analysis problems. It can be executed in both the batch and interactive modes. The SPAR system analyzes the stress, buckling, vibration, and thermal loads of large, linear, finite-element structural models (some exceeding 50,000 degrees of freedom). Processing cost, execution time, central memory storage, and secondary data storage are kept low through the use of sparse matrix solution techniques and other computational and data-management procedures.

In contrast to the many data files used in conventional finite-element systems, the 26 SPAR processors (programs) store and retrieve information and communicate with each other through a unified data base. A package of general-purpose matrix, data base, and analysis utilities permits significant user control and flexibility in solving problems. For example, one can modify control parameters (i.e., iteration and convergence controls) at the initiation of calculations in each processor. This can reduce unnecessary calculations and allows parameters to be adjusted according to "just-computed" results.

The SPAR structural-element library includes a very general class of beam elements (offsets for shear center and

centroid, effects of transverse shear stiffness, and nonuniform torsion), 3- and 4-node plate/shell membrane and bending elements (isotropic, anisotropic, or composite laminate), 6- and 8-node brick (three-dimensional) elements, and fluid elements. Elements may be defined singly, through a variety of network generators, or by combinations of both. The joints to which they are connected are specified, along with pointers to applicable entries in tables, such as section properties and material constants.

Efficient eigensolver techniques often allow the same finite-element model to be used for both static and dynamic analyses. In linear vibration and bifurcation buckling problems, the eigenvalue and eigenvector extraction procedure uses an iterative process consisting of a Stodola procedure, followed by a Rayleigh-Ritz procedure, followed by a second Stodola procedure, etc. This results in successively refined approximations. The eigensolver component of SPAR can also solve "shifted" vibrational eigenproblems. This is useful when computing the vibrational modes associated with eigenvalues in the neighborhood of specified constant values.

The graphics capabilities include undeformed, deformed, and vibrational-mode plots of the structure and plots of the structure modeling, including node and element labeling. Plot routines are written for a Tektronix 4014, or any standard RS-232 terminal, on the PRIME and machine-independent minicomputer versions. The PRIME 300/400/500-series PRIMOS (11-14) version of SPAR (LAR-12370) and the machine-independent minicomputer version of SPAR (LAR-12371) have a central memory requirement of approximately 64K of 16-bit words. The machine-independent minicomputer versions of SPAR are 100 percent FORTRAN, but may require minor modifications to adapt to host machines of other manufacturers.

This program was written by Olaf O. Storaasli of Langley Research Center. For further information on the PRIME version of SPAR [LAR-12370], Circle F or on the machine-independent minicomputer version [LAR-

12371], Circle G on the COSMIC Request Card.

LAR-12370 and LAR-12371

Hinge-Connected Rigid Bodies

Attitude dynamics simulation subroutines

A package of subroutines solves minimum-dimension sets of discrete-coordinate equations of motion for an arbitrary number of hinge-connected rigid bodies assembled in a tree topology. Since Hooker and Margulies published their derivation of the vector-dyadic equations of motion for an arbitrary number of point-connected rigid bodies in a topological tree, numerous computer programs based on the equations and similar generic formulations have come into wide use in the aerospace industry.

A variation on Hooker's subsequent work yields a procedure for deriving a minimum-dimension set of equations of motion for a hinge-connected system of rigid bodies. This set of discrete-coordinate equations has been derived in a detailed and systematic manner.

The subroutines in this package are dynamic simulation tools that solve the hinged-body equations for three possible situations. The first case is a system in which all the system bodies are permitted large and unrestricted rotations. The second case is a system in which all system rotations and their derivatives are small, allowing total linearization of the equations. The third case is a system with mixed large and small rotations for which partial linearization is appropriate.

These subroutines are written in FORTRAN IV and have been implemented on a UNIVAC 1108 with a central memory requirement of approximately 35K of 36-bit words.

This program was written by Gerald E. Fleischer and P. W. Likins of Caltech for NASA's Jet Propulsion Laboratory. For further information, Circle H on the COSMIC Request Card.

NPO-11964



Centroids, Moments, and Radii of Gyration

Graphical curves are digitized, and 15 quantities are displayed.

A computer program finds the area, centroid, moments of inertia, product of inertia, and radii of gyration of any closed curve given in graphical form, such as on an engineering drawing or a strip chart.

The program can be used by structural engineers to find areas, centroids, moments of inertia, and products of inertia of the cross sections of beams of complicated or irregular shapes in order to calculate beam strength and deflection. In naval architecture, it can be used to find the volume and center of gravity of liquid tanks and the center of buoyancy of tanks or hull sections. It can also be used to estimate the height of the metacenter above the center of buoyancy. These quantities are used in calculating stability.

An additional application is in chemical engineering in scaling up

chemical reactors where the dispersed plug flow model is applicable. In this case, the program is used to find the variance of one or more concentrations versus time strip charts when a tracer is added at the inlet.

All quantities are found by manually moving the cursor of a chart digitizer clockwise around a curve once, coming back to the starting point. The curve may be curved everywhere or have straight segments or have mixed curves and straight segments. In the latter two cases, the accuracy of the results can be improved by digitizing only each end of a straight segment rather than the entire straight segment.

Fifteen quantities are displayed each time a curve is digitized. They are:

1. area,
2. moment of inertia of area with respect to digitizer x-axis,
3. moment of inertia of area with respect to digitizer y-axis,
4. product of inertia of area with respect to digitizer x and y axes,
5. first moment of x for digitizer axes,
6. first moment of y for digitizer axes,

7. x coordinate of centroid,
8. y coordinate of centroid,
9. moment of inertia of area with respect to x axis through centroid,
10. moment of inertia of area with respect to y axis through centroid,
11. product of inertia of area with respect to x and y axes through centroid,
12. polar moment of inertia of area around centroid,
13. radius of gyration about digitizer x axis,
14. radius of gyration about digitizer y axis, and
15. variance in the x direction.

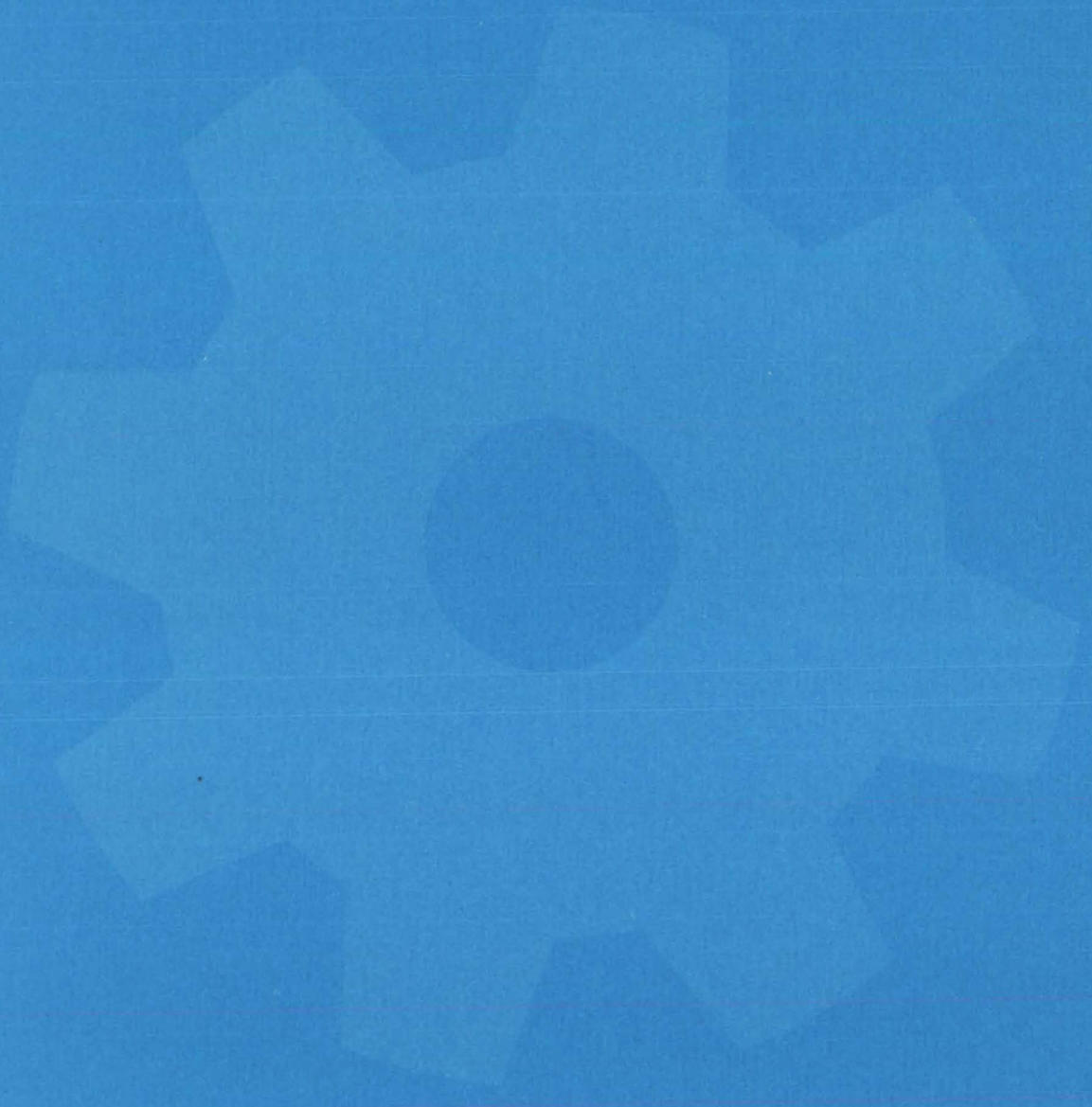
The digitizer origin may be set anywhere on the digitizer table.

The program is written in BASIC for a Hewlett-Packard HP 9830A electronic desk calculator with 9864A digitizer. However, it may be adapted for other hardware. A version is available for a Hewlett-Packard 9100A calculator with 9107A digitizer and 9101A extended memory.

This program was written by Richard W. Patch of Lewis Research Center. For further information, Circle J on the COSMIC Request Card.

LEW-12765

Machinery



Hardware, Techniques, and Processes

- 117 Ensuring Flat Cuts in Longwall Mining
- 118 Film-Advance Monitor
- 119 Plug and Drill Template
- 120 Antenna Deployment Mechanism
- 121 Remote Manipulator for IC Wafers
- 122 Volume-Change Indicator for Molding Plastic
- 123 Removable Fastener for Insulating Tiles
- 124 Rubber Valve Seal With Tough Skin
- 125 Parachute Deploy/Release Mechanism
- 126 Removable Fastener for Large Structures
- 127 Quartz Ball Valve
- 127 Metallic Vibration Isolators
- 128 Controller for a Stirling Engine
- 130 Precision Leveling of Large Machinery

Books and Reports

- 131 Stiffness and Damping of Elastomeric O-Rings

Computer Programs

- 132 Annular Acoustic Liners for Turbofan Engines

Ensuring Flat Cuts in Longwall Mining

System prevents curves or bows in the cut face by measuring the angle between adjacent sections of mining-machine track.

Marshall Space Flight Center, Alabama

A microcomputer-controlled towed vehicle (see Figure 1) automatically determines the flatness of a wall of coal or other mineral as it is being cut by a mining machine and allows the machine operator to correct the cut as necessary. It is important that the wall be kept fairly flat as it is cut, because excessive bowing can create unbalanced stresses in the mine roof, possibly causing it to collapse on the machine.

Already built and tested successfully as a prototype, the vehicle will be used for longwall mining, in which the mineral vein is divided into blocks about 900 ft (270 m) wide and 5,000 feet (1,500 m) long. A longwall shearer (with the vehicle in tow) moves on tracks along the 900-foot face of such a block, as shown in Figure 2, cutting away the mineral and dumping it on a conveyor that transports it to one of the main tunnels.

The vehicle measures the angle between adjacent sections of the track on which the mining machine moves. Since this angle is related to the curvature of the mine face, the positions of succeeding track sections can be adjusted accordingly.

In the past, wall flatness has been determined by such methods as pulling a string or directing a light beam along the cut face to observe bulges. The string method is time consuming, often taking several hours during which the mining machine cannot be used. The light beam cannot be used when the floor of the mine undulates so that the light is not visible from the end of the tunnel. Most recently, a gyroscope has been used to sense deviations from flatness, but gyroscopes require a warm-up period and may drift from their baseline settings.

In the new system, two independently-pivoted sensor-wheel assemblies press against the inside surface of the track. The two sensor-wheels are joined by an arm, and the angle between each sensor-wheel assembly and the arm is detected by a resolver.

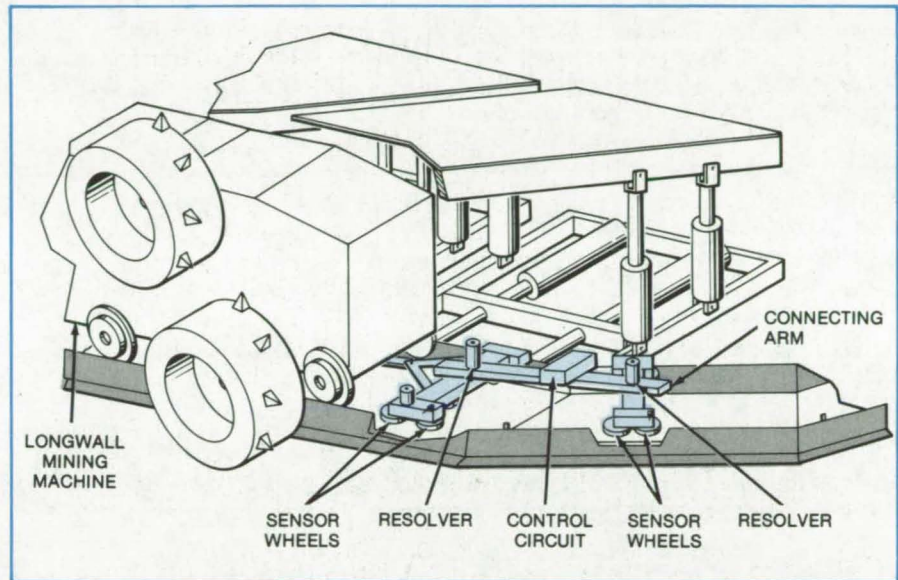


Figure 1. The **Towed Vehicle** monitors the angle between adjacent sections of track on which a longwall mining machine moves. The displacement of the mine face from the desired straight-line path is calculated by a microprocessor in the control circuit.

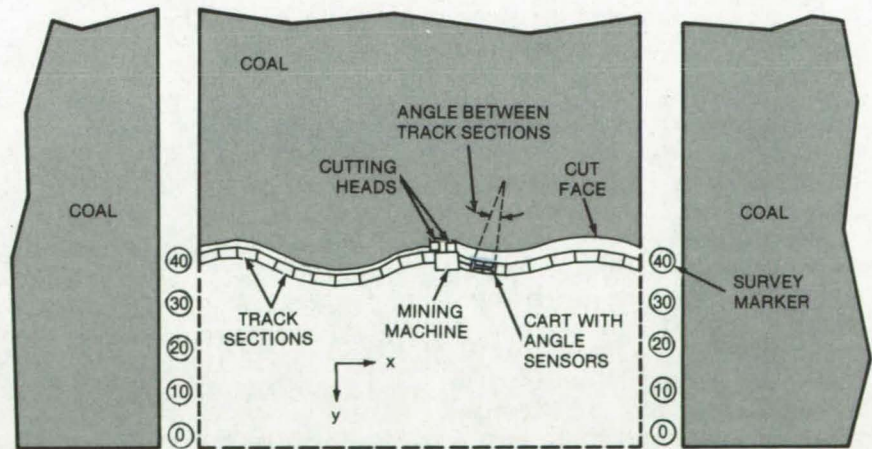


Figure 2. The **Longwall Mining Machine** makes successive cuts on the vertical face of a longwall block. Material cut from the face is loaded on a conveyor and transferred to one of the main tunnels.

The resulting electrical signal is converted to digital form by electronic circuitry on the towed vehicle.

When the sensor-wheel assemblies are on adjoining sections of track, the sum of the detected angles indicates the angle between the track sections.

Using simple trigonometry, the known length of track (5 feet, or 1.5 meters), and the measured angle, a microprocessor calculates the y-axis displacement of each track section.

(continued on next page)

Since these angle measurements are relative to the orientation of the first section of track, they only guarantee that the mine face will be cut parallel to this track, and any misalignment in this first section will be propagated down the length of the mine face.

Although it is possible in principle to orient the first track correctly by careful surveying relative to the mine main tunnel, in practice this is a rather laborious procedure. A more convenient approach makes use of the survey markers in the mine main tunnel (see Figure 2).

To compensate for the uncertainty in the starting angle, repeated sitings are made on the markers as the

machine proceeds along the track. A siting is made every 40 feet (12 meters; eight track sections). The difference between two consecutive sitings is equal to the net displacement along the y-axis of the mining machine. From this displacement and the known length of track (40 feet), it is possible for the microprocessor to determine the starting angle. Thus, every 40 feet, the calculated displacements from one track section to the next are redetermined by using an updated starting-angle error. In this way the error induced by a nonzero starting angle is made progressively smaller.

The repeated error checks also reduce calibration errors and errors

induced by the curvature of individual track sections. The measurements, calculations, and a plot of the track path are printed out or are displayed on a cathode-ray tube.

This work was done by Richard A. Campbell, James R. Currie, Ensley T. Deaton, and Ralph R. Kissel of **Marshall Space Flight Center**. For further information, Circle 89 on the TSP Request Card.

This invention is owned by NASA, and a patent application has been filed. Inquiries concerning nonexclusive or exclusive license for its commercial development should be addressed to the Patent Counsel, Marshall Space Flight Center [see page A8]. Refer to MFS-23726.

Film-Advance Monitor

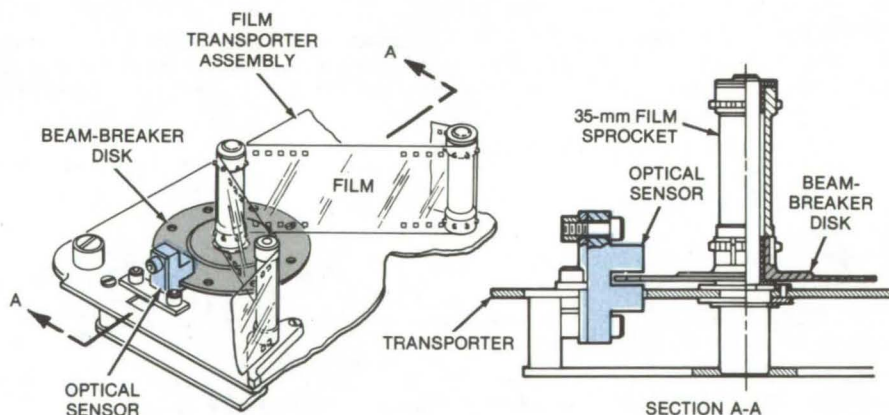
A simple add-on checks film advancement in remote cameras.

Langley Research Center, Hampton, Virginia

The problem of monitoring film advancement in a remote camera can be solved with a relatively simple modification of the film transporter. By adding an optoelectronic sensor and an idler sprocket with a beam-breaker disk, it is possible to generate an electronic output that registers the motion of the film. This approach, which is used in a 35-mm camera aboard the Space Shuttle, can be very helpful to operators of cameras placed in hostile environments.

The film-monitoring hardware used in the Shuttle camera is illustrated in the figure. A perforated disk is securely attached to a 35-mm film sprocket, and this assembly is installed in the film path. The perimeter of the disk passes through a slot in an optical sensor consisting of a light-emitting-diode (LED) source and a phototransistor detector. This sensor is available from several commercial vendors.

Each time one of the holes in the disk passes through the sensor, it allows light to reach the phototransistor, and a pulse appears at the sensor output. Thus, the film is



This **Film-Advance Monitor** consists of a beam-breaker disk and an optoelectronic sensor. If the film breaks or jams, the malfunction is indicated by the cessation of pulses from the sensor.

advancing properly if the pulses appear at the correct frequency while the transporter is operating. If the film breaks or the film drive jams, the pulses cease, indicating a malfunction to the operator. In the Shuttle experiments, the film-advance indicator is also used in a "dry run" before a flight to check that the film has been packaged correctly.

This work was done by Francis R. Dreisbach, E. Thomas Freeman, and Charles W. Stump of **Langley Research Center**. No further documentation is available.

Inquiries concerning rights for the commercial use of this invention should be addressed to the Patent Counsel, Langley Research Center [see page A8]. Refer to LAR-12474.

Plug and Drill Template

A template spots holes and plugs in honeycomb panels.

Lyndon B. Johnson Space Center, Houston, Texas

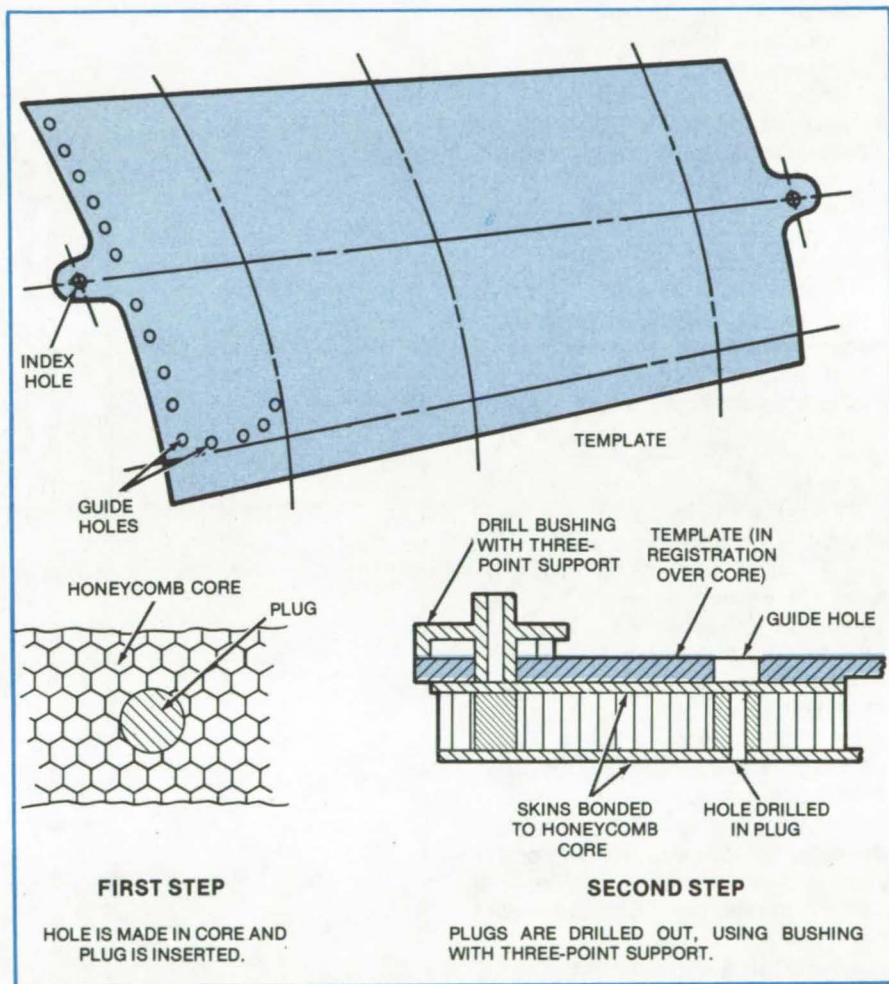
Special reinforcing plugs are often installed in the core of a honeycomb sandwich panel to reinforce the panel at points where rivets or other fasteners are to be inserted. Once the plugs are in place, the sandwich facesheets are attached, concealing the plugs from view.

To eliminate guesswork in relocating the plugs for drilling and to eliminate the need to make the plugs oversized to accommodate inevitable misalignments, designers working on the Space Shuttle devised a template for both installing the plugs and then drilling them after the sandwich facesheets are in place. The template, with holes precisely at the plug locations, guides a drill bit into the center of each concealed plug. This approach saved considerable time and reduced weight by allowing smaller plugs to be used.

When assembling the panel, the template (see figure, top) with properly-laid-out guide holes is placed over the bare honeycomb core. Holes are drilled in the core through every guide hole in the template, and plugs having the same diameter as the template holes are inserted (see figure, bottom left). The honeycomb core is then covered with skin.

When the fastener holes are to be drilled through the concealed plug centers, the template is repositioned over the skin. (Index holes on the template align with registering marks on the skin.) This aligns each guide hole directly above each plug. A bushing with a three-point support guides a drill bit precisely through the plug center (see figure, bottom right). This procedure is repeated until every plug is drilled.

This work was done by Saverio Orella of Grumman Aerospace Corp. for **Johnson Space Center**. No further documentation is available.
MSC-16748



A **Drill Template** (top) spots the holes into which plugs (bottom, left) are inserted in a honeycomb core. With the plugs installed and the sandwich skins in place, the template is again in place (bottom, right), and a special three-point drill bushing will guide a drill through the plug centers.



Antenna Deployment Mechanism

A reliable mechanical system operates a telescoping mast.

Goddard Space Flight Center, Greenbelt, Maryland

An all-mechanical antenna deployment system is operated by a single cable tensioned by an electrically driven drum. The cable runs through a set of pulleys fixed to the telescoping antenna mast. The tension produces forces that extend the mast; a ratchet prevents premature antenna retraction; and a special latch holds the antenna in a retracted position.

Figure 1 illustrates the arrangement. The mast, as shown, is retracted. It comprises a set of telescoping tubes. The exterior tube is rigidly fixed to a stable support. The interior tubes are latched in a retracted position by a cam-operated latching mechanism, actuated by the operating cable.

The cable is guided through a set of pulleys. Each upper and lower pulley pair is rigidly fixed to its respective tube. The cable is terminated inside a small tube at the base of the innermost telescoping tube section. The opposite cable ends are connected through two idler pulleys to two grooves of the drum. The grooves wind the cable ends on opposite sides of the drum (same direction).

The drum is driven by a pair of dual-drive motors, the pair being used for improved system reliability. The motors are coupled to the drum by a set of bevel gears.

Located directly above the drum is the ratchet wheel (see Figure 2). This wheel, controlled by spring-urged pawl (not shown), prevents inadvertent reverse rotation of the drum while the antenna is being deployed. The wheel is coupled to the drum by two parallel pins of a driving fork; the pins pass through a pair of openings in the drum and the wheel. The driving fork is spring-biased to remain engaged with the wheel. It can be disengaged via a handle to permit the drum to rotate in the opposite direction as the antenna is retracted.

A second important feature is the latch on the top of the support plate. It keeps the innermost tube (and therefore the entire mast) latched until deployment.

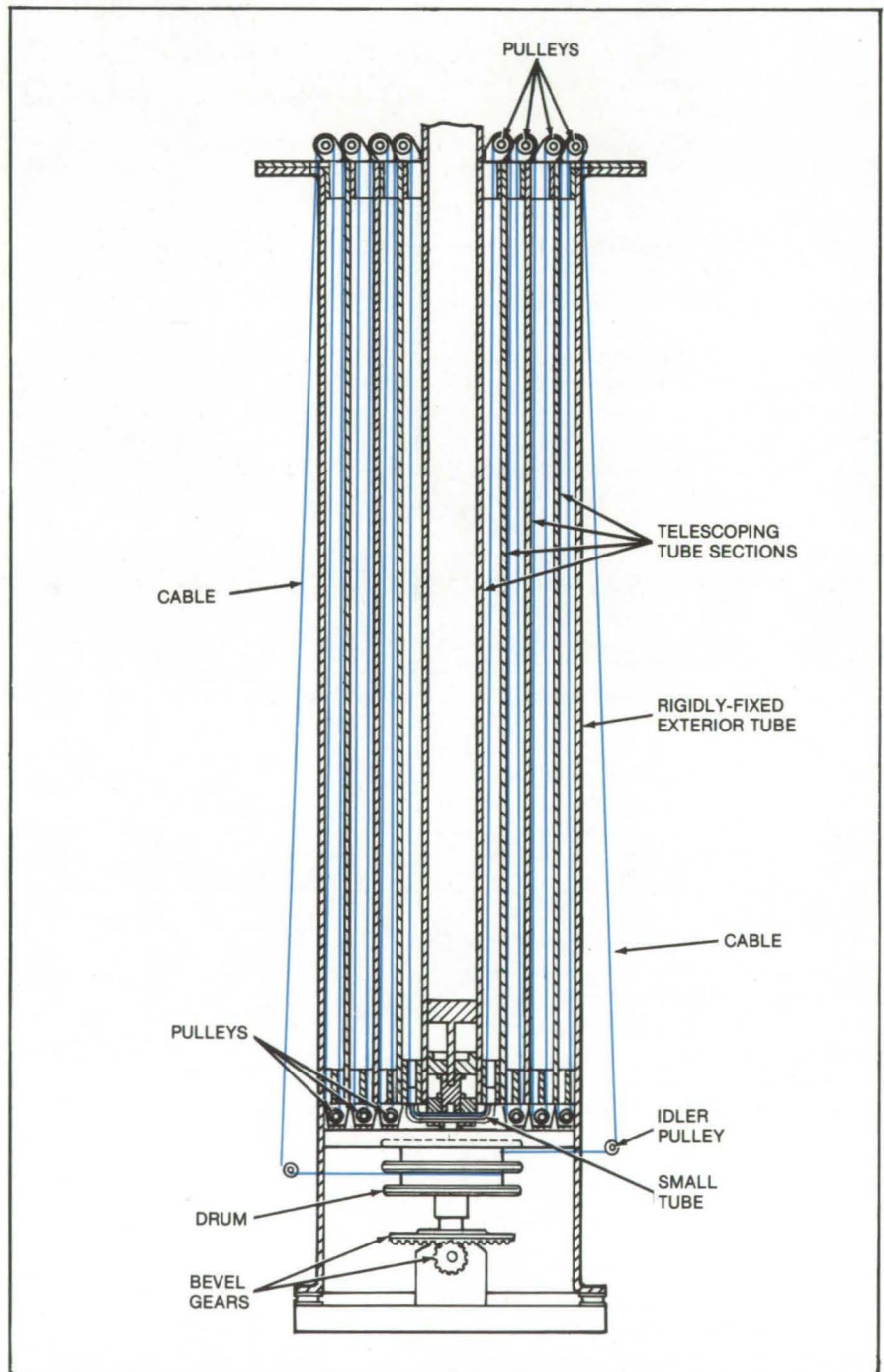


Figure 1. An **All-Mechanical Antenna Deployment System** is operated by cable driven by a pair of electrical motors. As two ends of the cable are wound onto the drum, the resulting forces extend the telescoping antenna mast tubes through a system of pulleys.

An opposing pair of spring-biased latchbolts are mounted in guide holders that are secured to the support plate. Each bolt, biased inwardly to the system axis, has a transverse camming head (see detail). The top and bottom sides of the head are beveled. Depressed from the top or bottom by an oppositely beveled member (cam elements), these heads momentarily unlatch the bolts.

As the antenna is retracted, a downward, spring-biased, external caging member strikes the bolt camming heads with oppositely-beveled cam elements. This opens the bolts momentarily, until the interior caging-member latching head negotiates the bolt latches. Further downward motion releases the latchbolts, locking the antenna.

During the antenna deployment, the bolts are unlatched in the same way, this time from the bottom. As the drive tube moves up in the tunnel slot due to cable tension, force on the inner caging member is translated directly to the outer member. The cam elements strike the camming heads from the bottom, unlatching the bolts to release the antenna for deployment.

This work was done by C. Russell Griffin and William A. Leavy of **Goddard Space Flight Center**. For further information, Circle 90 on the TSP Request Card.

This invention is owned by NASA, and a patent application has been filed. Inquiries concerning nonexclusive or exclusive license for its commercial development should be

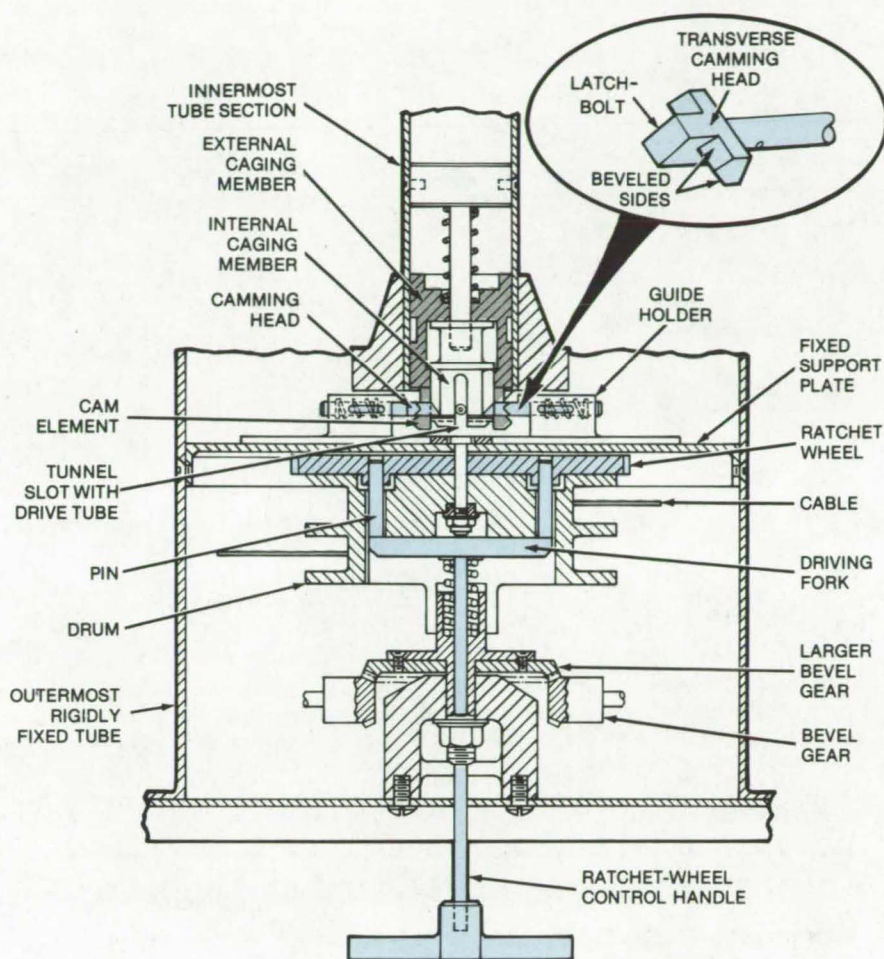


Figure 2. **Major Mechanism Features** include a ratchet wheel and a latching mechanism. The former prevents inadvertent drum rotation in the opposite direction during deployment. The latter latches and unlatches the retracted antenna automatically.

addressed to the Patent Counsel, Goddard Space Flight Center [see page A8]. Refer to GSC-12331.

Remote Manipulator for IC Wafers

Computer-controlled mechanical arm loads wafers for processing.

Marshall Space Flight Center, Alabama

A mechanical manipulator automatically loads, transports, and unloads silicon wafers between processing stations in a large-scale-integrated-circuit fabrication facility at Marshall Space Flight Center. It thus eliminates the need for human operators at various stages in the IC processing cycle, reducing the possibility of contaminating the wafers.

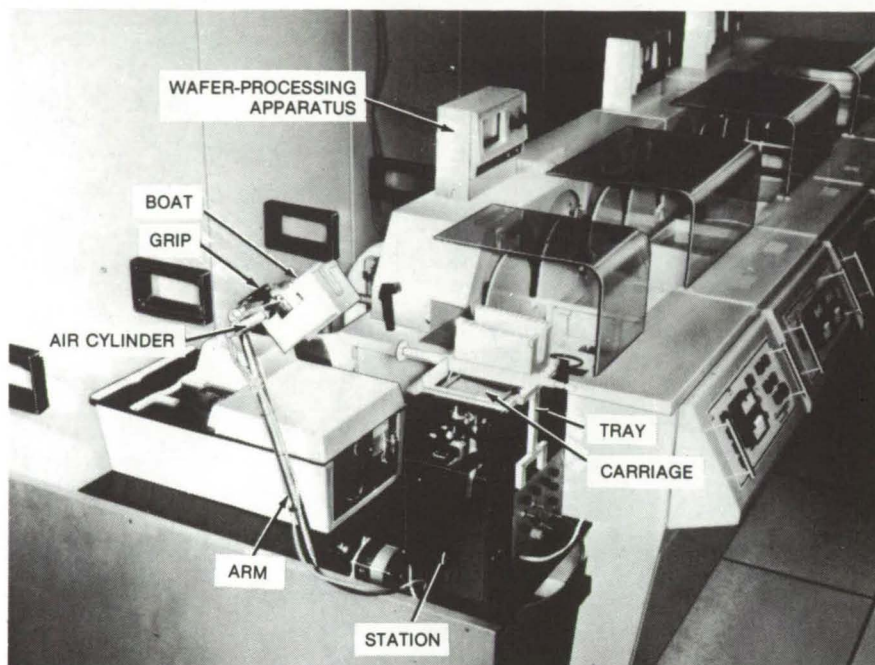
This manipulator (one of several planned for different steps in the processing cycle) handles tetrafluoroethane boats that are loaded with 25 silicon wafers each and stacks two boats on a supporting tray (see figure). Another manipulator, not shown in the figure, lifts the tray and transports it to the wafer-processing equipment. The entire load/transport/

unload operation is controlled by computer.

The manipulator has a movable arm, with a gripping device at its end, and a carriage that slides along the top of a fixed station. The arm rotates in a fixed plane about a pivot point at its base, and the carriage slides to move the tray into the path of the gripping device. In the photo, the support tray

(continued on next page)





A **Wafer Boat Is Handled** without human intervention by this manipulator. Each boat holds 25 wafers for integrated-circuit fabrication. Two boats are loaded on the support tray shown and are transported by another manipulator (not shown) for batch chemical processing.

rests on the carriage and one boat has been loaded by the manipulating arm. A second boat is held by the grip and is about to be positioned in the empty rectangular slot. After both boats are loaded, the carriage will be displaced downward, and the boats will drop into their slots in the tray.

The grip and the carriage are activated by air-pressure-driven shafts. A solenoid drives the arm around the pivot point at its base. After a boat has been deposited on the tray, a coil spring returns the arm to its original position. Microswitches next to the moving parts monitor the operation and feed signals to the managing computer.

This work was done by Jerry L. Hudgins of **Marshall Space Flight Center**. For further information, Circle 91 on the TSP Request Card.

Inquiries concerning rights for the commercial use of this invention should be addressed to the Patent Counsel, Marshall Space Flight Center [see page A8]. Refer to MFS-23846.

Volume-Change Indicator for Molding Plastic

A mechanical device monitors the molding of thermosetting resins.

Langley Research Center, Hampton, Virginia

A simple mechanical device monitors the change in volume of a plastic charge during compression/displacement molding. [See "New Compression Molding Process of Thermosetting Plastic Compounds" (LAR-10782), NASA Tech Brief B72-10356, July 1972.] The monitor helps the operator to decide whether the process pressure and temperature are set properly and whether sufficient material has been placed in the mold.

In the compression/displacement molding, the thermosetting resin is formed into a finished part during a five-step operation as outlined in Figure 1. The plastic is shaped during the displacement step as both the force and balance mandrels move through the die. It is essential that this changing cavity configuration not increase in volume during this phase, or the physical properties of the finished piece will be impaired. This can be avoided with the new monitor

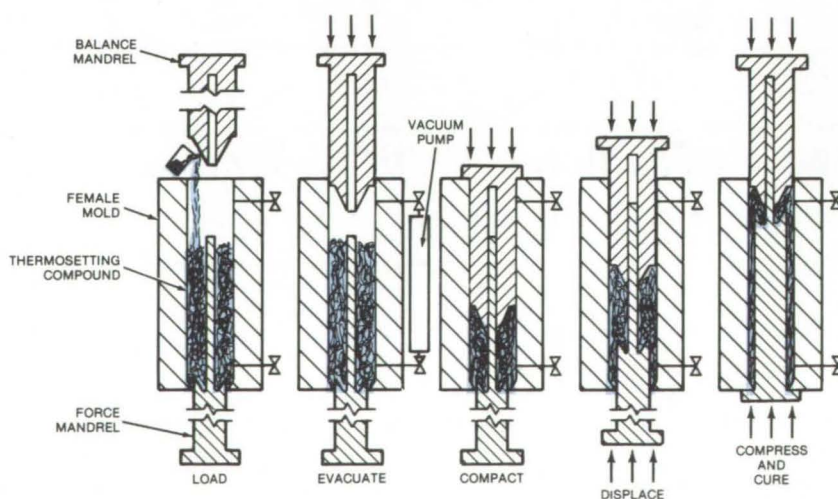


Figure 1. In **Compression/Displacement Molding**, a charge of thermosetting resin is formed into a long thin-walled tube.

that tracks the relative positions of the two mandrels.

The monitor has two concentric disks (see Figure 2), each of which is

independently driven by one of the rams of the mold. The outside disk is rotated by movement of the force ram, and the inside disk is rotated by

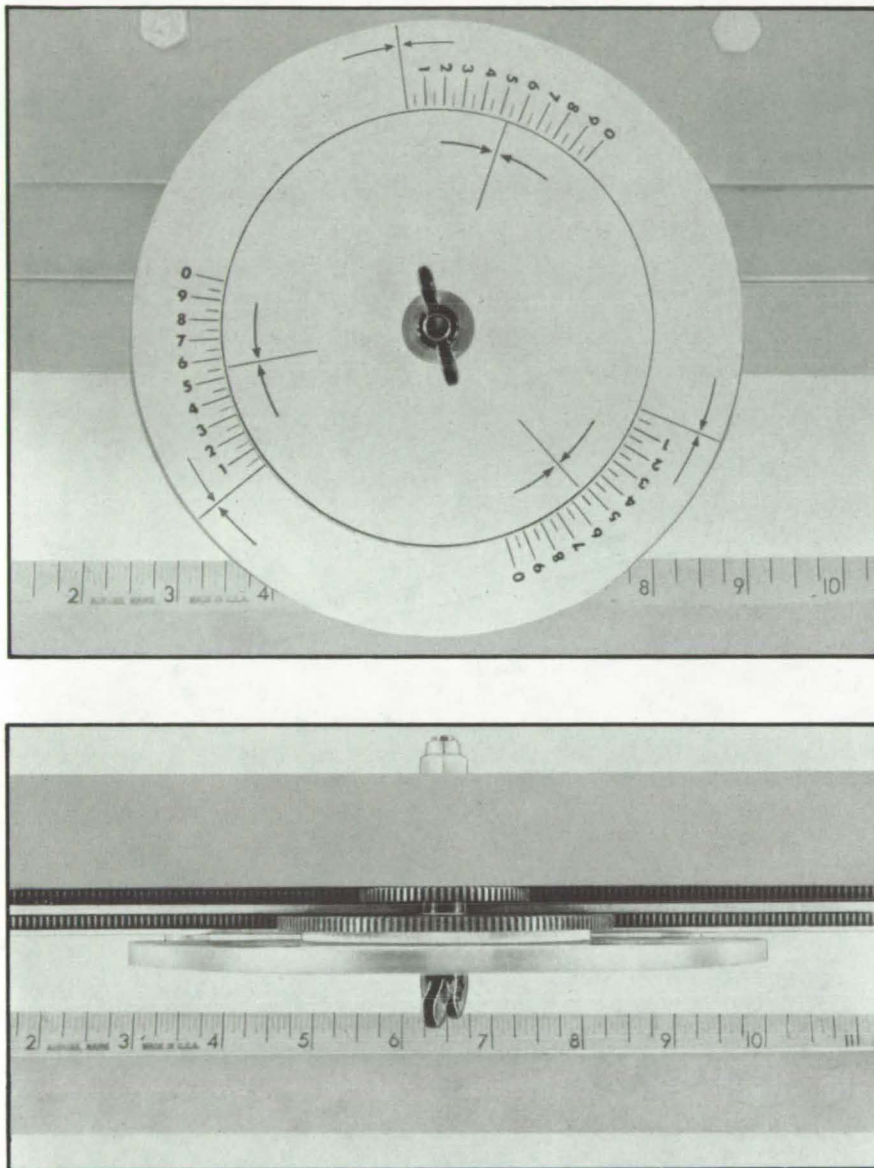


Figure 2. This **Dual-Disk Indicator** (top figure) monitors the changes in molding volume during the displacement stroke. The disks are driven independently by racks (bottom figure) that move with the mandrels in the molding apparatus.

movement of the balance ram. At the end of the compression phase and before the start of the displacement stroke, the index points on the two disks are aligned.

If the volume between the rams changes during the displacement, the index of one of the disks turns to the red or green portion of the other disk, indicating expansion or contraction, respectively, of the molding compound. A green indication is desirable since it denotes a decreasing volume and increasing plastification of the compound. A red indication is undesirable, since expansion means that the molding conditions are not properly regulated. The disks are calibrated so that deviations from batch to batch can be noted, and adjustments in temperature and pressure can be made as necessary to ensure uniformity.

The disks mate with pinion gears on a common axis: The larger of the two gears is mounted on a hollow outer shaft; the smaller gear is set-screwed directly to a solid inner shaft. The larger gear shares a ball-bearing mount with the outer disk and turns independently of the rotation of the inner shaft.

Racks driven by the rams turn the gears. The racks and gears mesh at guides attached to a baseplate. Although more sophisticated instrumentation is available for measuring relative displacements, the concentric disks are less costly and are suited to small-quantity production.

This work was done by Wilbur C. Heier of Langley Research Center. For further information, Circle 92 on the TSP Request Card.
LAR-12280



Removable Fastener for Insulating Tiles

Combination of contoured ceramic and rubber parts seals tightly and absorbs thermal expansion.

Lyndon B. Johnson Space Center, Houston, Texas

A fastening device seals holes in ceramic tiles securely over wide temperature excursions without cracking from thermal stresses. The fastener consists of an internally threaded silica insert, a threaded

silica plug, and a molded rubber retainer (see figure). The insert is bonded in a hole in the tile, and the plug with the retainer is screwed into the insert by a pronged tool. The retainer, which has a cloverleaf cross

section, is designed to absorb the expansion of the parts when the assembly is hot, and thus prevent cracking, and yet prevent the parts from loosening when the assembly is cool. The fastener can withstand temperatures up to 500° F (260° C).

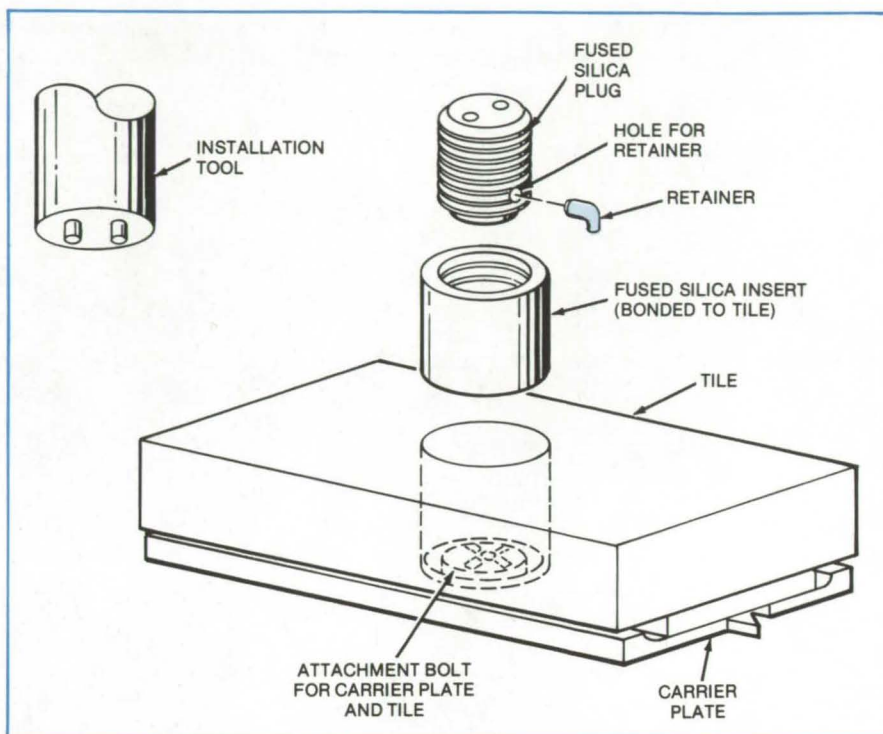
(continued on next page)

A single size of retainer fits a variety of plug sizes. The retainer is reusable, but can easily be replaced if necessary. The leg section of the retainer produces the required thread-area interference, and its body produces the required plughole interference. The locking load is the same for all plug sizes; however, the locking torque increases with plug size.

The fastener was designed to cover access holes in insulating tiles on the Space Shuttle. Such holes give access to bolts that hold tiles to the airframe, and they must be easy to seal after a tile has been attached and to unseal when a tile must be detached — hence the screwplug design of the fastener. It is expected to be useful in high-temperature industrial applications where ceramic parts must be removed and replaced.

Previous versions of the fastener used silica-topped metal pieces. These, however, tended to fail because of large internal stresses at high temperatures.

This work was done by James N. Brown, Dale H. Cade, and Harry A. Logston of Rockwell International Corp. for Johnson Space Center. For further information, Circle 93 on the TSP Request Card. MSC-16483



Rubber Retainer with cloverleaf cross section holds plug securely but accommodates expansion at temperatures up to 500° F.

Rubber Valve Seal With Tough Skin

Temperature gradient during curing is proposed for producing variable-viscosity rubber that is both pliant and durable.

Langley Research Center, Hampton, Virginia

Ideally, rubber valve seals should be made from soft rubber that fits easily into all the nooks and crannies of the surfaces to be sealed when the valve is closed. Potentially such seals can form a bond as strong as the rubber itself, if not stronger. Most practical valve seals, however, are made from a more durable, harder rubber. Harder, or higher viscosity, rubber does not spread into all the irregularities of a facing plate and, hence, is a poorer seal.

Now a new curing technique has been proposed for producing a variable viscosity seal that has a relatively hard sealing surface supported by softer rubber. The tough-skinned seal would be made by using a viselike apparatus that had two jaws equipped with independent temperature controls. In this concept, the valve seal is clamped between the two jaws for curing. The hotter jaw is set to a temperature of approximately 350° F (180° C), while the other remains at

room temperature. Under the pressure, the hotter side is cured to higher (tougher) viscosity, while the cooler side is softer. The result is a durable tight valve-seal.

This work was done by Jon W. Martin of TRW, Inc., for Langley Research Center. No further documentation is available.

Inquiries concerning rights for the commercial use of this invention should be addressed to the Patent Counsel, Langley Research Center [see page A8]. Refer to LAR-11776.

Parachute Deploy/Release Mechanism

A simple, remotely controlled device for staged, sequential deployment and release.

Langley Research Center, Hampton, Virginia

A relatively simple mechanism deploys and releases a small drogue parachute from flying aircraft. The unit is operated by signals from a single radio-control channel. Its simple approach to the problem of staged, sequential deployment and release by remote control could have uses in industrial process control and in recreational and hobby applications.

The mechanism, as shown in Figure 1, has two cables, one for deploy and the other for release, that connect to a radio-controlled servo (Figure 2). There are three servo positions: loaded, deployed, and jettison. When the deploy signal is given, the servo rotates by 45° , and the deploy cable is pulled, withdrawing a pin that holds the parachute elastic band. The loose parachute spreads out behind the flying aircraft and is held by a steel plunger through a parachute attachment riser. Because it is held at the forward portion of the perimeter of the servo disk, the release line is not pulled during the 45° rotation.

The parachute continues to trail the aircraft until the signal to release is given. This turns the servo through 135° , which pulls the release cable and the steel plunger. When the plunger is pulled back, the parachute is disengaged from the aircraft.

This work was done by David B. Robelen of **Langley Research Center**. Further information may be found in the U.S. Patent referenced below, which may be purchased from the U.S. Patent and Trademark Office, Washington, DC 20231 for \$0.50 a copy.

This invention has been patented by NASA [U.S. Patent No. 3,930,628]. Inquiries concerning nonexclusive or exclusive license for its commercial development should be addressed to the Patent Counsel, Langley Research Center [see page A8]. Refer to LAR-11575.

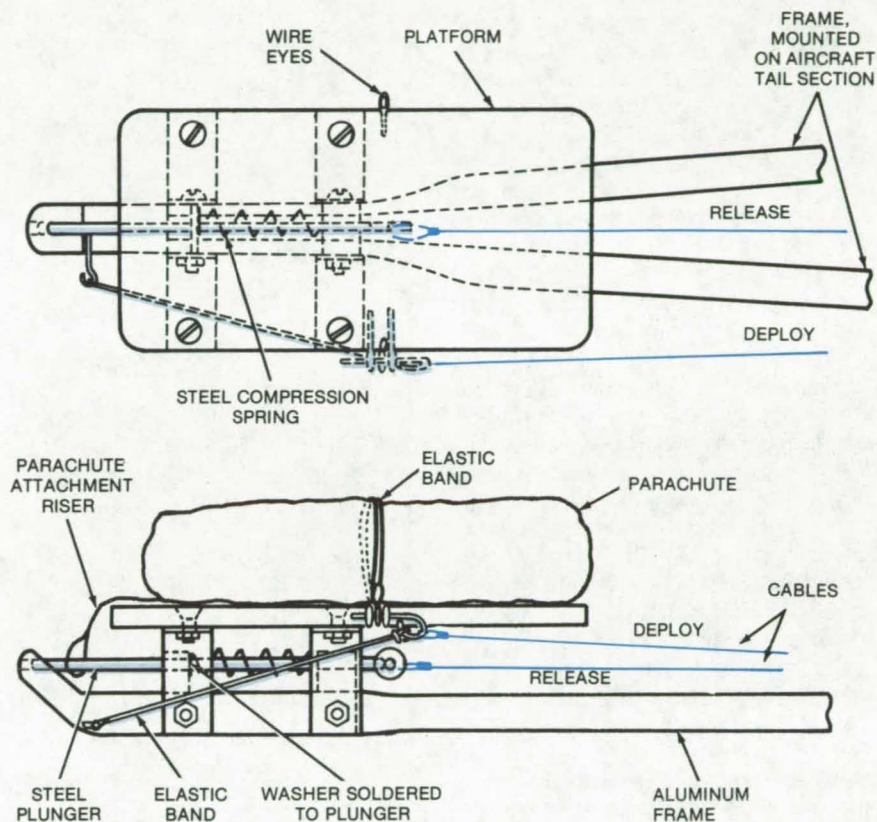


Figure 1. This **Drogue-Parachute Deploy/Release Mechanism** is mounted in the tail section of an aircraft or aircraft model. A radio-controlled servo actuates the deploy and release.

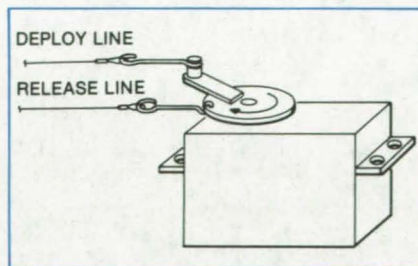


Figure 2. This **Radio-Controlled Servo** rotates to pull the deploy and release cables. The first 45° of rotation deploys the parachute, and the remaining 135° releases it.



Removable Fastener for Large Structures

Frame clamps to lateral braces for assembling trusses, scaffolds, and other structures.

Marshall Space Flight Center, Alabama

Large trusses are joined together quickly and easily, using an approach originally proposed for assembling antennas and solar arrays in space. On Earth, the method could be useful in temporary structures such as scaffolds and grandstands and for holding trusses together before they are welded or otherwise permanently bonded.

In the proposed method, four extruded beams are joined at their ends to form a square frame. This frame is the interface between the two trusses (Figure 1). The extruded beams nest on the lateral braces of the trusses and are clamped to them (Figure 2). Two parallel beams attach to one truss, and the other two beams attach to the other. The fastener can be assembled and disassembled with little effort and is adaptable to trusses of various sizes.

The extruded beam illustrated is intended for lateral braces with V-shaped cross sections; however, the cross section of the beam can be changed to accommodate other shapes, such as U- or L-channels. In addition, it may be possible to form the beam from sheet metal instead of extruding it, saving cost and weight.

This work was done by M. D. Thulson of Martin Marietta Corp. for **Marshall Space Flight Center**. No further documentation is available.

Inquiries concerning rights for the commercial use of this invention should be addressed to the Patent Counsel, Marshall Space Flight Center [see page A8]. Refer to MFS-23990.

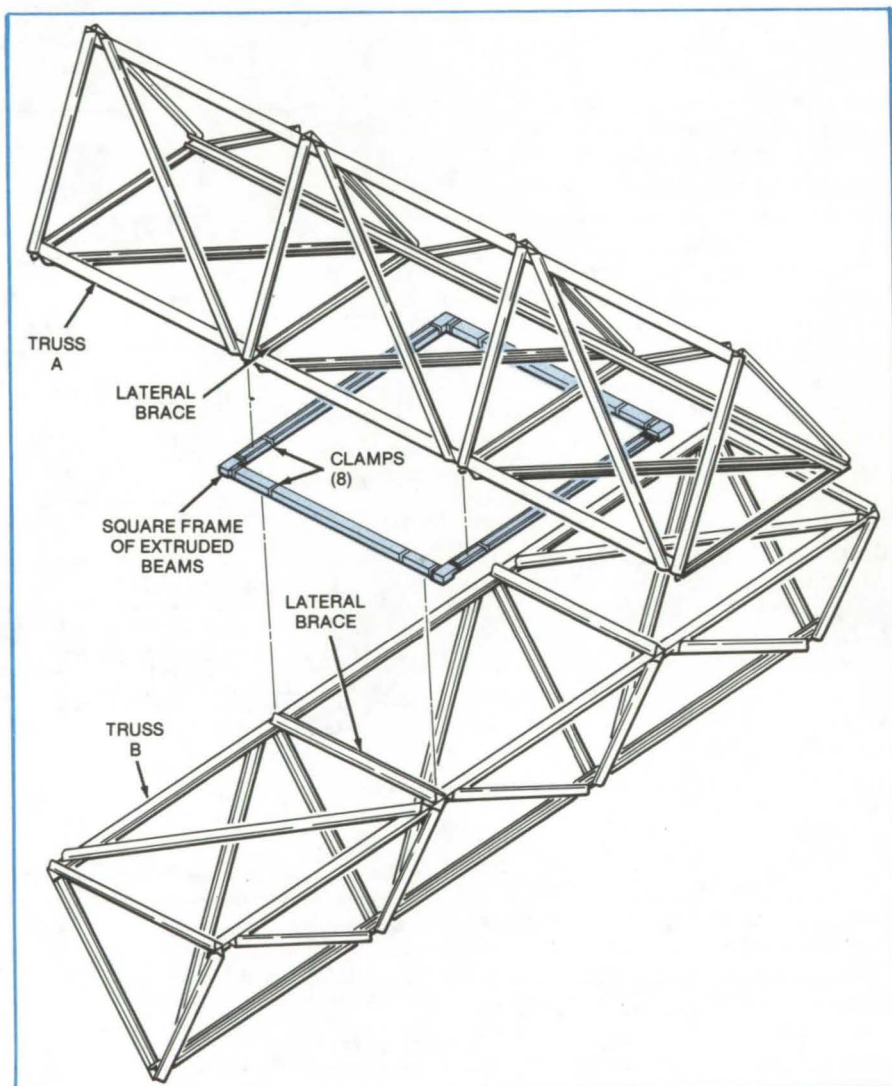


Figure 1. A **Square Frame of Extruded Beams** holds truss A to truss B. The extruded beams nest on lateral braces on each truss.

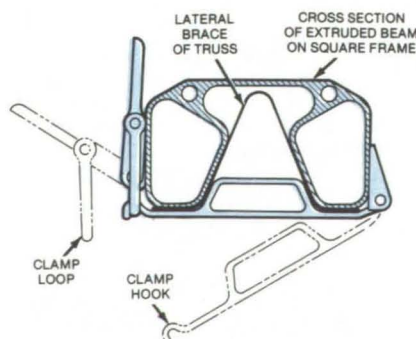


Figure 2. The **Clamp Loop Slips Over the Clamp Hook** to press the extruded beam against the lateral brace.

Quartz Ball Valve

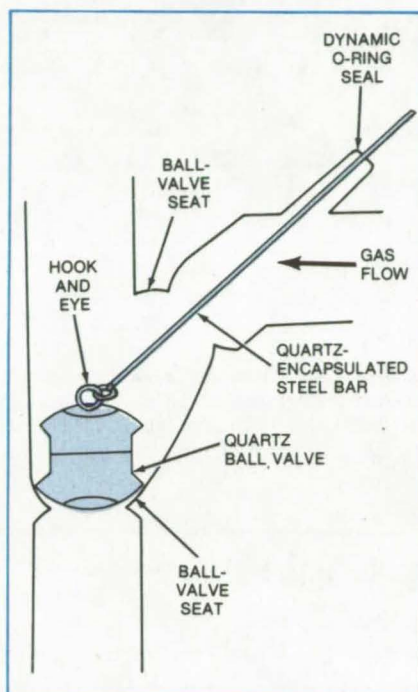
A valve for corrosive fluids
and high temperatures

NASA's Jet Propulsion Laboratory, Pasadena, California

A quartz ball valve constructed from commercially available components consists of two quartz joints sealed back-to-back and seated in quartz sockets. The valve performs at temperatures of up to 1,250° C and in corrosive chemical environments without contamination or degradation.

As shown in the figure, two quartz joints are sealed back-to-back and seat into quartz sockets. The quartz ball-and-socket joints may have an inside diameter as large as 6 in. (15 cm). The valve is operated via a quartz-encapsulated steel bar connected to the valve through a hook-and-eye arrangement.

The valve may be actuated by either an electronic solenoid coupled to the quartz-encapsulated steel bars or manually (as shown) by manipulating the steel bar sealed with dynamic O-ring seals. Both the solenoid and



The **Quartz Ball Valve** is used in corrosive, high-temperature environments. The valve may be activated manually, as shown, or by a solenoid. The valve is readily built from commercially available components.

the O-ring must be in a relatively low-temperature environment. For example, temperatures at the seal must be below 250° C for minimal O-ring degradation.

The valve was successfully used to control the flow of Si_3F_8 gases in the manufacture of semiconductors. No deterioration was observed after 1 week of operation.

This work was done by Carl Goetz and William M. Ingle of Motorola, Inc., for NASA's Jet Propulsion Laboratory. For further information, Circle 94 on the TSP Request Card.

This invention is owned by NASA, and a patent application has been filed. Inquiries concerning nonexclusive or exclusive license for its commercial development should be addressed to the Patent Counsel, NASA Resident Legal Office-JPL [see page A8]. Refer to NPO-14473.

Metallic Vibration Isolators

Woven metallic replacements for rubber isolators
withstand heat, vacuum, and thermal shock.

Marshall Space Flight Center, Alabama

Metallic vibration isolators made from woven steel replace rubber isolators in harsh environments. The metallic isolators, which absorb shock as well as vibration, are compressed into "biscuits" and encased in a steel mounting assembly. The steel is selected for its strength, corrosion resistance, and ability to absorb shock. Un-

der an applied load, the biscuits behave like cantilever springs.

The isolators will find uses where rubber deteriorates or its mechanical properties are inadequate. Potential applications are in power generators, vehicles, machinery, and portable tools.

Originally, the isolators were developed to reduce shock and vibration in the Space Shuttle rocket booster. The biscuits for this application accept loads in a single direction, in two mutually perpendicular directions, and in three mutually perpendicular directions. They are sized to absorb the expected stresses (see figure).

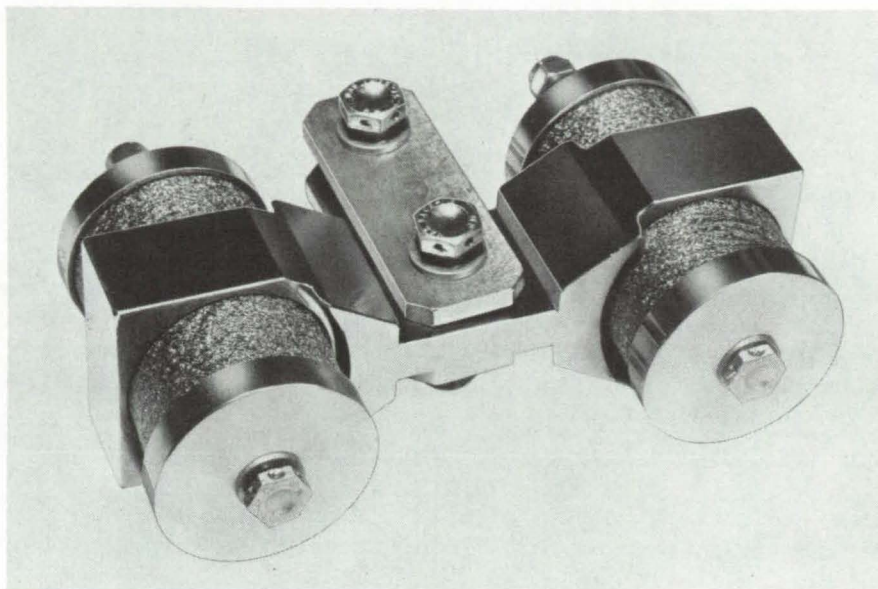
(continued on next page)



The isolators function at temperatures ranging from 20° to 250° F and pressures ranging from near vacuum to 45 psig (0.31×10^6 N/m²); they can handle up to 150 psig (1.03×10^6 N/m²) for short periods. Shock loads up to 70 pounds per square inch (0.48×10^6 N/m²) of biscuit cross section can be tolerated; the isolators withstand the thermal shock of a temperature drop in 5 minutes from 250° F (with the engine operating) to 20° F (immersion in seawater).

This work was done by Season Benado and Kenneth J. Hotz, Jr., of Sundstrand Corp. for **Marshall Space Flight Center**. For further information, Circle 95 on the TSP Request Card.

Inquiries concerning rights for the commercial use of this invention should be addressed to the Patent Counsel, Marshall Space Flight Center [see page A8]. Refer to MFS-23949.



Woven Wire "Biscuits" absorb vibration and shock. The design shown here absorbs forces in a direction parallel to the axes of the cylindrical biscuits. Other biscuit arrangements are available to isolate vibrations in two or three mutually perpendicular directions.

Controller for a Stirling Engine

A hydraulic mechanism controls the power and direction of the engine output.

NASA's Jet Propulsion Laboratory, Pasadena, California

A proposed hydraulic mechanism would make it possible for an operator to adjust the power and rotational direction of the output of a Stirling engine by applying only a relatively small force to a control lever. The new mechanism operates as a kind of "hydraulic ratchet" that makes use of the variations in the torque applied by the displacer portion of the engine. In one complete engine cycle, both positive and negative torques are applied, but the ratchet allows a control arm to move in response to torque in one direction only, preventing motion due to torque in the other direction.

The Stirling engine has expander and displacer sections that are connected to separate crankshafts. The expander delivers the engine power output through a shaft, and it also supplies power to operate the displacer. The engine output depends on the phase relationship between the rotating crankshafts.

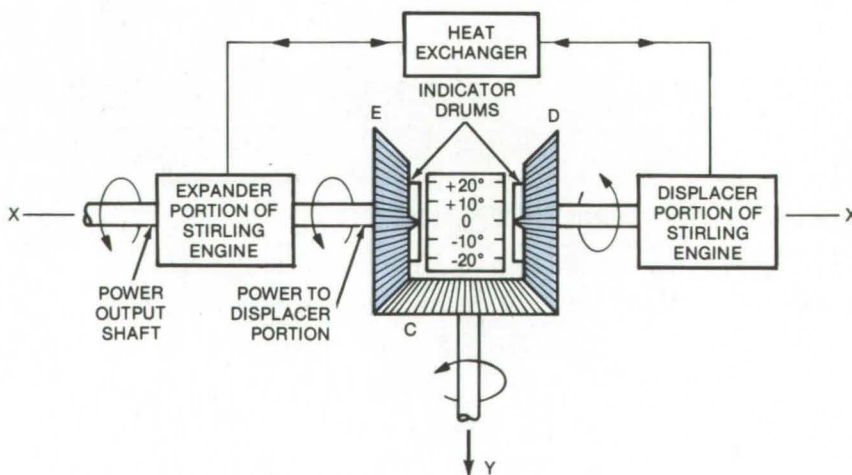


Figure 1. A **Stirling Engine** is controlled by changing the phase relationship between gears E and D. This is done by raising or lowering the gear C shaft perpendicular to the plane of the illustration. A phase difference of +90° puts the engine into a full-forward mode, and a -90° difference puts the engine into full reverse.

A simplified diagram (Figure 1) of the Stirling engine shows how this phase relationship can be changed. Bevel gears E, D, and C synchronize the two portions of the engine. Gears E and D have the same number of teeth, and both gears mesh with control gear C. The phase is changed by moving the shaft of gear C about the x-x axis (i.e., in the y-z plane, z being orthogonal to the plane of the figure). For example, moving the gear C shaft by 10° displaces gear D by $+20^\circ$ with respect to gear E and causes a corresponding phase shift between the expander and the displacer. When the phase relationship between E and D is 0° , the net engine power output is zero. Full-power forward or reverse is obtained by changing the phase to $+90^\circ$ or -90° , respectively. A stationary cylinder mounted between gears E and D indicates the phase relationship between the two gears.

The new hydraulic actuator (Figure 2) moves the shaft of gear C up or down according to the position of the phase control lever. When the lever is shifted into "forward," fluid from the left master cylinder opens pilot valve F and allows hydraulic fluid to flow from the chamber above piston A to the chamber below the piston; however, check valve R prevents the backflow of fluid into the upper chamber. Thus, the yoke will be moved forward during the positive torque portion of the displacer cycle but will not move back during the negative torque portion.

A switch of the phase control lever into "reverse" activates pilot valve R. The flow of hydraulic fluid allows piston A to move down, and the corresponding phase change between the expander and displacer puts the engine in reverse.

The hydraulic actuator holds the yoke in a steady position regardless of the external torques imposed on the shaft. The control is continuous, and it can be shifted from full forward to full reverse with intermediate settings

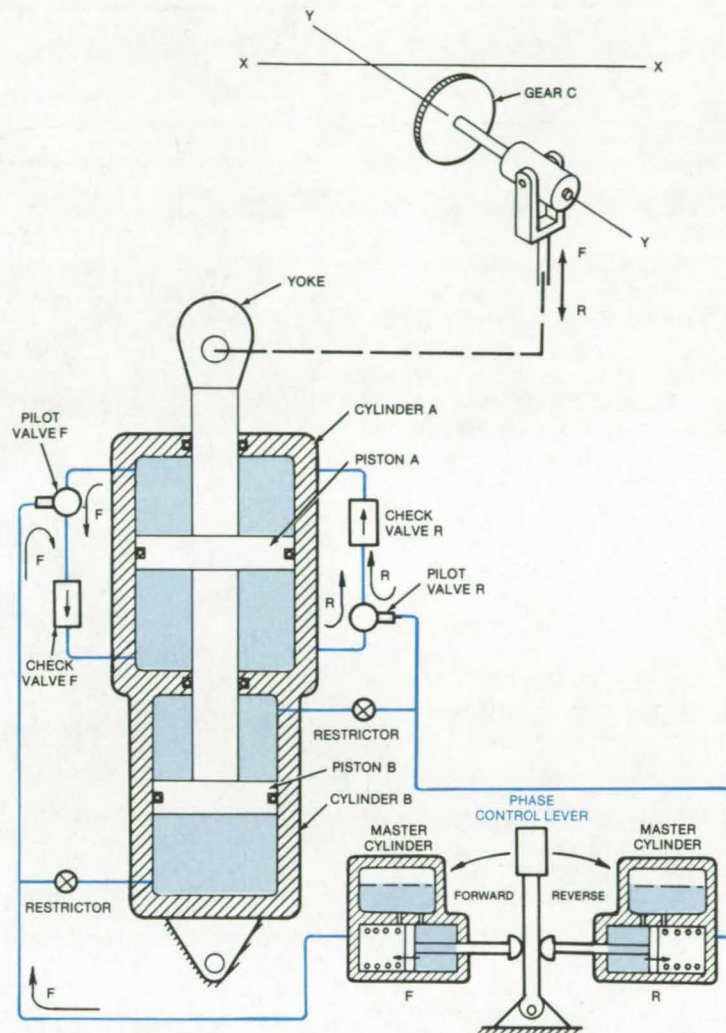


Figure 2. This **Hydraulic Actuator** assists in overcoming high torques in the gear C shaft. A manually-operated phase control lever, shifted into forward or reverse, activates the left or the right hydraulic circuit. A shift into "forward" forces piston A up, which forces the gear C shaft up. The procedure is reversed with the lever in "reverse."

between.

If the engine starts from dead center, there is no torque from the displacer. Thus, cylinder B is included to handle this situation by applying a power assist, operated by the master cylinder, which pushes the displacer over the dead zone.

This work was done by Allan R. McDougal of Caltech for **NASA's Jet**

Propulsion Laboratory. For further information, Circle 96 on the TSP Request Card.

Inquiries concerning rights for the commercial use of this invention should be addressed to the Patent Counsel, NASA Resident Legal Office-JPL [see page A8]. Refer to NPO-14388.



Precision Leveling of Large Machinery

A lightweight electronic instrument is faster and more accurate than surveying.

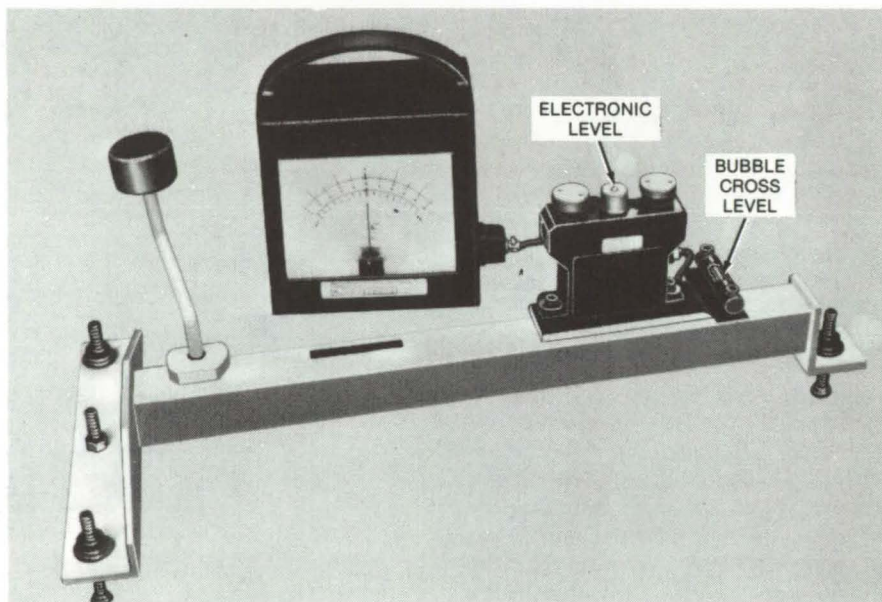
NASA's Jet Propulsion Laboratory, Pasadena, California

A small easy-to-use tool, originally developed to level massive circular runners on antennas for communicating with space vehicles, could be modified to accurately align and level other large machines. Although the tool is only about 1 meter long, it leveled the 23.4 meter in diameter runner so that its maximum elevation variation is only 2.4 mm. A traverse along the leveled runner has a closure of only 0.11 mm.

The T-shaped tool contains a bubble cross level and a commercial electronic level (see figure). The electronic level shows skewness in arc-seconds. The bubble cross level ensures that the T-structure transverse orientation is within the range (1 minute-of-arc or less) for which the electronic level can make accurate measurements.

The dimensions of the instrument are determined by the size of the machine to be installed. For the antenna, two sizes were built: one 46 in. (1.17 m) long and the other 21¾ in. (0.55 m) long. For the longer version, 1 arc-second on the electronic meter indicates an out-of-levelness of 0.0056 mm, and for the shorter one, 1 arc-second equals 0.0024 mm.

The antenna bearing runner is a steel ring 23.4 m in diameter at its centerline. It is 112 cm wide and 17.8 cm thick. The runner consists of 11 segments that are connected tightly together before the leveling operation is started. Each segment has leveling lugs arranged in radial pairs along its inside and outside edges. The segments are supported on studs that extend through the lugs and are welded to the antenna pedestal. The long T-



This **T-Shaped Leveling Tool** supports an electronic level and a bubble cross level. When placed on the runner, one arm of the T overhangs the edge of the runner. A counterweight is swung into position to stabilize the instrument while it is being read. The length of the tool is determined by the dimensions of the machinery to be leveled.

structure measures levelness between lugs within a runner segment, and the short T measures levelness between lugs adjacent to a joint between two segments.

The leveling procedure consists of placing the T between two lugs, reading the electronic-level meter, rotating the T orientation by 180°, and again reading the meter. The mean of the two readings is the elevation difference. Nuts on the studs are adjusted, and the procedure is repeated until the

elevation is within tolerance. The inter-lug elevation is measured and adjusted around the entire ring. A traverse adjustment (measurements only) of the runner takes about 3 hours, and complete adjustment of the runner takes about 1 week.

This work was done by Horace P. Phillips of Caltech for NASA's Jet Propulsion Laboratory. For further information, Circle 97 on the TSP Request Card. NPO-13257

Solar-Powered Pump

A pump for solar-heating systems and other applications is powered by steam. Operating on a pressurize/condense/refill cycle, it generates a pressure head of up to 50 feet and an average flow rate of up to 10 gal/min. Steam forces liquid through the pump; then it condenses to draw in more liquid for the next cycle. (See page 39.)

Fastening Hardware to Honeycomb Panels

The tendency for composite honeycomb panels to fracture when riveted floating nuts are attached is reduced by an adhesive-bonding technique. The nut is first riveted to a washer, and the washer is bonded to the honeycomb skin. Since the washer spreads the load over a wide area, it reduces stresses to a tolerable level. (See page 141.)

Laser Alignment of Large Assemblies

An electronically-leveled laser instrument simplifies the alignment of large structures. It is operated from a single alignment tower adjacent to the structure. Tiltmeter-controlled laser transits are placed at several points on the tower and are aligned with photosensitive targets as the operator monitors the procedure. (See page 99.)

Books and Reports

These reports, studies, and handbooks are available from NASA as Technical Support Packages (TSP's) when a Request Card number is cited; otherwise they are available from one of NASA's Industrial Application Centers or the National Technical Information Service.

Stiffness and Damping of Elastomeric O-Rings

Study to determine characteristics under dynamic conditions

The use of support damping to control rotationally excited vibrations in advanced turbomachinery is increasing. Support damping is also important in advanced flexible power-transmission shafting. Presently, the most common form of damper in these applications is the squeeze film damper in parallel with some type of mechanical flexure.

Elastomeric dampers are an attractive alternative to squeeze film dampers for rotating machinery and for other applications because of their simplicity, their lack of need for seals or oil supply. In the form of O-rings or cartridges, they are being considered for low-cost aircraft engine applications and for helicopter transmission shafting.

Two factors that inhibit the use of elastomeric dampers are limited data on their dynamic behavior and limited quantification of problems encountered in their application.

Accordingly, a parameterperturbation test program for elastomeric O-rings was conducted for a range of materials, temperatures, amplitudes, squeeze values, stretch values, cross-sectional diameters, and groove widths. Test parameters included:

- Three materials: The commercially-available Viton-70 and Viton-90 and Buna N-70 nitrile rubber;

- Five temperatures: 77°, 100°, 151°, 300°, and 421° F (25°, 38°, 66°, 149°, and 216° C);
- Three amplitudes: 3×10^{-4} , 10×10^{-4} , and 50×10^{-4} in. (7.62×10^{-6} , 25.4×10^{-6} , and 127×10^{-6} m);
- Five squeeze values: 5, 10, 15, 25, and 30 percent;
- Three stretch values: 0, 5, and 10 percent;
- Three nominal cross-sectional diameters: 1/16, 1/8, and 3/16 inch (1.59, 3.18, and 4.76 mm); and
- Three groove widths: 115, 135, and 150 percent of cross-sectional diameters.

Test hardware was designed and fabricated to allow controlled variations in imposed squeeze and stretch, in cross-sectional diameter, and in O-ring groove width. A thermally insulated housing with hot and cold air supplies was designed and fabricated to allow temperatures to be controlled up to 450° F (232° C).

In the test method used, two O-rings support a mass on a large electrodynamic shaker, forming a single-degree-of-freedom spring mass system. When the shaker was excited near the resonant frequency of the system, amplified deflection of the O-rings with a phase angle near 90° resulted. Accelerations of the table and supported mass were measured, and accurate values for stiffness and damping of the O-rings were calculated. The test apparatus allows the supported mass to be varied by a factor of more than 100, and resonant testing over a wide range of frequencies is possible.

Fifty O-rings each of three different materials and three different cross-sectional diameters were obtained from commercial sources. All of the O-rings had nominal outside diameters of 2.5 in. (6.35 cm): For consistency all O-rings of each material were made from the same raw material mix.

Nineteen combinations of test parameters were investigated, and test

data were plotted in the form of stiffness and loss coefficient versus frequency for each test combination over the full frequency range investigated. Power law lines were fitted to each set of test data, and trend summaries were plotted that allow the effect of each test parameter on dynamic O-ring characteristics to be assessed directly.

Conclusions from the test program were:

1. Material and radial squeeze are the factors that offer the designer most direct control over the dynamic characteristics of an O-ring.
2. Temperature and vibration amplitude also have a strong effect and must be carefully accounted for in designing for particular applications.
3. The high loss coefficient of Viton at room temperature declines sharply with temperature increase; stiffness follows a similar trend.
4. Increasing amplitude decreases the effective stiffness and loss coefficient of Viton.
5. Pronounced trends have not been observed in the effects of stretch, cross-sectional diameter, and groove width on O-ring dynamic characteristics.

These data should be of immediate interest to designers of flexible mounted rotating machines and provide a more rational basis for selection of flexible bearing mounts and O-ring seals.

This work was done by M. S. Darlow, R. K. Mehta, and A. J. Smalley of Mechanical Technology Inc. for Lewis Research Center. Further information may be found in NASA CR-135328 [N78-18460], "Stiffness and Damping of Elastomeric O-Ring Bearing Mounts," a copy of which may be obtained at cost from the New England Research Application Center [see page A7].

LEW-13079



Computer Programs

These programs may be obtained at very reasonable cost from COSMIC, a facility sponsored by NASA to make new programs available to the public. For information on program price, size, and availability, circle the reference letter on the COSMIC Request Card in this issue.

Annular Acoustic Liners for Turbofan Engines

Design procedure helps reduce noise.

A computer program for the design annular acoustic liners for turbofan engines first estimates the noise generated by the turbofan engine. This

noise spectrum is then used along with a flat, annoyance-weighted goal spectrum to generate the required suppressor attenuation spectrum.

The design procedure combines results from theoretical models of wave attenuation in acoustically treated passages with correlations of experimental data from full-scale fan suppressors. This accounts for "real world effects," such as wall boundary layers, duct terminations, sound modal structure, and other similar effects, so that the influence of these effects can be generalized for a variety of fans and engines.

The program permits the methodical examination of alternative choices of treatment for noise reduction, such as the number of splitter rings traded off against length, which are important

as they affect engine nacelle weight, aerodynamic losses, and engine economics.

The design procedure is limited to wall construction of perforated plates over honeycomb, since the wall impedance model is for this type of structure.

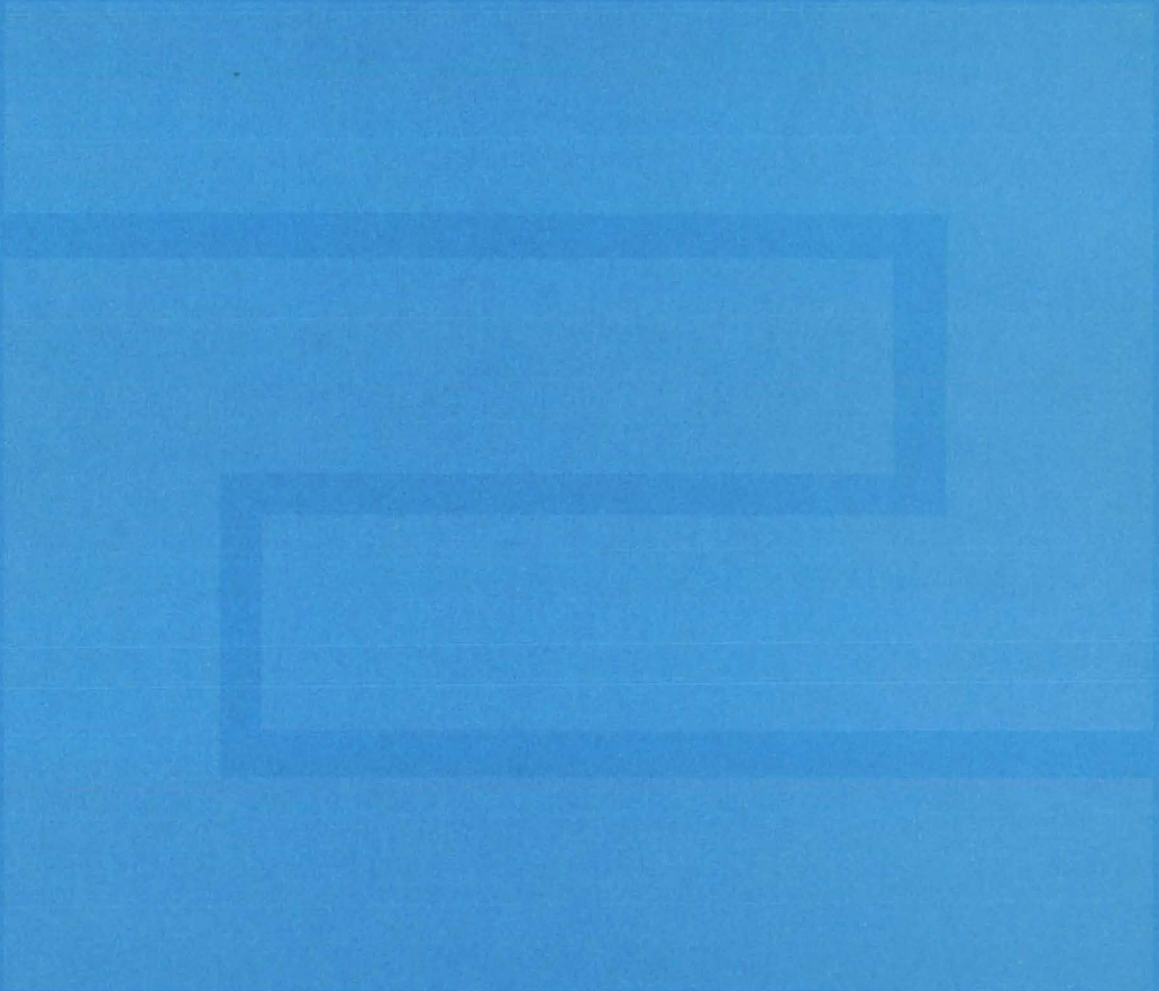
This program is written in FORTRAN V and has been implemented in batch mode on a UNIVAC 1100-series computer with a central memory requirement of 12K (decimal) of 36-bit words.

This program was written by Gene L. Minner and Edward J. Rice of

Lewis Research Center. For further information, Circle K on the COSMIC Request Card.

LEW-12810

Fabrication Technology



Hardware, Techniques, and Processes

- 135 Repairing Cracked Glass
- 136 Fixture for Limited-Access Welding
- 137 Giant-Electrode Welder
- 138 Furnace Brazing Under Partial Vacuum
- 138 Room-Temperature Bonding of Thin Plastic Sheets
- 139 Temporary Insulation With Polyurethane Foam
- 140 Electroplating Offers Embrittlement Protection
- 140 Window With Integral Seal
- 141 Fastening Hardware to Honeycomb Panels
- 142 Vapor-Deposited Graded-Thickness Films
- 143 Applying Photosensitive Emulsions to Enamel Surfaces
- 143 Plastic Film Insulates Solar Cells from Metal Substrate
- 144 Cutting Silicon for Solar Cells
- 145 Fixture for Assembling Solar Panels

Books and Reports

- 146 CMOS Circuit-Fabrication Handbook

Repairing Cracked Glass

A simple filling procedure produces a homogeneous seal in thin glass.

John F. Kennedy Space Center, Florida

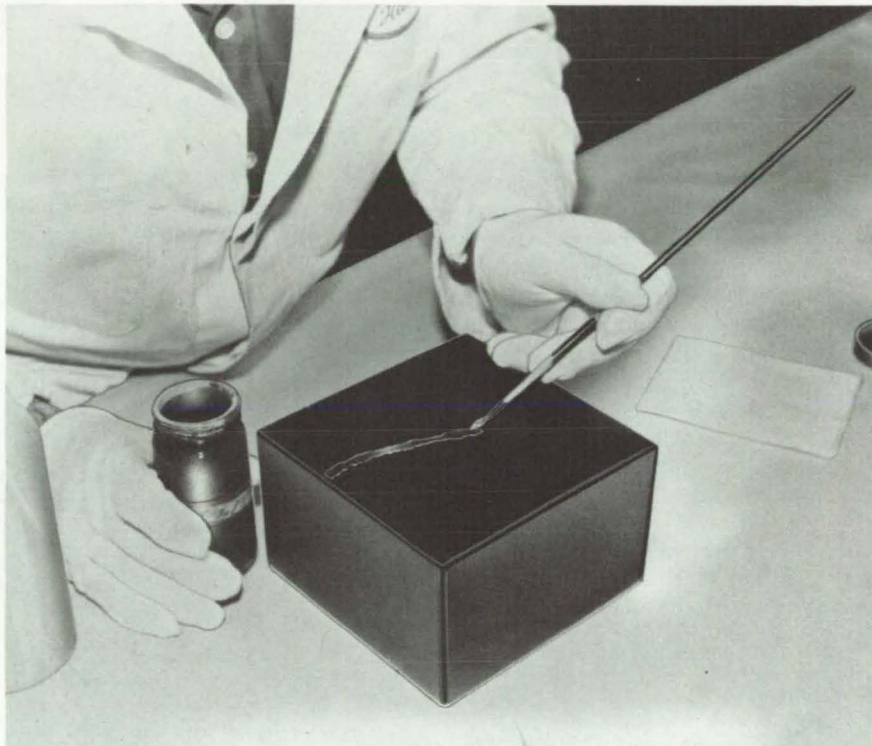
Although holes and cracks in glass are generally considered nonrepairable, a new technique makes it possible to correct such damage in very thin glass. The technique has been used to repair punctures and heal cracks in glass that is 0.010 to 0.020 inch (0.25 to 0.5 mm) thick. The maximum thickness of glass that can be repaired by the process is not yet known, but it is expected to be useful in repairing glass envelopes, X-ray tube windows, Dewar flasks, and similar thin glass objects.

The process was developed for the reusable surface insulation (RSI) for the Space Shuttle. RSI consists of machined lightweight fused-silica tiles coated with a thin layer of borosilicate glass. This coating is fragile and highly susceptible to punctures and cracks. Before the repair method, damaged tiles had to be removed and replaced — a procedure that required about 35 hours. Repairing the tiles requires only one-tenth that time and thus will help to keep the Space Shuttle on schedule when it is turned around for a new mission.

The first step in the repair process is preparation of a slurry of about 92 parts high-silica frit, 5 parts of lower-fusing-temperature borosilicate frit, and silicon boride in enough alcohol to yield a 50-percent solids mixture by weight. The slurry is milled for 3 hours, then diluted with more alcohol to 36 percent solids by weight.

The slurry is applied to the damaged area by brushing or spraying (see figure). The repair coating is dried in ambient air for 5 hours or in an oven at 150° F (65° C) for 1 hour.

Finally the repair coating is cured for 5 minutes by radiant heat from a quartz lamp at 2,100° F (1,170° C), the heat being applied uniformly over the tile surface. During this cure, the



As Good as New: A crack in a glass layer on a ceramic tile is filled with a slurry of glass frits, applied with an artist's brush as shown here or with a spray gun. The slurry is then cured under a quartz heat lamp. This procedure has been successful in repairing glass layers 0.25 to 0.5 mm thick.

silicon boride particles oxidize, forming a boron-oxide-rich glass. This glass is very fluid and readily wets and reacts with the other frits. In a short time, the reactive liquid consumes enough of the available frits to form an impervious, highly refractory layer.

Scanning electron micrographs of such repairs show that cracks are completely sealed and the repair material and base glass are homogeneous. Tile coatings repaired by this process have successfully withstood 15 simulated Space Shuttle reentry cycles in vacuum at 2,300° F (1,300°

C) maximum temperature and 25 thermal cycles at atmospheric pressure and the same maximum temperature.

This work was done by Donald D. Helman, Jack W. Holt, and Laurence W. Smiser of Rockwell International Corp. for Kennedy Space Center. No further documentation is available.

Inquiries concerning rights for the commercial use of this invention should be addressed to the Patent Counsel, Kennedy Space Center [see page A8]. Refer to KSC-11097.

Fixture for Limited-Access Welding

Expansion clamps and a backup bar hold large plates for welding.

Lyndon B. Johnson Space Center, Houston, Texas

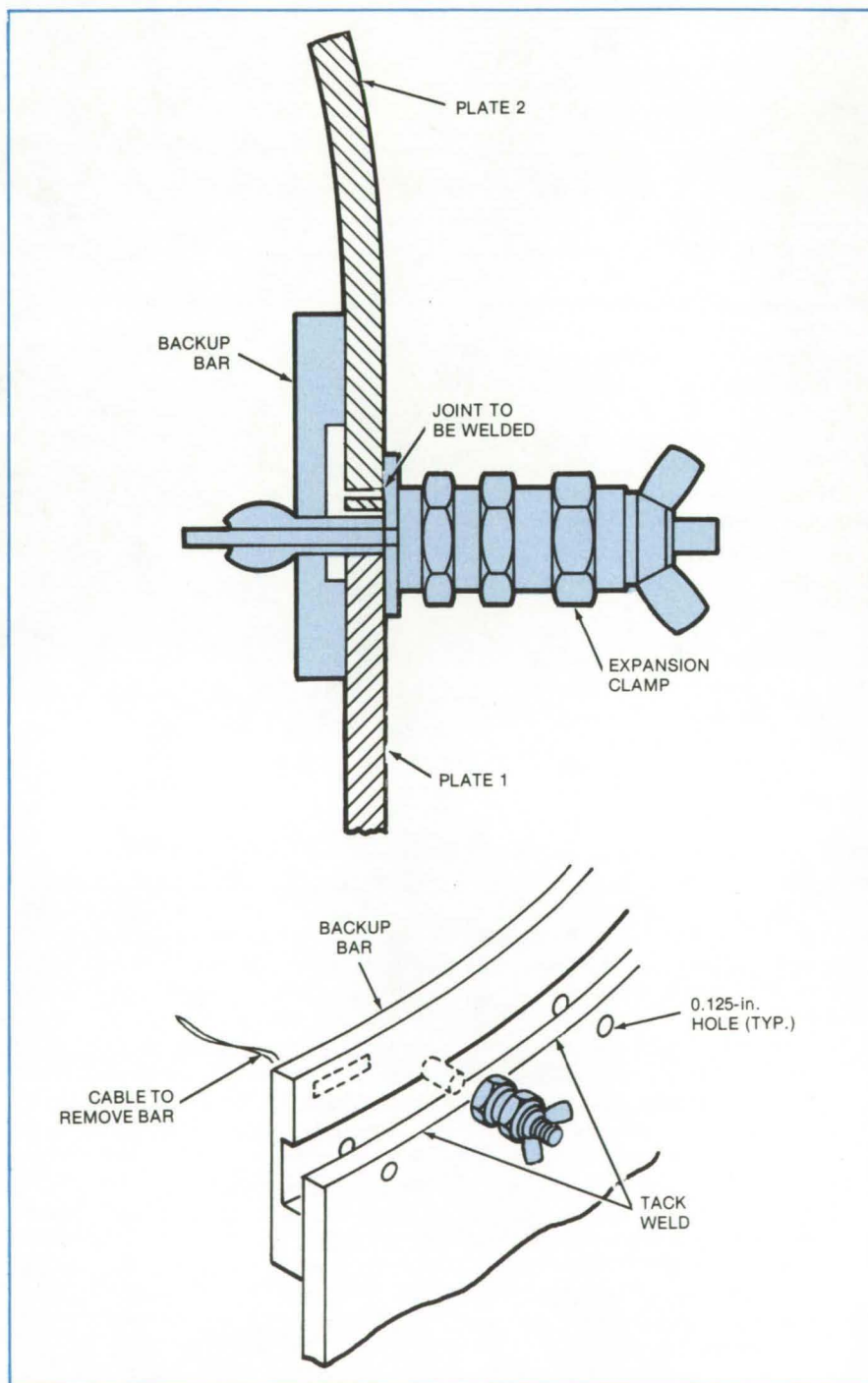
A sample fixture aligns the edges of plates for precision butt welding. The tooling consists of commercially-available, screw-on expansion clamps and a backup bar (see figure). The clamps are inserted through holes drilled in one of the plates to be welded and into aligned holes in the backup bar. The second plate is then placed in position, and the expansion clamps are tightened. The tooling holds the plates securely, without offset, and it allows welding and clamp disassembly to be completed when there is access from only one side of the structure.

After the fixture has been set up, the plates are welded in the region between the clamps. Then the clamps are loosened and removed, and the clamp holes are welded closed to complete the joint. (The plates are welded from the screw side of the clamp.)

If the backup bar has been previously tack-welded to the plate, it can be left there after welding; or the backup bar can be removed (with the help of a previously attached cable) after the clamps have been released. Since the clamps are installed away from the weld line, there is little danger of their being accidentally welded.

The fixture has been used when welding tanks for the Space Shuttle. The plates were 2219 aluminum alloy, 0.185 in. (4.70 mm) thick. The backup bar was 0.125 in. (3.18 mm) thick and 5/8 in. (15.8 mm) high, and it contained a groove 0.020 in. (0.51 mm) deep and 0.250 in. (6.35 mm) wide.

This work was done by Jerry R. Tryon of Rockwell International Corp. for Johnson Space Center. No further documentation is available.
MSC-16698

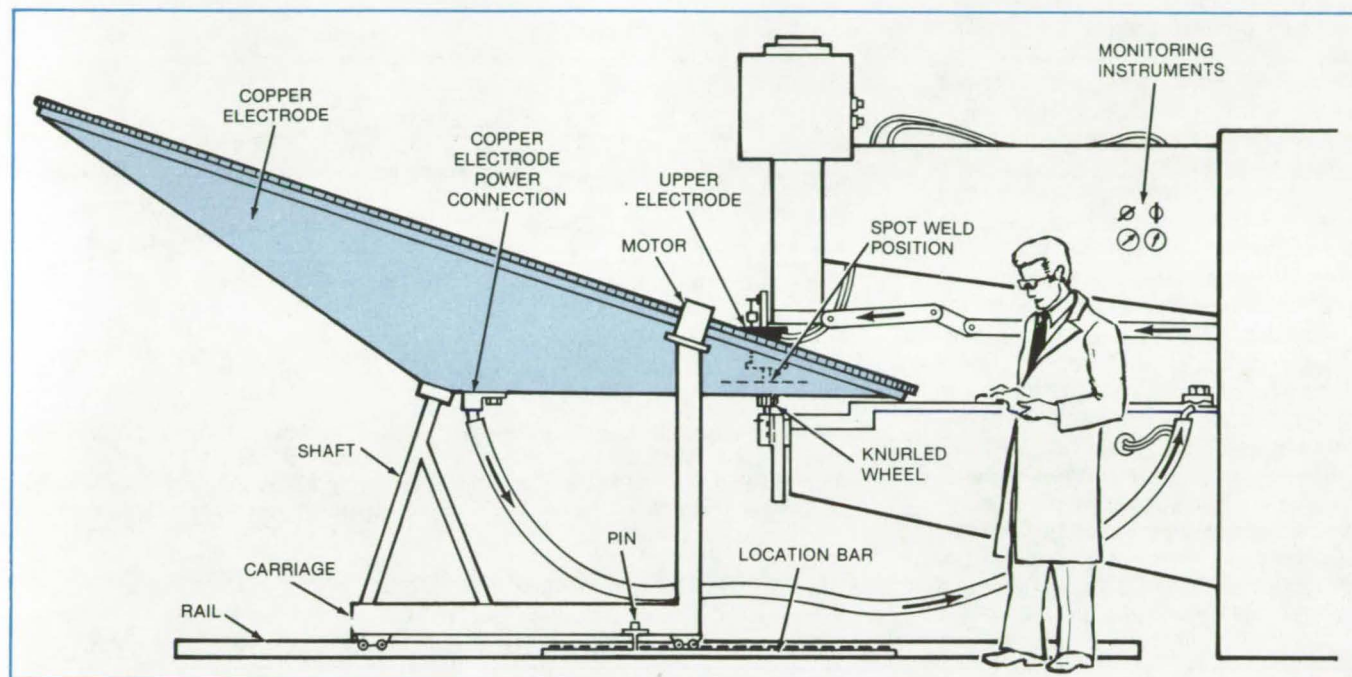


This **Welding Fixture** uses expansion clamps and a backup bar to eliminate offset between the edges of mating plates. A cable on the backup bar allows it to be removed after the clamps have been withdrawn and welding is complete.

Giant-Electrode Welder

A large welding unit saves costs in fabricating aeroshell structures.

Langley Research Center, Hampton, Virginia



The **Giant-Electrode Welder** unit uses a large copper-cone electrode to mold and support a cone-shaped aeroshell that is being assembled. The aeroshell consists of a thin aluminum skin stiffened by 27 concentric circular aluminum frames. The upper electrode squeezes the frame to the skin during welding.

Aeroshell skin structures are conventionally assembled by riveting, which is time-consuming and requires many tools. A more efficient approach is to use a 500-kVA welder to produce spot-welds in place of the rivets and thus save time and money.

The new unit has a very-large conical copper electrode (see figure) with an 11.5-ft (3.51-m) base diameter. This electrode is shaped to hold an entire conical aeroshell during assembly. The thin aluminum skin for the aeroshell is molded inside the copper electrode, and concentric ring-shaped aluminum frames are welded to the skin. Other electrode shapes are also possible to match different aeroshell configurations.

The electrode is made from 0.250-inch-thick (6.35-mm) copper plates that have been slip rolled and bonded to a 1-1/4-inch-thick (3.2-cm) rigid aluminum base cone. The entire conical dish is mounted on a shaft tipped 20° from the vertical, so one

"side" is parallel to the ground. The tipped shaft is mounted on a carriage set on rails. Thus, the entire assembly can be pushed straight along under the upper welding head, with the height of the upper electrode remaining constant in relation to the copper surface.

The copper dish is fixed in one of a number of frame positions by a pin in a carriage bracket that drops down into a locator bar mounted on the floor. This arrangement allows spot welding along a fixed circle while the cone is rotated. The height of the upper electrode remains constant in relation to the cone surface.

The cone is rotated by a motor geared to the rim of the dish. The motor is indexed to stop automatically so that the spot-welds are evenly spaced 0.500 inch (12.70 mm) apart. Indexing is done with a knurled wheel pressing the bottom of the dish directly under the upper electrode. This wheel is bolted to a cammed wheel; as soon as the proper distance is measured,

the cammed wheel presses against a microswitch. Through a series of relays, the microswitch stops the motor and starts the welder. The welder head lowers and the part is spotwelded for a predetermined time. Following this step the welder head is raised automatically, tripping another microswitch for another operational cycle.

The unit is also capable of welding very thin (0.016-inch or 0.41-mm) hard 2024-T81 aluminum alloy. A 9-lb (4-kg) low-inertia welding head is mounted on the plate at the bottom of the regular heavy head (150 lb or 68 kg) that is locked in place. The low-inertia head duplicates the squeeze, forge, and hold functions of the large head by regulated air pressure.

This work was done by B. R. Atkins, Russ A. Chihoski, and Frank Yashiro of Martin Marietta Corp. for Langley Research Center. For further information, Circle 99 on the TSP Request Card.

LAR-11429

Furnace Brazing Under Partial Vacuum

Partial-vacuum technique reduces tooling requirements and produces a better bond.

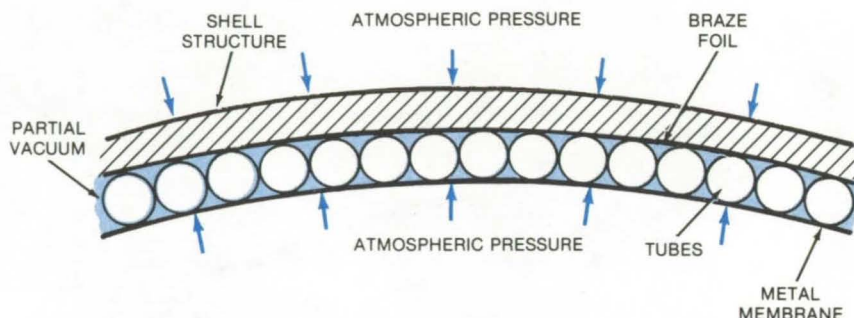
Marshall Space Flight Center, Alabama

Large areas are joined in a brazing furnace utilizing partial vacuum and inert gas for improved bond. Because of the partial vacuum created inside the operating area, atmospheric pressure is sufficient to compress the parts together. An added benefit is that partial vacuum helps to dissociate metal oxides that inhibit the metal flow. An argon purge is applied to protect oxide-free surfaces.

The illustration shows how this technique is used to join tubes to a shell structure. The tubes are fitted into the shell structure, which has braze alloy already applied to the shell surface. After the tubes are positioned, a metal membrane is placed over the assembly and sealed to the shell by welding. An inert-gas purge manifold and a vacuum manifold (not shown) are also sealed inside the structure.

The manifolds are connected to their respective supplies, and the vacuum pump is started to remove air from the sealed assembly. Following a short timespan, an argon source is opened and regulated to maintain the desired partial vacuum in the system.

The braze assembly is enclosed in a retort, which is purged with argon



Tubes Are Joined to the Shell Structure with assistance from vacuum system and an inert-gas source. Parts are held together by atmospheric pressure applied to the metal membrane and to the shell structure due to partial vacuum in between. The partial vacuum also helps metal oxide dissociation. Argon supplied to the area maintains oxide-free surfaces during brazing.

through separate inlet and exhaust, to obtain desired braze environment (dewpoint). Next, the assembly is heated inside the brazing furnace. During the process, contact between the parts is maintained at 100 percent and carefully regulated by controlling the inert-gas-flow throttle valve and the vacuum-pump throttle valve.

The new approach eliminates heavy tooling required to hold the parts

together during the brazing. In addition, the double inert-gas shield reduces the chances of parts being contaminated by air during the process.

This work was done by Ross D. McKown of Rockwell International Corp. for Marshall Space Flight Center. For further information, Circle 100 on the TSP Request Card. MFS-19363

Room-Temperature Bonding of Thin Plastic Sheets

Metallic coatings and light pressure join plastic sheets.

NASA's Jet Propulsion Laboratory, Pasadena, California

Thin sheets of plastic can be bonded together, without heat, by depositing metal films on the plastic and applying light pressure. Unlike conventional adhesives, which require a cure at high temperature before they develop strong bonds, the metal films are simply pressed together at room temperature. This technique makes it possible to join organic materials (such as polyimides) without the high temperature necessary for conventional adhesive bonding.

The new method was developed for the Solar Sail program, in which the dimensions of the polyimide sail are larger than sheets available from commercial vendors. It is therefore necessary to bond the polyimide sheets at their edges. (The method may also be useful to manufacturers of thin plastic films and to the packaging industry.)

One of the plastic sheets to be bonded is coated with a thin layer of indium, a metal that melts at slightly above room temperature. Indium

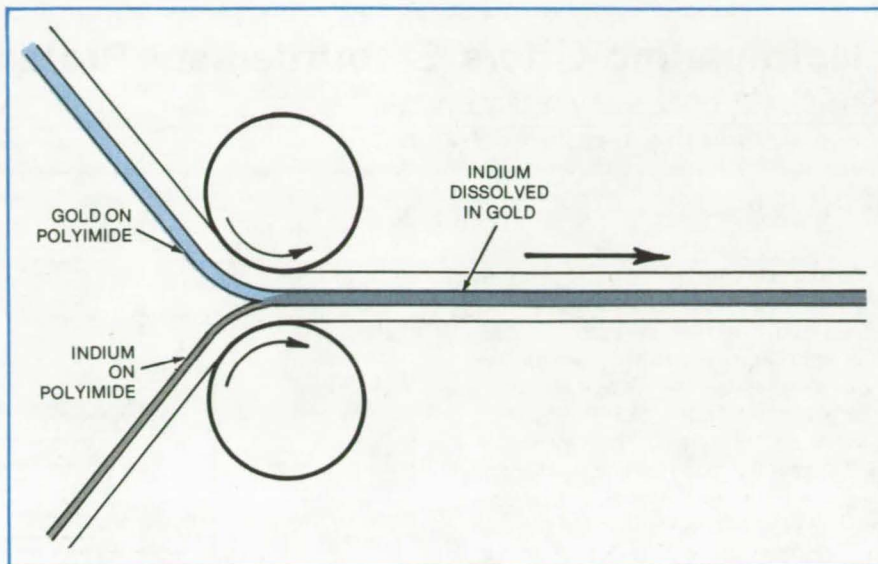
resists oxidation and thus presents a clean surface for the bonding process. The other plastic sheet is coated with a thin layer of a high-melting-point metal such as gold. Both metallic layers are applied to the plastic by vacuum deposition.

The coated sheets are lightly pressed together in a fixture (see figure). Under the pressure, the indium layer forms a binary alloy with the gold, creating a strong bond between the plastic sheets. The bond

can be exposed to temperatures up to 300° C without melting. For best results, the original gold layer should be about 10 times the thickness of the indium. This ensures that the final alloy is an approximately 10-percent solid solution of indium in gold.

Indium is a desirable choice for the solute because it melts at a conveniently low temperature and it resists oxidation; however, other metals such as tin, silver, or copper might prove to be acceptable (perhaps with a gold coating to protect against oxidation). Nickel has already been used instead of gold as the host metal. Other candidates are chromium, chromium nickel, iron nickel, aluminum, iron copper, and chromium copper.

The essential requirements for the host metal are that it be wettable by the indium or other solute metal and that it bonds to the plastic sheet without attacking the sheet material. If necessary, the host could be isolated from the plastic by a barrier film of a less active metal or a dielectric material.



Rollers Apply Pressure to melt the film of indium on the bottom sheet, which then dissolves in a film of gold on the top sheet.

This work was done by Robert E. Frazer of Caltech for NASA's Jet Propulsion Laboratory. For further information, Circle 101 on the TSP Request Card.
NPO-14346

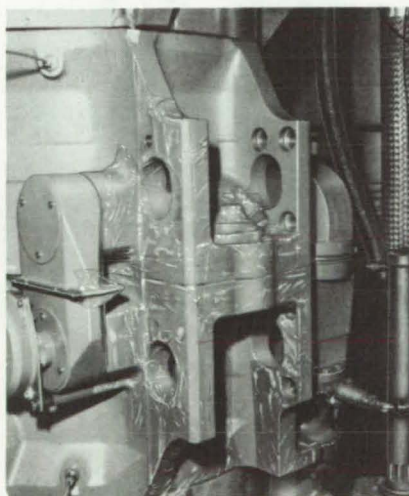
Temporary Insulation With Polyurethane Foam

Masking parts with TFE tape allows easy removal of the insulation.

Lyndon B. Johnson Space Center, Houston, Texas

Sprayed or poured polyurethane foam, used to insulate cryogenic components, can be removed easily and cleanly if the component is masked with tetrafluoroethylene (TFE) tape before the foam is applied. Therefore, insulation can be used temporarily while testing of parts and then removed for their reworking.

This technique was developed specifically to test an expensive liquid-hydrogen (LH₂) valve. To prevent LH₂ boil-off, it was necessary to insulate or otherwise contain the hardware. Vacuum-chamber or vacuum-bag insulation was impractical, so a polyurethane cover had to be used. Chemical release agents for easy removal of the



Masking a Part with pressure-sensitive tape made of TFE before application of polyurethane-foam insulation allows the insulation to be removed without damaging or contaminating the part.

foam were not acceptable because they might contaminate the metal surface and might not ensure foam removal from cavities or crevasses. Therefore, the valve was covered with a pressure-sensitive TFE tape (see figure), sprayed with foam, and tested. When the valve failed to function properly, the foam was peeled away from the tape without damage to the valve, which was then modified, retested, and shipped.

This work was done by Richard G. Jackson and Guillermo Lerma of Rockwell International Corp. for Johnson Space Center. No further documentation is available.
MSC-18298

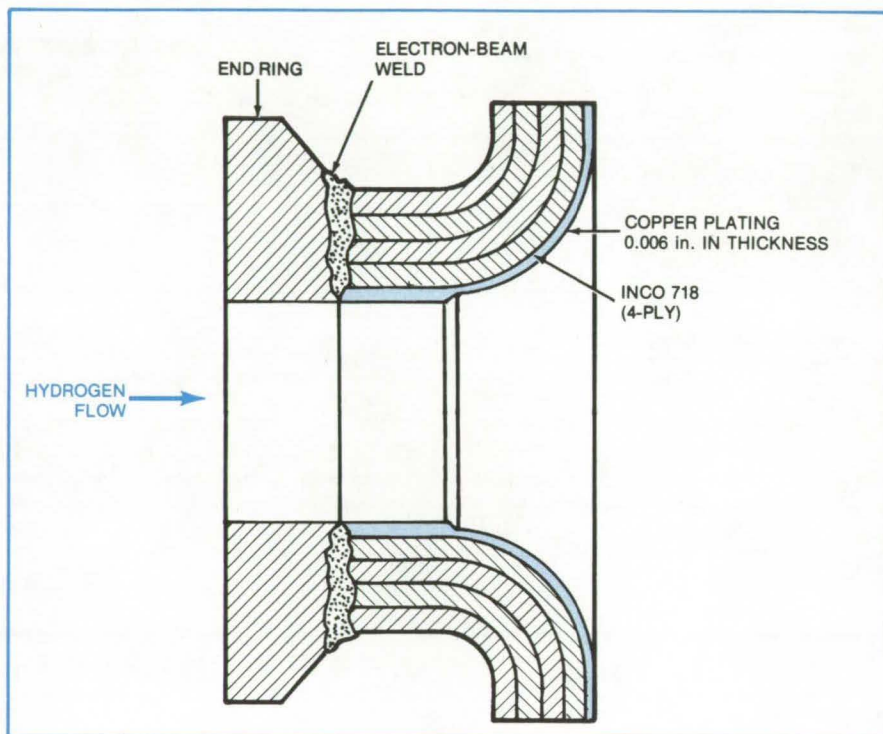
Electroplating Offers Embrittlement Protection

A thin layer of copper protects nickel alloys from high-pressure hydrogen.

Marshall Space Flight Center, Alabama

A thin electrodeposited layer can protect metal parts in environments with which they may be incompatible. This approach was developed for the main engine of the Space Shuttle, where high-strength nickel-alloy bellows must operate in high-pressure [5,000-psi (35×10^6 -N/m²)] hydrogen. To protect the embrittlement-susceptible nickel, a thin outer layer of copper is electrodeposited on the inside surface of the nickel-alloy tubing before its formed into the bellows shape. The copper protects the nickel, and it is unaffected by the forming process or by subsequent heat treatment and other preinstallation processing.

An iron/cobalt/nickel alloy was chosen for the bellows in the Shuttle-engine turbine-drive and discharger ducts because of its strength and fatigue resistance. However, nickel alloys are also notoriously susceptible to hydrogen embrittlement, which causes a loss of ductility and a sharp reduction in low-cycle fatigue life. Thus, as shown in the figure, a copper plate approximately 0.006 in. (0.015 cm) in thickness was electrodeposited on the inner surface of the four-ply nickel alloy bellows prior to forming. This layer prevents the alloy from contacting the hydrogen atmosphere, and it is not excessively thinned when the bellows shape is formed.



Copper Plating Over Nickel Alloy protects bellows from embrittlement by high-pressure, room-temperature hydrogen. Inco 718 was used in this application, although the approach should work for other alloys.

*This work was done by Charles M. Daniels, Jr., of Rockwell International Corp. for **Marshall Space Flight Center**. No further documentation is available.*

Inquiries concerning rights for the commercial use of this invention should be addressed to the Patent Counsel, Marshall Space Flight Center [see page A8]. Refer to MFS-19330.

Window With Integral Seal

The extension of the adhesive layer of a laminated window forms a built-in gasket.

Lyndon B. Johnson Space Center, Houston, Texas

An installation concept for an air-tight, watertight, laminated window does away with the O-rings and sealants ordinarily needed for an effective edge seal. In the proposed window, the pliable inner layer of laminating adhesive extends around the window edges (see figure), forming

a built-in gasket. The cost of special tooling required to cast the overlapping edge could be offset by savings in part and assembly costs.

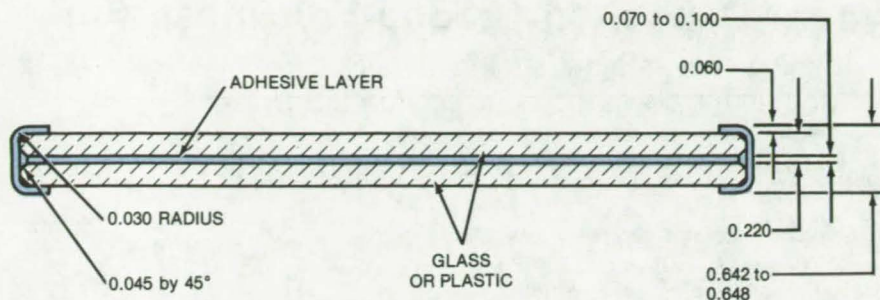
The concept can be used for plastic or glass windows where space for gaskets and sealing rings is limited. It would be adaptable, for example, to

windows, canopies, and shields for military, private, and commercial aircraft and for marine- and land-transportation vehicles.

The integral seal concept was originally proposed for a camera port on the Space Shuttle Orbiter. In this application, the laminated window

would replace a double-pane window that requires a nitrogen purge of the space between sheets (to remove moisture and prevent fogging), followed by a complex O-ring sealing procedure. The new design gives the same redundant pane protection against damage, but eliminates the space between glass panes; and since the window does not require a purge and has an integral seal, it is lighter and easier to install and maintain.

This work was done by Joseph M. Behar of Rockwell International Corp. for **Johnson Space Center**. No further documentation is available. MSC-16490



NOTE: ALL DIMENSIONS ARE IN INCHES.

In this proposed **Self-Sealing Window**, the inner adhesive layer overlaps the edges to form sealing gaskets.

Fastening Hardware to Honeycomb Panels

Adhesive bonding reduces the likelihood of skin failure.

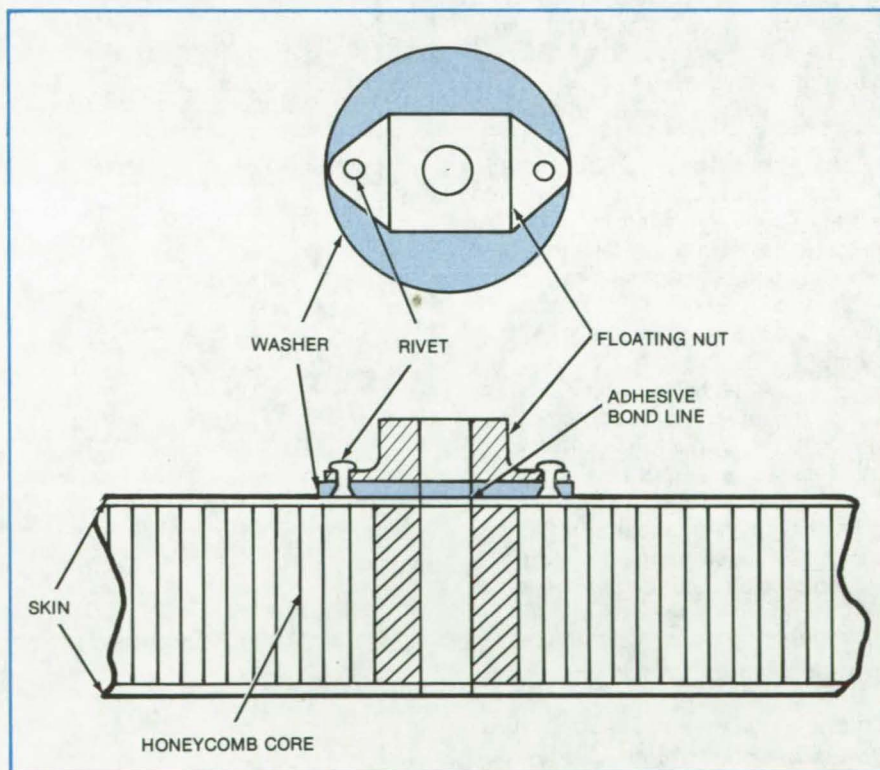
Lyndon B. Johnson Space Center, Houston, Texas

Riveted floating nuts and other hardware attached to composite honeycomb panels can be the source of skin peeling and fractures when excessive forces or torques are applied. Under high loads, stress concentrations at the rivet can easily exceed the limit that can be supported by the glass-fiber and epoxy skin material.

An adhesive bonding approach that solved this problem for floating nuts attached to the wing of the Space Shuttle could be useful in other applications of the composites, such as in aircraft, automobiles, and home appliances. In this method, the nut is first riveted to a washer, and the washer is bonded with an adhesive to the honeycomb skin (see figure). Since the washer spreads an applied load over a much larger area than would the rivets alone, it reduces stress on the skin to a tolerable level.

This work was done by Arthur Kenger of Grumman Aerospace Corp. for **Johnson Space Center**. No further documentation is available.

MSC-16752



A **Riveted Floating-Nut and Washer Combination** is adhesively-bonded to the skin of a composite honeycomb panel. When torque is applied to the nut, the washer distributes the stress to the panel skin, preventing peel or fracture.

Vapor-Deposited Graded-Thickness Films

A rotating substrate and a slotted mask allow a varying film thickness to be deposited from vapor.

Goddard Space Flight Center, Greenbelt, Maryland

A novel vacuum-deposition technique produces circular films with radially-varying density distributions. The technique was originally developed to make neutral-density filters for studies of the solar corona during an eclipse. In this application, the graded density distribution was needed to flatten the corona intensity profile so that the brightest and darkest portions would be within the detection range of the sensing instrument.

In the new technique, the film substrate is exposed to the metal vapor through a circular mask (see Figure 1). The mask has a radial aperture, shaped to give the required density profile. During the deposition, the substrate is rotated at constant speed and the mask is held stationary.

The film density at a given radius is determined by two factors: (1) the substrate angular velocity (more precisely, the substrate tangential velocity at that point) and (2) the aperture width at that radius. Thus, for a given rotation speed, the aperture width that will give the desired film thickness can be calculated. The actual density variation of the filter made for the corona study is quite close to the predicted profile (Figure 2).

The new technique can produce filters for other light sources. For example, a variable-thickness film could adjust the output of a lamp with a hot spot at its center to improve the uniformity of the light pattern. Or, in a non-optical application, the evaporation technique could be used in fabricating variable-thickness coatings for controlling thermal, electrical, or other properties.

This work was done by Howard Herzig and Rodney S. Spencer of Goddard Space Flight Center. No further documentation is available.
GSC-11806

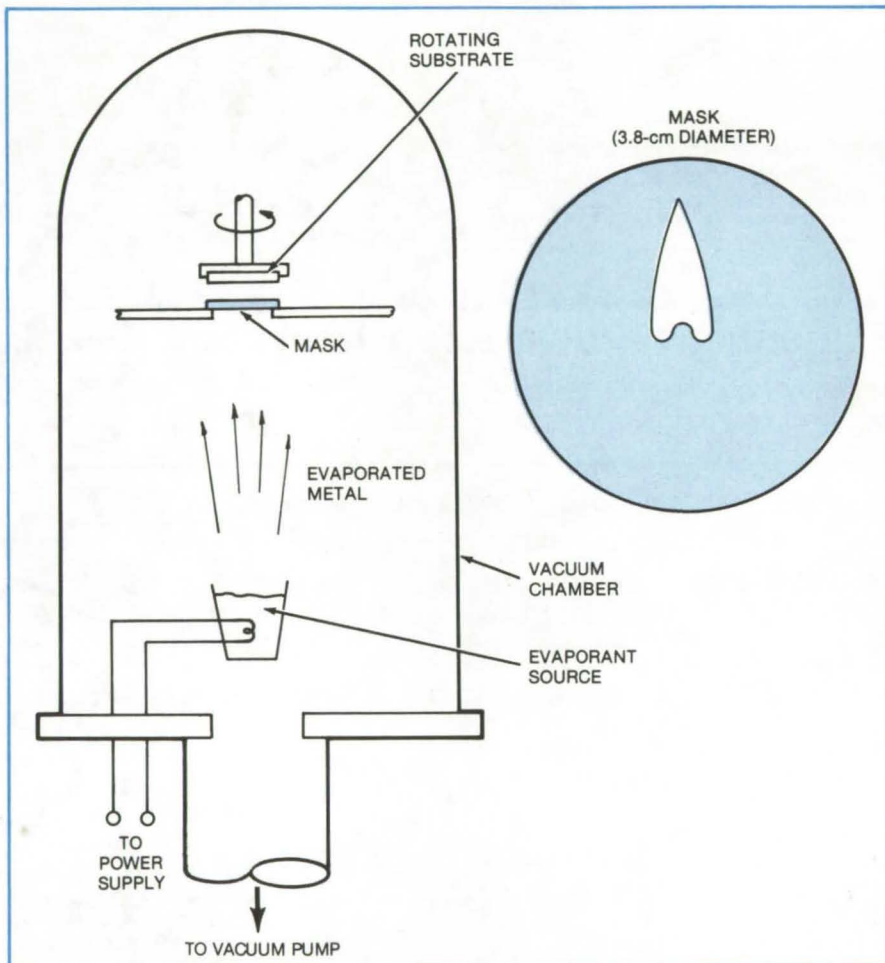


Figure 1. **Evaporated Metal in a Vacuum Chamber** passes through a mask before depositing on a rotating substrate. The mask aperture shape shown here produces a radial thickness variation suitable for a graded-density optical filter.

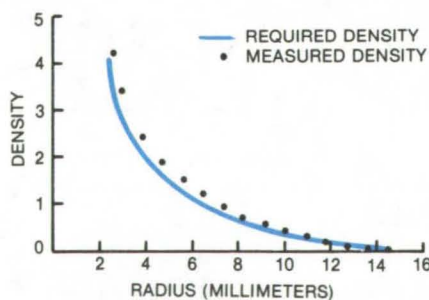


Figure 2. The measured **Metal-Film-Thickness Profile** created by the mask shown in Figure 1 is indicated by the dots. The calculated profile is also shown.

Applying Photosensitive Emulsions to Enamel Surfaces

Two layers of lacquer solve the problem of adhesion to an incompatible surface.

Lyndon B. Johnson Space Center, Houston, Texas

In attempting to photoetch enamel-coated panels used aboard the Space Shuttle, it was found that commercially-available photosensitive emulsions (resists) would not adhere to the enamel surface. Although the resists do adhere to lacquer finishes, lacquer paint could not be used because it discolors at the elevated temperatures at which the panels are baked. This problem has been resolved by priming the enamel with two coats of lacquer that are subsequently removed with solvents.

The procedure begins with panels that are already coated with uncured (not baked) enamel paint. A noncuring clear lacquer (which does not become

solvent resistant by high-temperature baking) is sprayed over the enamel. Next, a second coat, using another clear lacquer, is sprayed on top of the noncuring lacquer. The resist has been found to adhere to this lacquer but not to the noncuring lacquer.

After a photosensitive resist is applied over the top lacquer coat, the panel is exposed and developed; the unexposed photoresist is removed by dissolving. Following this step, the panel shows the desired pattern; however, the two lacquer coats must be removed.

The panel is baked to cure the enamel under the two lacquer coats,

and a solvent spray is applied to the panel surface. The solvent attacks the clear lacquer, especially the non-curing layer, allowing the lacquer to be stripped off the panel easily. This leaves intact the already-cured and photomarked enamel paint.

This work was done by Wolfgang Fuhr of U.S. Radium Corp. for Johnson Space Center. For further information, Circle 103 on the TSP Request Card.

Inquiries concerning rights for the commercial use of this invention should be addressed to the Patent Counsel, Johnson Space Center [see page A8]. Refer to MSC-18107.

Plastic Film Insulates Solar Cells from Metal Substrate

A polyimide film, bonded using epoxy-impregnated fiberglass cloth, serves as an insulating layer.

Marshall Space Flight Center, Alabama

Certain solar-cell systems incorporate two layers of epoxy-impregnated fiberglass cloth as insulating material separating the cells from an aluminum supporting plate. The plate is face-sheet of a honeycomb structure. The insulation, however, is often inadequate due to porosity of the fiberglass. Trapped air and volatile materials create voids in the fiberglass through which shorts develop.

An alternate approach uses a solid polyimide film (Kapton, or equivalent)

0.002 in. (0.051 mm) thick as the insulating layer. The film is bonded to the aluminum plate using epoxy-impregnated fiberglass cloth as an adhesive layer. The solar cell is adhesively bonded to the polyimide film. An autoclave applies pressure during the bonding.

Because the film is nonporous, problems due to voids are eliminated. The insulator resistance is uniform (breakdown voltage is greater than 500 volts) over the entire honeycomb

surface area. Currently the film is used to insulate structures measuring 54 by 30 in. (137 by 76 cm).

This work was done by Thomas C. Dvorak of TRW, Inc., for Marshall Space Flight Center. No further documentation is available.

Inquiries concerning rights for the commercial use of this invention should be addressed to the Patent Counsel, Marshall Space Flight Center [see page A8]. Refer to MFS-25007.



Cutting Silicon for Solar Cells

Multiple blades and special guides could speed up production.

NASA's Jet Propulsion Laboratory, Pasadena, California

Multiple bandsaw blades can be used to produce multiple cuts on several silicon boules simultaneously. The method is faster and more reliable than using a single saw or multiple-cut reciprocating-blade. In the proposed system each blade is separately tensioned, so that if one blade fails, the others are not affected.

The approach incorporates a set of bandsaw blades as shown in Figure 1, each 0.005 to 0.006 in. (0.13 to 0.15 mm) thick and 1/2 in. (1.3 cm) wide, running around pulleys. The blades are all of identical length for easy replacement. Each has its own tensioning device, so that if any blade breaks, the system is not disrupted.

Blade position is carefully controlled by easily replaceable guides. A pair of guides before and after the cut stabilizes each blade, eliminating wobble that tends to produce bad slices. The guides rotate 180° during the cutting cycle in the direction shown in Figure 2; thus an unworn portion of the guide will be next to the cutting zone. They are made of low-cost soft material, which reduces blade damage. Each guide is basically (see Figure 2) a set of alternating large- and small-diameter washers with the blades running in line with the small washers. The guides are replaced as a unit rather than individually to reduce system downtime.

Because the system uses looped blades, each blade makes two adjacent cuts on the same side of the boule as the blade passes in opposite directions. Before making the cut, the blade is passed over a knurling wheel that impresses a slight, standard knurl in the cutting edge. This process constantly rebuilds teeth on the cutting edge to transport abrasive slurry to the cutting surface. Undesirable flare of the blade sides following the knurling wheel is removed by a pair of rollers pressing the blade sides flat.

High-velocity air and a vacuum system clean the slurry away from the blades before they travel around the pulleys. (Slurry remaining beyond the cutting area can damage the system

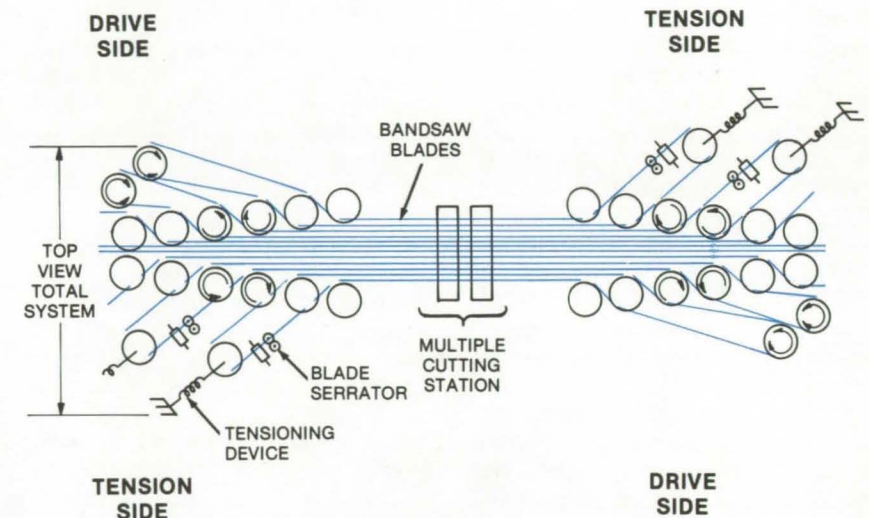


Figure 1. A **Proposed Method for Cutting Silicon Crystals** uses an array of saw blades. Each blade is of the same length for convenient maintenance and is very thin to reduce waste in cutting. A separate tensioning device for each blade makes the system more reliable for operating without interruption even if one blade breaks.

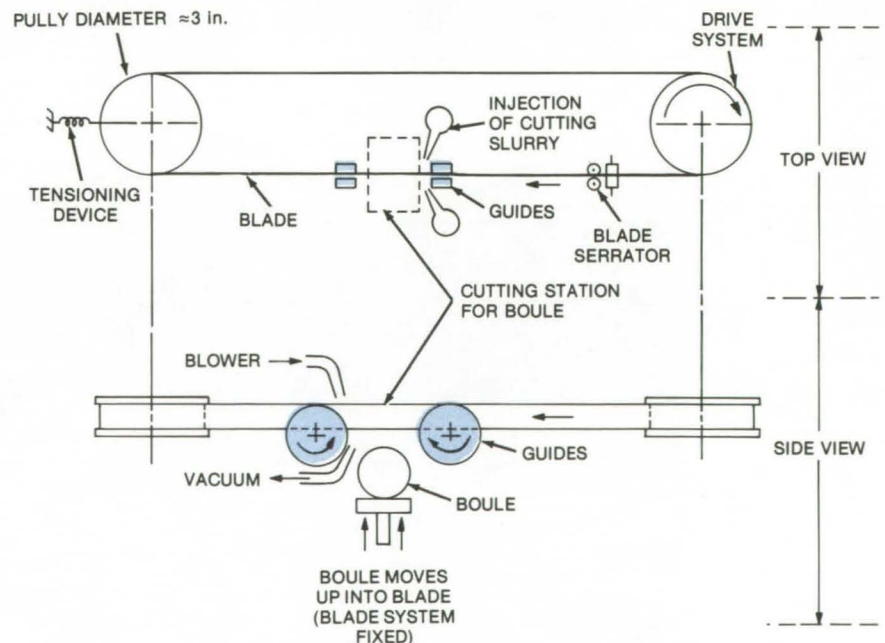


Figure 2. The **Guides** prevent bandsaw wobble. The illustration is simplified for clarity and does not show the other side of the blade, which also cuts the surface.

by causing excessive wear.) The slurry is collected, filtered, and then pumped back into the cutting area. Normal cutting time is expected to last between 5 and 10 min.

This work was done by Earl R. Collins of Caltech for **NASA's Jet Propulsion Laboratory**. For further information, Circle 104 on the TSP Request Card.

This invention is owned by NASA, and a patent application has been filed. Inquiries concerning nonexclusive or exclusive license for its

commercial development should be addressed to the Patent Counsel, NASA Resident Legal Office-JPL [see page A8]. Refer to NPO-14406.

Fixture for Assembling Solar Panels

Device for vacuum-bonding solar cells to a glass cover plate minimizes handling by operators.

NASA's Jet Propulsion Laboratory, Pasadena, California

A vacuum fixture attaches an array of silicon solar cells, complete with their interconnections, to a mounting plate. The solar cells are positioned with their face, or "sunny side," against the mounting plate, which is made of clear glass. The plate thus both holds and protects the cells. The glass plate also transmits, rather than absorbs, the solar energy that passes between the waferlike cells. The plate therefore does not heat up; it cools the cells for efficient operation.

The vacuum fixture prevents air from being trapped between the cells and the plate, and allows an operator to view the cells to ensure that they are completely wet by adhesive. The fixture consists essentially of two transparent walls, each with a vacuum-port valve and a rubber vacuum seal around the periphery of one of its faces. One of the transparent walls is placed on a work table, seal side up. A transparent plastic membrane is placed over the wall, extending beyond the rubber seal on all four sides. Next, a cell/interconnect registration tool (CIRT), holding the adhesive-coated solar cells and their interconnects, is lowered onto the membrane. The glass mounting plate is placed on the CIRT (see figure), and finally the second transparent wall of the vacuum fixture is placed on the mounting plate.

Vacuum lines are connected to the vacuum-port valves of the fixture walls, and a vacuum is drawn on both sides of the membrane. After the air is removed from the fixture, the bottom-wall valve is opened. Air rushes into the bottom half of the fixture, and atmospheric pressure pushes the membrane through holes in the CIRT, lifting the cells and pressing them into the adhesive and against the glass mounting plate. The operator observes the wetting and spreading of the adhesive through the top transparent wall. When the process is complete, he releases



Glass Cover for Solar Panel is loaded on solar-cell array already in vacuum fixture.

the vacuum from the upper half of the fixture and removes the mounting plate and solar-cell assembly.

The CIRT reduces the handling of cells and interconnecting conductors to one operation: loading the parts. Pins in the CIRT, which is essentially a flat plate with holes, align the cells and interconnections as they are loaded. The holes in the CIRT give access to the back of the cells for cleaning and for soldering the interconnects. Before the CIRT is placed in the vacuum fixture, a premeasured amount of adhesive is dispensed on the top of each cell. During the adhesive bonding process, the CIRT's alignment pins support the glass mounting plate, and its holes allow the vacuum membrane to press the cells uniformly into the adhesive.

Because the CIRT must be inverted during part of the preparations for bonding, it is provided with a padded cover that holds the parts firmly but

gently in registration with each other. Loading parts into the CIRT is now a manual operation, but can easily be automated for large-scale production.

This work was done by Paul A. Dillard and Walter M. Fritz of Lockheed Missiles & Space Co., Inc., for NASA's Jet Propulsion Laboratory. For further information, Circle 98 on the TSP Request Card.

This invention is owned by NASA, and a patent application has been filed. Inquiries concerning nonexclusive or exclusive license for its commercial development should be addressed to the Patent Counsel, NASA Resident Legal Office-JPL [see page A8]. Refer to NPO-14303.

Books and Reports

These reports, studies, and handbooks are available from NASA as Technical Support Packages (TSP's) when a Request Card number is cited; otherwise they are available from one of NASA's Industrial Application Centers or the National Technical Information Service.

CMOS Circuit-Fabrication Handbook

Detailed information for a CMOS facility

A report has been released that describes the complementary metal-oxide-semiconductor (CMOS) process used to fabricate integrated circuits at Marshall Space Flight Center. Detailed information on the multilevel metalization process has been included along with general discussions of circuit design, mask making, packaging, and testing. The report, which includes hard data such as diffusion, oxidation, and etch rates, should be useful to those wishing to establish a CMOS facility. Examples of circuits that were designed and fabricated are also given.

The CMOS process is essentially a six-phase operation that includes the following steps:

1. *Computer-Aided Design.* The Boolean logic required for the circuit is converted to mask artwork with the help of an interactive computer-graphics system.
2. *Mask Making.* Seven to nine high-resolution photographic plates are imaged and developed by using a computer-controlled pattern generator and the magnetic tape output from step 1.
3. *Wafer Processing.* Blank silicon wafers are processed into finished circuits in about 2 weeks and are inspected for defects.
4. *Testing.* Static parameters such as threshold voltage, breakdown voltage, and transconductance are measured, and the circuit is stepped through all possible input states for dynamic measurements, using automated test apparatus.
5. *Packaging.* The finished circuits are sealed in flatpacks, "TO" cans, or dual-in-line packages, and the electrical interconnections to the package leads are made by thermocompression or ultrasonic wire bonding.
6. *Final Testing.* The completed circuits are dynamically tested to screen those that failed during the packaging step.

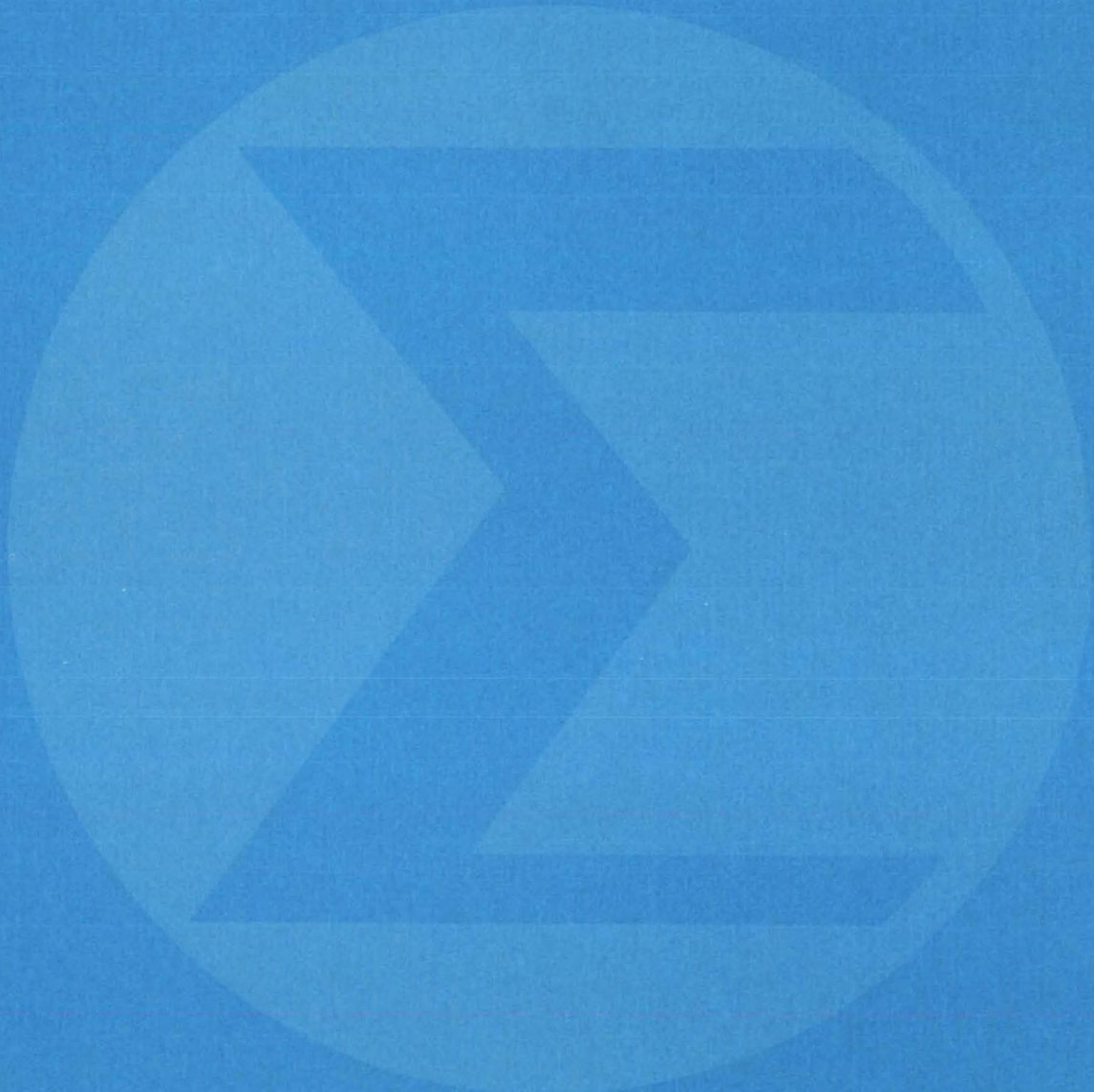
Roughly half of the 60-page report is devoted to details of the third phase, the wafer-processing cycle, with ex-

amples of data sheets and notes of in-process measurements. Twenty-six drawings and accompanying text take the reader through the etching, diffusion, ion-implantation, and other steps that convert the silicon wafer to a finished circuit. Typical exposure times, etch times, and test values are included.

The final part of the report discusses the rationale for the various segments of the process, including a description of the facility requirements, the specifications to be met by the silicon wafers, and the ion-implantation and diffusion procedures. An appendix gives the compositions of the chemical solutions used in the process, graphs of the silicon dioxide growth rates, boron nitride and boron oxide diffusion rates, and oxide etch rates.

This work was done by David L. Bouldin, Richardson W. Eastes, William R. Feltner, Ben R. Hollis, and Donald E. Routh of Marshall Space Flight Center. Further information may be found in NASA TM-78188 [N78-78648], "The MSFC Complementary Metal Oxide Semiconductor (Including Multilevel Interconnect Metallization) Process Handbook," a copy of which may be obtained at cost from the New England Research Application Center [see page A7].
MFS-25034

Mathematics and Information Sciences



Hardware, Techniques, and Processes

- 149 Estimating The Cost of Production Stoppage
- 150 Inexpensive Land-Use Maps Extracted From Satellite Data

Books and Reports

- 150 Landsat and Water Pollution
- 151 Analyzing Earth's Surface Data

Computer Programs

- 152 Redundant System Reliability Analysis

Estimating The Cost of Production Stoppage

Estimation model considers learning curve, quantities, and time of break.

Marshall Space Flight Center, Alabama

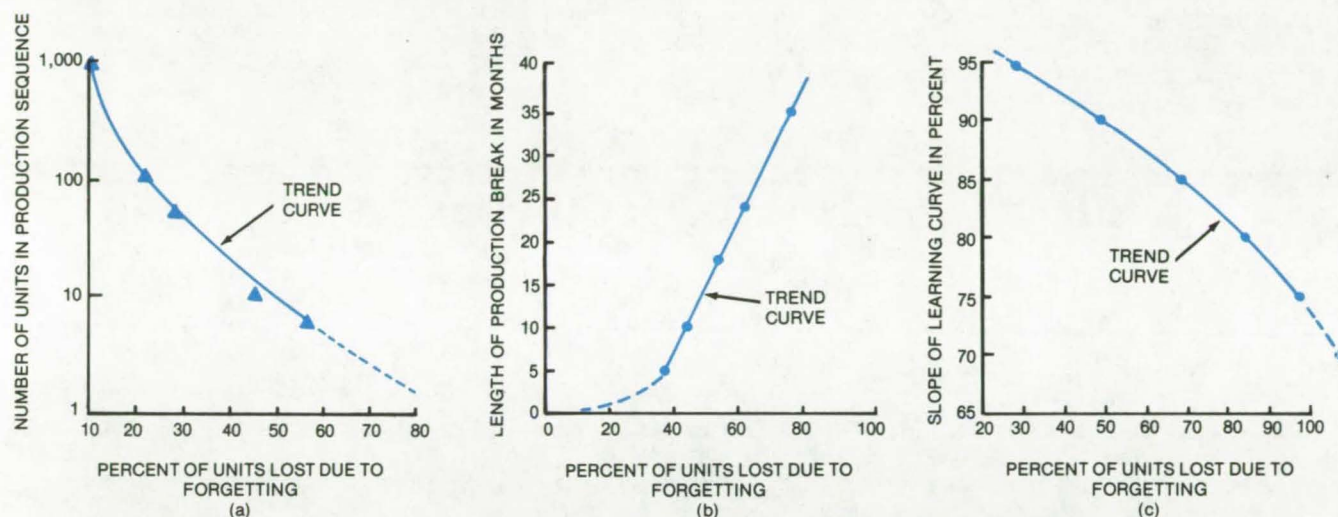


Figure 1. A **Set of Curves** is used to obtain cost impact from a break in a production schedule. Plots (a), (b), and (c), given as percent of units lost due to forgetting, are used to construct a characteristic curve for a given production system.

A time-series figure-of-merit approach is proposed to forecast losses due to a break in a production schedule. Three sensitive parameters are defined that play a key role in the cost of the interrupted production. These are combined to generate two- and three-parameter models capable of predicting costs in terms of units not produced during the waiting period.

The three major parameters are:

1. The number of units already made in a production sequence,
2. The length of the projected production break, and
3. The slope of the learning curve for the units produced prior to the break.

Each of the three is plotted as a function of the percentage of units lost due to "forgetting" (see Figure 1). Here the concept of forgetting reflects that portion of learning lost due to the retrogression during the production break. In other words, whether and to what extent the break is sufficiently long for production people to forget some details of the process. The model assumes that the production rate and unit complexity remain the same as before once the production is resumed.

(continued on next page)

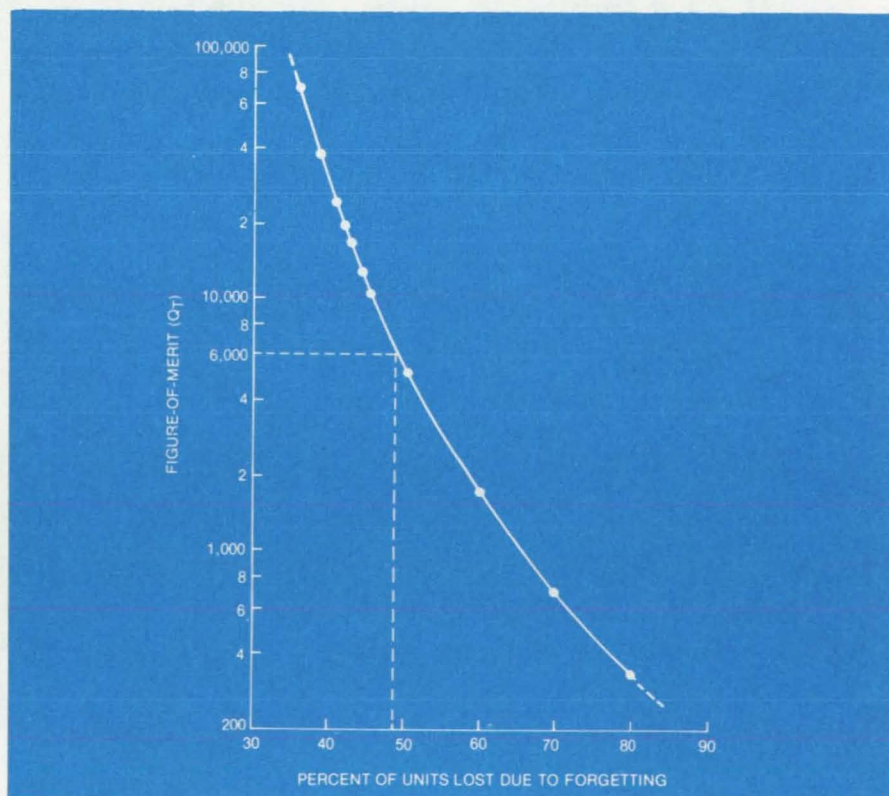


Figure 2. This **Characteristic Curve** is a product of parameters (a), (b), and (c) of Figure 1. For any given figure-of-merit, the cost of a proposed production stoppage is obtained from the percentage on the abscissa of the last production run multiplied by the cost per unit.

The curves of the three parameters are developed empirically for individual production systems. Obviously, the parameters differ for different production systems.

Figure 2 illustrates the figure-of-merit (Q_T) obtained using the three parameters. Each value of Q_T is a product of parameters (a), (b), and (c) of Figure 1 taken at identical percentage values of the abscissas. Parameter Q_T is plotted as a function of the

percent of units lost due to forgetting.

Once such a characteristic curve is developed, one can estimate the effect of an anticipated break in a given production system. After obtaining the figure-of-merit, a percentage value is found from the curve. This percentage is applied to the last production run to estimate the number of units lost and hence the cost of the interruption.

This work was done by Leon M. Delionback of Marshall Space Flight Center. Further information may be found in NASA TM-78131 [N77-34044], "A Prediction Model to Forecast the Cost Impact From a Break in the Production Schedule," a copy of which may be obtained at cost from the New England Research Application Center [see page A7].
MFS-23884

Inexpensive Land-Use Maps Extracted From Satellite Data

Satellite images are interpretable with minimal skill and equipment.

Marshall Space Flight Center, Alabama

A simple and inexpensive method of extracting land-cover and land-use data from satellite images is intended for those who have little or no experience with satellite imagery, have little time and money available, and have no image-interpretation equipment, such as a computer. The method employs a 36- by 36-in. (91- by 91-cm) false-color composite print of the image of an area transmitted from the Landsat satellite. Over the composite print, which is scaled at 1:250,000, is placed a transparent overlay; and on the overlay various natural and artificial features (obtained from maps of the area) are marked. Such features include towns, rivers, lakes, and highways. Then areas that appear similar on the composite are blocked out on the overlay and assigned a land-use category, such as urban or built-up land, cropland, hay and pasture land, forest land, disturbed land, and water.

The land-use classification assigned to a block is determined by several factors: the color of the block or the composite print, the shape and location of the block, adjacent natural and artificial features, and the interpreter's knowledge of the area. Aerial photographs may be consulted as aids in interpretation. Guidelines for successful image interpretation are available in the report referenced at the end of this article.

In a test of the procedure, land use in Boone County, Missouri, was evaluated from Landsat photographs with an average accuracy of 74 percent. (The evaluation was compared to classifications obtained from aerial photographs.) Success with specific land categories varied from 61 percent for cropland to 100 percent for bodies of water. The lower success rate for cropland is partially attributable to a confusion between forest land and plowed soil, which look

identical on the satellite photo. Some of this error can be reduced by attention to landscape position and field patterns.

The Boone County study evaluated land use at a cost of about \$0.25 per square mile (\$0.09 per square kilometer). This estimate includes costs for premapping, overlay preparation, mapping, labor, and materials. Labor was calculated at a rate of \$5 per hour.

This work was done by Terry W. Barney, David J. Barr, C. Dale Elifrits, and C. J. Johannsen of the University of Missouri for Marshall Space Flight Center. Further information may be found in NASA CR-2952 [N78-17446], "Mapping Land Cover From Satellite Images: A Basic, Low Cost Approach," a copy of which may be obtained at cost from the New England Research Application Center [see page A7].
MFS-25111

Books and Reports

These reports, studies, and handbooks are available from NASA as Technical Support Packages (TSP's) when a Request Card number is cited; otherwise they are available from one of NASA's Industrial Application Centers or the National Technical Information Service.

Landsat and Water Pollution

Data derived from satellite images predict pollution loads after rainfall.

A report describes the application of Landsat data to a study of water pollution in Baltimore and five surrounding

Maryland counties. The study is part of a program to develop pollution-abatement plans for the 2,204-square-mile (6,123-km²) area comprising the city of Baltimore and Anne Arundel, Baltimore, Carroll, Harford, and Howard Counties.

The study was concerned with "non-point-source" pollution, which is pollution from diffuse sources such as fertilizers rather than from localized sources such as factories.

The amount of non-point-source pollution that flows into rivers depends on the amount of rainfall and the nature of the land cover. Thus, the report explains the method for converting Landsat images of the Eastern United States into land-cover maps for the pertinent Baltimore/five-county region. Initially, an attempt was made to determine ground-cover patterns and types by computer analysis. Although promising, this approach is not accurate enough at its present level of development. Instead, people inspect Landsat images and draw land-cover maps on transparent overlays. This manual-inspection method gives errors that are less than 5 percent. Data were also gathered on pollution loads in rivers and streams and on rainfall in the area. These were obtained by field measurements and from weather records.

The data on land cover, pollution loads, and rainfall were used in a computer model developed for the study. With this data base, the model predicts water pollution for given weather conditions.

As the report explains, a section of the Baltimore/five-county region (the Magothy River basin in Anne Arundel County) was used to calibrate the model. The accuracy of land-cover classifications was checked by comparing the satellite-derived land-cover map for the basin with aerial photographs. Guidelines for interpreting Landsat images were altered as necessary to improve accuracy.

Similarly, the rainfall and pollution-load measurements for the Magothy River basin were fed to the computer so that the model response could be adjusted to bring predictions in line with observations. For example, the pollution load attributable to each type of land cover can be adjusted to improve the agreement with measured pollution levels.

The report includes a description of the model and its FORTRAN listing. The model reads from its files data on rainfall and land-cover characteristics for each basin in the region. It then computes overland flow as a function of time for each basin. The model routes the flow from stream to stream until the basin outlet is reached. The computer printout includes a tabulation of time from the start of rainfall, the rain and discharge rate for each

basin, and the cumulative rain and discharge rate. Finally, the model computes and prints out a tabulation of monthly pollutant loads.

This work was done by Peter Castruccio, Thomas Fowler, and Harry Loats, Jr., of ECOsystems International, Inc., for Marshall Space Flight Center. Further information may be found in NASA CR-3041 [N78-32526], "Applications of Remote Sensing to Hydrologic Planning," a copy of which may be obtained at cost from the New England Research Application Center (see page A7). MFS-25099

Analyzing Earth's Surface Data

Inexpensive methods are presented.

A new manual discusses simple, inexpensive, image analysis techniques used in interpreting photographs and scanner data of the Earth's surface. The manual is designed for those who have no need for sophisticated computer-automated analysis procedures.

The equipment recommended for low-cost data analyses includes stereoscopes, light tables, additive and subtractive color devices, photographic processes, microviewers, transfer devices, and drafting and cartographic equipment.

The stereoscopes are available as pocket or mirror models. Pocket stereoscopes are somewhat smaller and do not require extra lighting. The mirror stereoscopes are larger and require more working area.

Light tables are simply backlighted frosted-glass fixtures suitable for viewing transparencies at a temperature that will not damage the materials. These tables can be either built in a local shop or purchased at a reasonable cost.

The color devices are used to enhance specific images of multispectral Landsat imagery. The least expensive of these systems is the subtractive Diazo processor. Additive color viewers are more versatile and more expensive, permitting optical superposition of up to four Landsat transparencies produced from each of

four Landsat multispectral channels. An alternative is to boresight several 35-mm slide projectors onto a screen to approximate the same effect.

Photographic equipment consisting of a camera, a copy stand, and standard darkroom equipment may be used for enhancement or enlargement of specific terrain features. Contrasting filters may be used to obtain an enlarged detail with improved definitions.

Microviewers are used for viewing microfilm or microfiche. Depending on the model, 35-mm slides may be enlarged to a 16- by 20-in. (40- by 50-cm) projection.

Transfer devices are used to plot or replot data at a scale different from the original photo, image, or map. These devices are used to zoom the photo to the base-map scale and to superimpose the photo onto the base map for recording data on an overlay to the base map.

Standard drafting equipment includes at least a technical fountain-pen set and lettering set along with suitable tables. Standard supplies include ink and acetate sheets.

The manual proceeds with techniques used in interpreting the photographic data. Various photo tone and texture combinations are presented. For example, uniform light tones represent barren rock or coarse textured soils without vegetative cover, whereas dark tones represent moist areas, and so on. Other criteria are used in identifying populated areas, manmade and natural drainage erosion areas, and well-vegetated areas.

A similar discussion follows for Landsat displays. Both black and white and color Landsat displays are discussed. Details are given on how to identify manmade and natural surfaces.

Three image-enhancement techniques are presented: additive color technique, subtractive color (Diazo Process) technique, and enlargement. The former two are used on Landsat imagery, whereas the latter is used on all types of imagery.

The manual concludes by presenting various applications of the analysis techniques. For example the techniques may be used in land-use/land-resource mapping, engineering soils mapping, geologic mapping, water-

(continued on next page)



resource mapping, environmental assessment, and crop and vegetation mapping.

This work was done by David J. Barr and C. Dale Elifrits of the University of

*Missouri-Rolla for **Marshall Space Flight Center**. To obtain a copy of the manual, Circle 102 on the TSP Request Card.*
MFS-25051

Computer Programs

These programs may be obtained at very reasonable cost from COSMIC, a facility sponsored by NASA to make new programs available to the public. For information on program price, size, and availability, circle the reference letter on the COSMIC Request Card in this issue.

Redundant System Reliability Analysis

Partitioned Markov model reduces complexity.

The Computer Aided Redundant System Reliability Analysis (CARSRA) program facilitates the reliability assessment of fault-tolerant reconfigurable systems. CARSRA accounts for influences from transient faults and can be used to model a wide range of redundancy management strategies.

Many previous reliability-estimation tools, based on success-path tabulation methods, required costly examination of many paths in highly redundant systems. They were also unable to model transient faults and failure coverage effects. Recently, Markov modeling has been utilized to model the effect of failure coverage. The flexible Markov model makes it possible to account for most factors of interest, in-

cluding fault transients, failure coverage, and the possibility of spares or maintenance action.

A basic disadvantage of the direct Markov-model approach is the very large number of Markov states required to model a system with many internal signal-consolidation nodes. The most significant feature of CARSRA is the partitioning of the system into smaller entities, each of which may be treated by a Markov model of lower dimension. This preserves the Markov-model flexibility while avoiding an exorbitant number of Markov states.

CARSRA assesses functional readiness as well as failure probability. Functional readiness is of considerable importance for a mission containing a critical subtask that may or may not be preformed, depending on the operational redundancy level at the time of demand. An example is an automatic aircraft landing for which a certain level of hardware is required.

In CARSRA, a system is partitioned into stages; for example, each sensor type in a flight control system constitutes a stage, as do the processors, and each of these serves a function. The operational status of each stage is modeled by a finite-order Markov process in which each state corresponds to a particular redundancy state. Transition rates are assumed constant, and up to 10 states per stage can be

handled. The operational status of a module in a particular stage may or may not depend on modules in other stages being operational.

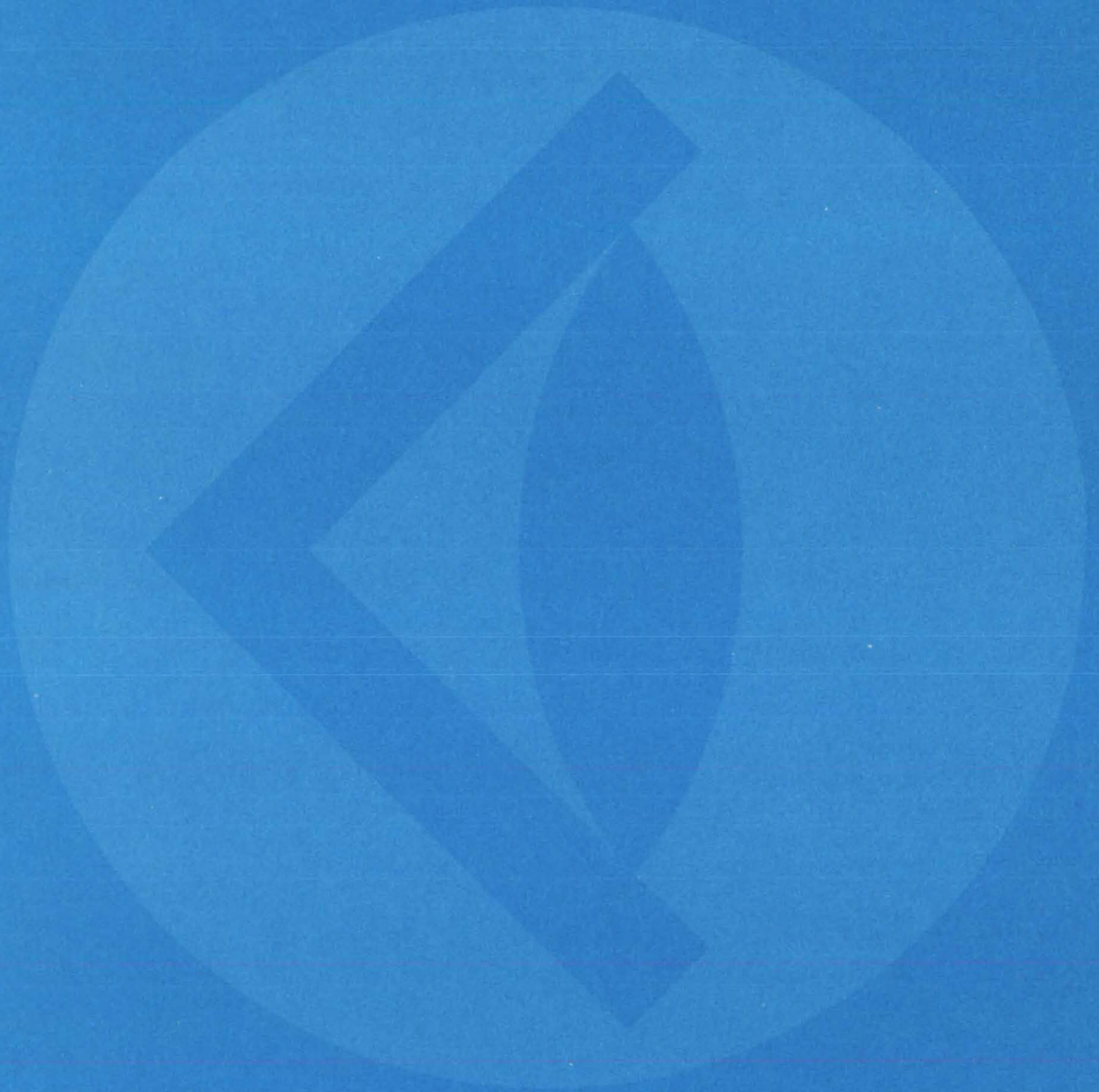
Thus there are "dependency" and "nondependency" stages. Some stages may be both. The dependency structure of a system is described by a dependency tree. Dependency between stages is handled by an approach called "exhaustive conditioning". Each nondependency stage is math independent via conditioning upon the failure status of the dependency states.

Success probability is computed from specification of the functions needed for success, using success configuration tabulation. A functional readiness feature assesses the probability of experiencing a certain redundancy degradation, and its associated failure probability, for a fault-tolerant system that continues to function even after one or more module failures.

CARSRA is written in FORTRAN IV and has been implemented on a CDC 6000-series machine with a central memory requirement of approximately 67K of 60-bit words.

*This program was written by C.J. Masreliez of The Boeing Co. for **Langley Research Center**. For further information, Circle B on the COSMIC Request Card.*
LAR-12069

SUBJECT INDEX



ABERRATION

Improved flight-simulator viewing lens
page 50 LAR-12251

ABSORBENTS

Low-absorptance porcelain-on-aluminum coating
page 75 MFS-23879

"Self-packaging" desiccant
page 67 NPO-14354

ABSORPTION SPECTRA

All-electric gas detector
page 45 NPO-14341

Low-noise spectrophone
page 46 NPO-14362

ACOUSTIC ATTENUATION

Annular acoustic liners for turbofan engines
page 132 LEW-12810

ACOUSTIC MEASUREMENTS

Low-noise spectrophone
page 46 NPO-14362

ACTUATORS

Controller for a Stirling engine
page 128 NPO-14388

ADHESIVE BONDING

Fastening hardware to honeycomb panels
page 141 MSC-16752

AERIAL PHOTOGRAPHY

Analyzing Earth's surface data
page 151 MFS-25051

Electronic pictures from charge-coupled devices
page 17 GSC-12324

Film-advance monitor
page 118 LAR-12474

AGRICULTURE

Solar energy in the dairy industry
page 62 NPO-14498

AIR FLOW

Electrical indication of airflow rate
page 92 MFS-23873

AIR POLLUTION

Burning crude oil without pollution
page 76 NPO-14344

AIRCRAFT ENGINES

Annular acoustic liners for turbofan engines
page 132 LEW-12810

Stiffness and damping of elastomeric O-rings
page 131 LEW-13079

AIRCRAFT INSTRUMENTS

LED display for solo aircraft instrument navigation
page 26 LAR-12292

ALUMINUM

Giant-electrode welder
page 137 LAR-11429

Low-absorptance porcelain-on-aluminum coating
page 75 MFS-23879

ALUMINUM OXIDES

Controlled metal-film deposition on alumina
substrates
page 78 ARC-11214

ANAEROBES

Fuel gas from biodigestion
page 48 MFS-23957

ANALOG TO DIGITAL CONVERTERS

Real-time video-image analysis
page 20 NPO-14282

ANGULAR RESOLUTION

Synthetic-aperture-radar azimuth correlator
page 22 NPO-14019

ANTENNA COMPONENTS

Antenna deployment mechanism
page 120 GSC-12331

Components for an S-band communication
subsystem
page 24 NPO-13955

Low-backlobe microwave transmitting horn
page 5 NPO-14077

ANTENNA DESIGN

Efficient dichroic plate for microwaves
page 4 GSC-12171

Signal separator for dual-frequency antenna
page 23 NPO-14022

Synthetic-aperture-radar azimuth correlator
page 22 NPO-14019

ANTENNA RADIATION PATTERNS

Analysis of aperture antenna radiation pattern
page 63 MSC-16246

Low-backlobe microwave transmitting horn
page 5 NPO-14077

ATMOSPHERIC MOISTURE

Measuring moisture in the atmosphere
page 110 MFS-25032

ATTENUATORS

Low-frequency attenuator circuit
page 11 FRC-11012

AUDIO FREQUENCIES

TV audio and video on the same channel
page 19 MSC-16241

AUTOMATIC GAIN CONTROL

Decision-directed automatic gain control
page 10 NPO-13639

AVALANCHE DIODES

Fiber-optic crossbar switches
page 8 KSC-11104

Low-noise current regulator
page 12 NPO-14070

BACKGROUND NOISE

Improved InSb photodiode preamplifier circuit
page 9 NPO-14418

BACKLOBES

Low-backlobe microwave transmitting horn
page 5 NPO-14077

BACTERIA

Fuel gas from biodigestion
page 48 MFS-23957

Identification of micro-organisms
page 85 MSC-18358

BEARINGS

Friction coefficients of PTFE bearing liner
page 110 MFS-19389

BIBLIOGRAPHIES

An annotated energy bibliography
page 62 LAR-12488

BODY KINEMATICS

Dynamic simulation and stability analysis
page 111 GSC-12422

BONDING

Room-temperature bonding of thin plastic sheets
page 138 NPO-14346

BOULES

A method for cutting silicon
page 144 NPO-14406

BRAZING

A furnace brazing technique
page 138 MFS-19363

BUILDING STRUCTURES

Analysis of building heating and cooling
page 63 NPO-14683

BURNING TIME

Burn-test apparatus for fiber composites
page 109 NPO-14578

BURNS (INJURIES)

Computers help evaluate skin burns
page 82 NPO-14402

BUTT JOINTS

Fixture for limited-access welding

CABLES

Cable-fault locator
page 27 KSC-10899

Simpler cabling and power link for remote readouts
page 30 GSC-12411

CALIBRATING

Self-calibrating threshold detector for noisy
signals
page 10 MSC-16370

CALORIMETERS

Containerless high-temperature calorimeter
page 89 MFS-23923

CAMERAS

Film-advance monitor
page 118 LAR-12474

CARBON FIBER REINFORCED PLASTICS

Burn-test apparatus for fiber composites
page 109 NPO-14578

CASES (CONTAINERS)

Antitheft container for instruments
page 104 GSC-12399

CATALYSTS

Controlled metal-film deposition on alumina
substrates
page 78 ARC-11214

CENTER OF GRAVITY

Accurate measurements of mass and center of
mass
page 96 NPO-14428

Accurate measurements of mass and center of
mass
page 96 NPO-14428

Centroid, moments, and radii of gyration
page 114 LEW-12765

Centroid, moments, and radii of gyration
page 114 LEW-12765

Centroid, moments, and radii of gyration
page 114 LEW-12765

CERAMICS

Characterizing glass frits for slurries
page 103 MSC-18322

Low-absorptance porcelain-on-aluminum coating
page 75 MFS-23879

Repairing cracked glass
page 135 KSC-11097

CHARGE COUPLED DEVICES

Electronic pictures from charge-coupled devices
page 17 GSC-12324

Reliability of imaging CCD's
page 14 MFS-25039

Reliability of imaging CCD's
page 14 MFS-25039

Reliability of imaging CCD's
page 14 MFS-25039

Reliability of imaging CCD's
page 14 MFS-25039

Reliability of imaging CCD's
page 14 MFS-25039

CHEMICAL REACTORS

A reactor for more efficient solar cells
page 72 NPO-14381

Chemical-vapor-deposition reactor
page 73 NPO-14137

Quartz ball valve
page 127 NPO-14473

Quartz ball valve
page 127 NPO-14473

Quartz ball valve
page 127 NPO-14473

Quartz ball valve
page 127 NPO-14473

Quartz ball valve
page 127 NPO-14473

Quartz ball valve
page 127 NPO-14473

Quartz ball valve
page 127 NPO-14473

Quartz ball valve
page 127 NPO-14473

Quartz ball valve
page 127 NPO-14473



COAL

- Ensuring flat cuts in longwall mining
page 117 MFS-23726
- Fluidized coal combustion
page 69 NPO-14273
- Improved coal-slurry pipeline
page 47 NPO-14425
- Irradiation pretreatment for coal desulfurization
page 68 NPO-14104

COATING

- A continuous silicon-coating facility
page 70 NPO-14373
- Audible monitor for electroplating
page 106 MFS-19333
- Low-absorptance porcelain-on-aluminum coating
page 75 MFS-23879
- Production of large-area electrets
page 55 MFS-23186
- Repairing cracked glass
page 135 KSC-11097
- Silicon source for vacuum deposition
page 74 LAR-12356
- Vapor-deposited graded-thickness films
page 142 GSC-11806

COAXIAL CABLES

- Simpler cabling and power link for remote readouts
page 30 GSC-12411

COCKPIT SIMULATORS

- A closed-loop control-loading system
page 32 LAR-12167

CODING

- A telephone multiline signaling system
page 33 KSC-11023
- TV audio and video on the same channel
page 19 MSC-16241

COEFFICIENT OF FRICTION

- Friction coefficients of PTFE bearing liner
page 110 MFS-19389

COHERENT RADAR

- Eliminating clutter in synthetic-aperture radar
page 21 NPO-14035

COLLIMATORS

- Optical system for multispectral scanner
page 52 MSC-18255

COMBUSTION

- Burning crude oil without pollution
page 76 NPO-14344

COMBUSTION CHAMBERS

- Fluidized coal combustion
page 69 NPO-14273

COMPOSITE MATERIALS

- Burn-test apparatus for fiber composites
page 109 NPO-14578

COMPOSITE STRUCTURES

- Electrical insulation for an aluminum plate
page 143 MFS-25007
- Fastening hardware to honeycomb panels
page 141 MSC-16752
- Plug and drill template
page 119 MSC-16748

COMPRESSION TESTS

- Static load testing of a liquid solar collector
page 59 MFS-25115

COMPUTER STORAGE DEVICES

- Optical memories in digital computing
page 35 MFS-23897
- Real-time video-image analysis
page 20 NPO-14282
- Troubleshooting plated-wire memories
page 100 MFS-23903

COMPUTER TECHNIQUES

- Computers help evaluate skin burns
page 82 NPO-14402

COMPUTERIZED SIMULATION

- Dynamic simulation and stability analysis
page 111 GSC-12422

CONCENTRATORS

- Variable-shape solar-energy concentrator
page 44 NPO-13736

CONFIGURATION MANAGEMENT

- Test configuration identifiers
page 103 KSC-11087

CONSTRUCTION

- Laser for alignment of large assemblies
page 99 MSC-19346

CONTROL EQUIPMENT

- Fast-response power saver for induction motors
page 6 MFS-23988

CONTROL-LOADING

- A closed-loop control-loading system
page 32 LAR-12167

CONTROLLERS

- Controller for solar heating — design package
page 61 MFS-25009

COOLING SYSTEMS

- Analysis of building heating and cooling
page 63 NPO-14683
- Rankine-cycle heating and cooling systems
page 58 MFS-23998
- Rankine-cycle solar-cooling systems
page 57 MFS-25094

CORE STORAGE

- Improving low-illumination video
page 18 MSC-14841

CORRELATION DETECTION

- Eliminating clutter in synthetic-aperture radar
page 21 NPO-14035

CORRELATORS

- Synthetic-aperture-radar azimuth correlator
page 22 NPO-14019

COST ANALYSIS

- Cost analysis of hot-air solar-heating systems
page 61 MFS-25092

COST ESTIMATES

- Cost impact from break in production
page 149 MFS-23884

COUPLERS

- Components for an S-band communication
subsystem
page 24 NPO-13955

COUPLINGS

- Artificial limb connector
page 83 KSC-11069

CRACKS

- Inspecting cracks in foam insulation
page 107 MFS-23799
- Repairing cracked glass
page 135 KSC-11097

CRUCIBLES

- A continuous silicon-coating facility
page 70 NPO-14373

CRUDE OIL

- Burning crude oil without pollution
page 76 NPO-14344

CRYSTALS

- A method for cutting silicon
page 144 NPO-14406

CURRENT DISTRIBUTION

- Theory of back-surface-field solar cells
page 57 NPO-14451

CURRENT REGULATORS

- Low-noise current regulator
page 12 NPO-14070

CURVES [GEOMETRY]

- Centroid, moments, and radii of gyration
page 114 LEW-12765

CUTTING

- A method for cutting silicon
page 144 NPO-14406

DAMPING

- Stiffness and damping of elastomeric O-rings
page 131 LEW-13079

DATA ACQUISITION

- Electrical indication of airflow rate
page 92 MFS-23873

DATA PROCESSING

- Optical memories in digital computing
page 35 MFS-23897

DECONTAMINATION

- Continuous sterilization of plumbing systems
page 77 KSC-11085

DEHYDRATION

- "Self-packaging" desiccant
page 67 NPO-14354

DELAY LINES

- Group-delay standards
page 14 NPO-13938

DEMODULATION

- Self-calibrating threshold detector for noisy
signals
page 10 MSC-16370

DEPLOYMENT

- Parachute deploy/release mechanism
page 125 LAR-11575

DEPOSITION

- Controlled metal-film deposition on alumina
substrates
page 78 ARC-11214
- Production of large-area electrets
page 55 MFS-23186
- Vapor-deposited graded-thickness films
page 142 GSC-11806

DESICCANTS

- "Self-packaging" desiccant
page 67 NPO-14354

DESULFURIZING

- Irradiation pretreatment for coal desulfurization
page 68 NPO-14104
- Soda ash removes sulfur from fuels
page 69 GSC-12403

DIAGNOSIS

- Computers help evaluate skin burns
page 82 NPO-14402

DICHROISM

- Efficient dichroic plate for microwaves
page 4 GSC-12171
- Optical system for multispectral scanner
page 52 MSC-18255

DIELECTRIC POLARIZATION

- Production of large-area electrets
page 55 MFS-23186

DIES

- Volume-change indicator for molding
page 122 LAR-12280

DIGITAL COMPUTERS

- Optical memories in digital computing
page 35 MFS-23897

DIGITAL SYSTEMS

- Real-time video-image analysis
page 20 NPO-14282
- Self-calibrating threshold detector for noisy
signals
page 10 MSC-16370

DIGITAL TECHNIQUES

- A telephone multiline signaling system
page 33 KSC-11023
- Decision-directed automatic gain control
page 10 NPO-13639
- Differential oil flowmeter
page 91 MFS-23959
- Improving low-illumination video
page 18 MSC-14841
- LED display for solo aircraft instrument navigation
page 26 LAR-12292
- Synthetic-aperture-radar azimuth correlator
page 22 NPO-14019
- TV audio and video on the same channel
page 19 MSC-16241

DIPLEXERS Components for an S-band communication subsystem page 24	NPO-13955	ELECTRIC WIRE Nondestructive pull tester page 93	MSC-18329	Soda ash removes sulfur from fuels page 69	GSC-12403
DIPOLE ANTENNAS Efficient dichroic plate for microwaves page 4	GSC-12171	Push test for stitch welds page 94	MFS-25027	ENAMELS Applying photosensitive emulsions to enamel surfaces page 143	MSC-18107
DISASTERS Monitoring disaster areas via satellites page 30	LAR-12344	ELECTRICAL FAULTS Cable-fault locator page 27	KSC-10899	Low-absorptance porcelain-on-aluminum coating page 75	MFS-23879
DISPLAY DEVICES LED display for solo aircraft instrument navigation page 26	LAR-12292	ELECTRICAL INSULATION Electrical insulation for an aluminum plate page 143	MFS-25007	ENERGY CONSERVATION Analysis of building heating and cooling page 63	NPO-14683
DRIFT [INSTRUMENTATION] Low-noise current regulator page 12	NPO-14070	Fixture for measuring resistance or conductance page 98	MSC-18132	Fuel gas from biodigestion page 48	MFS-23957
DRILLING Plug and drill template page 119	MSC-16748	Measuring insulation thickness page 108	MFS-23798	Irradiation pretreatment for coal desulfurization page 68	NPO-14104
DRYING "Self-packaging" desiccant page 67	NPO-14354	ELECTRICAL MEASUREMENT Adapting an electrical output to a mechanical flowmeter page 90	MFS-23958	Performance test for a solar water heater page 59	MFS-25114
DUST COLLECTORS Production of large-area electrets page 55	MFS-23186	Differential oil flowmeter page 91	MFS-23959	Solar-heating system — performance tests page 58	MFS-25116
DYNAMIC LOADS A closed-loop control-loading system page 32	LAR-12167	Fixture for measuring resistance or conductance page 98	MSC-18132	Static load testing of a liquid solar collector page 59	MFS-25115
DYNAMIC RESPONSE Fader and ramp shaper replace linear filters page 34	MSC-16115	ELECTRO-OPTICAL PHOTOGRAPHY Electronic pictures from charge-coupled devices page 17	GSC-12324	ENERGY CONVERSION Improved coal-slurry pipeline page 47	NPO-14425
EARTH SURFACE Analyzing Earth's surface data page 151	MFS-25051	ELECTRODES Audible monitor for electroplating page 106	MFS-19333	Solar power conditioner page 41	NPO-14356
ECHOCARDIOGRAPHY High-resolution echocardiography page 81	NPO-14349	Fixture for measuring resistance or conductance page 98	MSC-18132	Variable-shape solar-energy concentrator page 44	NPO-13736
ECOLOGY Marine chlorophyll a analysis page 54	LAR-12293	Giant-electrode welder page 137	LAR-11429	ENERGY POLICY An annotated energy bibliography page 62	LAR-12488
ECONOMIC ANALYSIS Cost impact from break in production page 149	MFS-23884	ELECTROMAGNETIC WAVE FILTERS Efficient dichroic plate for microwaves page 4	GSC-12171	Solar energy in the dairy industry page 62	NPO-14498
ECONOMIC FACTORS Solar energy in the dairy industry page 62	NPO-14498	Signal separator for dual-frequency antenna page 23	NPO-14022	ENERGY REQUIREMENTS Solar power conditioner page 41	NPO-14356
EDDY CURRENTS Measuring insulation thickness page 108	MFS-23798	ELECTRON BEAM WELDING Checking weld penetration page 95	MFS-19395	ENGINE CONTROL Controller for a Stirling engine page 128	NPO-14388
ELASTIC DEFORMATION Dynamic simulation and stability analysis page 111	GSC-12422	Ultrasonic grating checks electron-beam welds page 95	MFS-19422	ENGINEERING DRAWINGS Centroid, moments, and radii of gyration page 114	LEW-12765
ELASTOMERS Stiffness and damping of elastomeric O-rings page 131	LEW-13079	ELECTRONIC EQUIPMENT TESTS Nondestructive pull tester page 93	MSC-18329	ENVIRONMENT POLLUTION Burning crude oil without pollution page 76	NPO-14344
ELECTRETS Production of large-area electrets page 55	MFS-23186	Push test for stitch welds page 94	MFS-25027	Landsat and water pollution page 150	MFS-25099
ELECTRIC CONTACTS Nondestructive pull tester page 93	MSC-18329	ELECTRONIC FILTERS Components for an S-band communication subsystem page 24	NPO-13955	EQUATIONS OF MOTION Dynamic simulation and stability analysis page 111	GSC-12422
Push test for stitch welds page 94	MFS-25027	Fader and ramp shaper replace linear filters page 34	MSC-16115	EQUIPMENT SPECIFICATIONS Controller for solar heating — design package page 61	MFS-25009
Wraparound contacts for solar cells page 3	LEW-13089	Low-frequency attenuator circuit page 11	FRC-11012	Design information for solar-heating systems page 58	MFS-25097
ELECTRIC DISCHARGES Cloud-to-ground lightning detector page 28	KSC-11099	ELECTRONIC PACKAGING Wraparound contacts for solar cells page 3	LEW-13089	Design of a concentrating solar collector page 60	MFS-25098
ELECTRIC MOTORS Fast-response power saver for induction motors page 6	MFS-23988	ELECTRONIC TRANSDUCERS Electrical indication of airflow rate page 92	MFS-23873	Rankine-cycle heating and cooling systems page 58	MFS-23998
ELECTRIC POWER SUPPLIES Solar power conditioner page 41	NPO-14356	ELECTROPLATING Audible monitor for electroplating page 106	MFS-19333	Rankine-cycle solar-cooling systems page 57	MFS-25094
		Electroplating offers embrittlement protection page 140	MFS-19330	ESTIMATES Cost impact from break in production page 149	MFS-23884
		ELECTROSTATIC CHARGE Production of large-area electrets page 55	MFS-23186	ETHYLENE OXIDE Continuous sterilization of plumbing systems page 77	KSC-11085
		EMBRITTLEMENT Electroplating offers embrittlement protection page 140	MFS-19330	EYE MOVEMENTS Eye-controlled switch page 84	MFS-25091
		EMULSIONS Applying photosensitive emulsions to enamel surfaces page 143	MSC-18107	FABRICATION Assembling solar-cell arrays page 43	NPO-14416



CMOS circuit-fabrication handbook page 146	MFS-25034	FOLDING STRUCTURES Parachute deploy/release mechanism page 125	LAR-11575	GLASS Characterizing glass frits for slurries page 103	MSC-18322
FADING Fader and ramp shaper replace linear filters page 34	MSC-16115	FORCE DISTRIBUTION A closed-loop control-loading system page 32	LAR-12167	Repairing cracked glass page 135	KSC-11097
FARMLANDS Inexpensive land-use maps extracted from satellite data page 150	MFS-25111	FOSSIL FUELS Fluidized coal combustion page 69	NPO-14273	GLASS FIBER REINFORCED PLASTICS Electrical insulation for an aluminum plate page 143	MFS-25007
FASTENERS Fastening hardware to honeycomb panels page 141	MSC-16752	Improved coal-slurry pipeline page 47	NPO-14425	GLASS FIBERS Measuring insulation thickness page 108	MFS-23798
Plug and drill template page 119	MSC-16748	FRACTIONATION Irradiation pretreatment for coal desulfurization page 68	NPO-14104	GLAZES Characterizing glass frits for slurries page 103	MSC-18322
Removable fastener for insulating tiles page 123	MSC-16483	FREQUENCY MULTIPLIERS VHF frequency multiplier page 7	NPO-13700	Repairing cracked glass page 135	KSC-11097
Removable fastener for large structures page 126	MFS-23990	FRICTION REDUCTION Friction coefficients of PTFE bearing liner page 110	MFS-19389	GRAPHIC ARTS Centroid, moments, and radii of gyration page 114	LEW-12765
FIBER OPTICS Fiber-optic crossbar switch page 8	KSC-11104	FRIT Characterizing glass frits for slurries page 103	MSC-18322	HEART High-resolution echocardiography page 81	NPO-14349
FILM THICKNESS Measuring the thickness of plastic films page 100	ARC-11219	FUEL CONSUMPTION Analysis of building heating and cooling page 63	NPO-14683	HEART RATE Low-frequency attenuator circuit page 11	FRC-11012
Vapor-deposited graded-thickness films page 142	GSC-11806	FUEL GAGES Adapting an electrical output to a mechanical flowmeter page 90	MFS-23958	HEAT EXCHANGERS Design information for solar-heating systems page 58	MFS-25097
FINANCIAL MANAGEMENT Cost impact from break in production page 149	MFS-23884	Differential oil flowmeter page 91	MFS-23959	HEAT PUMPS Rankine-cycle heating and cooling systems page 58	MFS-23998
FINISHES Applying photosensitive emulsions to enamel surfaces page 143	MSC-18107	FUEL INJECTION Fluidized coal combustion page 69	NPO-14273	Rankine-cycle solar-cooling systems page 57	MFS-25094
FIXTURES A furnace brazing technique page 138	MFS-19363	FUELS Fuel gas from biodigestion page 48	MFS-23957	HEATING Analysis of building heating and cooling page 63	NPO-14683
Fixture for assembling solar panels page 145	NPO-14303	Soda ash removes sulfur from fuels page 69	GSC-12403	Fuel gas from biodigestion page 48	MFS-23957
Fixture for limited-access welding page 136	MSC-16698	FURNACES A furnace brazing technique page 138	MFS-19363	HEATING EQUIPMENT Air solar collector — installation package page 59	MFS-25031
Fixture for measuring resistance or conductance page 98	MSC-18132	Differential oil flowmeter page 91	MFS-23959	Concentrating solar collector — performance tests page 60	MFS-25086
FLANGES Signal separator for dual-frequency antenna page 23	NPO-14022	FUSION [MELTING] Checking weld penetration page 95	MFS-19395	Controller for solar heating — design package page 61	MFS-25009
FLIGHT SIMULATION A closed-loop control-loading system page 32	LAR-12167	GAS DETECTORS All-electric gas detector page 45	NPO-14341	Cost analysis of hot-air solar-heating systems page 61	MFS-25092
FLIGHT SIMULATORS Improved flight-simulator viewing lens page 50	LAR-12251	Low-noise spectrophone page 46	NPO-14362	Design information for solar-heating systems page 58	MFS-25097
FLOOD PREDICTIONS Monitoring disaster areas via satellites page 30	LAR-12344	GAS FLOW Electrical indication of airflow rate page 92	MFS-23873	Design of a concentrating solar collector page 60	MFS-25098
FLOW DIRECTION INDICATORS Bidirectional fluid-flow monitor page 92	MSC-16762	Quartz ball valve page 127	NPO-14473	Fluidized coal combustion page 69	NPO-14273
FLOW DISTRIBUTION Projection optics for a laser velocimeter page 51	LAR-12328	GAS GENERATORS Fuel gas from biodigestion page 48	MFS-23957	Liquid solar collector — performance evaluation page 59	MFS-25090
FLOW MEASUREMENT Extending the range of leak detectors page 105	MFS-19411	GAS STREAMS Chemical-vapor-deposition reactor page 73	NPO-14137	Performance test for a solar water heater page 59	MFS-25114
FLOWMETERS Adapting an electrical output to a mechanical flowmeter page 90	MFS-23958	GAS-METAL INTERACTIONS Electroplating offers embrittlement protection page 140	MFS-19330	Rankine-cycle heating and cooling systems page 58	MFS-23998
Differential oil flowmeter page 91	MFS-23959	GASKETS Rubber valve seal with tough skin page 124	LAR-11776	Solar-heating system — performance tests page 58	MFS-25116
FLUID FLOW Bidirectional fluid-flow monitor page 92	MSC-16762	Window with integral seal page 140	MSC-16490	Solar-powered pump page 39	MFS-23996
FOAMS Inspecting cracks in foam insulation page 107	MFS-23799	GEARS Controller for a Stirling engine page 128	NPO-14388	HERMETIC SEALS Window with integral seal page 140	MSC-16490
Temporary insulation with polyurethane foam page 139	MSC-18298			HIGH TEMPERATURE AIR Air solar collector — installation package page 59	MFS-25031

HIGH TEMPERATURE TESTS

Containerless high-temperature calorimeter
page 89 MFS-23923

HINGES

Hinge-connected rigid bodies
page 113 NPO-11964

HOME HEATING SYSTEMS

Effects of weathering on a liquid solar collector
page 60 MFS-25113

Fuel gas from biodigestion
page 48 MFS-23957

Performance test for a solar water heater
page 59 MFS-25114

Solar-heating system — performance tests
page 58 MFS-25116

Static load testing of a liquid solar collector
page 59 MFS-25115

HONEYCOMB STRUCTURES

Electrical insulation for an aluminum plate
page 143 MFS-25007

Fastening hardware to honeycomb panels
page 141 MSC-16752

Plug and drill template
page 119 MSC-16748

HORN ANTENNAS

Low-backlobe microwave transmitting horn
page 5 NPO-14077

Signal separator for dual-frequency antenna
page 23 NPO-14022

HOT WATER

Performance test for a solar water heater
page 59 MFS-25114

Solar-heating system — performance tests
page 58 MFS-25116

HUMAN FACTORS ENGINEERING

LED display for solo aircraft instrument navigation
page 26 LAR-12292

HUMIDITY

Measuring moisture in the atmosphere
page 110 MFS-25032

HYDRAULIC ACTUATORS

Controller for a Stirling engine
page 128 NPO-14388

HYDROCARBON FUELS

Improved coal-slurry pipeline
page 47 NPO-14425

HYDROGEN EMBRITTLEMENT

Electroplating offers embrittlement protection
page 140 MFS-19330

HYGROMETERS

Measuring moisture in the atmosphere
page 110 MFS-25032

IMAGE ENHANCEMENT

Improving low-illumination video
page 18 MSC-14841

IMAGERY

Analyzing Earth's surface data
page 151 MFS-25051

Electronic pictures from charge-coupled devices
page 17 GSC-12324

High-resolution echocardiography
page 81 NPO-14349

Improved flight-simulator viewing lens
page 50 LAR-12251

Inexpensive land-use maps extracted from satellite
data
page 150 MFS-25111

Landsat and water pollution
page 150 MFS-25099

Optical coupling of tunable diode lasers
page 49 LAR-12438

Projection optics for a laser velocimeter
page 51 LAR-12328

Real-time video-image analysis
page 20 NPO-14282

IMMUNOLOGY

Identification of micro-organisms
page 85 MSC-18358

INDICATING INSTRUMENTS

Electrical indication of airflow rate
page 92 MFS-23873

Precision leveling of large machinery
page 130 NPO-13257

Volume-change indicator for molding
page 122 LAR-12280

INDUCTION MOTORS

Fast-response power saver for induction motors
page 6 MFS-23988

INDUSTRIAL ENERGY

Solar energy in the dairy industry
page 62 NPO-14498

INDUSTRIAL WASTES

Marine chlorophyll a analysis
page 54 LAR-12293

INFRARED DETECTORS

Improved InSb photodiode preamplifier circuit
page 9 NPO-14418

Optical system for multispectral scanner
page 52 MSC-18255

INJURIES

Computers help evaluate skin burns
page 82 NPO-14402

INSOLATION

Sun tracker for clear or cloudy weather
page 42 MFS-23999

INSPECTION

Inspecting cracks in foam insulation
page 107 MFS-23799

Ultrasonic grating checks electron-beam welds
page 95 MFS-19422

INSTRUMENT PACKAGES

Antitheft container for instruments
page 104 GSC-12399

INSULATION

Inspecting cracks in foam insulation
page 107 MFS-23799

Removable fastener for insulating tiles
page 123 MSC-16483

Temporary insulation with polyurethane foam
page 139 MSC-18298

INTEGRATED CIRCUITS

CMOS circuit-fabrication handbook
page 146 MFS-25034

Remote manipulator for IC wafers
page 121 MFS-23846

INTERFEROMETERS

Chevron beam splitter interferometer
page 51 NPO-14502

INVERTERS

Reliable inverter systems
page 29 NPO-14163

IRRADIATION

Irradiation pretreatment for coal desulfurization
page 68 NPO-14104

ISOLATORS

Metallic vibration isolators
page 127 MFS-23949

JIGS

Fixture for assembling solar panels
page 145 NPO-14303

Fixture for limited-access welding
page 136 MSC-16698

JOINTS [JUNCTIONS]

Hing-connected rigid bodies
page 113 NPO-11964

LAND USE

Inexpensive land-use maps extracted from satellite
data
page 150 MFS-25111

LANDSAT DATA

Electronic pictures from charge-coupled devices
page 17 GSC-12324

Inexpensive land-use maps extracted from satellite
data
page 150 MFS-25111

Landsat and water pollution
page 150 MFS-25099

LAQUERS

Applying photosensitive emulsions to enamel
surfaces
page 143 MSC-18107

LASER APPLICATIONS

All-electric gas detector
page 45 NPO-14341

Laser for alinement of large assemblies
page 99 MSC-19346

Low-noise spectrophone
page 46 NPO-14362

LASER DOPPLER VELOCIMETERS

Projection optics for a laser velocimeter
page 51 LAR-12328

LASERS

Optical coupling of tunable diode lasers
page 49 LAR-12438

Projection optics for a laser velocimeter
page 51 LAR-12328

LATCHES

Antenna deployment mechanism
page 120 GSC-12331

LEAKAGE

Extending the range of leak detectors
page 105 MFS-19411

LENSES

Improved flight-simulator viewing lens
page 50 LAR-12251

LEVELING

Precision leveling of large machinery
page 130 NPO-13257

LIGHT EMITTING DIODES

LED display for solo aircraft instrument navigation
page 26 LAR-12292

Simpler cabling and power link for remote readouts
page 30 GSC-12411

LIGHT TRANSMISSION

Fiber-optic crossbar switch
page 8 KSC-11104

Transparent solar cell modules
page 40 NPO-14304

LIGHTNING

Cloud-to-ground lightning detector
page 28 KSC-11099

LIMBS [ANATOMY]

Artificial limb connector
page 83 KSC-11069

LINEAR FILTERS

Fader and ramp shaper replace linear filters
page 34 MSC-16115

LININGS

Annular acoustic liners for turbofan engines
page 132 LEW-12810

LIQUID-GAS MIXTURES

Silicon tetrachloride spray feeder
page 71 NPO-14382

LOAD TESTS

Static load testing of a liquid solar collector
page 59 MFS-25115

LOCKS [FASTENERS]

Antitheft container for instruments
page 104 GSC-12399

LOW FREQUENCIES

Low-frequency attenuator circuit
page 11 FRC-11012



LOW PASS FILTERS

Fader and ramp shaper replace linear filters
page 34 MSC-16115

MAINTENANCE

Cost analysis of hot-air solar-heating systems
page 61 MFS-25092

MANDRELS

Volume-change indicator for molding
page 122 LAR-12280

MANIPULATORS

Remote manipulator for IC wafers
page 121 MFS-23846

MAPPING

Analyzing Earth's surface data
page 151 MFS-25051

Inexpensive land-use maps extracted from satellite
data
page 150 MFS-25111

MARINE ENVIRONMENTS

Marine chlorophyll a analysis
page 54 LAR-12293

MARKOV PROCESSES

Redundant system reliability analysis
page 152 LAR-12069

MASKING

Temporary insulation with polyurethane foam
page 139 MSC-18298

MASS

Accurate measurements of mass and center of
mass
page 96 NPO-14428

MASS SPECTROMETERS

Extending the range of leak detectors
page 105 MFS-19411

MEDICAL ELECTRONICS

Low-frequency attenuator circuit
page 11 FRC-11012

MEDICAL EQUIPMENT

Artificial limb connector
page 83 KSC-11069

MESH

Metallic vibration isolators
page 127 MFS-23949

METAL BONDING

A furnace brazing technique
page 138 MFS-19363

Room-temperature bonding of thin plastic sheets
page 138 NPO-14346

METAL FILMS

Controlled metal-film deposition on alumina
substrates
page 78 ARC-11214

METAL JOINTS

Push test for stitch welds
page 94 MFS-25027

METAL OXIDE-SEMICONDUCTORS

CMOS circuit-fabrication handbook
page 146 MFS-25034

METAL OXIDES

Controlled metal-film deposition on alumina
substrates
page 78 ARC-11214

METEOROLOGICAL INSTRUMENTS

Measuring moisture in the atmosphere
page 110 MFS-25032

MICROBIOLOGY

Identification of micro-organisms
page 85 MSC-18358

MICROMINIATURIZATION

CMOS circuit-fabrication handbook
page 146 MFS-25034

MICROORGANISMS

Identification of micro-organisms
page 85 MSC-18358

MICROWAVE ANTENNAS

Analysis of aperture antenna radiation pattern
page 63 MSC-16246

Low-backlobe microwave transmitting horn

page 5 NPO-14077

MICROWAVE EQUIPMENT

Components for an S-band communication
subsystem
page 24 NPO-13955

Efficient dichroic plate for microwaves
page 4 GSC-12171

Group-delay standards
page 14 NPO-13938

Signal separator for dual-frequency antenna
page 23 NPO-14022

MINING

Ensuring flat cuts in longwall mining
page 117 MFS-23726

MISSION PLANNING

Aircraft mission analysis
page 110 LAR-12299

Goddard trajectory determination
page 112 GSC-11946

MIXING CIRCUITS

Improved isolation in double-balanced mixers
page 13 NPO-14415

MOISTURE METERS

Measuring moisture in the atmosphere
page 110 MFS-25032

MOLDS

Volume-change indicator for molding
page 122 LAR-12280

MOMENTS OF INERTIA

Centroid, moments, and radii of gyration
page 114 LEW-12765

MONITORS

Audible monitor for electroplating
page 106 MFS-19333

Bidirectional fluid-flow monitor
page 92 MSC-16762

Film-advance monitor
page 118 LAR-12474

MOTORS

Fast-response power saver for induction motors
page 6 MFS-23988

MULTIPLEXING

Optical memories in digital computing
page 35 MFS-23897

Simpler cabling and power link for remote readouts
page 30 GSC-12411

MULTIPLIERS

VHF frequency multiplier
page 7 NPO-13700

MULTISPECTRAL BAND SCANNERS

Optical system for multispectral scanner
page 52 MSC-18255

MULTISPECTRAL PHOTOGRAPHY

Marine chlorophyll a analysis
page 54 LAR-12293

NAVIGATION INSTRUMENTS

LED display for solo aircraft instrument navigation
page 26 LAR-12292

NICKEL ALLOYS

Electroplating offers embrittlement protection
page 140 MFS-19330

NOISE REDUCTION

Annular acoustic liners for turbofan engines
page 132 LEW-12810

NOISE SPECTRA

Self-calibrating threshold detector for noisy
signals
page 10 MSC-16370

NONDESTRUCTIVE TESTS

Measuring the thickness of plastic films
page 100 ARC-11219

NUTS (FASTENERS)

Fastening hardware to honeycomb panels
page 141 MSC-16752

O-RING SEALS

Rubber valve seal with tough skin
page 124 LAR-11776

Stiffness and damping of elastomeric O-rings
page 131 LEW-13079

Window with integral seal
page 140 MSC-16490

OILS

Burning crude oil without pollution
page 76 NPO-14344

OPTICAL COMMUNICATION

Fiber-optic crossbar switch
page 8 KSC-11104

OPTICAL COUPLING

Optical coupling of tunable diode lasers
page 49 LAR-12438

OPTICAL EQUIPMENT

Improved flight-simulator viewing lens
page 50 LAR-12251

OPTICAL MEASURING INSTRUMENTS

Chevron beam splitter interferometer
page 51 NPO-14502

Eye-controlled switch
page 84 MFS-25091

Measuring the thickness of plastic films
page 100 ARC-11219

OPTICAL MEMORY [DATA STORAGE]

Optical memories in digital computing
page 35 MFS-23897

OPTICAL PROPERTIES

Transparent solar cell modules
page 40 NPO-14304

OPTICAL REFLECTION

Determination of total surface reflectivity
page 102 MFS-25024

OPTICAL SCANNERS

Optical system for multispectral scanner
page 52 MSC-18255

ORBITAL MECHANICS

Goddard trajectory determination
page 112 GSC-11946

PARACHUTES

Parachute deploy/release mechanism
page 125 LAR-11575

PATTERN RECOGNITION

Real-time video-image analysis
page 20 NPO-14282

PERFORMANCE PREDICTION

Minicomputer version of SPAR
page 113 LAR-12370 and LAR-12371

PERFORMANCE TESTS

Concentrating solar collector — performance tests
page 60 MFS-25086

Liquid solar collector — performance evaluation
page 59 MFS-25090

PHASE CONTROL

Fast-response power saver for induction motors
page 6 MFS-23988

PHASE SHIFT

Group-delay standards
page 14 NPO-13938

PHASE SHIFT KEYING

Decision-directed automatic gain control
page 10 NPO-13639

Improved isolation in double-balanced mixers
page 13 NPO-14415

PHOTODIODES

Improved InSb photodiode preamplifier circuit
page 9 NPO-14418

PHOTOELECTRIC CELLS

Theory of back-surface-field solar cells
page 57 NPO-14451

PHOTOGRAPHIC EMULSIONS

Applying photosensitive emulsions to enamel
surfaces
page 143 MSC-18107

PHOTOGRAPHIC EQUIPMENT

Film-advance monitor
page 118 LAR-12474

PHOTOSENSITIVITY

Applying photosensitive emulsions to enamel
surfaces
page 143 MSC-18107

PHOTOVOLTAIC DEVICES

Assembling solar-cell arrays
page 43 NPO-14416

PILOT TRAINING

Improved flight-simulator viewing lens
page 50 LAR-12251

PIPELINES

Improved coal-slurry pipeline
page 47 NPO-14425

PLASTICS

Room-temperature bonding of thin plastic sheets
page 138 NPO-14346

PLUGGING

Removable fastener for insulating tiles
page 123 MSC-16483

POLLUTION CONTROL

Burning crude oil without pollution
page 76 NPO-14344

Irradiation pretreatment for coal desulfurization
page 68 NPO-14104

Landsat and water pollution
page 150 MFS-25099

POLYMERIC FILMS

Measuring the thickness of plastic films
page 100 ARC-11219

Room-temperature bonding of thin plastic sheets
page 138 NPO-14346

POLYURETHANE FOAM

Temporary insulation with polyurethane foam
page 139 MSC-18298

PORCELAIN

Low-absorptance porcelain-on-aluminum coating
page 75 MFS-23879

PORTS (OPENINGS)

Window with integral seal
page 140 MSC-16490

POTABLE WATER

Continuous sterilization of plumbing systems
page 77 KSC-11085

POWER

An annotated energy bibliography
page 62 LAR-12488

POWER CONDITIONING

Fast-response power saver for induction motors
page 6 MFS-23988

Solar power conditioner
page 41 NPO-14356

POWER EFFICIENCY

Controller for a Stirling engine
page 128 NPO-14388

POWER LINES

Cable-fault locator
page 27 KSC-10899

POWER SUPPLIES

Reliable inverter systems
page 29 NPO-14163

PREAMPLIFIERS

Improved InSb photodiode preamplifier circuit
page 9 NPO-14418

PRINTED CIRCUITS

Troubleshooting plated-wire memories
page 100 MFS-23903

Wraparound contacts for solar cells
page 3 LEW-13089

PROCUREMENT

Cost analysis of hot-air solar-heating systems
page 61 MFS-25092

PRODUCTION ENGINEERING

Remote manipulator for IC wafers
page 121 MFS-23846

PRODUCTION MANAGEMENT

Cost impact from break in production
page 149 MFS-23884

PROSTHETIC DEVICES

Artificial limb connector
page 83 KSC-11069

Eye-controlled switch
page 84 MFS-25091

PROTECTIVE COATINGS

Electroplating offers embrittlement protection
page 140 MFS-19330

PSYCHROMETERS

Measuring moisture in the atmosphere
page 110 MFS-25032

PUMPS

Solar-powered pump
page 39 MFS-23996

PURIFICATION

Continuous sterilization of plumbing systems
page 77 KSC-11085

QUALITY CONTROL

Checking weld penetration
page 95 MFS-19395

Measuring the thickness of plastic films
page 100 ARC-11219

Ultrasonic grating checks electron-beam welds
page 95 MFS-19422

RADAR

Eliminating clutter in synthetic-aperture radar
page 21 NPO-14035

Synthetic-aperture-radar azimuth correlator
page 22 NPO-14019

RADIAL DISTRIBUTION

Vapor-deposited graded-thickness films
page 142 GSC-11806

RADIATION DISTRIBUTION

Analysis of aperture antenna radiation pattern
page 63 MSC-16246

RADIO COMMUNICATION

Self-calibrating threshold detector for noisy
signals
page 10 MSC-16370

RADIO FREQUENCIES

VHF frequency multiplier
page 7 NPO-13700

RADIOGRAPHY

High-resolution echocardiography
page 81 NPO-14349

Improving low-illumination video
page 18 MSC-14841

RAIN

Landsat and water pollution
page 150 MFS-25099

RAMP FUNCTIONS

Fader and ramp shaper replace linear filters
page 34 MSC-16115

RANGEFINDING

Group-delay standards
page 14 NPO-13938

Synthetic-aperture-radar azimuth correlator
page 22 NPO-14019

RANKINE CYCLE

Rankine-cycle heating and cooling systems
page 58 MFS-23998

Rankine-cycle solar-cooling systems
page 57 MFS-25094

REACTORS

Chemical-vapor-deposition reactor
page 73 NPO-14137

READOUT

Simpler cabling and power link for remote readouts
page 30 GSC-12411

RECEIVERS

Decision-directed automatic gain control
page 10 NPO-13639

VHF frequency multiplier
page 7 NPO-13700

REDUNDANT COMPONENTS

Redundant system reliability analysis
page 152 LAR-12069

REFLECTANCE

Determination of total surface reflectivity
page 102 MFS-25024

REFLECTOMETERS

Determination of total surface reflectivity
page 102 MFS-25024

RELIABILITY

Redundant system reliability analysis
page 152 LAR-12069

Reliable inverter systems
page 29 NPO-14163

Reliability of imaging CCD's
page 14 MFS-25039

REMOTE HANDLING

Remote manipulator for IC wafers
page 121 MFS-23846

REMOTE SENSORS

Cloud-to-ground lightning detector
page 28 KSC-11099

Simpler cabling and power link for remote readouts
page 30 GSC-12411

REPAIRING

Repairing cracked glass
page 135 KSC-11097

RETROREFLECTION

Chevron beam splitter interferometer
page 51 NPO-14502

RIGID STRUCTURES

Hinge-connected rigid bodies
page 113 NPO-11964

RIVERS

Landsat and water pollution
page 150 MFS-25099

RIVETS

Fastening hardware to honeycomb panels
page 141 MSC-16752

RUBBER

Rubber valve seal with tough skin
page 124 LAR-11776

SATELLITE OBSERVATION

Monitoring disaster areas via satellites
page 30 LAR-12344

SAWS

A method for cutting silicon
page 144 NPO-14406

SCAFFOLDS

Removable fastener for large structures
page 126 MFS-23990

SCANNERS

Optical system for multispectral scanner
page 52 MSC-18255

SCRUBBERS

Burning crude oil without pollution
page 76 NPO-14344

SEALING

Window with integral seal
page 140 MSC-16490

SEALS [STOPPERS]

Removable fastener for insulating tiles
page 123 MSC-16483

Rubber valve seal with tough skin
page 124 LAR-11776

SECURITY

Antitheft container for instruments
page 104 GSC-12399

SEMICONDUCTOR JUNCTIONS

Theory of back-surface-field solar cells
page 57 NPO-14451



SEMICONDUCTOR LASERS					
Optical coupling of tunable diode lasers			Controller for solar heating — design package		
page 49	LAR-12438		page 61	MFS-25009	
SERVMOTORS			Design of a concentrating solar collector		
A closed-loop control-loading system			page 60	MFS-25098	
page 32	LAR-12167		Effects of weathering on a liquid solar collector		
SHOCK ABSORBERS			page 60	MFS-25113	
Metallic vibration isolators			Liquid solar collector — performance evaluation		
page 127	MFS-23949		page 59	MFS-25090	
SHORT CIRCUITS			Rankine-cycle solar-cooling systems		
Cable-fault locator			page 57	MFS-25094	
page 27	KSC-10899		Solar-powered pump		
SIGNAL FADING			page 39	MFS-23996	
Fader and ramp shaper replace linear filters			Static load testing of a liquid solar collector		
page 34	MSC-16115		page 59	MFS-25115	
SIGNAL RECEPTION			Sun tracker for clear or cloudy weather		
Decision-directed automatic gain control			page 42	MFS-23999	
page 10	NPO-13639		SOLAR ENERGY		
Self-calibrating threshold detector for noisy			A reactor for more efficient solar cells		
signals			page 72	NPO-14381	
page 10	MSC-16370		Air solar collector — installation package		
Signal separator for dual-frequency antenna			page 59	MFS-25031	
page 23	NPO-14022		Design of a concentrating solar collector		
SIGNAL TRANSMISSION			page 60	MFS-25098	
TV audio and video on the same channel			Effects of weathering on a liquid solar collector		
page 19	MSC-16241		page 60	MFS-25113	
SILANES			Performance test for a solar water heater		
Chemical-vapor-deposition reactor			page 59	MFS-25114	
page 73	NPO-14137		Rankine-cycle heating and cooling systems		
SILICON			page 58	MFS-23998	
A continuous silicon-coating facility			Rankine-cycle solar-cooling systems		
page 70	NPO-14373		page 57	MFS-25094	
A method for cutting silicon			Solar energy in the dairy industry		
page 144	NPO-14406		page 62	NPO-14498	
A reactor for more efficient solar cells			Solar-heating system — performance tests		
page 72	NPO-14381		page 58	MFS-25116	
Silicon source for vacuum deposition			Solar power conditioner		
page 74	LAR-12356		page 41	NPO-14356	
SILICON TETRACHLORIDE			Solar-powered pump		
Silicon tetrachloride spray feeder			page 39	MFS-23996	
page 71	NPO-14382		Static load testing of a liquid solar collector		
SIMULATION			page 59	MFS-25115	
Dynamic simulation and stability analysis			Theory of back-surface-field solar cells		
page 111	GSC-12422		page 57	NPO-14451	
SKIN [ANATOMY]			Transparent solar cell modules		
Computers help evaluate skin burns			page 40	NPO-14304	
page 82	NPO-14402		Variable-shape solar-energy concentrator		
SKIN [STRUCTURAL MEMBER]			page 44	NPO-13736	
Fastening hardware to honeycomb panels			Wraparound contacts for solar cells		
page 141	MSC-16752		page 3	LEW-13089	
SLURRIES			SOLAR ENERGY ABSORBERS		
Characterizing glass frits for slurries			Low-absorptance porcelain-on-aluminum coating		
page 103	MSC-18322		page 75	MFS-23879	
Improved coal-slurry pipeline			SOLAR HEATING		
page 47	NPO-14425		Concentrating solar collector — performance tests		
SODIUM CARBONATES			page 60	MFS-25086	
Soda ash removes sulfur from fuels			Controller for solar heating — design package		
page 69	GSC-12403		page 61	MFS-25009	
SOLAR CELLS			Cost analysis of hot-air solar-heating systems		
A reactor for more efficient solar cells			page 61	MFS-25092	
page 72	NPO-14381		Design information for solar-heating systems		
Assembling solar-cell arrays			page 58	MFS-25097	
page 43	NPO-14416		Design of a concentrating solar collector		
Electrical insulation for an aluminum plate			page 60	MFS-25098	
page 143	MFS-25007		Liquid solar collector — performance evaluation		
Fixture for assembling solar panels			page 59	MFS-25090	
page 145	NPO-14303		Rankine-cycle heating and cooling systems		
Theory of back-surface-field solar cells			page 58	MFS-23998	
page 57	NPO-14451		Solar-powered pump		
Transparent solar cell modules			page 39	MFS-23996	
page 40	NPO-14304		SOLAR POSITION		
Wraparound contacts for solar cells			Sun tracker for clear or cloudy weather		
page 3	LEW-13089		page 42	MFS-23999	
SOLAR COLLECTORS			SPECIFIC HEAT		
Concentrating solar collector — performance tests			Containerless high-temperature calorimeter		
page 60	MFS-25086		page 89	MFS-23923	
			SPECTROMETERS		
			Improved InSb photodiode preamplifier circuit		
			page 9	NPO-14418	
			Optical coupling of tunable diode lasers		
			page 49	LAR-12438	
			Optical system for multispectral scanner		
			page 52	MSC-18255	
			SPEED CONTROL		
			Controller for a Stirling engine		
			page 128	NPO-14388	
			SPOT WELDS		
			Giant-electrode welder		
			page 137	LAR-11429	
			SPRAY NOZZLES		
			Silicon tetrachloride spray feeder		
			page 71	NPO-14382	
			SPRAYED COATINGS		
			Inspecting cracks in foam insulation		
			page 107	MFS-23799	
			STANDARDS		
			Group-delay standards		
			page 14	NPO-13938	
			STARK EFFECT		
			All-electric gas detector		
			page 45	NPO-14341	
			Low-noise spectrophone		
			page 46	NPO-14362	
			STATIC PRESSURE		
			Static load testing of a liquid solar collector		
			page 59	MFS-25115	
			STERILIZATION		
			Continuous sterilization of plumbing systems		
			page 77	KSC-11085	
			STRAIN GAGES		
			Attaching strain transducers to fragile materials		
			page 106	MSC-16580	
			STRUCTURAL ANALYSIS		
			Minicomputer version of SPAR		
			page 113	LAR-12370 and LAR-12371	
			STRUCTURAL STABILITY		
			Dynamic simulation and stability analysis		
			page 111	GSC-12422	
			STEAM		
			Solar-powered pump		
			page 39	MFS-23996	
			STIRLING CYCLE		
			Controller for a Stirling engine		
			page 128	NPO-14388	
			SULFUR		
			Burning crude oil without pollution		
			page 76	NPO-14344	
			Soda ash removes sulfur from fuels		
			page 69	GSC-12403	
			SURFACE FINISHING		
			Applying photosensitive emulsions to enamel		
			surfaces		
			page 143	MSC-18107	
			SURFACE PROPERTIES		
			Determination of total surface reflectivity		
			page 102	MFS-25024	
			SURVEYS		
			Analyzing Earth's surface data		
			page 151	MFS-25051	
			SWITCHES		
			Fiber-optic crossbar switch		
			page 8	KSC-11104	
			SWITCHING CIRCUITS		
			A telephone multiline signaling system		
			page 33	KSC-11023	
			Reliable inverter systems		
			page 29	NPO-14163	
			SWITCHING ELEMENTS		
			Components for an S-band communication		
			subsystem		
			page 24	NPO-13955	
			SYNTHETIC ARRAYS		
			Eliminating clutter in synthetic-aperture radar		
			page 21	NPO-14035	

SYSTEM EFFECTIVENESS

Redundant system reliability analysis
page 152 LAR-12069

TEFLON [TRADEMARK]

Friction coefficients of PTFE bearing liner
page 110 MFS-19389

TELEPHONES

A telephone multiline signaling system
page 33 KSC-11023

TELEVISION EQUIPMENT

Electronic pictures from charge-coupled devices
page 17 GSC-12324

Improving low-illumination video
page 18 MSC-14841

Real-time video-image analysis
page 20 NPO-14282

TELEVISION TRANSMISSION

TV audio and video on the same channel
page 19 MSC-16241

TEMPERATURE CONTROL

Containerless high-temperature calorimeter
page 89 MFS-23923

TEMPERATURE EFFECTS

Friction coefficients of PTFE bearing liner
page 110 MFS-19389

TEMPLATES

Plug and drill template
page 119 MSC-16748

TEST FACILITIES

Test configuration identifiers
page 103 KSC-11087

THERMAL INSULATION

Inspecting cracks in foam insulation
page 107 MFS-23799

Measuring insulation thickness
page 108 MFS-23798

THERMODYNAMIC PROPERTIES

Containerless high-temperature calorimeter
page 89 MFS-23923

THERMOSETTING RESINS

Volume-change indicator for molding
page 122 LAR-12280

THICKNESS

Measuring insulation thickness
page 108 MFS-23798

Measuring the thickness of plastic films
page 100 ARC-11219

THIN FILMS

Chemical-vapor-deposition reactor
page 73 NPO-14137

Controlled metal-film deposition on alumina
substrates
page 78 ARC-11214

THUNDERSTORMS

Cloud-to-ground lightning detector
page 28 KSC-11099

TILES

Repairing cracked glass
page 135 KSC-11097

TOPOGRAPHY

Analyzing Earth's surface data
page 151 MFS-25051

TORQUE

Controller for a Stirling engine
page 128 NPO-14388

TRACKING [POSITION]

Sun tracker for clear or cloudy weather
page 42 MFS-23999

TRAJECTORY ANALYSIS

Goddard trajectory determination
page 112 GSC-11946

TRANSDUCERS

Attaching strain transducers to fragile materials
page 106 MSC-16580

TRANSMISSIVITY

Measuring the thickness of plastic films
page 100 ARC-11219

TRANSPARENCE

Transparent solar cell modules
page 40 NPO-14304

TROUBLESHOOTING

Troubleshooting plated-wire memories
page 100 MFS-23903

TRUSSES

Removable fastener for large structures
page 126 MFS-23990

TUNNELING [EXCAVATION]

Ensuring flat cuts in longwall mining
page 117 MFS-23726

TURBOFAN ENGINES

Annular acoustic liners for turbofan engines
page 132 LEW-12810

TURBOMACHINERY

Stiffness and damping of elastomeric O-rings
page 131 LEW-13079

ULTRASONIC TESTS

High-resolution echocardiography
page 81 NPO-14349

Ultrasonic grating checks electron-beam welds
page 95 MFS-19422

VACUUM DEPOSITION

Silicon source for vacuum deposition
page 74 LAR-12356

Vapor-deposited graded-thickness films
page 142 GSC-11806

VACUUM FURNACES

A furnace brazing technique
page 138 MFS-19363

VALVES

Quartz ball valve
page 127 NPO-14473

Rubber valve seal with tough skin
page 124 LAR-11776

VAPOR DEPOSITION

Chemical-vapor-deposition reactor
page 73 NPO-14137

Silicon source for vacuum deposition
page 74 LAR-12356

Vapor-deposited graded-thickness films
page 142 GSC-11806

VELOCITY DISTRIBUTION

Projection optics for a laser velocimeter
page 51 LAR-12328

VERY HIGH FREQUENCIES

VHF frequency multiplier
page 7 NPO-13700

VIBRATION DAMPING

Stiffness and damping of elastomeric O-rings
page 131 LEW-13079

VIBRATION ISOLATORS

Metallic vibration isolators
page 127 MFS-23949

VIDEO COMMUNICATION

Real-time video-image analysis
page 20 NPO-14282

TV audio and video on the same channel
page 19 MSC-16241

VISUAL CONTROL

Eye-controlled switch
page 84 MFS-25091

VOLTAGE REGULATORS

Solar power conditioner
page 41 NPO-14356

VOLUME

Volume-change indicator for molding
page 122 LAR-12280

WAFERS

Remote manipulator for IC wafers
page 121 MFS-23846

WARNING SYSTEMS

Cloud-to-ground lightning detector
page 28 KSC-11099

WASTE DISPOSAL

Marine chlorophyll a analysis
page 54 LAR-12293

WATER HEATERS

Performance test for a solar water heater
page 59 MFS-25114

WATER LOSS

"Self-packaging" desiccant
page 67 NPO-14354

WATER POLLUTION

Landsat and water pollution
page 150 MFS-25099

Marine chlorophyll a analysis
page 54 LAR-12293

WATER VAPOR

Measuring moisture in the atmosphere
page 110 MFS-25032

WEATHERING

Effects of weathering on a liquid solar collector
page 60 MFS-25113

WEIGHT [MASS]

Accurate measurements of mass and center of
mass
page 96 NPO-14428

WELD TESTS

Nondestructive pull tester
page 93 MSC-18329

Push test for stitch welds
page 94 MFS-25027

WELDING

Checking weld penetration
page 95 MFS-19395

Fixture for limited-access welding
page 136 MSC-16698

Giant-electrode welder
page 137 LAR-11429

Removable fastener for large structures
page 126 MFS-23990

Ultrasonic grating checks electron-beam welds
page 95 MFS-19422

WHEELCHAIRS

Eye-controlled switch
page 84 MFS-25091

WIND TUNNEL TESTS

Projection optics for a laser velocimeter
page 51 LAR-12328

WINDOWS [APERTURES]

Window with integral seal
page 140 MSC-16490

WIRING

Nondestructive pull tester
page 93 MSC-18329

Push test for stitch welds
page 94 MFS-25027



National Aeronautics and
Space Administration


Washington, D.C.
20546

Official Business
Penalty for Private Use \$300

SPECIAL FOURTH-CLASS RATE
BOOK

FOURTH-CLASS MAIL
POSTAGE & FEES PAID
NASA
WASHINGTON, D.C.
PERMIT No. G 27

NASA



A high-temperature self-lubricating coating for bearings, developed at NASA's Lewis Research Center, is applied by plasma-spraying. Effective at temperatures to 1,650° F, the coated bearings have found uses in jet-engine control systems, piston rings for reciprocating compressors, and many other high-temperature applications.